EBM Experimental Biology and Medicine

Volume 251 | Issue 2

Experimental Biology and Medicine

Editor-in-Chief

Nicola Conran
University of Campinas, Brazil

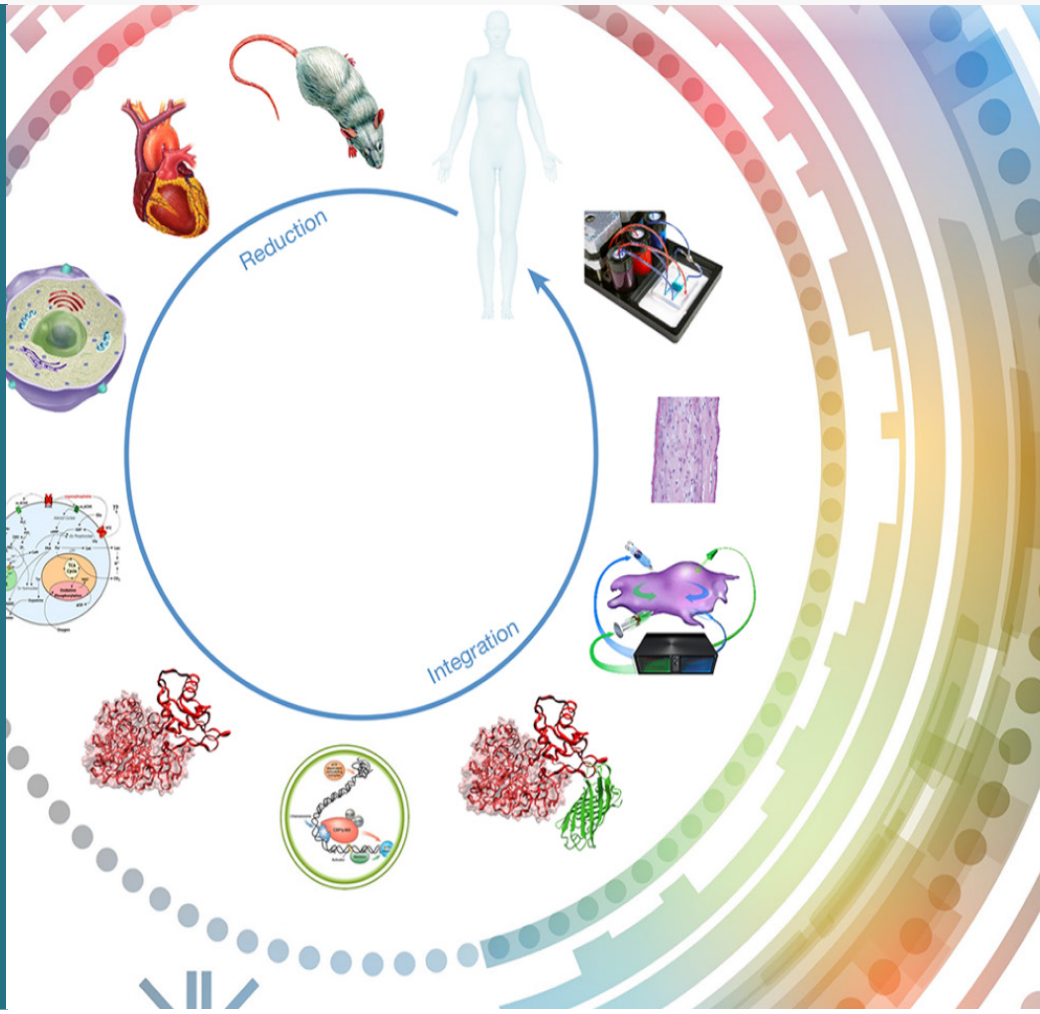

ISBN 978-2-8325-7666-3
DOI 10.3389/978-2-8325-7666-3

frontiers | Publishing Partnerships

Society for Experimental Biology and Medicine
3220 N Street NW, #179
Washington DC 20007, USA
Executive Director – ed@sebm.org

www.sebm.org

EBM Experimental Biology and Medicine

Editorial Board

ISSN 1535-3699
ISBN 978-2-8325-7666-3
DOI 10.3389/978-2-8325-7666-3

Generative AI statement
Any alternative text (Alt text) provided alongside figures in the articles in this ebook has been generated by Frontiers with the support of artificial intelligence and reasonable efforts have been made to ensure accuracy, including review by the authors wherever possible. If you identify any issues, please contact us.

EBM Experimental Biology and Medicine

2026 | Volume 251 | Issue 2 | ISSN 1535-3699

Table of contents

Immunology

Neuroscience

Pharmacology and Toxicology

Highlight

EBM Experimental Biology and Medicine

TYPE Original Research
PUBLISHED 26 January 2026
DOI 10.3389/ebm.2025.10601

OPEN ACCESS

*CORRESPONDENCE
Yuhong Tao,
TaoYuhong16@163.com
Hui Guo,
guohui02411@126.com

RECEIVED 26 March 2025
REVISED 24 September 2025
ACCEPTED 24 November 2025
PUBLISHED 26 January 2026

CITATION
Zeng S, Tao Y and Guo H (2026) Role of NAD metabolism-related genes in diabetic nephropathy: subtype classification, biomarker identification, and association with renal function. *Exp. Biol. Med.* 250:10601. doi: 10.3389/ebm.2025.10601

Role of NAD metabolism-related genes in diabetic nephropathy: subtype classification, biomarker identification, and association with renal function

Shengnan Zeng[1,2], Yuhong Tao[1,2]* and Hui Guo[1,2]*

[1]Department of Pediatric Nephrology, West China Second Hospital, Sichuan University, Chengdu, China, [2]Key Laboratory of Birth Defects and Related Diseases of Women and Children (Sichuan University), Ministry of Education, Chengdu, China

Abstract

Diabetic nephropathy (DN) remains a major complication of diabetes, significantly impacting renal function. Emerging evidence suggests that NAD metabolism plays a crucial role in DN pathogenesis. This study investigates the roles of NAD metabolism-related genes in DN and how there are associated with different disease subtypes. We analyzed gene expression data from DN-associated datasets (GSE30528 and GSE30529) to identify differences in NAD metabolism-related genes between normal and DN samples. We classified DN into subtypes based on NAD gene expression and evaluated NAD scores using ssGSEA. Immune cell infiltration and pathway analyses were assessed using ssGSEA, Microenvironment Cell Populations-counter (MCPcounter), and Gene Set Variation Analysis (GSVA). Key biomarker genes were identified using machine learning algorithms and validated across multiple datasets. We further explored the relationship between gene expression and kidney function using the Nephroseq V5 tool. Thirteen differentially expressed NAD metabolism-related genes were identified, with distinctive expression patterns observed between normal and DN samples. Two distinct NAD-related subtypes were classified, demonstrating significant differences in gene expression, immune cell infiltration, and pathway activities. Immune-related pathways and cellular processes exhibited varied enrichment between subtypes. Six key NAD metabolism-related genes (FMO3, ALDH1A3, FMO5, TKT, LBR, HPGD) were identified as potential biomarkers. Higher levels of FMO3, ALDH1A3, TKT, and LBR were linked to worse kidney function, while FMO5 and HPGD were associated with better kidney function. The study highlights the significant involvement of NAD metabolism-related genes in DN pathogenesis and their association with disease subtypes and renal function. The identified biomarkers could be targets for new treatments and provide insight for future DN research.

KEYWORDS

diabetic nephropathy, redox, immune cell infiltration, bioinformatics, machine learning

Impact statement

Our findings highlight the significant involvement of NAD metabolism-related genes in DN pathogenesis and underscore their potential as biomarkers for disease classification and therapeutic intervention. This study provides a foundation for future research into DN mechanisms and underscores the translational potential of targeting NAD metabolism in DN treatment strategies.

Introduction

Diabetic nephropathy (DN) is acknowledged as a primary contributor to end-stage renal disease (ESRD) and a serious complication of diabetes mellitus, impacting millions globally [1]. The progressive characteristics of DN, which include albuminuria, a diminishing glomerular filtration rate (GFR), and eventual renal failure, place a significant strain on healthcare systems and highlight the urgent need for effective diagnostic and treatment approaches [2, 3]. The development of DN is influenced by multiple factors and involves a complex interaction of hemodynamic and metabolic elements. Persistent hyperglycemia triggers various pathogenic mechanisms, such as the activation of the renin-angiotensin-aldosterone system (RAAS), increased formation of advanced glycation end products (AGEs), oxidative stress, inflammation, and fibrosis [4–6]. These interconnected processes lead to glomerular hypertrophy, thickening of the basement membrane, loss of podocytes, and tubulointerstitial fibrosis, ultimately resulting in progressive renal impairment and ESRD [7, 8].

Nicotinamide adenine dinucleotide (NAD) metabolism plays a pivotal role in cellular bioenergetics, redox reactions, and signaling pathways [9]. NAD serves as a coenzyme in redox reactions, crucial for ATP production and cellular metabolism [10]. It also functions as a substrate for enzymes involved in post-translational modifications, such as sirtuins and poly (ADP-ribose) polymerases (PARPs), which are essential for DNA repair, gene expression regulation, and maintaining genomic stability [11, 12]. In the context of chronic kidney disease and DN, NAD metabolism has garnered attention due to its involvement in inflammatory and oxidative stress responses, mitochondrial dysfunction, and cellular senescence [13, 14]. Studies have demonstrated that NAD levels decline with age and in various disease states, including CKD and DN, contributing to exacerbated renal damage and impaired renal function [15–17]. NAD+ supplementation has been shown to ameliorate kidney injury in animal models, highlighting its potential as a therapeutic target [18].

However, despite these findings, the specific roles of NAD metabolism-related genes in DN pathogenesis and their potential as biomarkers for disease subtypes and renal function remain poorly understood. This study aims to fill this knowledge gap by investigating the expression and function of NAD metabolism-related genes in DN. We will classify DN subtypes based on their expression profiles and identify potential biomarkers that correlate with renal function. Figure 1 presents the flow chart of the study. Initially, NAD-related genes were extracted from the Molecular Signatures Database and differentially expressed genes (DEGs) were identified from datasets GSE30528 and GSE30529. Combining these sources, 13 NAD metabolism-related genes were determined. This set of genes underwent machine learning analysis, resulting in the identification of 6 signature genes. Concurrently, these 13 genes were used to classify samples into NAD-related subtypes, followed by enrichment analysis, immune correlation studies, and Gene Set Variation Analysis (GSVA). Finally, the expression of six marker genes was validated using additional datasets GSE96804, GSE104954, and GSE142025. The correlation between these marker genes and glomerular filtration rate (GFR) was assessed via the Nephroseq V5 tool, comprehensively elucidating their underlying mechanisms in DN.

Our findings highlight the significant involvement of NAD metabolism-related genes in DN pathogenesis and underscore their potential as biomarkers for disease classification and therapeutic intervention. This study provides a foundation for future research into DN mechanisms and underscores the translational potential of targeting NAD metabolism in DN treatment strategies.

Materials and methods

Data collection and preprocessing

The gene expression datasets GSE30528 and GSE30529 were obtained from the Gene Expression Omnibus (GEO) database. The raw expression matrix was extracted using the Affy package (version 1.86.0). Gene annotations were mapped using the GPL571 platform annotation file. For genes represented by multiple probes, the expression value was calculated as the average expression of the corresponding probes. Genes and samples with more than 50% missing values were excluded from further analysis to maintain data integrity. Finally, to standardize gene expression levels across samples, median normalization was applied.

Identification of NAD metabolism-related genes

Differential expression analysis of NAD metabolism-related genes between DN and normal samples was performed using the limma package (version 3.52.2) in R software (version 4.2.1). The analysis employed empirical Bayes statistics with moderated t-tests to identify significantly differentially expressed genes.

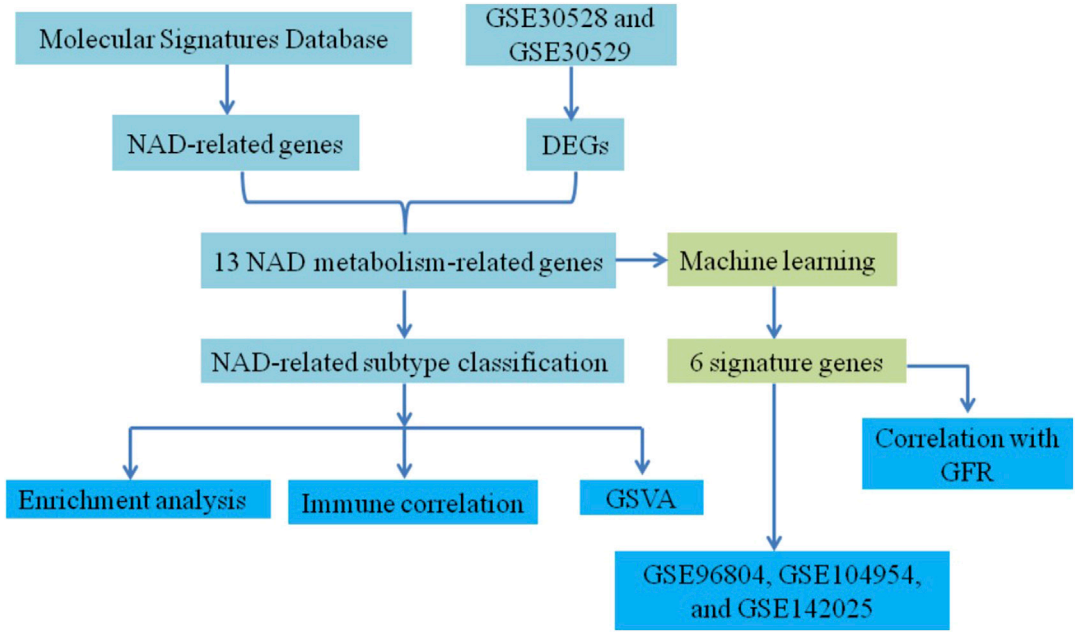

FIGURE 1
Flowchart of the study.

Statistical significance was determined using the adjusted p-value < 0.05 (false discovery rate correction using the Benjamini-Hochberg method). Genes meeting the threshold were considered significantly differentially expressed and included in subsequent analyses. A volcano plot was generated to visualize the DEGs, and a heatmap was created using the Complexheatmap package (version 2.13.1) to illustrate the expression patterns of the identified NAD metabolism-related genes. Box plots were constructed to further delineate the expression levels, confirming statistically significant differences. Correlation analysis among the NAD metabolism-related genes was conducted using the ggplot2 package (version 3.4.4), and results were visualized in a correlation pie chart.

NAD score evaluation

The single-sample Gene Set Enrichment Analysis (ssGSEA) algorithm from the GSVA package (version 1.44.5) was utilized to calculate NAD scores for each sample. The NAD metabolism gene sets were obtained from Molecular Signatures Database, including six pathways: GOBP_CELL_REDOX_HOMEOSTASIS, GOBP_NADP_METABOLIC_PROCESS, GOMF_NAD_BINDING, GOMF_NADP_BINDING, GOMF_NADPH_BINDING, and GOBP_NADPH_REGENERATION. The expression profiles of the genes within these sets were used to compute the enrichment scores for each sample. Normalization was performed using the z-score transformation to ensure comparability across samples.

Subtype classification

Based on the expression profiles of the 13 NAD metabolism-related genes, samples were classified into two NAD-related subtypes (subtype1 and subtype2) utilized the ConsensusClusterPlus package. The consensus clustering was performed with the following parameters: Pearson correlation distance metric, partitioning around medoids (PAM) clustering algorithm, maximum cluster number (k) tested from 2 to 10, 10 resampling iterations, and 80% subsampling ratio. The optimal number of clusters was determined based on the consensus matrix heatmap, consensus cumulative distribution function (CDF), and delta area plot. Cluster stability was assessed using silhouette analysis, and the clustering solution with the highest average silhouette score and most stable consensus was selected. Differential expression analysis between these subtypes was performed, and a volcano plot was generated to visualize the results.

Enrichment analysis

Gene Ontology (GO) and Kyoto Encyclopedia of Genes and Genomes (KEGG) pathway enrichment analyses were conducted using the clusterProfiler package (version 4.4.4). The results were visualized using lollipop and bubble plots to identify significant biological processes and pathways associated with the DEGs.

Immune cell infiltration analysis

The ssGSEA algorithm was again applied to assess immune cell infiltration levels between the two NAD-related subtypes. The MCPcounter package (version 1.2.0) was utilized to further evaluate immune cell types, and correlation analyses were performed to explore associations between NAD scores and immune cell infiltration levels.

Machine learning for biomarker identification

To identify key NAD metabolism-related biomarker genes, three machine learning algorithms were employed: LASSO regression, Random Forest (RF), and Support Vector Machine-Recursive Feature Elimination (SVM-RFE). For LASSO regression, the regularization parameter (lambda) was optimized through 10-fold cross-validation using cv.glmnet function, selecting the lambda value that minimized cross-validation error (lambda.min). For Random Forest, we used the randomForest package (version 4.7.1.1), setting the number of trees (ntree) to 500 and the number of variables tried at each split (mtry) to the square root of the total number of features. Hyperparameter tuning was conducted using grid search combined with 10-fold cross-validation to find the best mtry value. For SVM-RFE, the e1071 package (version 1.7.13) was used with a linear kernel. Feature selection was performed recursively, and the optimal number of features was determined through 10-fold cross-validation. The optimal features were determined, and a Venn diagram was created to illustrate the common genes identified across the algorithms.

Validation of biomarker genes

The expression of key NAD metabolism-related marker genes was validated using three independent datasets (GSE96804, GSE104954, and GSE142025). The relevant information for those datasets is presented in Supplementary Table S1.

Association with renal function

The relationship between NAD metabolism-related hub genes and renal function in DN patients was evaluated using the Nephroseq V5 tool.[1] The glomerular filtration rate (GFR) was used as a measure of renal function. Correlation analyses were performed to assess the associations between the expression levels of NAD metabolism-related hub genes and GFR. These analyses were conducted to provide a comprehensive understanding of the impact of gene expression on renal function in DN patients.

Results

Analysis of differentially expressed NAD metabolism-related genes in DN

NAD metabolism is essential for many cellular processes, including energy production, DNA repair, and regulation of cellular stress responses. Given its central role in maintaining cellular homeostasis, dysregulation of NAD metabolism is implicated in various diseases, including diabetic nephropathy (DN). Therefore, identifying differentially expressed NAD metabolism-related genes in DN could provide insights into the molecular mechanisms underlying this disease. The analysis of differential expression in the DN-associated combined datasets (GSE30528 and GSE30529) identified 13 differentially expressed NAD metabolism-related genes, visualized in the volcano plot (Figure 2A). Expression profiling of these 13 genes was conducted and illustrated through a heatmap, showcasing distinct expression patterns between normal and DN samples (Figure 2B). The corresponding box plot further delineates the expression levels of these genes, with statistically significant differences observed (**$p < 0.01$ and ***$p < 0.001$), reinforcing the differential expression identified (Figure 2C). Correlation analysis of the 13 NAD metabolism-related genes was visualized using a correlation pie chart (Figure 2D). This analysis underscored significant correlations among the genes, suggesting intricate co-regulatory mechanisms within the context of NAD metabolism in DN. Moreover, the NAD metabolism-related genes played a role in pathways related to fatty acid metabolism (Supplementary Figure S1). Overall, these findings highlight the critical role of NAD metabolism-related genes in DN, laying the groundwork for future research into their functional roles and potential as therapeutic targets.

NAD score evaluation and subtype classification in DN

Using the ssGSEA algorithm, we assessed the NAD score levels between the control group and the DN group. The NAD score was significantly increased in the DN group compared to the control group, as illustrated in Figure 3A (***$p < 0.001$). Based on the expression profiles of the 13 differentially expressed NAD-related genes, we classified the samples into two distinct NAD-related subtypes: C1 and C2 (Figure 3B). Differential

1 https://nephroseq.org/

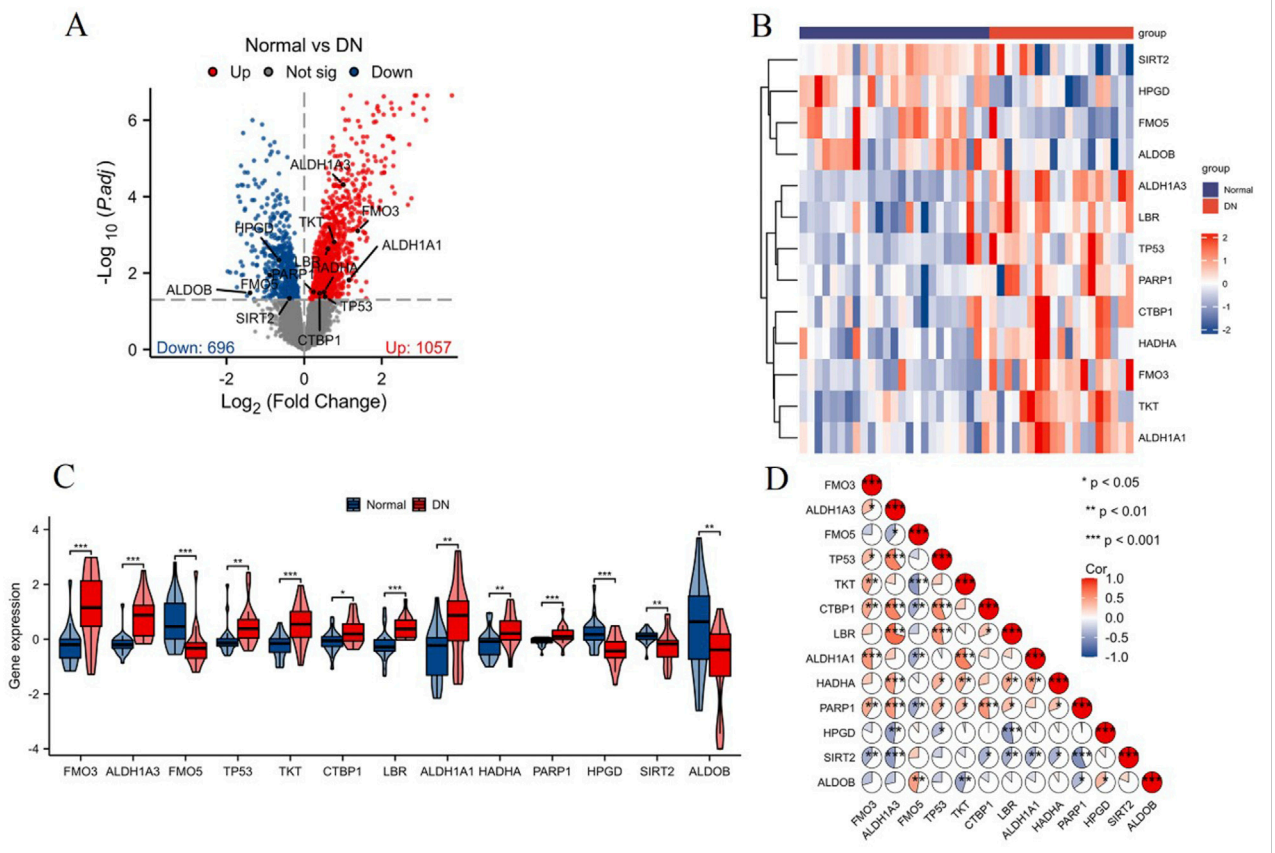

FIGURE 2
Analysis of differentially expressed NAD metabolism-related genes in DN. **(A)** Volcano plot showing 13 differentially expressed NAD metabolism-related genes identified in the combined datasets (GSE30528 and GSE30529). Significantly upregulated genes are highlighted in red, while downregulated genes are highlighted in blue. **(B)** Heatmap illustrating the expression levels of these 13 genes across normal and DN samples. Red indicates higher expression, and blue indicates lower expression. **(C)** Box plots showing the expression distribution of the 13 NAD metabolism-related genes in normal (blue) and DN (red) samples. Statistically significant differences are indicated by *p < 0.05, **p < 0.01, ***p < 0.001. **(D)** Correlation pie chart displaying the correlations among the 13 NAD metabolism-related genes. Positive correlations are shown in red, negative correlations in blue, with the significance levels noted as *p < 0.05, **p < 0.01, ***p < 0.001.

expression analysis between the C1 and C2 subtypes is presented in Figure 3C. The volcano plot depicts a significant number of genes being differentially expressed between the subtypes, with 1993 genes upregulated and 1281 genes downregulated in subtype C2 compared to subtype C1. Enrichment analysis of DEGs between C1 and C2 highlighted several key biological processes and signaling pathways. The Gene Ontology (GO) enrichment analysis (Figure 3D) revealed significant enrichment in molecular functions such as peptidase regulator activity and collagen binding, cellular components including extracellular matrix and secretory granule lumen, and biological processes such as humoral immune response, leukocyte mediated immunity, regulation of endopeptidase activity and cell adhesion. The KEGG pathway enrichment analysis (Figure 3E) identified several pathways significantly associated with the DEGs, including ECM-receptor interaction, focal adhesion, and phagosome. Notably, pathways involved in immune response and infection, such as systemic lupus erythematosus and *Staphylococcus aureus* infection, were also enriched, indicating potential roles in DN pathogenesis. The results of the functional enrichment analysis are presented in Supplementary Table S2. These results collectively highlight the heterogeneity in NAD metabolism-related gene expression in DN and underscore the relevance of specific pathways and biological processes in the disease pathology, providing valuable insights into potential therapeutic targets for DN.

Immune cell infiltration analysis in NAD-related subtypes of DN

Using the ssGSEA algorithm, we assessed the NAD score levels between the two NAD-related subtypes (Subtype 1 and Subtype 2). The results, depicted in Figure 4A, show that Subtype

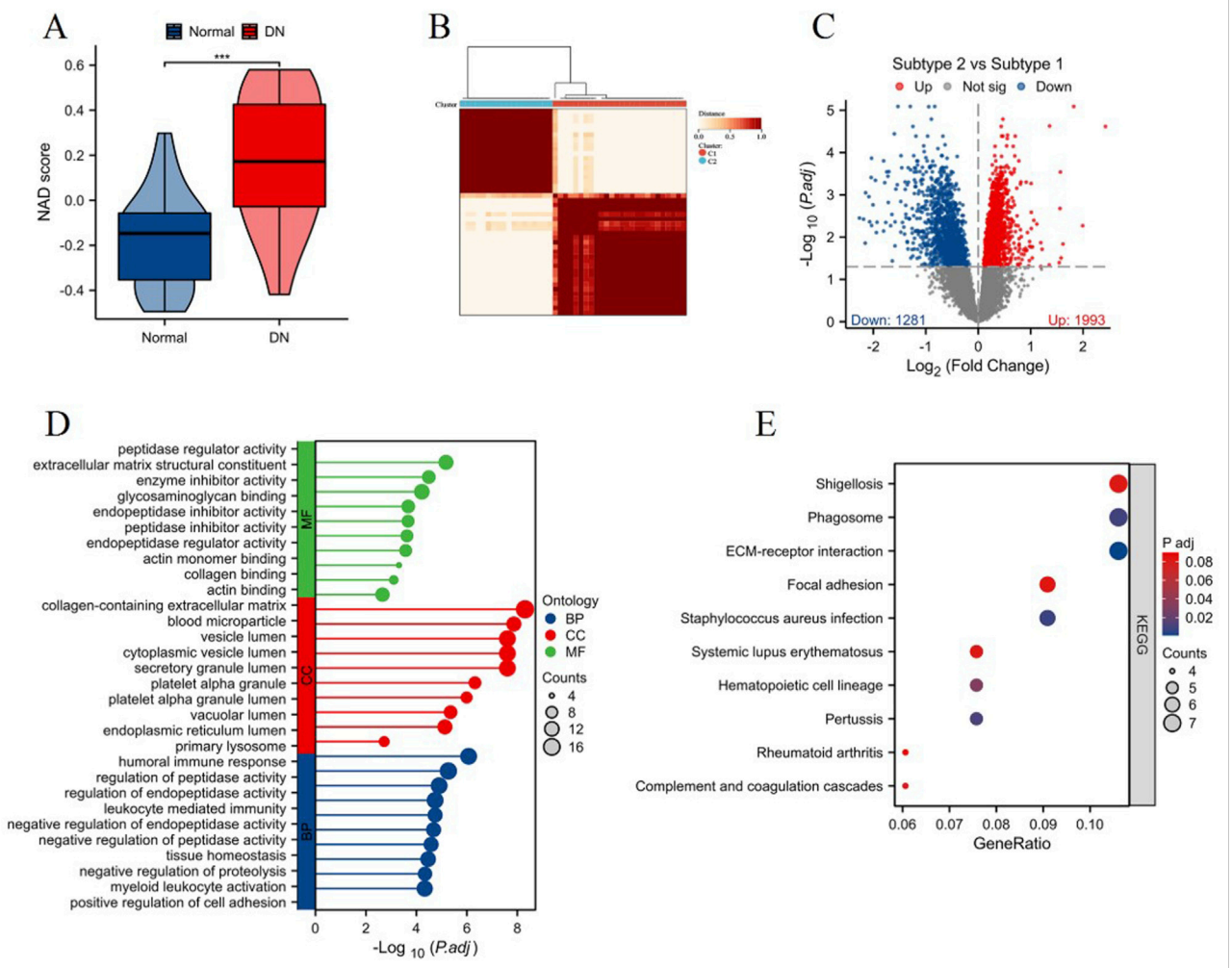

FIGURE 3
Analysis of NAD score and NAD-related subtypes in DN. **(A)** Violin plot showing the NAD score levels in control (blue) and DN (red) groups, assessed using the ssGSEA algorithm. **(B)** Heatmap depicting the clustering of samples into two NAD-related subtypes (C1 and C2) based on the expression profiles of 13 differentially expressed NAD-related genes. **(C)** Volcano plot displaying the differential expression analysis between subtypes C1 and C2. Significant upregulated genes in C2 compared to C1 are shown in red, and downregulated genes are shown in blue. **(D)** Gene Ontology (GO) enrichment analysis of differentially expressed genes between C1 and C2 subtypes, showing significantly enriched molecular functions (MF), cellular components (CC), and biological processes (BP). **(E)** KEGG pathway enrichment analysis illustrating the significant pathways associated with differentially expressed genes between the two subtypes.

1 exhibited a significantly higher NAD score compared to Subtype 2 (***$p < 0.001$). This indicates a differential NAD metabolic state between the two subtypes. We then evaluated the levels of immune cell infiltration between the two subtypes using the ssGSEA algorithm. As shown in Figure 4B, Subtype 1 had significantly higher infiltration levels of various immune cells including macrophages, T cells, TFH, and T helper cells. Complementing the ssGSEA analysis, the MCPcounter algorithm was utilized to further assess the immune cell infiltration between the two subtypes (Figure 4C). Consistent with the ssGSEA results, Subtype 1 showed significantly higher levels of fibroblasts and T cells compared to Subtype 2. These findings reinforce the notion of varied immune profiles between the NAD-related subtypes. Correlation analysis between NAD scores and immune cell infiltration levels revealed significant associations (Figure 4D). Specifically, NAD scores positively correlated with the infiltration levels of T helper cells, fibroblasts, and macrophages. Conversely, negative correlations were observed with NK CD56dim cells, Th1 cells, eosinophils, and NK cells. These results collectively demonstrate that NAD metabolic states are closely linked with immune cell infiltration profiles, offering valuable insights into the pathophysiological mechanisms underlying DN and potential avenues for targeted therapies.

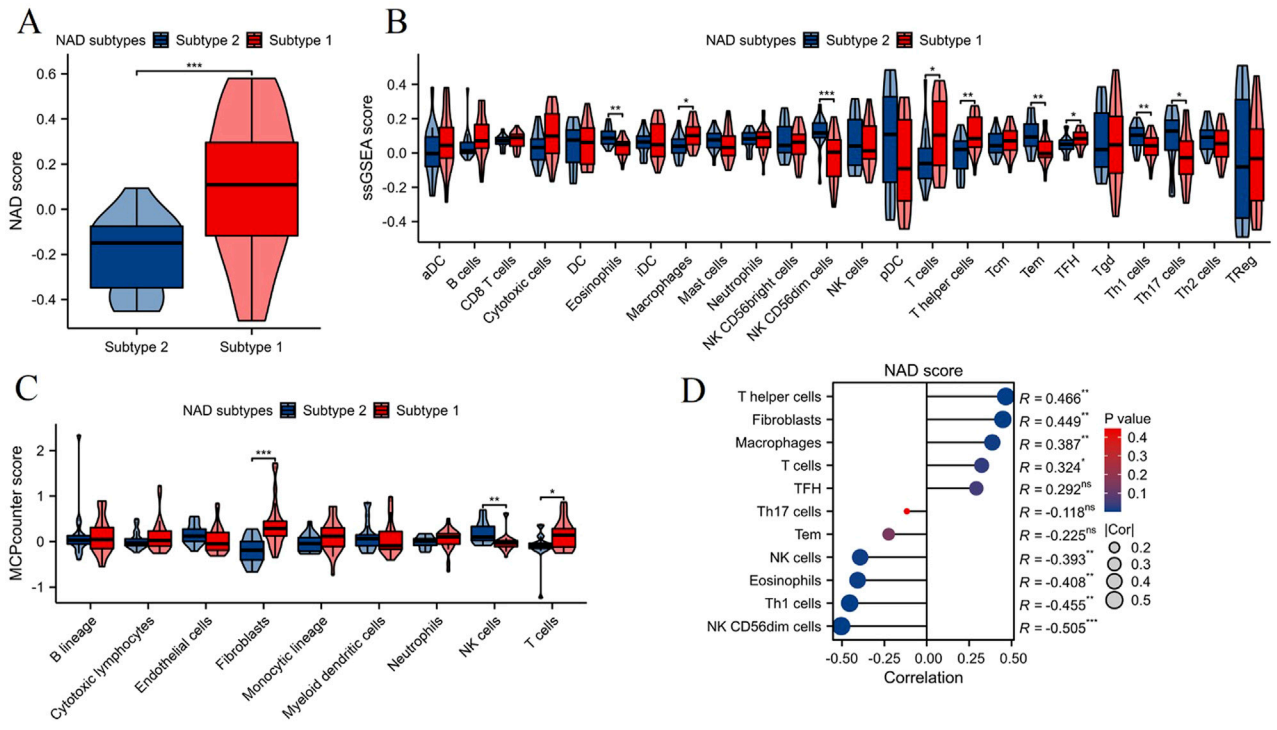

FIGURE 4
NAD score and immune cell infiltration analysis in NAD-related subtypes of DN. **(A)** Violin plot showing the NAD score levels in the two NAD-related subtypes (Subtype 1 and Subtype 2). **(B)** Immune cell infiltration levels assessed by the ssGSEA algorithm between the two subtypes. Significant differences in several immune cell types are marked (*p < 0.05, **p < 0.01, ***p < 0.001). **(C)** Immune cell infiltration levels assessed by the MCPcounter algorithm between the two subtypes. Significant differences in infiltration levels are indicated (*p < 0.05, **p < 0.01, ***p < 0.001). **(D)** Correlation analysis between NAD scores and immune cell infiltration levels.

Immune-related pathway analysis and correlation with NAD score in NAD-related subtypes of DN

The ssGSEA algorithm was employed to evaluate the levels of immune-related pathways between the two NAD-related subtypes (Subtype 1 and Subtype 2). As illustrated in Figure 5A, Subtype 1 exhibited significantly higher activity in several immune-related pathways compared to Subtype 2. Notably, pathways such as BCR signaling pathway and antigen processing and presentation were significantly upregulated in Subtype 1 (**p < 0.01). Correlation analysis between NAD scores and immune-related pathways revealed significant associations, as shown in Figure 5B. The most prominent positive correlation was observed between the NAD score and the antigen processing and presentation pathway (R = 0.503, ***p < 0.001). In contrast, negative correlations were noted between the NAD score and pathways such as the TGFβ family member, interferons, and cytokines (ranging from R = −0.341 to R = −0.514, *p < 0.05, ***p < 0.001). These observations indicate that higher NAD scores are associated with increased involvement in antigen processing and presentation, while decreasing activity in other immune-modulatory pathways. These findings collectively suggest that NAD metabolism variations affect immune pathway activities differentially across the NAD-related subtypes in DN. This could provide a foundation for understanding the mechanistic links between NAD metabolism and immune responses, offering potential therapeutic targets for managing diabetic kidney disease through modulating NAD-associated immune pathways.

GSVA enrichment analysis and correlation with NAD score in NAD-related subtypes

The GSVA enrichment analysis was conducted to evaluate pathway-level differences between the two NAD-related subtypes (Subtype 1 and Subtype 2). The heatmap in Figure 6A illustrates significant variations in pathway activity across the subtypes. Enriched pathways in Subtype 2 include KRAS signaling and pancreas beta cells, while Subtype 1 shows enrichment in pathways such as apoptosis, peroxisome, glycolysis, interferon gamma response, fatty acid metabolism, etc. These pathways are functionally relevant, as KRAS signaling is critical for cell

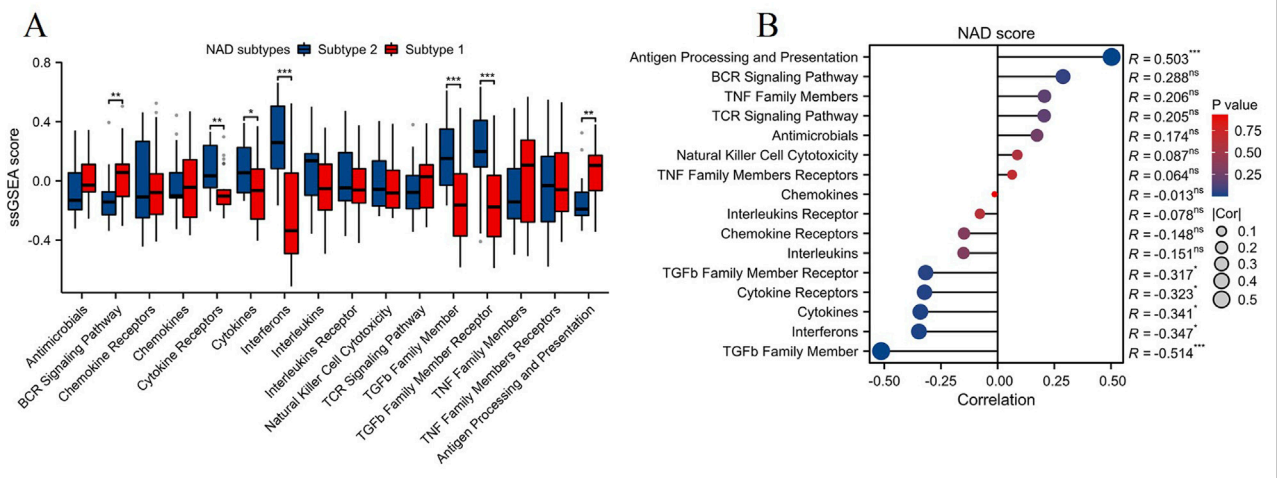

FIGURE 5
Immune-related pathway analysis and its correlation with NAD score in NAD-related subtypes of DN. **(A)** Box plot showing the levels of immune-related pathways in the two NAD-related subtypes (Subtype 1 and Subtype 2) assessed by the ssGSEA algorithm. Significant differences between the subtypes in various pathways are indicated (*p < 0.05, **p < 0.01, ***p < 0.001). **(B)** Correlation analysis between NAD scores and the levels of immune-related pathways.

proliferation and survival, while pancreatic beta cells are essential for insulin secretion and glucose homeostasis. The box plots in Figure 6B provide a more detailed comparison of the GSVA scores between the subtypes. Notably, pathways like KRAS signaling and pancreatic beta-cells functionality are significantly more enriched in Subtype 2 compared to Subtype 1. Conversely, Subtype 1 exhibits higher enrichment in pathways such as the reactive oxygen species pathway, fatty acid metabolism, p53 pathway, apoptosis, PI3K/AKT/mTOR signaling, glycolysis, interferon alpha response, and interferon gamma response. These pathways are integral to cellular stress responses, energy metabolism, and immune regulation, suggesting that Subtype 1 may be more responsive to metabolic dysregulation and oxidative stress. Correlation analysis between the NAD score and the differentially enriched pathways is presented in Figure 6C. Strong positive correlations were observed between the NAD score and pathways such as PI3K/AKT/mTOR signaling, estrogen response late, and MTORC1 signaling (R = 0.748, R = 0.576, R = 0.557; ***p < 0.001). Negative correlations were noted for pathways like pancreatic beta-cells and KRAS signaling DN (R = −0.549, R = −0.488; ***p < 0.001). These findings highlight the heterogeneity in pathway activities between the two NAD-related subtypes and their association with NAD metabolism. This underscores the importance of specific signaling and metabolic pathways in the context of DN, providing potential targets for therapeutic intervention.

Identification of key NAD metabolism-related biomarker genes in DN using machine learning algorithms

To identify key NAD metabolism-related biomarker genes in DN patients, we utilized three machine learning algorithms: LASSO, Random Forest (RF), and Support Vector Machine-Recursive Feature Elimination (SVM-RFE). The LASSO regression model was applied to select 7 critical features, and the binomial deviance indicated an optimal λ value (Figure 7A). Next, the RF algorithm was employed to evaluate feature importance. As shown in Figure 7B, the mean decrease in Gini index was calculated for each gene, identifying 10 top-performing genes critical for distinguishing between DN subtypes. Similarly, the SVM-RFE approach was applied to determine the optimal number of features by evaluating the cross-validation (CV) error rate (Figure 7C) and the associated CV accuracy (Figure 7D). The analysis suggested that a minimal error rate and maximal accuracy were achieved with nine features, confirming the robustness of these selected genes. Integrating the results from all three machine learning methods, the Venn diagram in Figure 7E illustrates the common genes identified by LASSO, RF, and SVM-RFE. Six key NAD metabolism-related genes (FMO3, ALDH1A3, FMO5, TKT, LBR, and HPGD) were consistently selected across the three algorithms, indicating their potential as reliable biomarkers for DN.

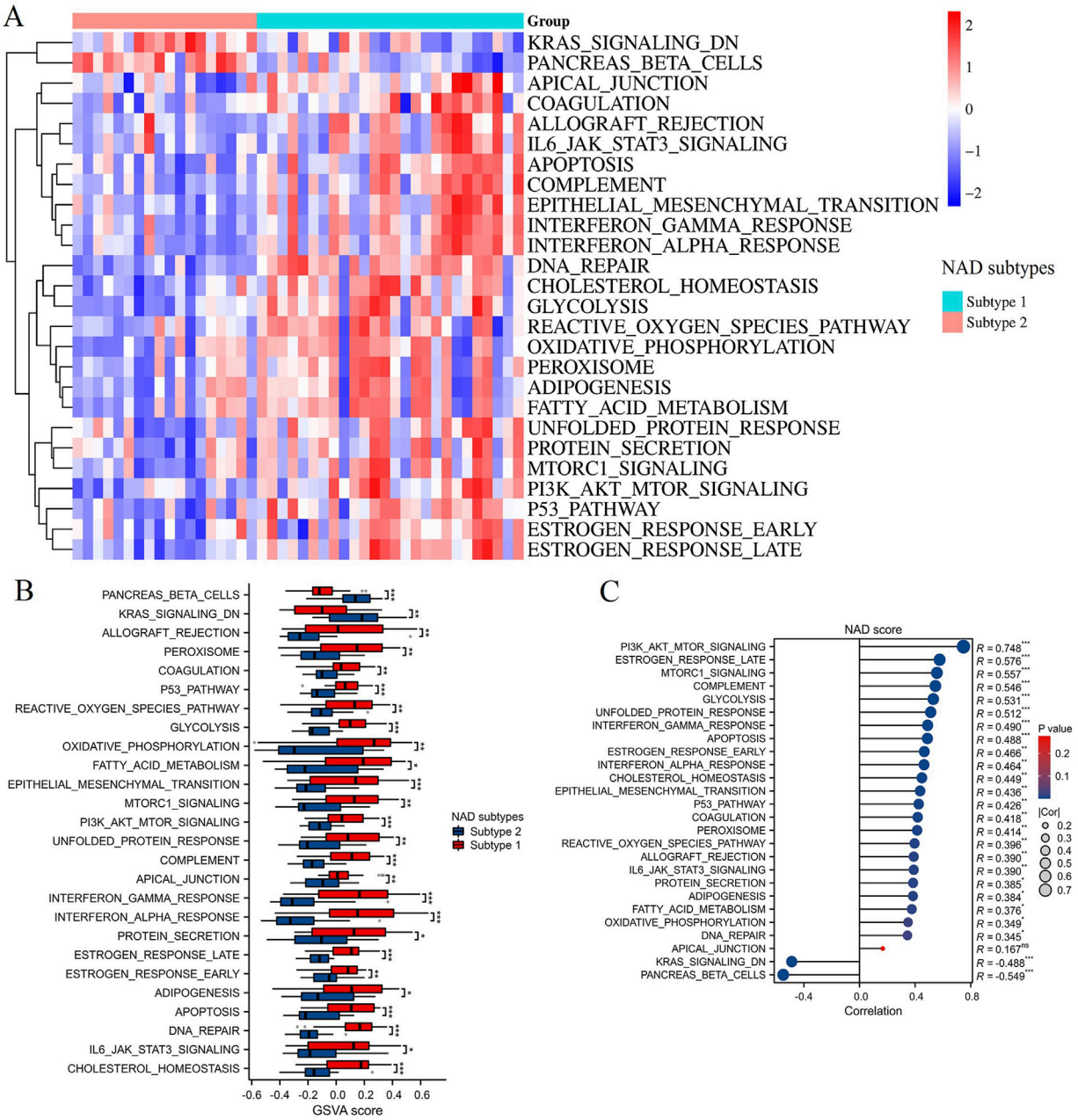

FIGURE 6
GSVA enrichment analysis. **(A)** Heatmap displaying the GSVA enrichment scores for various pathways between Subtype 1 and Subtype 2. Red indicates high enrichment, and blue indicates low enrichment. **(B)** Box plots showing the GSVA scores for significantly different pathways between NAD-related subtypes. Subtype 1 is represented in red, and Subtype 2 is represented in blue. **(C)** Correlation analysis between NAD scores and pathways differentially enriched in the NAD-related subtypes. *p < 0.05, **p < 0.01, ***p < 0.001.

Validation of key NAD metabolism-related marker genes in DN

To validate the expression of key NAD metabolism-related marker genes in DN, we analyzed three independent DN-associated datasets: GSE96804 (Figure 8A), GSE104954 (Figure 8B), and GSE142025 (Figure 8C). In all three datasets, FMO3, ALDH1A3, FMO5, and HPGD exhibited consistent and significant dysregulation in DN samples. Furthermore, analysis of the GSE104954 and GSE142025 datasets revealed a marked upregulation of TKT expression in DN samples, while LBR expression was notably increased in GSE96804 and

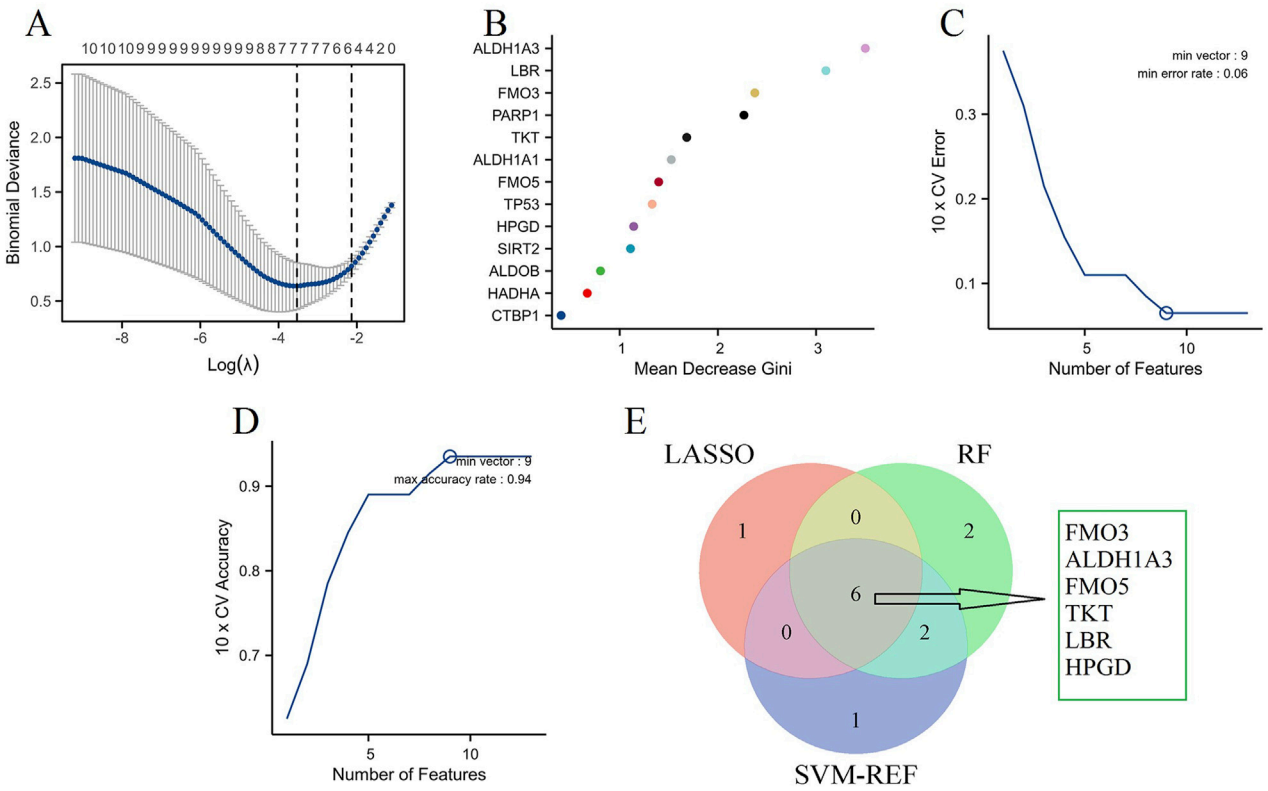

FIGURE 7
Machine learning algorithms. **(A)** LASSO regression analysis identifying significant genes based on the optimal λ value, as determined by binomial deviance. **(B)** RF analysis showing the mean decrease in Gini index for each gene, indicating their importance in distinguishing DN. **(C)** SVM-RFE analysis identifying the optimal number of features based on the 10-fold cross-validation (CV) error rate. **(D)** SVM-RFE analysis depicting the 10-fold CV accuracy for various numbers of features. **(E)** Venn diagram integrating results from LASSO, Random Forest, and SVM-RFE.

GSE104954. These results suggest that FMO3, ALDH1A3, FMO5, and HPGD are potential key marker genes in the context of NAD metabolism associated with DN.

Evaluation of NAD metabolism-related hub genes' association with renal function in DN patients

Using the Nephroseq V5 tool,[1] we evaluated the relationship between key NAD metabolism-related hub genes and renal function in DN patients. The renal function was assessed via the estimated glomerular filtration rate (GFR) (Figure 9). The expression levels of NAD metabolism-related hub genes show significant correlations with renal function in DN patients. Specifically, FMO3 ($R = -0.44$, $p = 0.04$), ALDH1A3 ($R = -0.623$, $p = 0.002$), TKT ($R = -0.629$, $p = 0.002$), and LBR ($R = -0.573$, $p = 0.005$) are inversely correlated with GFR, suggesting their increased expression is associated with worsening renal function. In contrast, FMO5 ($R = 0.699$, $p < 0.001$) and HPGD ($R = 0.676$, $p < 0.001$) are positively correlated with GFR, indicating their increased expression is linked with better renal function. These findings underscore the potential roles of these genes in the regulation of renal function in DN and their utility as biomarkers.

Discussion

DN is a significant complication of diabetes, leading to increased morbidity and mortality among affected individuals. Recent studies have highlighted the critical role of NAD metabolism in various metabolic disorders, including DN. Our study identified thirteen differentially expressed NAD metabolism-related genes in DN, with a notable increase in the NAD score among DN patients compared to controls. We classified two distinct NAD-related subtypes, revealing significant differences in gene expression, immune cell infiltration, and pathway activities. Key biomarkers, including FMO3, ALDH1A3, FMO5, TKT, LBR, and HPGD, were identified, with varying correlations to renal function.

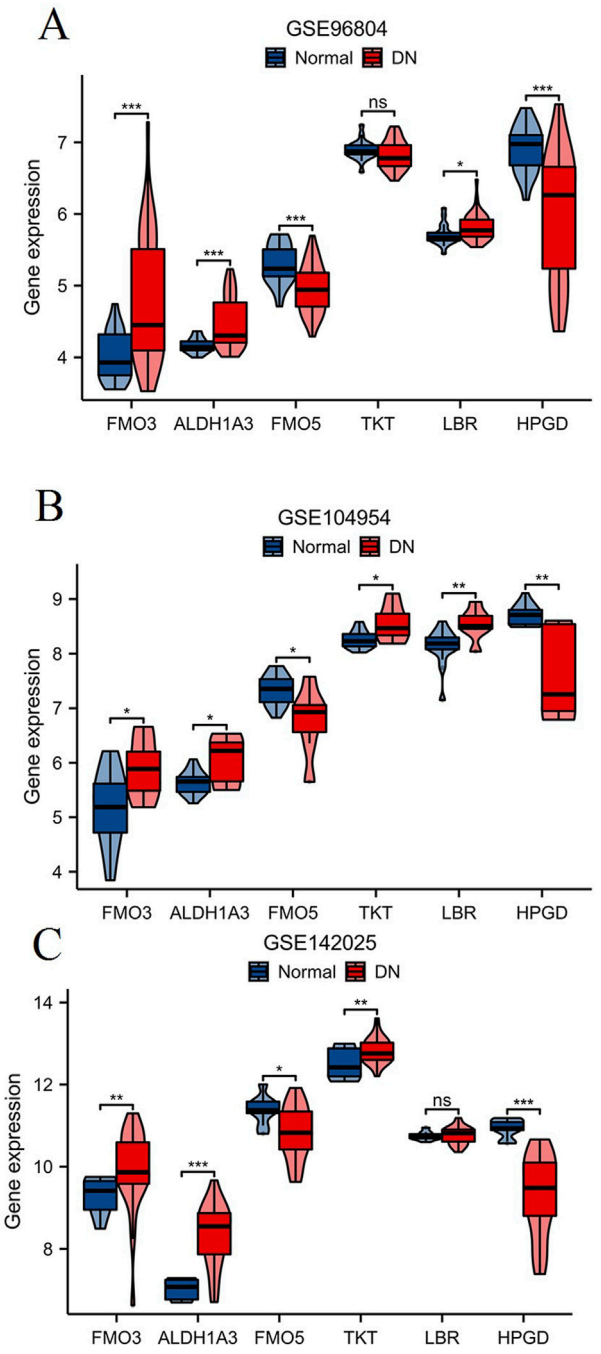

FIGURE 8
Validation of key NAD metabolism-related genes in DN. The expression levels of six NAD metabolism-related genes (FMO3, ALDH1A3, FMO5, TKT, LBR, HPGD) were analyzed in three independent DN-associated datasets: GSE96804 **(A)**, GSE104954 **(B)**, and GSE142025 **(C)**. *p < 0.05, **p < 0.01, ***p < 0.001.

Our findings align with previous research indicating that NAD metabolism is integral to the pathogenesis of DN. For instance, the altered NAD levels can influence oxidative stress and inflammation, both of which are critical in DN progression [19–21]. Additionally, NAD+ precursor administration mitigates inflammatory responses in the context of renal injury, suggesting a protective role of NAD metabolism in DN [22]. The identification of specific NAD-related subtypes in our study adds a new dimension to existing literature, suggesting that personalized approaches based on NAD metabolism could enhance therapeutic strategies. Moreover, research reinforces our conclusions by demonstrating that NAD metabolism can enhance mitochondrial function and decrease inflammation in DN, thereby underscoring the potential for therapeutic strategies that focus on NAD metabolism [20].

The identified biomarkers demonstrate distinct biological roles in DN pathogenesis through multiple mechanisms. FMO3 (Flavin-containing monooxygenase 3) plays a crucial role in xenobiotic metabolism and has been implicated in renal protection mechanisms. Beyond our finding that FMO3 deficiency confers renal protection following ischemia-reperfusion injury in murine models [23], recent studies demonstrate that FMO3 modulates trimethylamine N-oxide (TMAO) production, which is elevated in diabetic patients and correlates with renal dysfunction [24]. ALDH1A3 (Aldehyde dehydrogenase 1A3) serves as a critical enzyme in aldehyde detoxification and retinoic acid synthesis. Inhibition of ALDH1A3, whether through genetic means or pharmacological intervention, has been shown to reduce blood glucose levels and enhance insulin secretion in diabetic mice [25]. FMO5 is crucial in regulating diverse metabolic pathways and processes, notably those associated with lipid homeostasis and the absorption and metabolism of glucose [26]. It serves as a key regulator of body weight, glucose disposal, and insulin sensitivity [27]. TKT (Transketolase) is essential for the pentose phosphate pathway and NADPH generation [28]. TKT deficiency leads to a reduction in thioredoxin-interacting protein levels, which is a recognized inhibitor of GLUT4. This occurs by diminishing NADPH and glutathione levels, subsequently inducing oxidative stress in brown adipose tissue [29]. LBR (Lamin B receptor) is involved in nuclear envelope integrity and has emerging roles in metabolic regulation [30]. HPGD (15-hydroxyprostaglandin dehydrogenase) regulates prostaglandin metabolism. Conditional deletion of Hpgd in mouse Treg cells led to the buildup of functionally compromised Treg cells specifically in visceral adipose tissue, which in turn triggered local inflammation and systemic insulin resistance [31]. The identified NAD metabolism-related genes provide valuable insights into the pathogenesis of DN. Understanding these genes' roles may lead to novel therapeutic targets, particularly in managing the distinct subtypes of DN. The differential expression of these genes suggests that interventions could be tailored to individual patients based on their NAD-related profiles, potentially improving treatment outcomes. The biomarkers identified in our study hold significant promise for clinical applications. Their correlation with renal function

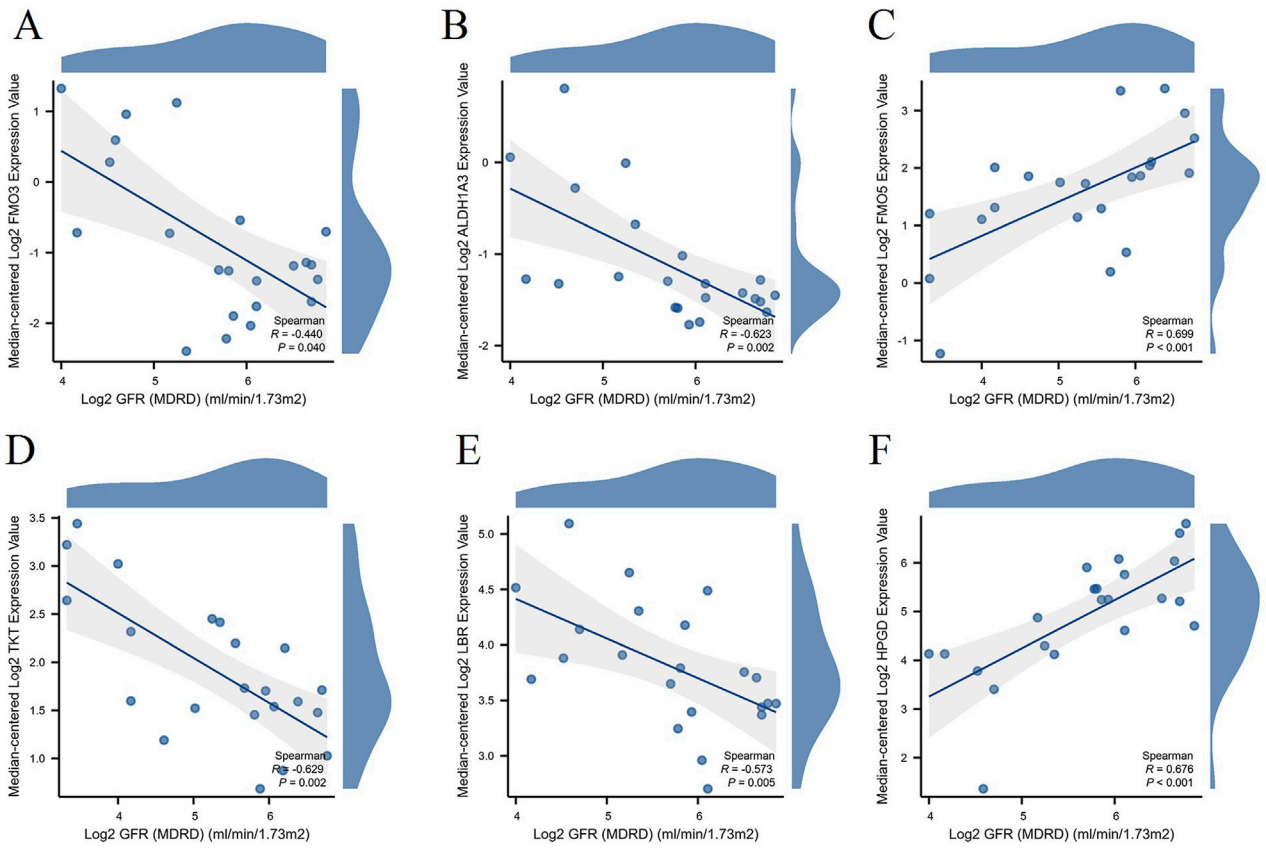

FIGURE 9
Correlation between hub gene expression and renal function in DN Patients. Scatter plots illustrating the correlation between the expression levels of hub genes and renal function, represented by Log2 GFR (MDRD), in DN patients. The genes analyzed include FMO3 **(A)**, ALDH1A3 **(B)**, FMO5 **(C)**, TKT **(D)**, LBR **(E)**, and HPGD **(F)**.

suggests they could serve as indicators for disease progression and treatment response. Incorporating these biomarkers into clinical practice may facilitate early diagnosis and personalized treatment plans for patients with DN.

Our findings provide mechanistic insights into how NAD metabolism influences DN. We specifically identified several key enriched pathways with distinct relevance to the pathogenesis of DN. Among these, the reactive oxygen species (ROS) pathway exhibited the higher enrichment in patients classified under subtype 1. This is particularly significant because the accumulation of ROS in diabetic kidneys contributes to podocyte apoptosis, mesangial cell proliferation, and the epithelial-mesenchymal transition of tubular cells [32, 33]. The enrichment of the fatty acid metabolism pathway in subtype 1 highlights the metabolic reprogramming occurring in diabetic kidneys, where increased lipid accumulation contributes to renal lipotoxicity and progressive fibrosis [34]. The enrichment of the glycolysis pathway in subtype 1 indicates a metabolic shift towards aerobic glycolysis in diabetic renal cells, which promotes inflammatory responses and extracellular matrix production [35]. The interferon alpha and gamma response pathways demonstrated significant enrichment in subtype 1, suggesting enhanced activation of the innate immune system. This contributes to chronic inflammation and progressive renal injury in DN [36]. Regarding immune cell infiltration, our analysis revealed specific patterns of immune dysregulation in DN subtypes. Subtype 1 demonstrated increased infiltration of macrophages, creating a pro-inflammatory microenvironment that perpetuates renal injury. This finding aligns with previous studies showing that macrophage accumulation in diabetic kidneys promotes inflammatory cytokine production and fibrosis progression [37]. Additionally, we observed increased T cell infiltration in subtype 1, which has been linked to direct cytotoxic effects on renal tubular cells and the promotion of interstitial fibrosis [38].

These pathways are crucial in understanding how dysregulation of NAD metabolism contributes to the development and progression of DN. Previous studies have shown that NAD+ depletion leads to increased oxidative stress and inflammation, which exacerbates renal injury in

diabetic models [39–41]. This suggests that therapeutic strategies aimed at restoring NAD+ levels could potentially mitigate the adverse effects associated with DN. Furthermore, the interplay between NAD metabolism and mitochondrial function cannot be overlooked, as mitochondria are central to both energy production and apoptosis in renal cells [42, 43]. It is essential to explore how enhancing NAD+ synthesis might improve mitochondrial bioenergetics, thereby reducing oxidative damage and promoting cell survival. Additionally, the association of NAD with fatty acid metabolism highlights another critical avenue for research. The dysregulation of lipid metabolism in diabetes is well-documented, and it may be beneficial to investigate how NAD+ supplementation could recalibrate lipid profiles in renal tissues [44, 45]. By addressing the metabolic inflexibility often seen in diabetic patients, we might uncover novel preventive strategies against DN. Moreover, the differential responses of DN subtypes to interferon alpha and gamma indicate that immune modulation could play a role in disease progression [46, 47]. Future studies should focus on how NAD+ influences immune cell activation and function in the renal microenvironment. By delineating these mechanisms, we can potentially identify biomarkers for DN progression and therapeutic targets that could enhance renal resilience. Overall, the intricate relationship between NAD metabolism and various biological pathways suggests a multifaceted approach to understanding and treating DN. As we deepen our investigation into these connections, we may pave the way for innovative interventions that not only restore metabolic balance but also improve patient outcomes in diabetic kidney disease.

The strengths of our study include a comprehensive analysis of multiple datasets and the application of robust machine learning algorithms to identify key biomarkers. Despite these strengths, certain limitations exist, such as the reliance on existing datasets, which may not capture all aspects of NAD metabolism in DN. In this study, we utilized two datasets, GSE30528 and GSE30529, which include 19 DN samples and 25 control samples. While these datasets are relevant, they have limitations in terms of sample size and potential heterogeneity. The relatively small sample size may limit the statistical power and generalizability of our findings. Additionally, potential biases inherent in these datasets, such as differences in sample collection, processing, and population demographics, could affect the robustness of our results. Future studies should strive for validation in larger, more diverse cohorts.

Future research should also focus on clarifying the precise mechanisms by which NAD metabolism-related genes influence DN. Longitudinal studies could provide insight into the interactions of these genes with environmental and genetic factors over time. Additionally, exploring therapeutic interventions targeting NAD metabolism may yield promising management strategies for DN. For instance, clinical trials assessing the efficacy of NAD+ precursors in diabetic patients could offer valuable data on their potential benefits in preventing or treating DN.

In conclusion, our study underscores the significant role of NAD metabolism-related genes in DN. The identification of distinct subtypes and potential biomarkers paves the way for future research and therapeutic interventions, ultimately contributing to improved patient outcomes in DN management. By advancing our understanding of NAD metabolism, we can enhance the precision of diabetes care and foster a healthier society.

Author contributions

All authors listed have made a substantial, direct, and intellectual contribution to the work and approved it for publication.

Data availability

The data utilized in this study were sourced from the GEO database and are publicly accessible at https://www.ncbi.nlm.nih.gov/geo/. The specific datasets analyzed include GSE30528, GSE30529, GSE96804, GSE104954, and GSE142025. We downloaded the raw data from the GEO website and conducted all bioinformatics analyses and visualizations using the processed data through the Xiantao Academic Online platform, which can be accessed at https://www.xiantaozi.com/. This platform also provides the relevant analysis scripts and code used in this study.

Funding

The authors declare that financial support was received for the research and/or publication of this article. This work was supported by the Chen Xiaoping Science and Technology Development Foundation's 2021 Immunological Disease Research (No. CXPJJH121002-202107).

Conflict of interest

The author(s) declared no potential conflicts of interest with respect to the research, authorship, and/or publication of this article.

Generative AI statement

The authors declare that no Generative AI was used in the creation of this manuscript.

Any alternative text (alt text) provided alongside figures in this article has been generated by Frontiers with the support of artificial intelligence and reasonable efforts have been made to ensure accuracy, including review by the authors wherever possible. If you identify any issues, please contact us.

Supplementary material

The Supplementary Material for this article can be found online at: https://www.ebm-journal.org/articles/10.3389/ebm.2025.10601/full#supplementary-material

References

1. Umanath K, Lewis JB. Update on diabetic nephropathy: core curriculum 2018. *Am Journal Kidney Diseases* (2018) **71**:884–95. doi:10.1053/j.ajkd.2017.10.026

2. Thipsawat S. Early detection of diabetic nephropathy in patient with type 2 diabetes mellitus: a review of the literature. *Diabetes Vasc Dis Res* (2021) **18**: 14791641211058856. doi:10.1177/14791641211058856

3. Samsu N. Diabetic nephropathy: challenges in pathogenesis, diagnosis, and treatment. *Biomed Research International* (2021) **2021**:1497449. doi:10.1155/2021/1497449

4. Reutens AT. Epidemiology of diabetic kidney disease. *Med Clin North America* (2013) **97**:1–18. doi:10.1016/j.mcna.2012.10.001

5. Li X, Lu L, Hou W, Huang T, Chen X, Qi J, et al. Epigenetics in the pathogenesis of diabetic nephropathy. *Acta Biochim Biophys Sinica* (2022) **54**:163–72. doi:10.3724/abbs.2021016

6. Yang J, Liu Z. Mechanistic pathogenesis of endothelial dysfunction in diabetic nephropathy and retinopathy. *Front Endocrinology* (2022) **13**:816400. doi:10.3389/fendo.2022.816400

7. Tervaert TW, Mooyaart AL, Amann K, Cohen AH, Cook HT, Drachenberg CB, et al. Pathologic classification of diabetic nephropathy. *J Am Soc Nephrol* (2010) **21**: 556–63. doi:10.1681/asn.2010010010

8. Oh SW, Kim S, Na KY, Chae DW, Kim S, Jin DC, et al. Clinical implications of pathologic diagnosis and classification for diabetic nephropathy. *Diabetes Research Clinical Practice* (2012) **97**:418–24. doi:10.1016/j.diabres.2012.03.016

9. Verdin E. NAD$^+$ in aging, metabolism, and neurodegeneration. *Science (New York, N.Y.)* (2015) **350**:1208–13. doi:10.1126/science.aac4854

10. Griffiths HBS, Williams C, King SJ, Allison SJ. Nicotinamide adenine dinucleotide (NAD+): essential redox metabolite, co-substrate and an anti-cancer and anti-ageing therapeutic target. *Biochem Soc Transactions* (2020) **48**: 733–44. doi:10.1042/bst20190033

11. Yaku K, Okabe K, Nakagawa T. NAD metabolism: implications in aging and longevity. *Ageing Research Reviews* (2018) **47**:1–17. doi:10.1016/j.arr.2018.05.006

12. Ross SM. Nicotinamide adenine dinucleotide (NAD+) biosynthesis in the regulation of metabolism, aging, and neurodegeneration. *Holist Nursing Practice* (2021) **35**:230–2. doi:10.1097/hnp.0000000000000461

13. Morevati M, Fang EF, Mace ML, Kanbay M, Gravesen E, Nordholm A, et al. Roles of NAD(+) in acute and chronic kidney diseases. *Int Journal Molecular Sciences* (2022) **24**:137. doi:10.3390/ijms24010137

14. Ralto KM, Rhee EP, Parikh SM. NAD(+) homeostasis in renal health and disease. *Nat Reviews. Nephrol* (2020) **16**:99–111. doi:10.1038/s41581-019-0216-6

15. Trammell SA, Weidemann BJ, Chadda A, Yorek MS, Holmes A, Coppey LJ, et al. Nicotinamide riboside opposes type 2 diabetes and neuropathy in mice. *Scientific Reports* (2016) **6**:26933. doi:10.1038/srep26933

16. Yan LJ. NADH/NAD(+) redox imbalance and diabetic kidney disease. *Biomolecules* (2021) **11**:730. doi:10.3390/biom11050730

17. Hershberger KA, Martin AS, Hirschey MD. Role of NAD(+) and mitochondrial sirtuins in cardiac and renal diseases. *Nat Reviews. Nephrol* (2017) **13**:213–25. doi:10.1038/nrneph.2017.5

18. Kumakura S, Sato E, Sekimoto A, Hashizume Y, Yamakage S, Miyazaki M, et al. Nicotinamide attenuates the progression of renal failure in a mouse model of adenine-induced chronic kidney disease. *Toxins* (2021) **13**:50. doi:10.3390/toxins13010050

19. Kang H, Park YK, Lee JY. Nicotinamide riboside, an NAD(+) precursor, attenuates inflammation and oxidative stress by activating sirtuin 1 in alcohol-stimulated macrophages. *Lab Investigation* (2021) **101**:1225–37. doi:10.1038/s41374-021-00599-1

20. Myakala K, Wang XX, Shults NV, Krawczyk E, Jones BA, Yang X, et al. NAD metabolism modulates inflammation and mitochondria function in diabetic kidney disease. *J Biol Chem* (2023) **299**:104975. doi:10.1016/j.jbc.2023.104975

21. Massudi H, Grant R, Guillemin GJ, Braidy N. NAD+ metabolism and oxidative stress: the golden nucleotide on a crown of thorns. *Redox Report* (2012) **17**:28–46. doi:10.1179/1351000212y.0000000001

22. Doke T, Mukherjee S, Mukhi D, Dhillon P, Abedini A, Davis JG, et al. NAD(+) precursor supplementation prevents mtRNA/RIG-I-dependent inflammation during kidney injury. *Nat Metabolism* (2023) **5**:414–30. doi:10.1038/s42255-023-00761-7

23. Wang J, Wang W, Zhang J, Xiao F, Li Z, Xu P, et al. Deficiency of flavin-containing monooxygenase 3 protects kidney function after ischemia-reperfusion in mice. *Commun Biology* (2024) **7**:1054. doi:10.1038/s42003-024-06718-0

24. Robinson-Cohen C, Newitt R, Shen DD, Rettie AE, Kestenbaum BR, Himmelfarb J, et al. Association of FMO3 variants and trimethylamine N-Oxide concentration, disease progression, and mortality in CKD patients. *PloS One* (2016) **11**:e0161074. doi:10.1371/journal.pone.0161074

25. Son J, Du W, Esposito M, Shariati K, Ding H, Kang Y, et al. Genetic and pharmacologic inhibition of ALDH1A3 as a treatment of β-cell failure. *Nat Communications* (2023) **14**:558. doi:10.1038/s41467-023-36315-4

26. Phillips IR, Veeravalli S, Khadayate S, Shephard EA. Metabolomic and transcriptomic analyses of Fmo5-/- mice reveal roles for flavin-containing monooxygenase 5 (FMO5) in NRF2-mediated oxidative stress response, unfolded protein response, lipid homeostasis, and carbohydrate and one-carbon metabolism. *PloS One* (2023) **18**:e0286692. doi:10.1371/journal.pone.0286692

27. Scott F, Gonzalez Malagon SG, O'Brien BA, Fennema D, Veeravalli S, Coveney CR, et al. Identification of flavin-containing monooxygenase 5 (FMO5) as a regulator of glucose homeostasis and a potential sensor of gut bacteria. *Drug Metabolism Disposition* (2017) **45**:982–9. doi:10.1124/dmd.117.076612

28. Gu N, Dai W, Liu H, Ge J, Luo S, Cho E, et al. Genetic variants in TKT and DERA in the nicotinamide adenine dinucleotide phosphate pathway predict melanoma survival. *Eur Journal Cancer (Oxford, Engl : 1990)* (2020) **136**:84–94. doi:10.1016/j.ejca.2020.04.049

29. Ji Y, Liu W, Zhu Y, Li Y, Lu Y, Liu Q, et al. Loss of transketolase promotes the anti-diabetic role of brown adipose tissues. *The J Endocrinology* (2023) **256**:e220047. doi:10.1530/joe-22-0047

30. Nikolakaki E, Mylonis I, Giannakouros T. Lamin B receptor: interplay between structure, function and localization. *Cells* (2017) **6**:28. doi:10.3390/cells6030028

31. Schmidleithner L, Thabet Y, Schönfeld E, Köhne M, Sommer D, Abdullah Z, et al. Enzymatic activity of HPGD in treg cells suppresses tconv cells to maintain adipose tissue homeostasis and prevent metabolic dysfunction. *Immunity* (2019) **50**:1232–48.e14. doi:10.1016/j.immuni.2019.03.014

32. Wagener FA, Dekker D, Berden JH, Scharstuhl A, van der Vlag J. The role of reactive oxygen species in apoptosis of the diabetic kidney. *Apoptosis* (2009) **14**: 1451–8. doi:10.1007/s10495-009-0359-1

33. Coughlan MT, Sharma K. Challenging the dogma of mitochondrial reactive oxygen species overproduction in diabetic kidney disease. *Kidney International* (2016) **90**:272–9. doi:10.1016/j.kint.2016.02.043

34. Fang Z, Liu R, Xie J, He JC. Molecular mechanism of renal lipid accumulation in diabetic kidney disease. *J Cellular Molecular Medicine* (2024) **28**:e18364. doi:10.1111/jcmm.18364

35. Song C, Wang S, Fu Z, Chi K, Geng X, Liu C, et al. IGFBP5 promotes diabetic kidney disease progression by enhancing PFKFB3-mediated endothelial glycolysis. *Cell Death and Disease* (2022) **13**:340. doi:10.1038/s41419-022-04803-y

36. Tang SCW, Yiu WH. Innate immunity in diabetic kidney disease. *Nat Reviews. Nephrol* (2020) **16**:206–22. doi:10.1038/s41581-019-0234-4

37. Li HD, You YK, Shao BY, Wu WF, Wang YF, Guo JB, et al. Roles and crosstalks of macrophages in diabetic nephropathy. *Front Immunology* (2022) **13**: 1015142. doi:10.3389/fimmu.2022.1015142

38. Law BM, Wilkinson R, Wang X, Kildey K, Lindner M, Beagley K, et al. Effector γδ T cells in human renal fibrosis and chronic kidney disease. *Nephrol Dialysis, Transplantation* (2019) **34**:40–8. doi:10.1093/ndt/gfy098

39. Massudi H, Grant R, Braidy N, Guest J, Farnsworth B, Guillemin GJ. Age-associated changes in oxidative stress and NAD+ metabolism in human tissue. *PloS One* (2012) **7**:e42357. doi:10.1371/journal.pone.0042357

40. Zhu C, Gu H, Jin Y, Wurm D, Freidhof B, Lu Y, et al. Metabolomics of oxidative stress: Nrf2 independent depletion of NAD or increases of sugar alcohols. *Toxicol Applied Pharmacology* (2022) **442**:115949. doi:10.1016/j.taap.2022.115949

41. Sundaram B, Pandian N, Kim HJ, Abdelaal HM, Mall R, Indari O, et al. NLRC5 senses NAD(+) depletion, forming a PANoptosome and driving PANoptosis and inflammation. *Cell* (2024) **187**:4061–77.e17. doi:10.1016/j.cell.2024.05.034

42. Quadri MM, Fatima SS, Che RC, Zhang AH. Mitochondria and renal fibrosis. *Adv Experimental Medicine Biology* (2019) **1165**:501–24. doi:10.1007/978-981-13-8871-2_25

43. Zhao X, Li Y, Yu J, Teng H, Wu S, Wang Y, et al. Role of mitochondria in pathogenesis and therapy of renal fibrosis. *Metabolism* (2024) **155**:155913. doi:10.1016/j.metabol.2024.155913

44. Eid S, Sas KM, Abcouwer SF, Feldman EL, Gardner TW, Pennathur S, et al. New insights into the mechanisms of diabetic complications: role of lipids and lipid metabolism. *Diabetologia* (2019) **62**:1539–49. doi:10.1007/s00125-019-4959-1

45. Hou Y, Tan E, Shi H, Ren X, Wan X, Wu W, et al. Mitochondrial oxidative damage reprograms lipid metabolism of renal tubular epithelial cells in the diabetic kidney. *Cell Molecular Life Sciences* (2024) **81**:23. doi:10.1007/s00018-023-05078-y

46. Hickey FB, Martin F. Diabetic kidney disease and immune modulation. *Curr Opinion Pharmacology* (2013) **13**:602–12. doi:10.1016/j.coph.2013.05.002

47. Hsieh CC, Chang CC, Hsu YC, Lin CL. Immune modulation by myeloid-derived suppressor cells in diabetic kidney disease. *Int Journal Molecular Sciences* (2022) **23**:13263. doi:10.3390/ijms232113263

EBM Experimental Biology and Medicine

TYPE Review
PUBLISHED 21 January 2026
DOI 10.3389/ebm.2026.10845

OPEN ACCESS

*CORRESPONDENCE
Wei Luo,
lw346772963@163.com
Shuming Guo,
guoshuming70@163.com

†These authors have contributed equally to this work

RECEIVED 01 October 2025
REVISED 14 December 2025
ACCEPTED 07 January 2026
PUBLISHED 21 January 2026

CITATION
Su Y, Su S, Li M, Zhang Z, Zhang S, Fan C, Luo W and Guo S (2026) Functional roles of Keratin 6A in disease pathogenesis across cancer and skin disorders. *Exp. Biol. Med.* 251:10845. doi: 10.3389/ebm.2026.10845

Functional roles of Keratin 6A in disease pathogenesis across cancer and skin disorders

Yanyan Su[1,2†], Shudong Su[3†], Min Li[4], Zhixia Zhang[2], Shiyi Zhang[5], Caixia Fan[5], Wei Luo[6*] and Shuming Guo[1,2*]

[1]Nursing College of Shanxi Medical University, Taiyuan, China, [2]Department of Nursing, Linfen Central Hospital, Linfen, China, [3]Department of Orthopaedics, People's Hospital of Linfen City, Linfen, China, [4]Department of Nursing, Changzhi Medical College, Changzhi, China, [5]Department of Gastroenterology, Linfen Central Hospital, Linfen, China, [6]Department of Thyroid and Neck Tumor, Tianjin Medical University Cancer Institute and Hospital, National Clinical Research Center for Cancer, Key Laboratory of Cancer Prevention and Therapy, Tianjin's Clinical Research Center for Cancer, Tianjin, China

Abstract

Keratin 6A (KRT6A) is an epithelial-specific type II keratin localized within cytoskeletal intermediate filaments and functions in cooperation with KRT16/17 to maintain epidermal homeostasis and tissue repair. Accumulating evidence highlights its multifaceted roles in cancer. Aberrant KRT6A expression promotes cell cycle progression, epithelial–mesenchymal transition, migration, and invasion, thereby driving tumor initiation and metastasis, although tumor-suppressive effects have been observed in specific contexts. Mechanistically, KRT6A regulates adhesion, cytoskeletal remodeling, and critical signaling pathways, thereby reshaping tumor immunity and metabolism to facilitate immune evasion and metabolic dysregulation. Elevated KRT6A expression is strongly associated with resistance to chemotherapy, targeted therapy, and radiotherapy. Therapeutic approaches targeting KRT6A include nucleic acid-based interventions, protein degradation strategies, inhibition of upstream regulatory pathways, and combinatorial regimens to overcome drug resistance. Clinically, KRT6A has emerged as both a diagnostic and prognostic biomarker, supporting treatment monitoring and enhancing predictive models for risk stratification and individualized outcome evaluation. Beyond oncology, mutations in KRT6A underlie pachyonychia congenita, and its dysregulation contributes to epidermal hyperproliferative disorders such as psoriasis. Overall, systematic elucidation of the structure–function–pathway–clinical axis of KRT6A offers new opportunities for precision medicine and supports its potential as a therapeutic target in cancer management.

KEYWORDS

cancer, dermatoses, drug resistance, epithelial–mesenchymal transition, KRT6A, pachyonychia congenita, therapeutic biomarker

Impact statement

Keratin 6A (KRT6A) has emerged as a stress-inducible keratin with multifaceted roles that extend beyond structural support. Its dysregulation is increasingly recognized as a driver of cancer progression, treatment resistance, and poor prognosis, while pathogenic mutations cause inherited skin disorders such as pachyonychia congenita. Although several studies and reviews have broadly examined keratin biology and the contextual roles of K6 proteins in cancer, comprehensive synthesis specifically integrating emerging mechanistic and clinical evidence on KRT6A across both cancer and dermatologic diseases remains limited. This review integrates recent advances in the molecular, cellular, and clinical aspects of KRT6A, highlighting its contributions to cell proliferation, plasticity, immune regulation, and cytoskeletal dynamics. By bridging findings from oncology and dermatology, we provide insights into KRT6A as both a pathogenic mediator and a potential therapeutic biomarker. This work reframes KRT6A from a structural keratin to a disease-relevant effector, thereby informing future mechanistic research and translational applications.

Introduction

Keratin 6A (KRT6A) is a member of the type II intermediate filament (IF) protein family, which plays a vital role in maintaining cytoskeletal integrity and epithelial tissue homeostasis. KRT6A, together with its isoforms KRT6B and KRT6C, forms part of the keratin 6 subfamily, which is primarily expressed in stratified epithelia and is essential for processes such as squamous epithelial differentiation and epidermalization [1–3].

Structurally, keratins assemble into obligate heteropolymers composed of one type I (acidic, low molecular weight) and one type II (basic to neutral, high molecular weight) keratin [1, 4, 5]. KRT6A shares the tripartite architecture typical of IF proteins, consisting of a non-helical head domain (residues 1–162), a central α-helical rod domain (163–476), and a non-helical tail domain (477–564). The rod domain is subdivided into several coiled-coil segments interspersed with linker regions, while the head domain contains an intrinsically disordered region at its N-terminus (residues 1–23) [6, 7].

Genetic mutations in KRT6A are implicated in various inherited skin disorders, such as pachyonychia congenita type I (PC-1) and focal non-epidermolytic palmoplantar keratoderma, highlighting its functional importance in epithelial integrity [8]. More recently, dysregulation of KRT6A has been linked to carcinogenesis, potentially via effects on mechanotransduction, cytoskeletal dynamics, and stress responses. KRT6A overexpression has also been associated with tumor aggressiveness and poor prognosis across several cancers [9]. Although prior studies and reviews have discussed keratin family biology and the roles of K6 proteins, including K6A, in cancer, analyses that integrate emerging mechanistic and clinical evidence on KRT6A across both cancer and dermatologic diseases remain limited [10–12]. Notably, many of these mechanistic insights are based on limited or single-study observations and therefore require further validation before firm conclusions can be drawn.

In this review, we comprehensively summarize current findings regarding the dual roles of KRT6A in both malignant and non-malignant epithelial diseases. Specifically, we focus on its contributions to tumor initiation, progression, metastasis, metabolic reprogramming, drug resistance, immune modulation, and prognostic relevance. Furthermore, we discuss the molecular mechanisms underlying KRT6A mutations in dermatoses and explore the potential of KRT6A-targeted strategies as future therapeutic options.

The literature included in this review was identified primarily through comprehensive searches of PubMed, supplemented by key studies published by major academic publishers (e.g., Elsevier, Wiley, and Springer Nature). Several relevant mechanistic studies were additionally retrieved through manual searches of CNKI. The search covered publications up to May 2025, with two newly published studies (June and October 2025) incorporated during revision to maintain currency. As this is a narrative review, no formal inclusion or exclusion criteria were applied; however, priority was given to influential and methodologically robust studies. In addition, we assessed key methodological features of the included studies, including sample size and whether *in vitro* findings were validated in animal models or human specimens, to better contextualize the strength of the available evidence.

Roles of KRT6A in cancer

Several members of the keratin family, including KRT8, KRT17, KRT18, and KRT6A, play critical roles in cancer biology. Dysregulation of their expression—whether through overexpression or downregulation—is strongly linked to cancer initiation, progression, and metastasis. However, the strength of evidence varies considerably across tumor types and study designs, much of the mechanistic evidence remains preliminary, with several observations derived from single-cell line or *in vitro* studies lacking *in vivo* validation. Although mutations in keratin genes are relatively rare, they have been implicated in the development and advancement of certain cancers.

Pro-tumorigenic role of KRT6A

Aberrant expression of KRT6A has been reported across multiple cancer types, often correlating with poor clinical

outcomes. Overexpression of KRT6A has been documented in various malignancies, including cutaneous melanoma (CM) [13, 14], head and neck squamous cell carcinoma (HNSCC) [15], non-small cell lung cancer (NSCLC) [16–18], lung adenocarcinoma (LUAD) [19–23], bladder cancer [24], pancreatic adenocarcinoma (PAAD) [25], pancreatic ductal adenocarcinoma (PDAC) [26, 27], triple-negative breast cancer (TNBC) [28], colon adenocarcinoma (COAD) [29], and oral squamous cell carcinoma [30].

For example, Enzyme-linked immunosorbent assay (ELISA) analysis of 54 matched tumor and margin samples from HNSCC patients revealed significantly elevated KRT6A protein levels in tumor tissues compared to surgical margins, with smokers exhibiting higher tumor KRT6A expression than non-smokers [15]. Similarly, Reverse transcription–quantitative polymerase chain reaction (RT–qPCR) analysis of 75 NSCLC specimens showed that KRT6A was significantly upregulated in tumors relative to adjacent normal tissues. This upregulation correlated with advanced Tumor–Node–Metastasis (TNM) stage, lymph node and distant metastasis, and daily smoking status. Moreover, high KRT6A expression predicted poorer prognosis in NSCLC smokers, as demonstrated by survival and Cox proportional hazards (Cox) regression analyses [17]. Although these findings suggest a potential link between KRT6A expression and tumor aggressiveness, the evidence is largely correlational, and the extent to which KRT6A contributes causally to disease progression remains uncertain.

Functional studies provide additional but still preliminary support for a pro-tumorigenic role. *In vivo* experiments using nude mice injected with A549 lung cancer cells showed that short hairpin RNA (shRNA)-mediated knockdown of KRT6A significantly reduced tumor volume and weight compared to controls. Immunohistochemical staining indicated decreased Ki67-positive proliferative cells in KRT6A-knockdown tumors, consistent with *in vitro* findings demonstrating impaired tumor cell proliferation [17]. While these findings indicate that KRT6A may influence proliferation in specific experimental contexts, they are derived from single-cell-line models with relatively small sample sizes and require validation across additional systems and in human tissues.

Genetically, a novel tumor-specific variant of KRT6A (c.1048_1049delGGinsCG, p.Ala350Arg) was reported in a single hepatocellular carcinoma (HCC) patient. Although this mutation was absent from major genomic databases such as Single Nucleotide Polymorphism database (dbSNP) and Catalogue Of Somatic Mutations In Cancer (COSMIC), indicating it may represent a rare or previously uncharacterized alteration, its functional and clinical significance remains speculative given the single-case evidence and lack of experimental validation [31]. In addition, KRT6A mutations (e.g., c.745T>C) have been recurrently detected in peripheral blood granulocytes of Philadelphia-negative myeloproliferative neoplasm (MPN) patients with secondary cancers (SCs). Unlike the predominantly solid tumor-associated KRT6A mutations cataloged in COSMIC, this observation raises the possibility of KRT6A involvement in the hematopoietic compartment. OncodriveCLUST, a clustering-based driver mutation analysis algorithm, further indicated a stronger mutation-clustering signal for KRT6A than for the canonical JAK2V617F mutation in MPN-SC granulocytes, suggesting a potential inflammation-associated mechanism in SC pathogenesis [32]. However, because clustering-based driver prediction relies on computational modeling and is sensitive to sample size and algorithmic assumptions, these mutation-related findings should be considered preliminary. Although they suggest potential oncogenic or inflammation-associated roles for KRT6A mutations, the evidence remains limited and largely associative, underscoring the need for validation in larger cohorts and through mechanistic studies.

Overall, the current understanding of KRT6A's pro-tumorigenic potential is shaped predominantly by *in vitro* studies, limited animal experiments, and bioinformatic analyses. While available data indicate possible roles in promoting malignant phenotypes, stronger evidence from mechanistic studies and large, well-characterized clinical cohorts is needed to clarify whether KRT6A acts as a functional driver, a context-dependent modulator, or simply a biomarker of tumor progression.

Role of KRT6A in cancer cell metastasis

Building upon its established role in tumor growth, KRT6A has also been implicated in cancer cell migration, invasion, and metastasis across various cancer types. *In vitro* studies have demonstrated that KRT6A knockdown significantly reduces migratory and invasive capabilities in several cancer cell lines. For instance, small interfering RNA (siRNA)-mediated silencing of KRT6A in A549 lung cancer cells inhibited both migration (wound-healing assay) and invasion (Transwell assay) [18]. Similar findings were observed in HCC827 lung cancer cells. KRT6A knockdown reduced cell viability and proliferation, as demonstrated by the Cell Counting Kit-8 (CCK-8), colony formation, and 5-ethynyl-2′-deoxyuridine (EdU) assays. It also suppressed cell invasion [20]. In colon cancer HCT116 cells, knockdown of KRT6A impaired proliferation, migration, and invasion, while its overexpression enhanced these malignant phenotypes. DLD-1 cells with KRT6A overexpression exhibited stronger migration and three-dimensional (3D) invasive activity, particularly at the tumor invasive front, correlating with tumor budding and poor differentiation [33, 34]. These phenotypic effects, however, have been demonstrated primarily in cell-line models, and their relevance in more physiological systems remains to be determined.

KRT6A also modulates key signaling pathways involved in metastasis. In NSCLC cell lines, KRT6A may act downstream of lysine-specific demethylase 1 (LSD1) and promote invasion through c-MYC (MYC proto-oncogene protein) and MYCN (MYC proto-oncogene, neuroblastoma-derived)-driven upregulation of glucose-6-phosphate dehydrogenase (G6PD), thereby potentially activating the pentose phosphate pathway (PPP) [16]. Additionally, it has been reported to promote radioresistance, invasion, and metastasis in lung cancer, with pathway enrichment analyses suggesting possible involvement of the p53 signaling pathway [18]. In nasopharyngeal carcinoma cell models, KRT6A silencing downregulated matrix metalloproteinases-2/9 (MMP-2/9) and β-catenin signaling components, while increasing E-cadherin and tissue inhibitor of metalloproteinases-2 (TIMP-2). These molecular changes are consistent with a reversal of epithelial–mesenchymal transition (EMT). Activation of the Wnt/β-catenin pathway rescued these effects, suggesting that KRT6A may promote invasion and metastasis through β-catenin signaling [35]. Nevertheless, most of these pathway connections are inferred from single *in vitro* studies and enrichment analyses, and causal relationships remain to be experimentally validated.

KRT6A may be involved in EMT and cancer stem cell (CSC) maintenance. In lung adenocarcinoma (LUAD) cells, KRT6A knockdown increased epithelial markers (E-cadherin, β-catenin) and reduced mesenchymal markers (N-cadherin, vimentin). It also significantly decreased the CSC subpopulation (CXCR4high/CD133high) and colony-forming capacity, suggesting a potential role in EMT and CSC-associated phenotypes [19]. While these findings are mechanistically suggestive, they are derived almost entirely from LUAD cell models, and their generalizability to other cancer types remains unclear.

Beyond lung and colon cancer, KRT6A may contribute to bladder cancer progression, partly as a target of microRNA-31-5p (miR-31-5p). Low levels of this microRNA result in upregulation of KRT6A, promoting tumor cell proliferation, adhesion, and invasion [24]. In gastric adenocarcinoma, mitogen-activated protein kinase 1 (MAPK1) was shown to transcriptionally regulate KRT6A expression, facilitating AGS (human gastric adenocarcinoma) cell motility and invasion [36]. Similarly, dexamethasone-induced upregulation of KRT6A enhanced pancreatic cancer cell migration and invasion [37]. Importantly, these regulatory interactions arise from isolated studies across different cancer types, and their generalizability remains unclear.

Transcriptomic and proteomic analyses suggest that KRT6A exhibits divergent associations with melanoma progression. Elevated KRT6A expression in primary melanomas was associated with thinner tumors (Breslow thickness) but poorer survival in metastatic disease. As part of the epidermal differentiation complex (EDC), KRT6A expression correlated—based on transcriptomic and reverse-phase protein array (RPPA) analyses—with EMT signatures and activation of mitogen-activated protein kinase kinase (MEK), epidermal growth factor receptor (EGFR), and activating transcription factor-2 (ATF2) pathways. These findings suggest that KRT6A may contribute to molecular networks that facilitate metastasis and invasion [14]. Moreover, these associations are primarily correlative—based on transcriptomic and RPPA analyses—and functional evidence supporting direct mechanistic involvement remains limited.

Collectively, these findings suggest that KRT6A may function as a multifunctional regulator of tumor metastasis, operating through EMT, CSC regulation, and diverse oncogenic pathways, as illustrated in Figure 1, although most supporting evidence comes from *in vitro* studies, single-model systems, or correlative transcriptomic analyses, highlighting the need for further mechanistic and *in vivo* studies to validate these proposed roles.

Potential anti-tumor roles of KRT6A

While numerous studies support the pro-tumorigenic role of KRT6A, a few isolated reports suggests it may exert anti-tumor effects under certain contexts. In LUAD, KRT6A overexpression inhibited cell proliferation, migration, and invasion, as shown by CCK-8, colony formation, wound-healing, and Transwell assays. Furthermore, immunohistochemical analysis revealed that higher KRT6A protein levels were associated with improved patient prognosis [38]. These findings, while informative, are based primarily on *in vitro* assays and a commercially sourced tissue microarray, and have not yet been independently validated or confirmed *in vivo*, making their broader relevance uncertain.

Interestingly, a prior study from the same research group reported that elevated KRT6A mRNA expression predicted poor prognosis in LUAD patients based on analyses of public transcriptomic datasets [39]. This discrepancy between mRNA and protein-level findings suggests possible post-transcriptional regulatory mechanisms—most notably, microRNA-mediated suppression of translation. These findings highlight the need for further investigation into the context-dependent and regulatory complexity of KRT6A function in cancer.

In addition to post-transcriptional regulation, several biological factors may contribute to the context-dependent behavior of KRT6A. First, isoform-specific functions may drive divergent phenotypes, as distinct KRT6A splice variants could engage different cytoskeletal partners or signaling pathways. Second, tumor microenvironmental influences—including stromal composition, immune infiltration, and extracellular stress cues—may alter KRT6A activity or subcellular localization, thereby shaping its functional output. Third, variation in protein stability or post-translational modifications such as phosphorylation or ubiquitination may further fine-tune KRT6A signaling across tissues or disease stages. Overall, discrepancies between

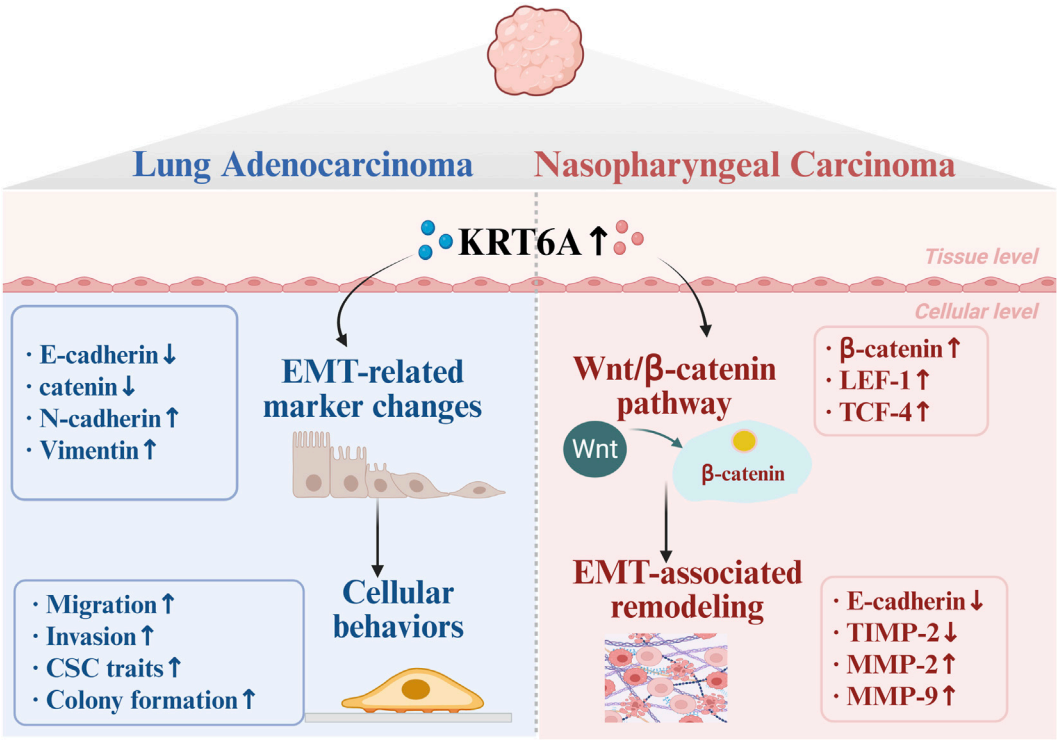

FIGURE 1
Schematic illustration of the role of KRT6A in regulating epithelial–mesenchymal transition (EMT) and malignant progression in lung adenocarcinoma and nasopharyngeal carcinoma. Accumulating evidence indicates that KRT6A regulates EMT-associated molecular alterations and malignant progression of cancer cells in a context-dependent manner. In lung adenocarcinoma, alterations in KRT6A expression are closely associated with dynamic changes in epithelial and mesenchymal markers, accompanied by phenotypic plasticity and enhanced invasiveness of cancer cells. In nasopharyngeal carcinoma, KRT6A is proposed to promote EMT-related phenotypic remodeling through activation of the Wnt/β-catenin signaling pathway. This schematic summarizes the currently available experimental and clinical evidence and highlights putative molecular mechanisms that require further experimental validation.

transcript-level and protein-level observations likely reflect multilayered regulatory complexity, underscoring the need to study KRT6A within defined cellular and microenvironmental contexts.

Role of KRT6A in cancer immunity

Although the immune-related functions of KRT6A remain largely unexplored, several correlative studies suggest a potential link between KRT6A expression and the tumor immune microenvironment, particularly tumor-associated macrophages (TAMs). In pancreatic ductal adenocarcinoma (PDAC), KRT6A expression shows a strong positive correlation with the TAM marker integrin alpha M (ITGAM/CD11b) (Pearson correlation coefficient, r = 0.95). Co-localization of KRT6A and ITGAM in tumor tissues was reported based on immunofluorescence and immunohistochemistry (IHC); however, these findings are descriptive in nature and do not establish cell-type specificity, functional interaction, or causal relationships. Gene co-expression network analysis further suggested that KRT6A may be linked to TAM-associated gene modules such as COL5A2, COL1A2, and SPARC, which are enriched in extracellular matrix remodeling, MAPK/Wnt signaling, and antigen presentation pathways [26]. Additionally, Cell type Identification By Estimating Relative Subsets Of RNA Transcripts (CIBERSORT)-based immune profiling indicated that high KRT6A expression in PDAC tissues is associated with increased infiltration of M2-polarized macrophages, supporting a potential link with an immunosuppressive microenvironment [40]. Taken together, these findings point to a potential association between KRT6A and TAM-related immunosuppression in PDAC, although mechanistic causality has not yet been established.

Beyond macrophages, KRT6A may also influence innate immune responses. It has been implicated in the regulation of antimicrobial peptides (AMPs) [41], which could indirectly affect immune cell recruitment. Moreover, in granulocytes, ginsenoside Rg1 treatment was shown to upregulate KRT6A along with laminin subunit gamma-2 (LAMC2), desmocollin-2

(DSC2), and FosB proto-oncogene (FOSB), reversing noradrenaline-induced immunosuppression and restoring their cancer-killing activity [42]. These observations were made in specific experimental systems, and their relevance to PDAC biology or *in vivo* immunity remains to be clarified.

Together, these studies suggest that KRT6A may influence tumor progression not only through intrinsic cancer cell pathways but also through interactions with the tumor immune microenvironment. Nevertheless, current evidence is preliminary, largely correlative, and highly context-specific. Definitive mechanistic studies—particularly those examining macrophage–tumor cell crosstalk, cell-type specificity, and *in vivo* immune modulation—are needed to determine whether KRT6A functions as an immune regulator or represents a potential target in PDAC immunotherapy.

Role of KRT6A in tumor metabolism

Although most studies focus on the structural and signaling functions of KRT6A, emerging evidence suggests its possible involvement in tumor metabolic reprogramming, although current findings remain limited and largely model-specific. In lung adenocarcinoma A549 cells, KRT6A expression increases under cobalt chloride ($CoCl_2$)-induced hypoxia in parallel with elevated hypoxia-inducible factor 1-alpha (HIF1A) levels, whereas this pattern is not observed in PC9 cells, indicating a potential cell-line–specific response. HIF1A is a master regulator of cellular adaptation to hypoxia and a key driver of metabolic shifts in tumors, and this context raises the possibility that KRT6A expression may be linked to hypoxia-related cellular responses [23]. Nevertheless, the evidence is derived from a single *in vitro* system, and no studies have investigated whether KRT6A directly modulates HIF1A activity or downstream metabolic pathways.

In addition, a single study suggests that KRT6A may be involved in metabolic reprogramming through regulation of the pentose phosphate pathway (PPP). Experiments in non–small cell lung cancer (NSCLC) cell lines suggest that KRT6A, acting downstream of LSD1, may enhance c-MYC/MYCN-mediated transcription of glucose-6-phosphate dehydrogenase (G6PD), the rate-limiting enzyme of the PPP. Such changes could potentially increase nicotinamide adenine dinucleotide phosphate (NADPH) production and anabolic biosynthesis, thereby supporting tumor growth, invasion, and redox homeostasis [16]. Nonetheless, these findings are primarily based on *in vitro* NSCLC cell-line experiments and currently lack *in vivo* validation. Moreover, the proposed LSD1–KRT6A–MYC–G6PD axis is supported by only one study and has not yet been corroborated by metabolic flux assays or clinical evidence, leaving its broader relevance uncertain.

Taken together, these findings suggest that KRT6A may influence cancer cell metabolic pathways, potentially involving hypoxia-related signaling and PPP activity. However, these connections are primarily supported by *in vitro* evidence, and further research is needed to determine whether KRT6A functions as a broader metabolic modulator across different tumor types.

Role of KRT6A in drug resistance

Drug resistance remains a major challenge in effective cancer therapy, and emerging evidence suggests that KRT6A expression is associated with reduced responsiveness to both chemotherapeutic and targeted agents in several cancer contexts. However, the mechanistic basis of this association remains incompletely understood. In NSCLC, *in vitro* experiments showed that KRT6A knockdown in H1299 and HCC827 cells increased their sensitivity to mitoxantrone and oxaliplatin, indicating that KRT6A may modulate chemotherapy responsiveness [43]. Similarly, in cisplatin-resistant cervical cancer cells (SiHa/DDP), downregulation of KRT6A impairs cell proliferation, promotes apoptosis, and enhances cisplatin sensitivity, implicating KRT6A as a potential therapeutic target to reverse platinum resistance [44]. However, these findings rely on short-term *in vitro* assays, and whether KRT6A directly modulates chemoresistance mechanisms remains unclear.

Beyond traditional chemotherapy, KRT6A has also been implicated in resistance to targeted therapies. In liver kinase B1 (LKB1)-deficient, KRAS-mutant NSCLC, studies in mouse models and organoids show that epigenetic activation of the C40 enhancer induces ΔNp63 and downstream KRT6A expression, driving adeno-to-squamous transition (AST). This phenotypic switch enables tumors to bypass KRAS dependency and confers resistance to KRAS inhibitors such as Adagrasib (G12C) and MRTX1133 (G12D). Consistently, patient biopsy data indicate that high KRT6A expression is associated with poor response and unfavorable prognosis [45]. Although the evidence is stronger due to cross-model consistency, direct functional validation of KRT6A as a driver of AST-mediated resistance is still limited.

Furthermore, KRT6A is identified as a core gene in a machine learning model for acquired resistance to EGFR-tyrosine kinase inhibitors (EGFR-TKIs; e.g., gefitinib, erlotinib, afatinib) and cetuximab, suggesting a potential broader involvement in resistance to anti-EGFR therapies [46]. As this conclusion is mainly based on computational modeling, experimental confirmation of KRT6A's functional contribution to anti-EGFR resistance is still lacking.

Collectively, current evidence suggests that KRT6A may contribute to diverse forms of therapy resistance across multiple cancer types; however, most available data are derived from isolated *in vitro* studies or computational predictions. Robust *in vivo* experiments and mechanistic

investigations are still lacking, and no causal link between KRT6A and drug resistance has been firmly established. Therefore, while KRT6A represents an intriguing candidate for therapeutic targeting, its functional role in treatment resistance requires substantially more experimental validation.

Role of KRT6A in radiation resistance

KRT6A has been implicated in the development of radioresistance in non–small cell lung cancer (NSCLC), although current evidence remains limited and largely context-dependent. In A549-derived radiation-resistant cells (A549-RR), KRT6A expression is markedly elevated, and its silencing enhances radiosensitivity. Mechanistically, Western blot analysis shows that β-catenin levels decline after KRT6A knockdown, whereas β-catenin overexpression rescues both EMT phenotypes and radiation resistance, supporting the involvement of the Wnt/β-catenin–EMT axis. However, these mechanistic data are derived from *in vitro* assays only and have not yet been validated *in vivo* [47].

In support of these findings, The Cancer Genome Atlas (TCGA) RNA sequencing (RNA-seq) data from lung squamous cell carcinoma (LUSC) patients revealed KRT6A as the most significantly upregulated gene in the low radiosensitivity index (RSI) group compared to the high RSI group [48], although this correlation does not imply a causal relationship between KRT6A expression and radiosensitivity.

Additionally, KRT6A may influence radiation response by modulating pathways such as p53 signaling and G2/M cell-cycle regulation—both of which are linked to DNA damage repair and tumor cell survival under irradiation stress. These associations are derived from public database analyses, and the underlying mechanisms require further validation in cellular and animal models [18].

Taken together, existing evidence suggests that KRT6A expression is associated with reduced radiosensitivity in NSCLC and may serve as a potential biomarker of radiation response. However, whether KRT6A functions as a direct mediator of radioresistance or represents a surrogate marker of resistant tumor states remains unresolved. Further *in vivo* and mechanistic studies are required before KRT6A can be considered a viable therapeutic target in the context of radiotherapy.

Targeting KRT6A: drugs and therapeutic strategies

Several studies have explored pharmacological approaches that may modulate KRT6A expression or function, although direct targeting of KRT6A remains largely conceptual and has not yet been broadly validated. Sinapine thiocyanate (ST) exerts anti-tumor activity in colorectal cancer (CRC) partly by suppressing the KRT6A/S100A2 axis, with S100A2 (a calcium-binding protein of the S100 family) serving as a downstream mediator. In CRC cell lines, ST decreases KRT6A mRNA and protein expression and inhibits cell proliferation and migration. *In vivo*, ST similarly reduces tumor growth in xenograft models. Rescue experiments further show that overexpression of KRT6A counteracts ST-induced inhibition of malignant phenotypes, supporting KRT6A as a functional target of ST. Consistent with these findings, elevated KRT6A/S100A2 expression correlates with poorer prognosis in CRC patients [49]. However, these findings are restricted to CRC models, and it remains unclear whether ST exerts comparable KRT6A-dependent effects in other tumor types or whether KRT6A is the primary molecular target of ST.

Taxifolin, a natural flavonoid, was identified as a candidate therapeutic agent through Connectivity Map (CMAP) analysis. This prediction was derived from a weighted gene co-expression network analysis (WGCNA) module in which KRT6A was one of 11 hub genes associated with poor prognosis across multiple cancer types [25]. However, this prediction is based on transcriptomic similarity rather than functional validation, and a direct mechanistic link between taxifolin and KRT6A regulation has not been experimentally confirmed.

Additionally, KRT6A has been reported as a gene associated with progression from Barrett's esophagus (BE) to esophageal adenocarcinoma (EAC). Bioinformatics analysis using the Drug–Gene Interaction Database (DGIdb) predicted TD101, an siRNA previously used for pachyonychia congenita, as a potential KRT6A-targeting therapeutic agent, although its efficacy in EAC remains to be experimentally validated [50].

Collectively, existing studies nominate KRT6A as a potential therapeutic vulnerability; however, no KRT6A-directed agents have yet demonstrated consistent efficacy across cancer models or advanced toward clinical translation. Rigorous mechanistic studies, validation in diverse tumor systems, and preclinical evaluations are required to determine whether KRT6A represents a viable and druggable target in oncology.

KRT6A as a diagnostic and therapeutic biomarker in cancer

KRT6A is emerging as a versatile biomarker across multiple cancer types. Its expression is significantly higher in lung squamous cell carcinoma (LSCC) compared to lung adenocarcinoma (LUAD), making it a potential diagnostic marker to distinguish these lung cancer subtypes [39, 51–53]. Proteomic analyses of exhaled breath condensate (EBC) further reported elevated KRT6A levels in lung cancer patients relative to controls, smokers, and Chronic Obstructive Pulmonary Disease (COPD) patients, suggesting promise for noninvasive early detection [54]. However, this conclusion is based on a small cohort from a single center, which constrains its broader

TABLE 1 KRT6A expression and prognostic significance across cancer types.

Cancer	Sample size	Expression tumor vs. normal	Prognostic of high KRT6A	OS	
				HR (95% CI)	p-value
NSCLC [13]	TCGA: 483 LUAD/486 LUSC Clinical IHC: 30	↑ mRNA & protein	Worse OS	1.491	0.016
LUAD [20]	TCGA: 535 tumors/59 normals	↑	Worse OS/DSS/PFI	1.156 (1.097–1.223)	<0.001
PDAC [34]	Clinical IHC: 130 TCGA-PAAD: 177	↑	Worse OS/DFS	2.704 (1.374–5.320)	0.004
PDAC [24]	TCGA-PAAD: 178 tumors/171 normals 7 paired cases	↑	Worser OS	1.09 (1.04–1.14)	0.00037
CRC [31]	Clinical IHC: 142 348 validation	↑Invasive front vs. center	Worse OS/DSS/PFS	3.081 (1.653–5.740)	0.0004
CM [10]	GEO: 99 CM vs 45 nevi TCGA: 475 CM Clinical IHC: 31 CM vs 31 nevi	↑Melanoma vs. nevus	Worse OS	1.07 (1.037–1.103)	<0.001
BLCA [21]	TCGA: 404 tumors vs. 28 normals	↑	Worse OS	1.42 (1.05–1.93)	0.023

Abbreviations: NSCLC, non-small cell lung cancer; LUAD, lung adenocarcinoma; PDAC, pancreatic ductal adenocarcinoma; CRC, colorectal cancer; CM, cutaneous melanoma; BLCA, bladder cancer; LUSC, lung squamous cell carcinoma; PAAD, pancreatic adenocarcinoma; TCGA, The Cancer Genome Atlas; GEO, Gene Expression Omnibus; IHC, immunohistochemistry; OS, overall survival; DSS, disease-specific survival; DFS, disease-free survival; PFS, progression-free survival; PEI, Progression-Event Interval; HR, hazard ratio.
"↑" Indicates higher KRT6A expression in tumor tissues or in aggressive tumor subsets.
References: NSCLC [13]; LUAD [20]; PDAC [24, 34]; CRC [31]; CM [10]; BLCA [21].

generalizability. Moreover, KRT6A expression correlates with smoking exposure and has been proposed as a potential early diagnostic biomarker in smoking-related NSCLC [17], although prospective validation is still lacking.

Beyond lung cancer, KRT6A has also been implicated in other malignancies. It serves as a characteristic biomarker for basal-subtype bladder cancer [55, 56], and its expression is significantly higher in progesterone receptor B–high (PRB-H) breast tumors than in progesterone receptor A–high (PRA-H) tumors [57]. These associations, however, are mostly derived from retrospective datasets and have not been systematically examined in larger, clinically annotated cohorts.

Collectively, available evidence suggests that KRT6A may serve as a diagnostic or subtype-associated biomarker in several cancer contexts. Nevertheless, its clinical utility remains exploratory, and rigorous validation in large, multicenter studies—ideally with standardized assays and longitudinal follow-up—will be required before KRT6A can be adopted for routine clinical use.

Prognostic biomarker correlation with poor outcomes

KRT6A expression has been consistently reported to correlate with tumor progression and poor prognosis across multiple cancer types, although the strength and consistency of these associations vary by tumor context and disease stage. In non-small cell lung cancer (NSCLC), particularly lung adenocarcinoma (LUAD), KRT6A overexpression is associated with aggressive clinicopathological features such as lymph node metastasis, advanced T stage, and worse overall survival (OS) and recurrence-free survival (RFS) [16, 18, 19, 23]. However, this correlation appears less clear in early-stage NSCLC [51]. In conjunction with LSD1, KRT6A may serve as a candidate prognostic indicator, with potential implications for therapeutic targeting in NSCLC [16]. To provide an integrated snapshot across tumor types, we compiled representative studies reporting KRT6A expression and its prognostic associations in major cancers (Table 1).

In pancreatic ductal adenocarcinoma (PDAC), elevated KRT6A expression is an independent predictor of poor OS and disease-specific survival (DSS), particularly in poorly differentiated tumors, reflecting its link to malignant phenotypes and tumor aggressiveness [26, 27, 37, 58, 59]. KRT6A has also been linked to alterations in the tumor immune microenvironment, particularly through associations with TAM-related pathways [26], however, these observations are primarily correlative.

In colorectal cancer (CRC), KRT6A has been identified as an independent prognostic factor for OS, DSS, and progression-free survival (PFS), correlating with lymph node metastasis and tumor stage [29, 34]. Interestingly, metastatic microsatellite instability–high (MSI–H) CRC tumors show reduced KRT6A

expression compared to non-metastatic cases, suggesting subtype-specific roles [60].

High KRT6A levels have been reported to associate with advanced disease and poor prognosis in melanoma [13] and bladder cancer [24]. In papillary thyroid microcarcinoma (PTMC), elevated expression of CK5/6 (encoded by KRT5/KRT6A) predicts central lymph node metastasis, supporting its utility as a predictive biomarker [61]. Furthermore, an aggressive basal-like tumor cell subpopulation expressing KRT6A, KRT5, and KRT17 correlates with poor outcomes in intrahepatic cholangiocarcinoma (ICC) [62].

Collectively, these studies suggest that KRT6A expression is frequently associated with adverse prognosis across diverse malignancies. Nevertheless, existing prognostic evidence is derived from heterogeneous study designs, retrospective cohorts, and variable analytical methodologies. As such, KRT6A should currently be regarded as a candidate prognostic biomarker rather than a validated clinical indicator, and prospective, standardized studies will be required to define its independent prognostic value and potential clinical utility.

KRT6A as a core component of predictive risk models

Multigene prognostic models have emerged as valuable tools in predicting cancer outcomes alongside traditional clinicopathological parameters. KRT6A, which harbors mutations across various cancers [21], is frequently included in these models. However, its inclusion should be interpreted as a statistical contributor rather than definitive evidence of causal biological centrality.

In triple-negative breast cancer (TNBC), KRT6A is consistently incorporated into multiple prognostic signatures—such as a 6-gene risk model, a necroptosis-related 7-gene model, and a senescence-associated 4-gene model—where it serves as a high-risk indicator linked to poor survival [28, 63]. Notably, the necroptosis-related model not only predicts survival but also explores potential therapeutic stratification based on predicted drug-response patterns, as reflected by estimated half-maximal inhibitory concentration (IC50) differences for cisplatin and lapatinib. A corresponding nomogram further demonstrates reasonable discriminative performance (AUC >0.84) [64]. Nevertheless, these findings are derived from retrospective analyses and predictive modeling rather than prospective therapeutic validation.

In pancreatic ductal adenocarcinoma (PDAC), 5-gene models that include KRT6A predict overall survival independently. These signatures link KRT6A to immune regulation, vascular invasion, and aggressive squamous subtypes, providing further evidence for its role as a malignancy-associated factor [65, 66], but they remain primarily correlative and model-dependent.

In lung adenocarcinoma (LUAD), KRT6A is embedded in a wide array of predictive models—such as those related to fatty acid metabolism [20], autophagy [67], tumor microenvironment (LATPS) [68], genomic instability (GSAGI) [69], DNA damage repair (DDR) [70], lymph node metastasis [71], RNA modification (RMScore) [72], TEAD4 (TEA domain transcription factor 4)-related pathways [73], pyroptosis [74], liquid–liquid phase separation (LLPS) [75], and ferroptosis [76]. Across these models, high KRT6A expression or inclusion in high-risk groups consistently correlates with worse outcomes (OS, DFS, or RFS). Additionally, KRT6A appears in independent 5- and 13-gene models [77, 78]. The breadth of its inclusion likely reflects its strong correlation with aggressive tumor states rather than pathway-specific causality.

In colorectal cancer (CRC), KRT6A functions as a key component of a validated 5-gene prognostic signature, showing independent predictive power across The Cancer Genome Atlas (TCGA), GSE39582, and GSE17538 cohorts for overall survival (OS), disease-free survival (DFS), and disease-specific survival (DSS). Enrichment analysis links the KRT6A-containing signature to extracellular matrix remodeling, particularly collagen-containing matrix pathways, which are commonly associated with tumor progression [33].

Collectively, these studies indicate that KRT6A is frequently incorporated into multigene prognostic models and consistently associated with adverse clinical outcomes. However, most existing models are derived from retrospective datasets and employ heterogeneous feature-selection and validation pipelines, raising concerns regarding overfitting and cross-study comparability. Accordingly, KRT6A should be viewed as a recurrent statistical risk-associated marker rather than a validated standalone predictor, and prospective validation will be essential to establish its clinical utility.

Emerging roles of KRT6A in HPV-related tumors and immunotherapy

Recent studies indicate that KRT6A, previously viewed mainly as a cytoplasmic structural keratin, can also localize to the nucleus in human papillomavirus 16 (HPV16)-positive cervical cancer cells. Nuclear KRT6A interacts with TEA domain (TEAD) transcription factors and is recruited to the HPV long control region, supporting E6/E7 transcription and promoting tumor cell proliferation. Loss-of-function and rescue-of-function studies indicate that KRT6A contributes to the maintenance of HPV E6/E7 expression [79]. Although these observations were generated in HPV16-positive squamous carcinoma cell lines and require validation across other high-risk HPV genotypes and primary tumor settings, they highlight an emerging interface between keratin biology and viral transcriptional programs, suggesting that aberrant KRT6A activity may contribute to HPV-driven carcinogenesis.

TABLE 2 KRT6A mutations in pachyonychia congenita (PC-K6a): functional and therapeutic implications.

Variant (protein)	Frequency in PC	Functional impact	Therapeutic notes
p.Asn172del	10.9%	Disrupts helix-initiation motif; induces cytoskeletal fragility	Symptomatic care; limited response to retinoids; Case-dependent EGFR/mTOR inhibitor responses; Emerging siRNA approaches; no mutation-specific evidence
p.Val181_Gln186del	3%	Alters L12 linker; reduces filament flexibility; weakens cytoskeletal network	
p.Glu472Lys	2%	Disrupts helix-termination motif; impairs filament maturation	
p.Asn171Lys	1.6%	Destabilizes helix-initiation motif; impairs filament assembly	
p.Leu469Pro	1.2%	Disrupts helix-termination motif; impairs filament stabilization and maturation; induces cytoskeletal fragility	

Representative KRT6A variants in PC-K6a. Variant nomenclature follows HGVS guidelines; mutation data are referenced from the International Pachyonychia Congenita Research Registry. EGFR, epidermal growth factor receptor; mTOR, mechanistic target of rapamycin; siRNA, small-interfering RNA.

Pan-cancer analyses link KRT6A to immune checkpoint pathways. In syngeneic immunotherapy models, KRT6A expression increased in responders to anti-cytotoxic T-lymphocyte–associated antigen 4 (CTLA-4) therapy, but decreased in non-responders receiving combined anti-CTLA-4 and anti-programmed cell death protein 1 (PD-1) treatment, whereas no significant changes were observed with other immune checkpoint blockade (ICB) regimens. These observations suggest that KRT6A expression dynamics may reflect treatment-specific immune responses rather than serving as a universal immunotherapy biomarker.

In parallel, drug-response profiling (CTRP/GDSC) further showed that high KRT6A expression was associated with greater sensitivity to several EGFR/HER (ErbB) family inhibitors [12]. However, these associations are derived from large-scale pharmacogenomic correlations and do not establish a direct mechanistic role for KRT6A in modulating immune checkpoint efficacy or targeted therapy response.

Collectively, these emerging findings expand the functional landscape of KRT6A to include potential roles in HPV-driven oncogenesis and therapy-associated immune contexts. Nevertheless, most supporting evidence remains correlative or model-specific, and further mechanistic and clinical validation will be required to determine whether KRT6A functions as an active regulator or a context-dependent biomarker in immunotherapy and virus-associated cancers.

KRT6A in dermatoses

KRT6A is a type II intermediate filament protein encoded by the KRT6A gene located on chromosome 12q13.13 [3]. Under normal conditions, KRT6A is selectively expressed in specialized epithelial tissues such as the palmar/plantar epidermis, nail bed, hair follicle, and oral mucosa [80, 81]. Upon epithelial injury, mechanical stress, or inflammatory stimulation, KRT6A expression is rapidly and robustly induced [82]. This response is mediated by signaling cascades involving pro-inflammatory cytokines (e.g., IL-1, TNF-α), growth factors, and transcriptional regulators (e.g., NF-κB, AP-1) [83]. However, the relative contribution of these pathways may vary depending on tissue context and experimental conditions.

Functionally, KRT6A enhances epithelial resilience against mechanical trauma and facilitates wound healing by supporting keratinocyte proliferation and migration [11, 84]. These roles are primarily supported by experimental models of skin injury and keratinocyte culture systems, and the extent to which they generalize across different epithelial tissues remains to be fully elucidated.

In pathological conditions, such as inflammatory skin diseases (e.g., psoriasis, lichen planus) and inherited keratin disorders, this inducible expression becomes dysregulated [3]. Aberrant KRT6A upregulation contributes to hyperproliferative phenotypes and epidermal barrier dysfunction [10]. Moreover, mutations in KRT6A are causally linked to pachyonychia congenita type I, a rare genodermatosis characterized by painful palmoplantar keratoderma, nail dystrophy, and oral leukokeratosis [85]. These findings underscore KRT6A's pivotal role not only in epithelial homeostasis but also in the pathogenesis of diverse dermatoses.

KRT6A in pachyonychia congenita

Pachyonychia Congenita (PC) is a rare autosomal dominant genodermatosis caused by mutations in genes encoding stress keratins, with KRT6A mutations accounting for approximately 30% of all PC cases (PC-K6a subtype) [85, 86]. According to data from the International Pachyonychia Congenita Research Registry (IPCRR), over 50 pathogenic variants of KRT6A have been documented—most of them being missense mutations (e.g., p.Asn171Lys, p.Arg162Pro), as well as deletions, insertions, and splice site alterations. These mutations predominantly affect the helix initiation and termination motifs critical for keratin filament assembly.

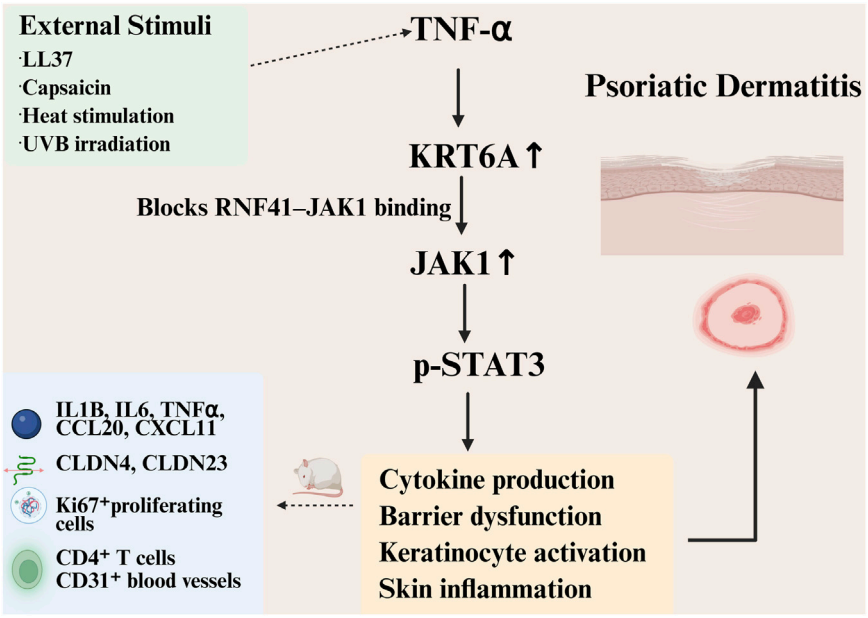

FIGURE 2
Schematic illustration of the KRT6A-mediated inflammatory signaling mechanism in psoriatic dermatitis. In psoriatic lesions and in the imiquimod (IMQ)-induced mouse model, KRT6A is markedly upregulated in epidermal keratinocytes in response to inflammatory stimuli. Elevated KRT6A may sustain activation of the JAK1–STAT3 signaling pathway by inhibiting RNF41-mediated ubiquitination and subsequent degradation of JAK1, thereby promoting the production of pro-inflammatory cytokines, aberrant activation of keratinocytes, impairment of skin barrier function, and amplification of cutaneous inflammation. This schematic model is primarily supported by evidence from *in vitro* and animal studies.

Mutant KRT6A proteins impair cytoskeletal integrity by disrupting filament organization, leading to cellular fragility and mechanical stress sensitivity [87]. The accumulation of misfolded keratin proteins triggers endoplasmic reticulum (ER) stress, activating c-Jun N-terminal kinase (JNK) and p38 mitogen-activated protein kinase (p38 MAPK) signaling pathways and promoting cellular stress responses [88]. In addition, mutant KRT6A induces dysregulated apoptosis via enhanced caspase-3 activation in basal keratinocytes [89]. Compensatory upregulation of KRT6A and KRT16 aggravates the pathology by driving keratinocyte hyperproliferation and impaired differentiation, contributing to disease progression [90].

Clinically, PC is characterized by a triad of focal palmoplantar keratoderma, hypertrophic nail dystrophy, and debilitating plantar pain. Other manifestations may include follicular hyperkeratosis, oral leukokeratosis, natal teeth, sebaceous cysts, hidradenitis suppurativa, hoarseness, and itching [85, 86, 91, 92]. Among patients with PC-K6a mutations, painful plantar keratoderma is often reported as the most debilitating and treatment-resistant symptom [91].

Currently, no definitive cure exists for PC, and management remains symptomatic. Conservative approaches include reducing plantar trauma, mechanical debridement, and application of topical keratolytic agents [93, 94]. Some patients benefit from oral retinoids [95], while botulinum toxin injections into the plantar region have been shown to alleviate pain, callus formation, and blistering [96–98]. Oral statins have also demonstrated efficacy in reducing callus thickness and pain levels in select patients [99–102].

Emerging targeted therapies are under exploration. A summary of representative KRT6A variants in PC-K6a and their mechanistic and therapeutic implications is provided in Table 2. These include small-molecule inhibitors, mechanistic target of rapamycin (mTOR) pathway modulators [103, 104], and gene therapy strategies such as small interfering RNA (siRNA) targeting KRT6A [105–107]. Notably, EGFR inhibitors (e.g., erlotinib, lapatinib) have been reported in individual cases to alleviate plantar hyperkeratosis and pain [108, 109]. Additionally, sunitinib, a multi-target tyrosine kinase inhibitor, was found to reduce KRT6A and serine protease inhibitor B1 (SERPINB1) expression *in vitro* by inhibiting extracellular signal-regulated kinase 1/2 (ERK1/2) and p38 MAPK signaling [110], suggesting a potential future therapeutic avenue. These findings are preliminary and largely based on case reports or experimental models, underscoring the need for systematic clinical evaluation.

KRT6A in psoriatic dermatitis

KRT6A expression is significantly upregulated in psoriasis-like dermatitis, contributing to disease development through multiple mechanisms [111–113].

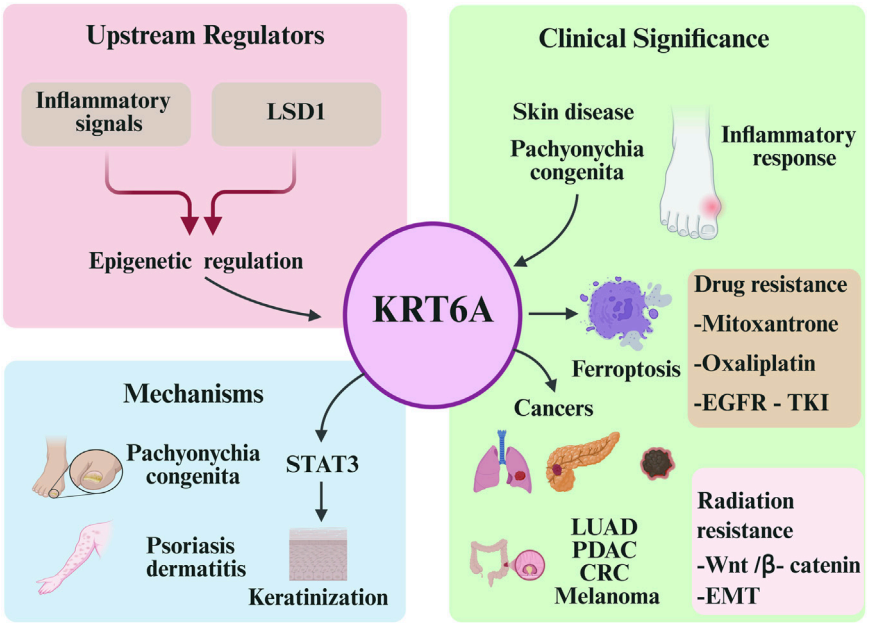

FIGURE 3
Schematic representation of the upstream regulation, molecular mechanisms, and clinical significance of KRT6A. Inflammatory signals (e.g., TNF-α, IL-1β) and the epigenetic regulator LSD1 can upregulate KRT6A expression. KRT6A is involved in multiple biological processes, including pachyonychia congenita and psoriatic dermatitis, partly via the STAT3 pathway, and is associated with ferroptosis and inflammatory responses. Clinically, KRT6A is closely linked to the development and progression of various cancers, and contributes to both chemotherapy and radiotherapy resistance. It holds potential as a diagnostic and prognostic biomarker.

In clinical psoriatic specimens and imiquimod (IMQ)-induced mouse models, KRT6A is markedly overexpressed in epidermal keratinocytes. Functional experiments demonstrate that KRT6A knockdown attenuates inflammation, while KRT6A overexpression worsens pathological phenotypes. Mechanistically, *in vitro* evidence suggests that KRT6A may enhance inflammatory responses by activating the signal transducer and activator of transcription 3 (STAT3) signaling pathway, likely through the inhibition of ring finger protein 41 (RNF41)-mediated ubiquitination and degradation of Janus kinase 1 (JAK1), thereby sustaining STAT3 activation and promoting the expression of proinflammatory cytokines in keratinocytes [114], as depicted in Figure 2. Nonetheless, these mechanistic insights are based largely on *in vitro* assays, and the RNF41–JAK1 axis has not been validated *in vivo*.

In addition, narrow-band ultraviolet-B (NB-UVB) therapy, a standard treatment for psoriasis, significantly downregulates KRT6A gene expression in both the peripheral and central regions of psoriatic plaques. This downregulation is associated with the normalization of keratinocyte differentiation, suggesting that KRT6A may act as a mediator of abnormal keratinization in psoriasis. However, these transcriptomic findings are based on a limited sample size and remain correlative [115].

Discussion

KRT6A, a stress-inducible type II keratin, plays a multifaceted and context-dependent role in both epithelial malignancies and dermatoses. In cancers, its overexpression is frequently associated with enhanced tumor aggressiveness, metastatic potential, poor prognosis, and resistance to standard therapies. Mechanistically, KRT6A contributes to malignant progression via promoting proliferation, migration, epithelial–mesenchymal transition (EMT), immune modulation, and cell death resistance. In contrast, pathogenic mutations in KRT6A underlie the inherited disorder pachyonychia congenita (PC), in which cytoskeletal disorganization, keratinocyte fragility, and ER stress result in severe skin phenotypes.

Current evidence indicates that KRT6A is subject to complex regulatory mechanisms at the transcriptional and post-translational levels, although our understanding of its upstream regulators, post-translational modifications (PTMs), and interactome remains incomplete. Proteomic insights suggest phosphorylation and possibly other PTMs may fine-tune KRT6A function in distinct pathophysiological contexts. However, comprehensive mapping of these modifications and their functional consequences is urgently needed.

From a translational perspective, KRT6A represents a promising candidate for both biomarker development and

therapeutic targeting. In oncology, its incorporation into multi-gene prognostic models has improved patient stratification and therapeutic guidance, particularly in TNBC, LUAD, PDAC, and CRC. In hereditary skin diseases, topical or systemic delivery of RNA interference (RNAi) or small-molecule inhibitors targeting KRT6A or its downstream effectors offers potential therapeutic benefit.

Several limitations should be considered when interpreting the available evidence. First, many clinical investigations were conducted with relatively small patient cohorts and often lacked multi-center validation, limiting the generalizability of the findings. Second, mechanistic insights into KRT6A function largely rely on *in vitro* cell line models, with limited *in vivo* or clinical evidence to support biological relevance. Third, several mechanistic conclusions originate from single-study observations or correlative transcriptomic and bioinformatic analyses, which do not establish causality. Additionally, cancer-type heterogeneity and varied experimental conditions further complicate the interpretation and comparison of results.

Future research should focus on: (1) large-scale clinical validation of KRT6A as a diagnostic and prognostic biomarker; (2) elucidation of its molecular network and upstream regulatory pathways across disease types; (3) development of safe and efficient delivery systems for RNAi and antibody-based therapeutics; (4) integration of single-cell and spatial multi-omics technologies to delineate KRT6A-associated cellular programs with high resolution; (5) establishment of KRT6A knockout and conditional genetic models to dissect its context-dependent functions *in vivo*; and (6) initiation of early-phase clinical trials for KRT6A-targeted inhibitors to accelerate therapeutic translation. In addition, mechanistic studies on KRT6A's role in immune regulation, ferroptosis, and tissue remodeling could uncover novel vulnerabilities for therapeutic exploitation.

A schematic summary of KRT6A's upstream regulation, molecular mechanisms, and clinical significance is illustrated in Figure 3, providing an integrated visual overview that complements these conclusions. In conclusion, KRT6A functions as a central epithelial regulator with significant implications for disease pathogenesis and therapeutic intervention. Ongoing efforts to decode its regulatory mechanisms and disease-specific functions will pave the way toward KRT6A-based precision medicine strategies in both oncology and dermatology.

Author contributions

All authors listed have made a substantial, direct, and intellectual contribution to the work and approved it for publication.

Funding

The author(s) declare that financial support was received for the research and/or publication of this article. This work was supported by the Clinical Research Project of Linfen Central Hospital (Grant No. LFSZXYY-KJK-YJ-2025035).

Conflict of interest

The author(s) declared no potential conflicts of interest with respect to the research, authorship, and/or publication of this article.

Generative AI statement

The author(s) declared that generative AI was not used in the creation of this manuscript.

Any alternative text (alt text) provided alongside figures in this article has been generated by Frontiers with the support of artificial intelligence and reasonable efforts have been made to ensure accuracy, including review by the authors wherever possible. If you identify any issues, please contact us.

References

1. Li P, Rietscher K, Jopp H, Magin TM, Omary MB. Posttranslational modifications of keratins and their associated proteins as therapeutic targets in keratin diseases. *Curr Opin Cell Biol* (2023) **85**:102264. doi:10.1016/j.ceb.2023.102264

2. Smith F. The molecular genetics of keratin disorders. *Am J Clin Dermatol* (2003) **4**:347–64. doi:10.2165/00128071-200304050-00005

3. Moll R, Divo M, Langbein L. The human keratins: biology and pathology. *Histochem Cell Biol* (2008) **129**:705–33. doi:10.1007/s00418-008-0435-6

4. Herrmann H, Aebi U. Intermediate filaments: structure and assembly. *Cold Spring Harb Perspect Biol* (2016) **8**:a018242. doi:10.1101/cshperspect.a018242

5. Toivola DM, Polari L, Schwerd T, Schlegel N, Strnad P. The keratin-desmosome scaffold of internal epithelia in health and disease - the plot is thickening. *Curr Opin Cell Biol* (2024) **86**:102282. doi:10.1016/j.ceb.2023.102282

6. Jacob JT, Coulombe PA, Kwan R, Omary MB. Types I and II keratin intermediate filaments. *Cold Spring Harb Perspect Biol* (2018) **10**:a018275. doi:10.1101/cshperspect.a018275

7. Takahashi K, Paladini RD, Coulombe PA. Cloning and characterization of multiple human genes and cDNAs encoding highly related type II keratin 6 isoforms. *J Biol Chem* (1995) **270**:18581–92. doi:10.1074/jbc.270.31.18581

8. Zieman AG, Coulombe PA. Pathophysiology of pachyonychia congenita-associated palmoplantar keratoderma: new insights into skin epithelial homeostasis and avenues for treatment. *Br J Dermatol* (2020) **182**:564–73. doi:10.1111/bjd.18033

9. Li Y, Sun Y, Yu K, Li Z, Miao H, Xiao W. Keratin: a potential driver of tumor metastasis. *Int J Biol Macromol* (2025) **307**:141752. doi:10.1016/j.ijbiomac.2025.141752

10. Romashin DD, Tolstova TV, Varshaver AM, Kozhin PM, Rusanov AL, Luzgina NG. Keratins 6, 16, and 17 in health and disease: a summary of recent findings. *Curr Issues Mol Biol* (2024) **46**:8627–41. doi:10.3390/cimb46080508

11. Zhang X, Yin M, Zhang LJ. Keratin 6, 16 and 17-Critical barrier alarmin molecules in skin wounds and psoriasis. *Cells* (2019) **8**:807. doi:10.3390/cells8080807

12. Lv Y, Liu X, Xiao Z, Zhan X, Tang W, Sun Q, et al. Comprehensive pan-cancer analysis of KRT6A as a prognostic and immune biomarker. *Sci Rep* (2025) **15**:35728. doi:10.1038/s41598-025-19599-y

13. Han W, Xu WH, Wang JX, Hou JM, Zhang HL, Zhao XY, et al. Identification, validation, and functional annotations of genome-wide profile variation between melanocytic nevus and malignant melanoma. *Biomed Res Int* (2020) **2020**:1840415. doi:10.1155/2020/1840415

14. Barbero G, Castro MV, Quezada MJ, Lopez-Bergami P. Bioinformatic analysis identifies epidermal development genes that contribute to melanoma progression. *Med Oncol* (2022) **39**:141. doi:10.1007/s12032-022-01734-8

15. Nałęcz D, Świętek A, Hudy D, Wiczkowski K, Złotopolska Z, Strzelczyk JK. Assessment of concentration KRT6 proteins in tumor and matching surgical margin from patients with head and neck squamous cell carcinoma. *Int J Mol Sci* (2024) **25**: 7356. doi:10.3390/ijms25137356

16. Che D, Wang M, Sun J, Li B, Xu T, Lu Y, et al. KRT6A promotes lung cancer cell growth and invasion through MYC-regulated pentose phosphate pathway. *Front Cell Dev Biol* (2021) **9**:694071. doi:10.3389/fcell.2021.694071

17. Zhou J, Jiang G, Xu E, Zhou J, Liu L, Yang Q. Identification of SRXN1 and KRT6A as key genes in smoking-related non-small-cell lung cancer through bioinformatics and functional analyses. *Front Oncol* (2021) **11**:810301. doi:10.3389/fonc.2021.810301

18. Xu Q, Yu Z, Mei Q, Shi K, Shen J, Gao G, et al. Keratin 6A (KRT6A) promotes radioresistance, invasion, and metastasis in lung cancer via p53 signaling pathway. *Aging (Albany NY)* (2024) **16**:7060–72. doi:10.18632/aging.205742

19. Yang B, Zhang W, Zhang M, Wang X, Peng S, Zhang R. KRT6A promotes EMT and cancer stem cell transformation in lung adenocarcinoma. *Technol Cancer Res Treat* (2020) **19**:1533033820921248. doi:10.1177/1533033820921248

20. Wang Y, Huang X, Fan H, Xu Y, Qi Z, Zhang Y, et al. Identification of fatty acid-related subtypes, the establishment of a prognostic signature, and immune infiltration characteristics in lung adenocarcinoma. *Aging (Albany NY)* (2023) **15**: 4202–35. doi:10.18632/aging.204725

21. Sui P, Liu X, Zhong C, Sha Z. Integrated single-cell and bulk RNA-seq analysis enhances prognostic accuracy of PD-1/PD-L1 immunotherapy response in lung adenocarcinoma through necroptotic anoikis gene signatures. *Sci Rep* (2024) **14**: 10873. doi:10.1038/s41598-024-61629-8

22. Meng X, Zhao X, Zhou B, Song W, Liang Y, Liang M, et al. FSTL3 is associated with prognosis and immune cell infiltration in lung adenocarcinoma. *J Cancer Res Clin Oncol* (2024) **150**:17. doi:10.1007/s00432-023-05553-w

23. Sun K, Zhang Z, Wang D, Huang Y, Zhang J, Lian C. Regulation of early diagnosis and prognostic markers of lung adenocarcinoma in immunity and hypoxia. *Sci Rep* (2023) **13**:6459. doi:10.1038/s41598-023-33404-8

24. Chen Y, Ji S, Ying J, Sun Y, Liu J, Yin G. KRT6A expedites bladder cancer progression, regulated by miR-31-5p. *Cell Cycle* (2022) **21**:1479–90. doi:10.1080/15384101.2022.2054095

25. Chen SJ, Ren LK, Fei XB, Liu P, Wang X, Zhu CH, et al. A study on the role of Taxifolin in inducing apoptosis of pancreatic cancer cells: screening results using weighted gene co-expression network analysis. *Aging (Albany NY)* (2024) **16**: 2617–37. doi:10.18632/aging.205500

26. Zhang J, Sun H, Liu S, Huang W, Gu J, Zhao Z, et al. Alteration of tumor-associated macrophage subtypes mediated by KRT6A in pancreatic ductal adenocarcinoma. *Aging (Albany NY)* (2020) **12**:23217–32. doi:10.18632/aging.104091

27. Lu Y, Li D, Liu G, Xiao E, Mu S, Pan Y, et al. Identification of critical pathways and potential key genes in poorly differentiated pancreatic adenocarcinoma. *Onco Targets Ther* (2021) **14**:711–23. doi:10.2147/ott.S279287

28. Cao T, Huang M, Huang X, Tang T. Research and experimental verification on the mechanisms of cellular senescence in triple-negative breast cancer. *PeerJ* (2024) **12**:e16935. doi:10.7717/peerj.16935

29. Wang H, Liu J, Li J, Zang D, Wang X, Chen Y, et al. Identification of gene modules and hub genes in colon adenocarcinoma associated with pathological stage based on WGCNA analysis. *Cancer Genet* (2020) **242**:1–7. doi:10.1016/j.cancergen.2020.01.052

30. Thiel UJ, Feltens R, Adryan B, Gieringer R, Brochhausen C, Schuon R, et al. Analysis of differentially expressed proteins in oral squamous cell carcinoma by MALDI-TOF MS. *J Oral Pathol Med* (2011) **40**:369–79. doi:10.1111/j.1600-0714.2010.00982.x

31. Sultana N, Rahman M, Myti S, Islam J, Mustafa MG, Nag K. A novel knowledge-derived data potentizing method revealed unique liver cancer-associated genetic variants. *Hum Genomics* (2019) **13**:30. doi:10.1186/s40246-019-0213-7

32. Hsu CC, Wang YH, Chen YY, Chen YJ, Lu CH, Wu YY, et al. The genomic landscape in Philadelphia-negative myeloproliferative neoplasm patients with second cancers. *Cancers (Basel)* (2022) **14**:3435. doi:10.3390/cancers14143435

33. Zhu Q, Rao B, Chen Y, Jia P, Wang X, Zhang B, et al. *In silico* development and *in vitro* validation of a novel five-gene signature for prognostic prediction in colon cancer. *Am J Cancer Res* (2023) **13**:45–65.

34. Harada-Kagitani S, Kouchi Y, Shinomiya Y, Kodama M, Ohira G, Matsubara H, et al. Keratin 6A is expressed at the invasive front and enhances the progression of colorectal cancer. *Lab Invest* (2024) **104**:102075. doi:10.1016/j.labinv.2024.102075

35. Chen C, Shan H. Keratin 6A gene silencing suppresses cell invasion and metastasis of nasopharyngeal carcinoma via the β-catenin cascade. *Mol Med Rep* (2019) **19**:3477–84. doi:10.3892/mmr.2019.10055

36. Wang Y, Guo Z, Tian Y, Cong L, Zheng Y, Wu Z, et al. MAPK1 promotes the metastasis and invasion of gastric cancer as a bidirectional transcription factor. *BMC Cancer* (2023) **23**:959. doi:10.1186/s12885-023-11480-3

37. Shinomiya Y, Kouchi Y, Harada-Kagitani S, Ishige T, Takano S, Ohtsuka M, et al. ECM1 and KRT6A are involved in tumor progression and chemoresistance in the effect of dexamethasone on pancreatic cancer. *Cancer Sci* (2024) **115**:1948–63. doi:10.1111/cas.16175

38. Xiao J, Kuang X, Dai L, Zhang L, He B. Anti-tumour effects of Keratin 6A in lung adenocarcinoma. *Clin Respir J* (2020) **14**:667–74. doi:10.1111/crj.13182

39. Xiao J, Lu X, Chen X, Zou Y, Liu A, Li W, et al. Eight potential biomarkers for distinguishing between lung adenocarcinoma and squamous cell carcinoma. *Oncotarget* (2017) **8**:71759–71. doi:10.18632/oncotarget.17606

40. Wang HZ, Yang X, Chen XY, Gu Y. Role of KRT6A in regulating the biological behavior of pancreatic ductal adenocarcinoma cells and its potential as a diagnostic and prognostic biomarker. *Chin J Cancer Biother* (2024) **31**:462–8.

41. Chan JKL, Yuen D, Too PH, Sun Y, Willard B, Man D, et al. Keratin 6a reorganization for ubiquitin-proteasomal processing is a direct antimicrobial response. *J Cell Biol* (2018) **217**:731–44. doi:10.1083/jcb.201704186

42. Zhu Y, Chen J, Li J, Zhou C, Huang X, Chen B. Ginsenoside Rg1 as a promising adjuvant agent for enhancing the anti-cancer functions of granulocytes inhibited by noradrenaline. *Front Immunol* (2023) **14**:1070679. doi:10.3389/fimmu.2023.1070679

43. Gong Y, Pang H, Yu Z, Wang X, Li P, Zhang Q. Construction of inflammatory associated risk gene prognostic model of NSCLC and its correlation with chemotherapy sensitivity. *Ann Med* (2023) **55**:2200034. doi:10.1080/07853890.2023.2200034

44. Xia NN, Yang AY, Yu MM. Screening of cisplatin-resistance–related genes in cervical cancer and the effect of KRT6A expression on the biological behavior of cisplatin-resistant SiHa cervical cancer cells. *Chin J Pract Diagn Ther* (2023) **37**: 252–60. doi:10.13507/j.issn.1674-3474.2023.03.009

45. Tong X, Patel AS, Kim E, Li H, Chen Y, Li S, et al. Adeno-to-squamous transition drives resistance to KRAS inhibition in LKB1 mutant lung cancer. *Cancer Cell* (2024) **42**:413–28.e7. doi:10.1016/j.ccell.2024.01.012

46. Kim YR, Kim SY. Machine learning identifies a core gene set predictive of acquired resistance to EGFR tyrosine kinase inhibitor. *J Cancer Res Clin Oncol* (2018) **144**:1435–44. doi:10.1007/s00432-018-2676-7

47. Yin C, Liu C, Feng G. KRT6A mediates the Wnt/β-catenin signaling pathway to regulate epithelial–mesenchymal transition and promote radioresistance in non-small cell lung cancer A549 cells. *J China Med Univ* (2024) **53**:628–34.

48. Du Y, Yuan S, Zhuang X, Zhang Q, Qiao T. Multiomics differences in lung squamous cell carcinoma patients with high radiosensitivity index compared with those with low radiosensitivity index. *Dis Markers* (2021) **2021**:3766659. doi:10.1155/2021/3766659

49. Yang Y, Zeng Z, Li L, Lei S, Wu Y, Chen T, et al. Sinapine thiocyanate exhibited anti-colorectal cancer effects by inhibiting KRT6A/S100A2 axis. *Cancer Biol Ther* (2023) **24**:2249170. doi:10.1080/15384047.2023.2249170

50. Jalali P, Yaghoobi A, Rezaee M, Zabihi MR, Piroozkhah M, Aliyari S, et al. Decoding common genetic alterations between Barrett's esophagus and esophageal adenocarcinoma: a bioinformatics analysis. *Heliyon* (2024) **10**:e31194. doi:10.1016/j.heliyon.2024.e31194

51. Charkiewicz R, Sulewska A, Karabowicz P, Lapuc G, Charkiewicz A, Kraska M, et al. Six-gene signature for differential diagnosis and therapeutic decisions in non-small-cell lung Cancer-A validation study. *Int J Mol Sci* (2024) **25**:25. doi:10.3390/ijms25073607

52. Chang HH, Dreyfuss JM, Ramoni MF. A transcriptional network signature characterizes lung cancer subtypes. *Cancer* (2011) **117**:353–60. doi:10.1002/cncr.25592

53. Shi P, Chen W. Genetic distinctiveness in lung adenocarcinoma and lung squamous cell carcinoma cancer: identifying key genomic signatures through differentially expressed gene analysis. *Curr Cancer Drug Targets* (2025) **25**. doi:10.2174/0115680096372957250322174718

54. López-Sánchez LM, Jurado-Gámez B, Feu-Collado N, Valverde A, Cañas A, Fernández-Rueda JL, et al. Exhaled breath condensate biomarkers for the early

diagnosis of lung cancer using proteomics. *Am J Physiol Lung Cell Mol Physiol* (2017) **313**:L664–l76. doi:10.1152/ajplung.00119.2017

55. Lobo J, Monteiro-Reis S, Guimarães-Teixeira C, Lopes P, Carneiro I, Jerónimo C, et al. Practicability of clinical application of bladder cancer molecular classification and additional value of epithelial-to-mesenchymal transition: prognostic value of vimentin expression. *J Transl Med* (2020) **18**:303. doi:10.1186/s12967-020-02475-w

56. Guo CC, Bondaruk J, Yao H, Wang Z, Zhang L, Lee S, et al. Assessment of luminal and basal phenotypes in bladder cancer. *Sci Rep* (2020) **10**:9743. doi:10.1038/s41598-020-66747-7

57. Rojas PA, May M, Sequeira GR, Elia A, Alvarez M, Martínez P, et al. Progesterone receptor isoform ratio: a breast cancer prognostic and predictive factor for antiprogestin responsiveness. *J Natl Cancer Inst* (2017) **109**:djw317. doi:10.1093/jnci/djw317

58. Posta M, Győrffy B. Analysis of a large cohort of pancreatic cancer transcriptomic profiles to reveal the strongest prognostic factors. *Clin Transl Sci* (2023) **16**:1479–91. doi:10.1111/cts.13563

59. Kalloger SE, Karasinska JM, Keung MS, Thompson DL, Ho J, Chow C, et al. Stroma vs epithelium-enhanced prognostics through histologic stratification in pancreatic ductal adenocarcinoma. *Int J Cancer* (2021) **148**:481–91. doi:10.1002/ijc.33304

60. Xu Y, Wang X, Chu Y, Li J, Wang W, Hu X, et al. Analysis of transcript-wide profile regulated by microsatellite instability of colorectal cancer. *Ann Transl Med* (2022) **10**:169. doi:10.21037/atm-21-6126

61. Rong L, Wang J, Wang Q, Zhu Y, Ren W. Exploration of immunocytochemical biomarkers related to central lymph node metastasis in papillary thyroid microcarcinoma. *Cytojournal* (2025) **22**:18. doi:10.25259/Cytojournal_162_2024

62. Liao C, Zhang Y, Yang J, Wang S, Li Z, Chen S, et al. Single-cell transcriptomic analysis reveals an aggressive basal-like tumor cell subpopulation associated with poor prognosis in intrahepatic cholangiocarcinoma. *J Gastroenterol Hepatol* (2025) **40**:1263–73. doi:10.1111/jgh.16915

63. Chen W, Yu Y, Wang C, Jiang Z, Huang X, Lin Y, et al. Construction of the bromodomain-containing protein-associated prognostic model in triple-negative breast cancer. *Cancer Cell Int* (2025) **25**:18. doi:10.1186/s12935-025-03648-7

64. Pu S, Zhou Y, Xie P, Gao X, Liu Y, Ren Y, et al. Identification of necroptosis-related subtypes and prognosis model in triple negative breast cancer. *Front Immunol* (2022) **13**:964118. doi:10.3389/fimmu.2022.964118

65. Raman P, Maddipati R, Lim KH, Tozeren A. Pancreatic cancer survival analysis defines a signature that predicts outcome. *PLoS One* (2018) **13**:e0201751. doi:10.1371/journal.pone.0201751

66. Wang P, Gao X, Zheng W, Zhang J. Potential impact of epithelial splicing regulatory protein 1 (ESRP1) associated with tumor immunity in pancreatic adenocarcinoma. *J Proteomics* (2024) **308**:105277. doi:10.1016/j.jprot.2024.105277

67. Wu ZX, Huang X, Cai MJ, Huang PD, Guan Z. Development and validation of a prognostic index based on genes participating in autophagy in patients with lung adenocarcinoma. *Front Oncol* (2021) **11**:799759. doi:10.3389/fonc.2021.799759

68. Huang J, Yuan L, Huang W, Liao L, Zhu X, Wang X, et al. LATPS, a novel prognostic signature based on tumor microenvironment of lung adenocarcinoma to better predict survival and immunotherapy response. *Front Immunol* (2022) **13**:1064874. doi:10.3389/fimmu.2022.1064874

69. Li S, Wang W, Yu H, Zhang S, Bi W, Sun S, et al. Characterization of genomic instability-related genes predicts survival and therapeutic response in lung adenocarcinoma. *BMC Cancer* (2023) **23**:1115. doi:10.1186/s12885-023-11580-0

70. Qin C, Fan X, Sai X, Yin B, Zhou S, Addeo A, et al. Development and validation of a DNA damage repair-related gene-based prediction model for the prognosis of lung adenocarcinoma. *J Thorac Dis* (2023) **15**:6928–45. doi:10.21037/jtd-23-1746

71. Yu J, Li G, Tian Y, Huo S. Establishment of a lymph node metastasis-associated prognostic signature for lung adenocarcinoma. *Genet Res (Camb)* (2023) **2023**:6585109. doi:10.1155/2023/6585109

72. Mao S, Chen Z, Wu Y, Xiong H, Yuan X. Crosstalk of eight types of RNA modification regulators defines tumor microenvironments, cancer hallmarks, and prognosis of lung adenocarcinoma. *J Oncol* (2022) **2022**:1285632. doi:10.1155/2022/1285632

73. Gong X, Li N, Sun C, Li Z, Xie H. A four-gene prognostic signature based on the TEAD4 differential expression predicts overall survival and immune microenvironment estimation in lung adenocarcinoma. *Front Pharmacol* (2022) **13**:874780. doi:10.3389/fphar.2022.874780

74. Zhu K, Yan A, Zhou F, Zhao S, Ning J, Yao L, et al. A pyroptosis-related signature predicts overall survival and immunotherapy responses in lung adenocarcinoma. *Front Genet* (2022) **13**:891301. doi:10.3389/fgene.2022.891301

75. Wang Q, Sun N, Li J, Huang F, Zhang Z. Liquid-liquid phase separation in the prognosis of lung adenocarcinoma: an integrated analysis. *Curr Cancer Drug Targets* (2024) **25**:323–34. doi:10.2174/0115680096345676241001081051

76. Zhang Z, Zhao W, Hu Z, Ding C, Huang H, Liang G, et al. Construction and validation of A prognostic model for lung adenocarcinoma based on ferroptosis-related genes. *Zhongguo Fei Ai Za Zhi* (2025) **28**:22–32. doi:10.3779/j.issn.1009-3419.2025.102.04

77. Cheng Y, Hou K, Wang Y, Chen Y, Zheng X, Qi J, et al. Identification of prognostic signature and gliclazide as candidate drugs in lung adenocarcinoma. *Front Oncol* (2021) **11**:665276. doi:10.3389/fonc.2021.665276

78. Ma C, Li F, He Z, Zhao S. A more novel and powerful prognostic gene signature of lung adenocarcinoma determined from the immune cell infiltration landscape. *Front Surg* (2022) **9**:1015263. doi:10.3389/fsurg.2022.1015263

79. Miyamura T, Mori S, Onuki M, Sekizawa A, Matsumoto K, Kukimoto I. Nuclear keratin 6A upregulates human papillomavirus oncogene expression through TEAD1 interaction. *Virol J* (2025) **22**:202. doi:10.1186/s12985-025-02832-5

80. Lessard JC, Piña-Paz S, Rotty JD, Hickerson RP, Kaspar RL, Balmain A, et al. Keratin 16 regulates innate immunity in response to epidermal barrier breach. *Proc Natl Acad Sci U S A* (2013) **110**:19537–42. doi:10.1073/pnas.1309576110

81. Schweizer J, Bowden PE, Coulombe PA, Langbein L, Lane EB, Magin TM, et al. New consensus nomenclature for mammalian keratins. *J Cell Biol* (2006) **174**:169–74. doi:10.1083/jcb.200603161

82. Cohen E, Johnson CN, Wasikowski R, Billi AC, Tsoi LC, Kahlenberg JM, et al. Significance of stress keratin expression in normal and diseased epithelia. *iScience* (2024) **27**:108805. doi:10.1016/j.isci.2024.108805

83. Coulombe PA. Wound epithelialization: accelerating the pace of discovery. *J Invest Dermatol* (2003) **121**:219–30. doi:10.1046/j.1523-1747.2003.12387.x

84. Kim KH, Chung WS, Kim Y, Kim KS, Lee IS, Park JY, et al. Transcriptomic analysis reveals wound healing of Morus alba root extract by Up-Regulating keratin filament and CXCL12/CXCR4 signaling. *Phytother Res* (2015) **29**:1251–8. doi:10.1002/ptr.5375

85. Wilson NJ, O'Toole EA, Milstone LM, Hansen CD, Shepherd AA, Al-Asadi E, et al. The molecular genetic analysis of the expanding pachyonychia congenita case collection. *Br J Dermatol* (2014) **171**:343–55. doi:10.1111/bjd.12958

86. Samuelov L, Smith FJD, Hansen CD, Sprecher E. Revisiting pachyonychia congenita: a case-cohort study of 815 patients. *Br J Dermatol* (2020) **182**:738–46. doi:10.1111/bjd.18794

87. Coulombe PA, Lee CH. Defining keratin protein function in skin epithelia: epidermolysis bullosa simplex and its aftermath. *J Invest Dermatol* (2012) **132**:763–75. doi:10.1038/jid.2011.450

88. Xu C, Bailly-Maitre B, Reed JC. Endoplasmic reticulum stress: cell life and death decisions. *J Clin Invest* (2005) **115**:2656–64. doi:10.1172/jci26373

89. Lehmann SM, Leube RE, Schwarz N. Keratin 6a mutations lead to impaired mitochondrial quality control. *Br J Dermatol* (2020) **182**:636–47. doi:10.1111/bjd.18014

90. Zieman AG, Poll BG, Ma J, Coulombe PA. Altered keratinocyte differentiation is an early driver of keratin mutation-based palmoplantar keratoderma. *Hum Mol Genet* (2019) **28**:2255–70. doi:10.1093/hmg/ddz050

91. Eliason MJ, Leachman SA, Feng BJ, Schwartz ME, Hansen CD. A review of the clinical phenotype of 254 patients with genetically confirmed pachyonychia congenita. *J Am Acad Dermatol* (2012) **67**:680–6. doi:10.1016/j.jaad.2011.12.009

92. Leachman SA, Kaspar RL, Fleckman P, Florell SR, Smith FJ, McLean WH, et al. Clinical and pathological features of pachyonychia congenita. *J Investig Dermatol Symp Proc* (2005) **10**:3–17. doi:10.1111/j.1087-0024.2005.10202.x

93. McCarthy RL, De Brito M, O'Toole E. Pachyonychia congenita: clinical features and future treatments. *Keio J Med* (2025) **74**:52–60. doi:10.2302/kjm.2023-0012-IR

94. Goldberg I, Fruchter D, Meilick A, Schwartz ME, Sprecher E. Best treatment practices for pachyonychia congenita. *J Eur Acad Dermatol Venereol* (2014) **28**:279–85. doi:10.1111/jdv.12098

95. Gruber R, Edlinger M, Kaspar RL, Hansen CD, Leachman S, Milstone LM, et al. An appraisal of oral retinoids in the treatment of pachyonychia congenita. *J Am Acad Dermatol* (2012) **66**:e193–9. doi:10.1016/j.jaad.2011.02.003

96. Koren A, Sprecher E, Reider E, Artzi O. A treatment protocol for botulinum toxin injections in the treatment of pachyonychia congenita-associated keratoderma. *Br J Dermatol* (2020) **182**:671–7. doi:10.1111/bjd.18169

97. Swartling C, Vahlquist A. Treatment of pachyonychia congenita with plantar injections of botulinum toxin. *Br J Dermatol* (2006) **154**:763–5. doi:10.1111/j.1365-2133.2005.07115.x

98. Thomas BR, Sahota A. Pachyonychia congenita and botulinum toxin. *Br J Dermatol* (2020) **182**:531–2. doi:10.1111/bjd.18784

99. Zhao Y, Gartner U, Smith FJ, McLean WH. Statins downregulate K6a promoter activity: a possible therapeutic avenue for pachyonychia congenita. *J Invest Dermatol* (2011) **131**:1045–52. doi:10.1038/jid.2011.41

100. Theocharopoulos I, O'Toole EA. Stopping pachyonychia congenita plantar pain with a statin? *Br J Dermatol* (2019) **181**:446–7. doi:10.1111/bjd.18254

101. Sharma S, Dayal S, Aggarwal K, Gowda VMV, Kaur R. Scrutinising the role of simvastatin in a patient of Pachyonychia Congenita with KRT6A gene mutation. *Australas J Dermatol* (2022) **63**:e145–e49. doi:10.1111/ajd.13835

102. Abdollahimajd F, Rajabi F, Shahidi-Dadras M, Saket S, Youssefian L, Vahidnezhad H, et al. Pachyonychia congenita: a case report of a successful treatment with rosuvastatin in a patient with a KRT6A mutation. *Br J Dermatol* (2019) **181**:584–6. doi:10.1111/bjd.17276

103. Hickerson RP, Leake D, Pho LN, Leachman SA, Kaspar RL. Rapamycin selectively inhibits expression of an inducible keratin (K6a) in human keratinocytes and improves symptoms in pachyonychia congenita patients. *J Dermatol Sci* (2009) **56**:82–8. doi:10.1016/j.jdermsci.2009.07.008

104. Daroach M, Dogra S, Bhattacharjee R, Tp A, Smith F, Mahajan R. Pachyonychia congenita responding favorably to a combination of surgical and medical therapies. *Dermatol Ther* (2019) **32**:e13045. doi:10.1111/dth.13045

105. Hickerson RP, Smith FJ, Reeves RE, Contag CH, Leake D, Leachman SA, et al. Single-nucleotide-specific siRNA targeting in a dominant-negative skin model. *J Invest Dermatol* (2008) **128**:594–605. doi:10.1038/sj.jid.5701060

106. Leachman SA, Hickerson RP, Hull PR, Smith FJ, Milstone LM, Lane EB, et al. Therapeutic siRNAs for dominant genetic skin disorders including pachyonychia congenita. *J Dermatol Sci* (2008) **51**:151–7. doi:10.1016/j.jdermsci.2008.04.003

107. Hickerson RP, Flores MA, Leake D, Lara MF, Contag CH, Leachman SA, et al. Use of self-delivery siRNAs to inhibit gene expression in an organotypic pachyonychia congenita model. *J Invest Dermatol* (2011) **131**:1037–44. doi:10.1038/jid.2010.426

108. Basset J, Marchal L, Hovnanian A. EGFR signaling is overactive in pachyonychia congenita: effective treatment with oral erlotinib. *J Invest Dermatol* (2023) **143**:294–304.e8. doi:10.1016/j.jid.2022.08.045

109. Greco C, Ponsen AC, Leclerc-Mercier S, Schlatter J, Cisternino S, Boucheix C, et al. Treatment of painful Palmoplantar Keratoderma related to Pachyonychia Congenita using EGFR inhibitors. *Biomedicines* (2022) **10**:841. doi:10.3390/biomedicines10040841

110. Yoshida A, Yamamoto K, Ishida T, Omura T, Itoh T, Nishigori C, et al. Sunitinib decreases the expression of KRT6A and SERPINB1 in 3D human epidermal models. *Exp Dermatol* (2021) **30**:337–46. doi:10.1111/exd.14230

111. Mommers JM, van Rossum MM, van Erp PE, van De Kerkhof PC. Changes in keratin 6 and keratin 10 (co-)expression in lesional and symptomless skin of spreading psoriasis. *Dermatology* (2000) **201**:15–20. doi:10.1159/000018422

112. Wang F, Chen S, Liu HB, Parent CA, Coulombe PA. Keratin 6 regulates collective keratinocyte migration by altering cell-cell and cell-matrix adhesion. *J Cell Biol* (2018) **217**:4314–30. doi:10.1083/jcb.201712130

113. Rotty JD, Coulombe PA. A wound-induced keratin inhibits src activity during keratinocyte migration and tissue repair. *J Cell Biol* (2012) **197**:381–9. doi:10.1083/jcb.201107078

114. Chen M, Wang Y, Wang M, Xu S, Tan Z, Cai Y, et al. Keratin 6A promotes skin inflammation through JAK1-STAT3 activation in keratinocytes. *J Biomed Sci* (2025) **32**:47. doi:10.1186/s12929-025-01143-9

115. Boonpethkaew S, Meephansan J, Charoensuksira S, Jumlongpim O, Tangtanatakul P, Wongpiyabovorn J, et al. Elucidating the NB-UVB mechanism by comparing transcriptome alteration on the edge and center of psoriatic plaques. *Sci Rep* (2023) **13**:4384. doi:10.1038/s41598-023-31610-y

EBM Experimental Biology and Medicine

TYPE Original Research
PUBLISHED 26 January 2026
DOI 10.3389/ebm.2026.10793

OPEN ACCESS

*CORRESPONDENCE
Joseph M. Cerreta,
cerretaj@stjohns.edu

RECEIVED 18 August 2025
REVISED 01 December 2025
ACCEPTED 08 January 2026
PUBLISHED 26 January 2026

CITATION
Renda RP and Cerreta JM (2026) Pulmonary injury following exposure to amorphous silicon dioxide nanoparticles in *Golden Syrian Hamsters*. *Exp. Biol. Med.* 251:10793. doi: 10.3389/ebm.2026.10793

Pulmonary injury following exposure to amorphous silicon dioxide nanoparticles in *Golden Syrian Hamsters*

Rachel P. Renda and Joseph M. Cerreta *

College of Pharmacy and Health Sciences, St. John's University, Queens, NY, United States

Abstract

Amorphous silicon dioxide nanoparticles (SiO_2 NPs) are abundant within the earth's crust and can be released into the air through industrial and manufacturing activities. Such materials are often used in industrial processes, in pharmaceutical and in the cosmetic industries. Amorphous SiO_2 NPs are pulmonary toxicants; however, the mechanism of toxicity is uncertain. In the current study, toxicity of SiO_2 NPs was assessed using inhalation exposure in an *in vivo* system to study a possible mechanism of pulmonary injury. Golden Syrian Hamsters were divided into 4 groups: 1- room air control, 2- vehicle control, 3- low concentration (6 mg/m^3) and 4- high concentration (12 mg/m^3). Hamsters were treated for 4 h a day for 8 days. Bronchoalveolar Lavage Fluid (BALF) analysis found increases in total cell counts ($p < 0.0001$), neutrophils ($p < 0.0001$), lymphocytes ($p < 0.001$), eosinophils ($p < 0.01$), multinucleated macrophages ($p < 0.01$), total protein ($p < 0.0001$), alkaline phosphatase ($p < 0.0001$), and lactate dehydrogenase ($p < 0.001$) in the high concentration group. Histopathological analysis found an increase in air space, quantified by Mean Linear Intercept ($p < 0.0001$), and a significant increase in TUNEL positive cells ($p < 0.001$), in the high concentration group. SEM and TEM found structural alterations to the lung tissue including increase in the number holes in the alveolar walls and in apoptotic bodies within tissue. Caspase 3 ($p < 0.05$), and 8 ($p < 0.05$), were significantly increased along with cellular inflammation markers TNF-α ($p < 0.05$), and HSP70 ($p < 0.05$) in the high concentration group. Results of the study indicate exposure to SiO_2 NPs may induce extrinsic apoptotic pathway, leading to tissue damage and significant airspace enlargement.

KEYWORDS

apoptosis, inhalation, nanoparticles, pulmonary, silicon dioxide

Impact statement

Humans are exposed to amorphous SiO_2 nanoparticles, occupationally, every day. There is limited research on the injury caused by inhalation of these materials and with their increasing use. With great focus on crystalline silica inducing silicosis there has been limited research on the amorphous form and its potential for toxicity. Often the

amorphous form is deemed safe. This study provides an analysis of injury after exposure to amorphous silicon dioxide nanoparticles and evaluation of an *in vivo* cell death mechanism that may occur when exposed beyond OSHA's limits.

Introduction

Silica Nanoparticles (NPs) are composed of silicon dioxide (SiO_2), one of the most abundant compound within the Earth's crust [1, 2]. Silica exists naturally in a crystalline (quartz) form and in an amorphous form (diatomaceous earth) while amorphous silica can also be synthetically produced in nano-sized forms [3]. Silica nanoparticles are particularly desirable for use in consumer products, as industrial additives, and in drug delivery because they remain stable over a wide range of temperatures, in organic solvents, and under acidic conditions [4].

Silica exposure can be harmful for those in an occupational setting, as silicosis is a known occupational disease linked to inhalation of crystalline SiO_2 NPs [5]. While crystalline silica is widely recognized as the more toxic form of inhaled silica, exploring the effects of exposure to amorphous SiO_2 NPs remains essential, as they are widely used and pose risks to those in an occupational setting [5].

SiO_2 NPs and various other oxide NPs have been shown to cause pulmonary injury [6–8]. Exposure to crystalline SiO_2 NPs has shown lysosomal disruption, blockage of autophagic flux, ROS generation, and apoptosis [7, 8]. Mice exposed to amorphous SiO_2 NPs through intratracheal instillation were found to have increased markers of pulmonary inflammation, increased neutrophils, and increased macrophage production of inflammatory mediators [6]. The current guidelines set by The Occupational Safety and Health Administration's (OSHA) Permissible Exposure Limit (PEL) for exposure to amorphous SiO_2 NPs in an 8-h period is 6 mg/m^3.

Nanoparticles can enter the body through several routes including, ingestion, dermal exposure with the most common pathway being inhalation. To understand the effects in the lungs after exposure to amorphous SiO_2 NPs this study design exposed animals through a full body exposure chamber, as it is most representative of a real-time exposure. Though many inhalation studies expose animals through intratracheal instillation there are advantages to the whole-body exposure method. The whole-body exposure chamber provides a pulmonary response to a typical exposure route with no discomfort to the animal [9–11]. Within the whole-body exposure chamber animals may receive an incidental exposure of NPs via the oral route due to grooming. Kwon et al., found intake of orally ingested SiO2 NPs are excreted in their intact particle form via feces [12].

The animal model used in the current study was the Golden Syrian Hamster that have been used to study models of pulmonary fibrosis, chronic bronchitis, emphysema and SARS-CoV-2 [13–19].

Apoptosis is a cell death mechanism that has been seen with exposure to crystalline silica [8]. Apoptosis can be broken into two pathways, an intrinsic mitochondrial-dependent, pathway and an extrinsic death-receptor based pathway [20]. The mitochondrial dependent intrinsic pathway is triggered by growth factor deprivation and cellular stress. Downstream events include the release of Cytochrome C from the mitochondria, binding to APAF-1 to form the apoptosome, activation of caspase 9 and cleavage of caspase 3 [21]. The alternate or extrinsic pathway is triggered by extracellular signals that death receptors on the plasma membrane recognize [21]. Death receptors then recruit adaptor molecules (FAS-associated death domain and TNFRS1A-associated death domain) [21]. The adaptors activate pro-caspase 8 to form, caspase 8 that then interacts to cleave caspase 3. Caspase 3 executes cell death through apoptosis [21].

The aim of this study is to explore the resulting injury after exposure to amorphous SiO_2 NPs in Golden Syrian Hamsters. This study hypothesizes that inhaled amorphous SiO_2 at the level of OSHA's PEL (6 mg/m^3) will show minimal pulmonary injury, but inhalation of the higher concentration (12 mg/m^3) will show internalization of amorphous SiO_2 NPs, activation of apoptosis and pulmonary injury to respiratory epithelium.

Materials and methods

Materials

Silicon dioxide nanoparticles were purchased from Nanostructured and Amorphous Materials, Inc. (Katy, TX). Methyl Green and Vectabond® Reagent were acquired from Vector Laboratories, Inc. (Burlingame, CA). Albumin Standard (2 mg/mL), Nanosphere™ Size Standards, Pierce™ BCA Protein Assay Kit, Pierce Protease and Phosphatase Inhibitor Mini Tablets, PROTOCOL® Hema 3® Stain Set, and Zeta Potential Standard were obtained from Thermo Fisher Scientific (Waltham, MA). ApopTag® Plus Peroxidase *In Situ* Apoptosis Detection Kit and Proteinase K were obtained from EMD Millipore Corp. (Burlington, MA). Caspase 3, Caspase 8, and Alkaline Phosphatase colorimetric assay kits were obtained from Abcam (Waltham, MA). LDH Cytotoxicity Assay Kit was obtained from Cayman Chemicals Inc., (Cambridge, MA, United States). Lamelli Sample Buffer, Mini-PROTEAN TGX Gels (7.5%, 12%, 4–20% and Any KD™), nonfat dry milk and Precision Plus Protein Dual Color Standards were purchased from Bio-Rad Laboratories, Inc. (Hercules, CA). MagicMark XP Western Protein Standard was purchased from Invitrogen, Thermo Fisher Scientific (Carlsbad, CA). Amersham ECL Prime Western Blotting Detection Reagents were purchased

from Global Life Science Solutions Operations UK Ltd., Cytiva (Buckinghamshire, UK). Antibodies to β-Actin, Caspase 3, 8, 9, and HSP70 were purchased from Cell Signaling Technology, Inc. (Danvers, MA). TNF-α ELISA and Cytochrome C ELISA KIT Abcam (Waltham, MA). Glutaraldehyde was purchased from Electron Microscopy Sciences (Hatfield, PA). Lead nitrate, osmium tetroxide, sodium cacodylate, sodium citrate, and uranyl magnesium acetate were purchased from Ted Pella, Inc. (Redding, CA).

Methods

Nanoparticle characterization

The average size of SiO_2 NPs according to the manufacturer was 20 nm with a purity of 99%. SiO_2 NPs were directly measured using TEM, by loading particles on a formvar coated copper grid. Nanosphere™ Size Standards with a mean diameter of 100 nm ± 4 nm were used as a calibration standard. TEM micrographs were analyzed using ImageJ software. The mean hydrodynamic diameter of SiO_2 NPs in water was determined by dynamic light scattering (DLS using a Delso Nano C Particle Size Analyzer (Beckman Coulter Inc.). The zeta potential of SiO_2 NPs was measured using the Malvern Zetasizer Nano ZS.

Animals

Female Golden Syrian Hamsters, age 7–8 weeks were obtained from Envigo (Indianapolis, IN). Animals were housed at St. John's Universities Animal Care Center, Queens, NY, an AAALAC approved facility. Upon arrival animals were given a seven-day acclimation period. Hamsters were kept under a controlled environment with a 12-h light-dark cycle and provided a standard laboratory diet and water *ad libitum*. Animal studies were carried out under an Institutional Animal Care and Use Committee (IACUC) approved protocol. 9 animals per treatment group were used.

Exposure system and experimental design

Studies were carried out using 4 animal groups: room air control (filtered room air), vehicle control (sterile aerosolized water), low concentration SiO_2 NPs (6 mg/m^3) and high concentration SiO_2 NPs (12 mg/m^3). Animals were exposed for 4 h a day for 8 days in a whole-body exposure chamber. In this repeated exposure model, animals were exposed to a concentration of either 6 mg/m^3 or 12 mg/m^3 amorphous SiO_2 NPs, continuously over the 4-h exposure period. The concentration of 6 mg/m^3 was chosen as it represents the PEL (OSHA) and TWA (NIOSH), 12 mg/m^3 was chosen as it is double the regulatory level. The high concentration (12 mg/m^3) was selected to represent approximately twice the current occupational exposure limit for amorphous SiO_2 NPs. This approach intended to examine pulmonary responses that could arise under conditions exceeding regulatory standards, during accidental release or short term over exposures that may occur in occupational settings. This additional exposure concentration provides a dose response relationship relative to the established exposure limit. Animals were euthanized with an overdose of ketamine (800 mg/kg) and xylazine (40 mg/kg) via an intraperitoneal route 24 h after the last exposure.

To form an aerosol, an 8-jet nebulizer (CH Technologies, Inc., NJ) attached to a collision jar was used with air supplied from a compressed air tank. SiO_2 Nanoparticle suspensions were prepared in advance using sterile distilled water and sonicated prior to treatment. To measure the concentration of particles in the chamber air samples were taken every minute and measured for mass aerosol concentration (mg/m^3) using a NanoScan SMPS 3910 (TSI, Inc., MN).

Analysis of bronchoalveolar lavage fluid (BALF)

Post euthanasia, lungs were lavaged with cold Dulbecco's phosphate buffer saline and the bronchoalveolar lavage fluid (BALF) was collected. BALF was centrifuged and the acellular component was aliquoted out and stored at −80 °C for further use. The cellular component was resuspended with RPMI media and used to determine differential cell counts of leukocytes. Smears of the BALF were prepared using cytocentrifugation and samples spun, dried and stained with PROTOCOL HEMA 3. Cells were counted and categorized as: macrophages, multinucleated macrophages, neutrophils, lymphocytes, and eosinophils. Cell counts were carried out as previously described [22].

The acellular component of the BALF was analyzed for total protein as measured using the Pierce BCA Protein Assay Kit, LDH and ALP levels using the LDH Colorimetric Assay Kit and Alkaline Phosphatase Colorimetric Kit (Abcam). LDH and ALP release was calculated from the generated standard curves.

Light microscopy

For morphologic examination, following euthanization, lungs were inflated by insufflation with 10% Neutral Buffered Formalin. Fixed tissue was dehydrated, cleared, and embedded in Paraplast X-TRA. Paraffin tissue blocks were sectioned using a microtome. Sections were cut, ~5 microns thick, placed on glass slides, deparaffinized in xylene and rehydrated in increasing concentrations of ethanol to distilled water. Tissue sections were stained with hematoxylin and eosin, dehydrated in ethanol and cleared with xylene and mounted with cover glass using permount.

Mean linear intercept

Photomicrographs taken of H&E-stained sections were analyzed for differences in alveolar size by calculating the Mean Linear Intercepts. Mean Linear Intercept was measured by the line intersection method and calculated from 20 random fields of view per animal [23]. Micrographs were analyzed using ImageJ software.

TUNEL assay

A TUNEL Assay was carried out using the ApopTag® Plus Peroxidase *In Situ* Apoptosis Detection Kit. Slides were prepared as stated above, deparaffinized, and rehydrated. Tissue sections were pretreated with Proteinase K and washed in distilled water. Slides were then quenched in 3% H_2O_2 and washed in PBS. The TUNEL Assay protocol (ApopTag®) was followed as directed by the manufacturer. Photomicrographs of tissue sections were taken, and apoptotic bodies were counted from 20 random fields of view.

Electron microscopy

Alterations to the ultrastructural morphology of the cells and tissue of the lung was evaluated following exposure to silicon dioxide NPs using scanning electron microscopy (SEM) and transmission electron microscopy (TEM). After animals were euthanized, lungs were fixed by insufflation with 3% glutaraldehyde. For SEM, samples following fixation were washed, dehydrated with increasing concentrations of acetone, and dried using the critical point method. Samples were mounted on aluminum stubs, and sputter coated with platinum and palladium. The samples were examined using a scanning electron microscope. For TEM, lung tissue blocks were cut, post-fixed in osmium tetroxide, stained in uranyl acetate, dehydrated in acetone and embedded in LX112-Ardalite resin mixture. Following polymerization, tissue blocks were sectioned and stained with uranyl acetate and lead citrate. Samples were examined using a transmission electron microscope.

Immunoblot analysis

Western blot analysis of Caspase 9, Caspase 8, Caspase 3, and HSP70 were carried out using the Bio-Rad protein guide protocol (Bio-Rad) and the Abcam western blot protocol (Abcam). Lung tissue was collected, washed in DPBS, frozen and stored in liquid nitrogen until use. Lung tissue was homogenized in cold RIPA buffer containing a protease and phosphatase inhibitor cocktail. Total Protein was determined using Pierce BCA Protein Assay Kit. Proteins were denatured and then separated using electrophoresis. Resolved proteins were transferred to a PVDF membrane, blocked in 5% (w/v) non-fat dry milk in Tris Buffered Saline (TBST) for 1 h at room temperature or overnight at 4 °C. TBST washed membranes were incubated with primary antibody for 3 h at room temperature or overnight at 4 °C. All primary antibodies were monoclonal derived from rabbit and an anti-rabbit IgG HRP-linked secondary antibody (1:2000) was used to probe the membranes. The following conditions were used (% SDS PAGE gel, amount of total protein, primary antibody incubation time, blocking time, and antibody dilutions), respectively for Caspase 9 (4–20%, 90 µg, 3 h, overnight, 1:1000), for Caspase 8 (4–20%, 90 µg, overnight, 1 h, 1:1000), for Caspase 3 (any KD™, 90 µg, overnight, 1 h, 1:1000), and for HSP70 (4–20%, 90 µg, 3 h, overnight, 1:1000). β-Actin, used as a loading control, was measured by probing with Anti-IgG B actin (1:5000) and incubated for 1 h. After incubation with the secondary antibody (anti-rabbit IgG HRP-linked), chemiluminescence was detected using Amersham™ ECL™ Prime Western Blotting Detection Reagent and membranes were photographed using a digital imager. Images were analyzed by densitometry using ImageJ software.

ELISA

TNF-α and Cytochrome C levels were determined in lung samples from control and treated animals using a sandwich ELISA technique kit (TNF-α Rat SimpleStep ELISA® Kit or Mouse/Rat Cytochrome C SimpleStep ELISA® Kit, Abcam). Concentration of lung homogenate used was based on manufacturer protocols and provided protocols were followed. Protein levels were calculated from the generated standard curves.

Statistical analysis

Data were presented as the mean ± SEM. Statistical analyses were carried out using Graph Pad Prism 9 with significance tested among and between groups using one-way analysis of variance (ANOVA) followed by Tukey's Post Hoc analysis. Differences between treated groups were significant at the 95% level ($P < 0.05$) and noted based on the following *$P < 0.05$, **$P < 0.01$, ***$P < 0.001$, ****$P < 0.0001$. Room air controls did not statistically differ from the vehicle controls; therefore, only vehicle control data are presented in the main figures, with room air control data provided in the Supplementary Material.

Results

Nanoparticle characterization

SiO_2 NPs were characterizing using TEM to determine particle size (Figure 1A), DLS to determine mean hydrodynamic diameter (Figure 1B) and Zeta Potential was measured (Figure 1C). The average individual particle size was measured to be 20 nm and had a spherical shape. The mean hydrodynamic diameter was 226 nm in water. The Zeta Potential of SiO_2 NPs in water was −20 mV.

BALF analyses

Exposure to SiO_2 NPs resulted in significant increase in total number of cells in the BALF. Cell numbers were increased from 67.9×10^4 cells/mL in the controls to 119.6×10^4 cells/mL and 770.1×10^4 cells/mL in the treated groups (6 mg/m^3 and 12 mg/m^3 respectively) (Figure 2A; Supplementary Figure S1). Inhalation of SiO_2 NPs did not cause a significant change in macrophages (Figure 2B; Supplementary Figure S1) but led to a significant increase in neutrophils from 4.3×10^4 cells/mL in controls to 19.4×10^4 cells/mL in 6 mg/m^3 and 648.9×10^4 cells/mL in 12 mg/m^3 (Figure 2C; Supplementary Figure S2).

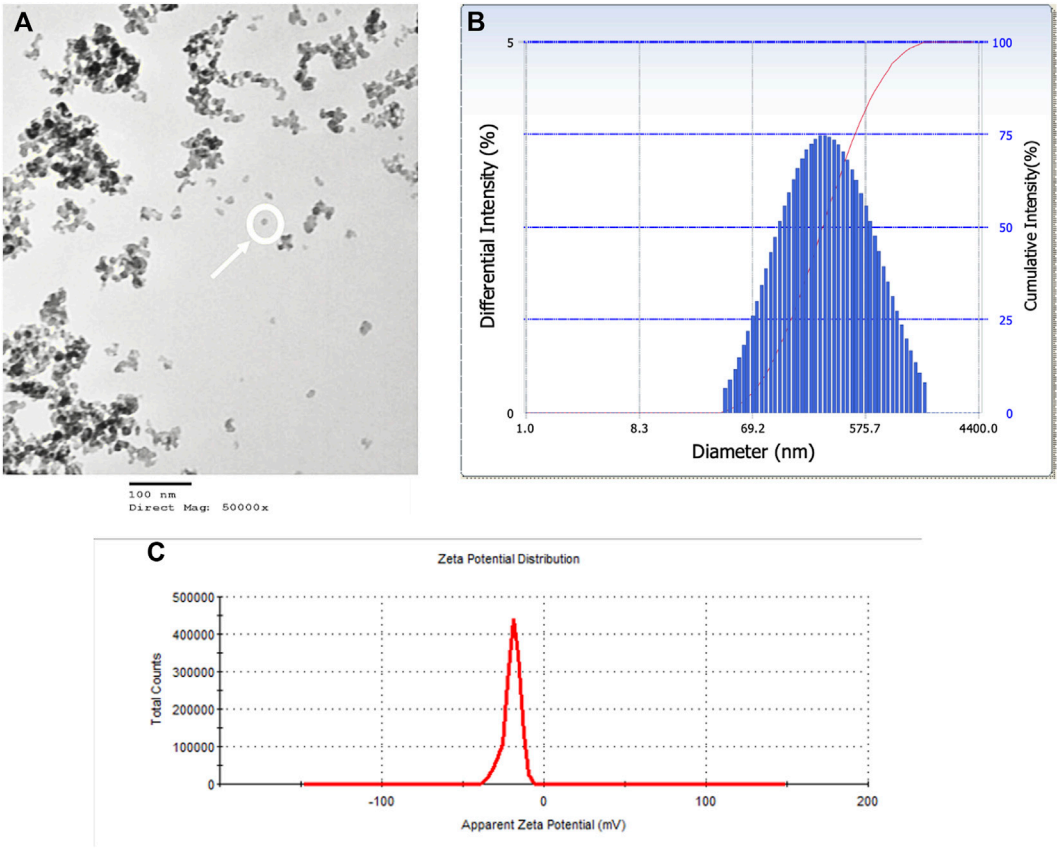

FIGURE 1
SiO_2 NPs were characterized by TEM, DLS, and Zeta Potential. **(A)** A TEM micrograph of SiO_2 NPs suspension on a copper coated grid. The micrograph shows single particles (encircled) among particle clumps. Average particle size measured 20 nm. **(B)** Representative distribution of particle size in aqueous suspension of amorphous SiO_2 NPs measured using DLS. The average hydrodynamic diameter was measured as 226 nm. **(C)** Zeta Potential distribution of amorphous SiO_2 NPs in water was measured as −20 mV.

Lymphocyte numbers were also significantly increased in the BALF of treated animals as compared to controls. Eosinophils were increased only in the 12 mg/m^3 group by 7-fold (Figure 2D; Supplementary Figure S1). The numbers of lymphocytes in the BALF of treated animals were 20-fold higher in 6 mg/m^3 and 33-fold higher in 12 mg/m^3 (Figure 2E; Supplementary Figure S1). Multi nucleated macrophages were significantly increased by 4-fold in 6 mg/m^3 and 5-fold in 12 mg/m^3 (Figure 2F; Supplementary Figure S1).

Total Protein in the BALF was significantly increased from 133 ± 15 µg/mL in the controls to 517 ± 25 µg/mL in the 12 mg/m^3 group (Figure 3A; Supplementary Figure S3). ALP activity in the BALF was significantly elevated in the 12 mg/m^3 group (4.4 ± 0.6 U/µg) when compared to vehicle control (1.3 ± 0.3 U/µg) (Figure 3B; Supplementary Figure S3). LDH activity in the BALF was significantly increased in the 12 mg/m^3 group (99 × 10^{-3} ± 29 × 10^{-3} mU/mL), when compared to vehicle control (11 × 10^{-3} ± 2.9 × 10^{-3} mU/mL) (Figure 3C; Supplementary Figure S3).

Morphological analysis using light and electron microscopy

Light microscopy and MLI

Lung tissue sections from vehicle control stained with H&E showed the architecture of parenchyma as seen in (Figure 4A; Supplementary Figure S4). Histopathological examination of lung tissue sections exposed to 6 mg/m^3 or 12 mg/m^3 SiO_2 NPs showed increase in average airway space (Figures 4B,C). Air space size seen in all groups was quantified by Mean Linear Intercept. Tissue sections of both low and high concentration treated groups showed a significant increase in the Mean Linear Intercept from ~44 µm in controls to ~86 µm in the 6 mg/m^3 treated group and to ~78 µm in the 12 mg/m^3 treated group (Figure 4D).

TUNEL Assay

Histopathological examination of lung tissue sections exposed to 6 mg/m^3 and 12 mg/m^3 SiO_2 NPs showed increase in numbers of apoptotic bodies when compared to control

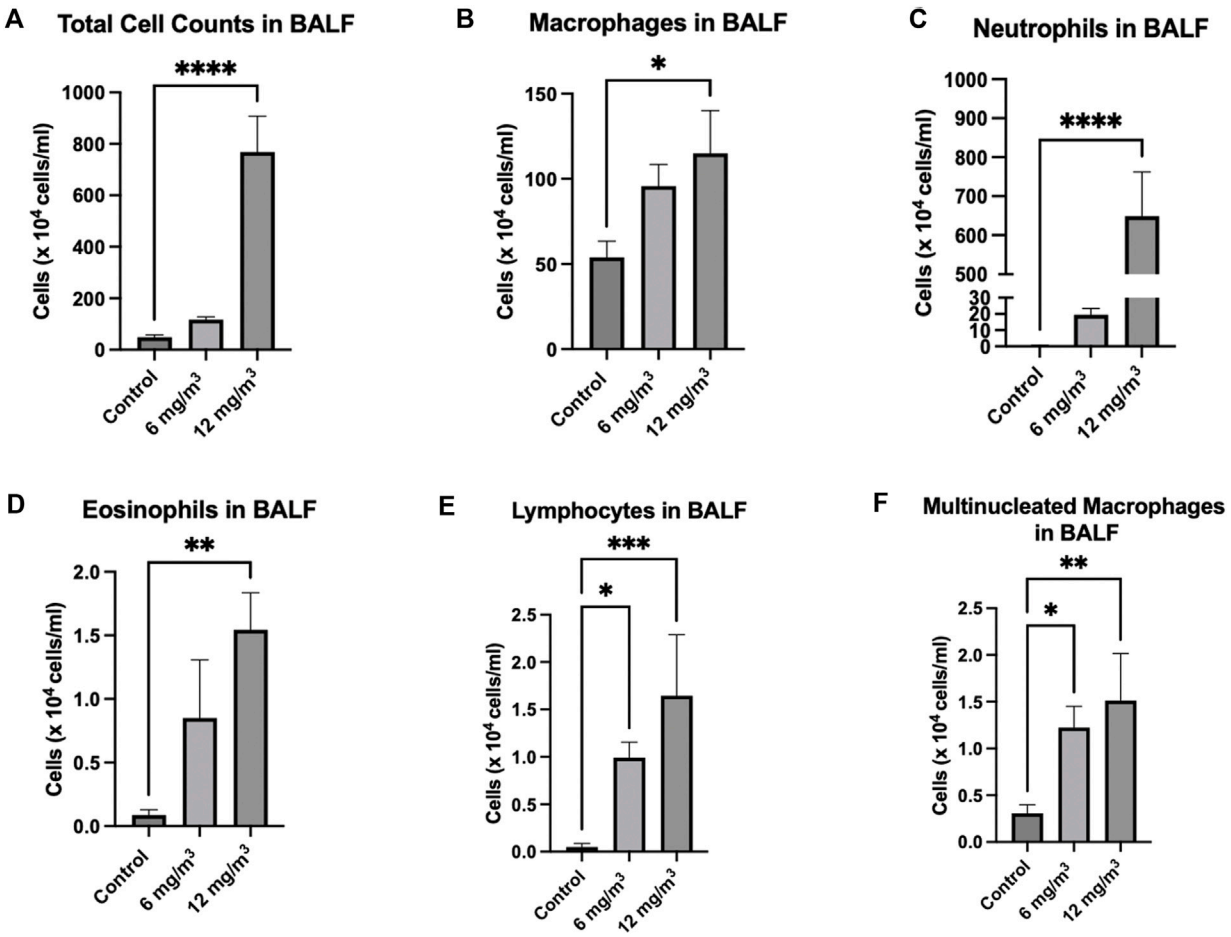

FIGURE 2
Total Cells and leukocytes in the bronchoalveolar lavage fluid (BALF) of Golden Syrian Hamsters were counted to determine if inflammation was occurring after exposure to inhaled SiO_2 NPs. The cells were re-suspended in 1 mL of RPMI media followed by determination of total cell numbers **(A)**. Total Cell numbers **(A)** were significantly increased by 16-fold in the 12 mg/m^3 treated group. Differential cell count **(B–F)** slide smears were prepared from the BALF of cells from the lung exposed to 6 and 12 mg/m^3 SiO_2 NPs for 4h/day for 8 days. Macrophages **(B)** of treated groups were not changed when compared to control. Neutrophils **(C)**, Eosinophils **(D)**, Lymphocytes **(E)**, and Multinucleated Macrophages **(F)** were significantly increased in the 12 mg/m^3 treated group when compared to control. N = 5.

(Figures 5A–C; Supplementary Figure S5). Average TUNEL positive cells in the vehicle control group were less than 1, while average TUNEL positive cells in the 6 mg/m^3 group had a mean of 3 TUNEL positive cells and the 12 mg/m^3 group was significantly increased with a mean of 4 TUNEL positive cells (Figure 5D).

Electron microscopy

Scanning Electron Microscopy was carried out to determine surface morphological alterations after exposure to both 6 mg/m^3 and 12 mg/m^3 SiO_2 NPs. Alveoli of vehicle control exposed animals had no pathological changes (Figure 6A). The 12 mg/m^3 treated group had a distinct change in morphology, with an increase in holes within the alveolar walls and noticeably thin septa between the alveoli (Figure 6B).

Transmission Electron Microscopy was done to determine ultrastructural cellular alterations after exposure to SiO_2 NPs. Within the interstitial region of the 12 mg/m^3 treated animal, apoptotic bodies, chromatin condensation (Figures 7A,B) and possible SiO_2 NPs (Figure 7C) were present. Control and treated animal tissue sections show intact Type II pneumocytes with lamellar bodies and mitochondria (Supplementary Figure S6).

Protein analysis of apoptosis and related cell markers

Caspase 9 and Cytochrome C levels, both part of the intrinsic apoptotic pathway, were unchanged in either treatment group when compared to control (Supplementary Figure S7). Caspase 8, part of the extrinsic pathway of apoptosis, was not changed in the 6 mg/m^3 group, but was significantly increased by 1.4-fold in

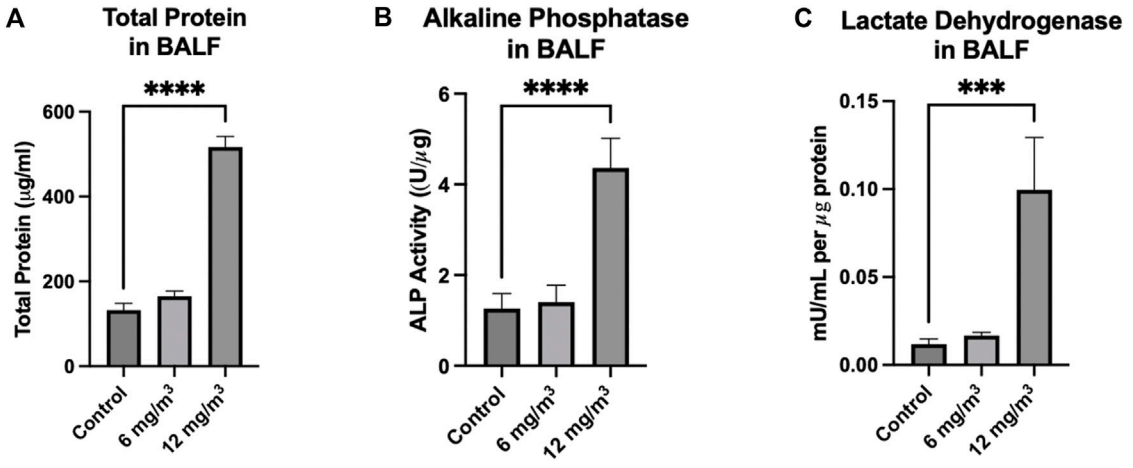

FIGURE 3
Markers measured in the BALF of Golden Syrian Hamsters from lungs exposed to 6 and 12 mg/m^3 SiO_2 NPs for 4h/day for 8 days were Total Protein (TP) Alkaline Phosphatase (ALP), and Lactate Dehydrogenase (LDH). **(A)** TP, **(B)** ALP), and **(C)** LDH were all significantly increased in the 12 mg/m^3 treated group when compared to vehicle control by 4-fold, 9-fold and 3-fold, respectively. N = 4.

the 12 mg/m^3 treatment group (Figure 8A; Supplementary Figure S8). Caspase 3 protein expression was not changed in the 6 mg/m^3 group but was significantly increased by 1.4-fold in the 12 mg/m^3 treatment group (Figure 8B; Supplementary Figure S8). Inflammatory and cellular stress proteins TNF-α and HSP70 were measured. HSP70 levels were not changed in the 6 mg/m^3 group but were significantly increased in the 12 mg/m^3 group by 7.5-fold (Figure 8C; Supplementary Figure S8). TNF-α levels were not changed in the 6 mg/m^3 group but were significantly increased in the 12 mg/m^3 group by 1.5-fold (Figure 8D; Supplementary Figure S8).

Discussion

Physical Characterization of a nanoparticle is important as physiochemical factors can alter their toxicity profile and action within a suspension, and the size and shape of a particle can influence its deposition in the lung [24]. To characterize the particle, the SiO_2 NPs were evaluated for size, aggregation, and zeta potential using transmission electron microscopy (TEM) and dynamic light scattering (DLS). Both wet and dry states of the particle size were evaluated to consider particle-particle and particle-fluid interactions alone and in suspension [25]. SiO_2 NPs measured by TEM were 20 nm while SiO_2 NPs in water had a mean hydrodynamic diameter of 226 nm. The apparent increase in size in water may be due to possible agglomeration within the chamber that is a characteristic likely based on the reported hydrodynamic diameter and zeta potential of the nanoparticles [16]. Agglomeration of particles within a whole-body chamber has been seen in Tungsten NPs when deposited on grids and analyzed by TEM [16]. The zeta potential of SiO_2 NPs was −20 mV in water, indicating stability with an anionic charge. Particles with a higher zeta potential have stronger electro-repulsion that can stabilize them preventing aggregation [26]. Negatively charged particles can easily move across mucus but have a difficult time crossing the cell membrane, often binding to a cell with positively charged surface proteins [26]. Such properties may inhibit NP cell entry through the cell membrane but may enhance numbers of inflammatory cells in the BALF.

Amorphous SiO_2 NPs were used to induce injury and identify a possible cell death pathway. To mimic real life exposure to SiO_2 NPs a whole-body exposure system was used. The selection of 4 h of exposure to SiO_2 NPs per day was based on the OECD Guidelines for acute inhalation toxicity studies [27]. To study the mechanism of toxicity animals were exposed continuously for 8 consecutive days for 4 h per day to either 6 mg/m^3 or 12 mg/m3 amorphous SiO_2 NPs, that is consistent with other studies [16, 19]. The concentration of 6 mg/m^3 was chosen based on OSHA's Permissible Exposure Limit (PEL) and NIOSH's Time Weighted Average (TWA) for amorphous silicon dioxide. The concentration of 12 mg/m^3 was chosen as it is double the set regulatory level, to simulate over exposure events. This additional concentration provides a dose response relationship that helps define a margin of safety relative to the exposure limit. These concentrations may not only capture regulatory relevant, but also high-end exposure scenarios to create a more comprehensive risk characterization.

Following exposure to 12 mg/m^3 amorphous SiO_2 NPs total leukocyte counts in the BALF were significantly increased indicating an inflammatory response [28]. The animal group

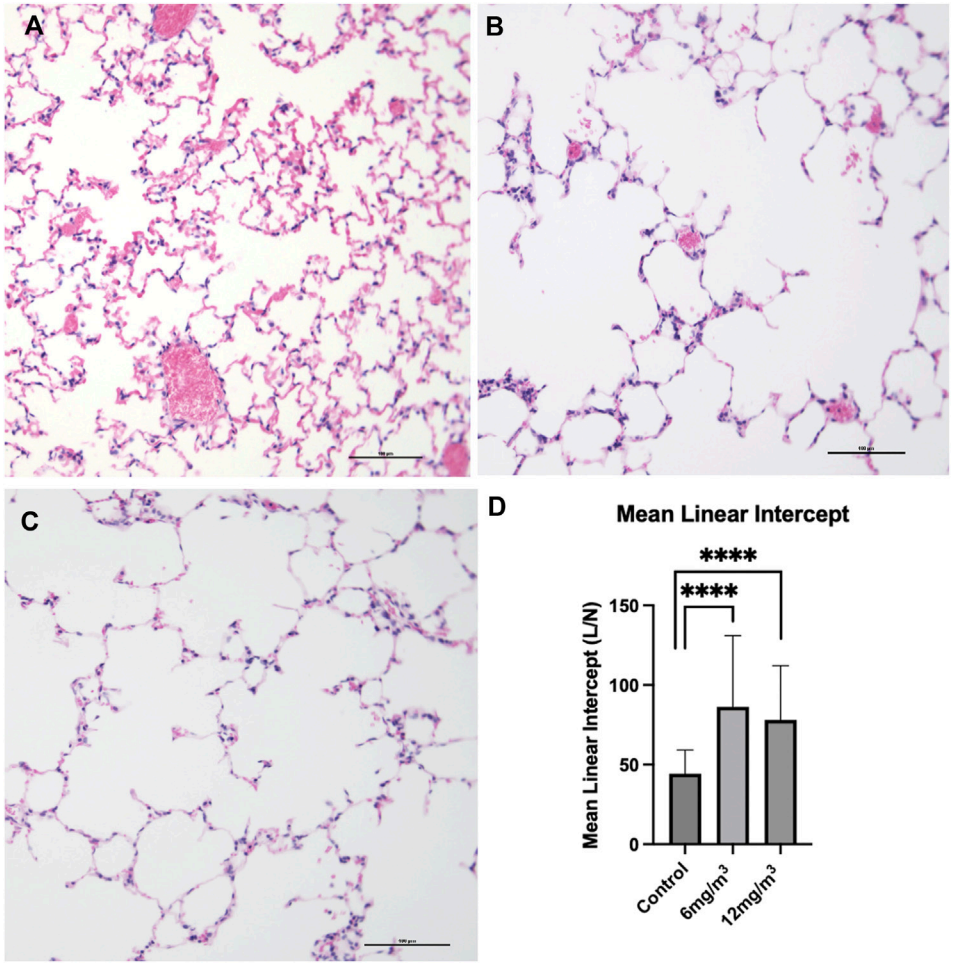

FIGURE 4
The photomicrographs are of formalin fixed, H&E-stained tissue sections from the lungs of **(A)** vehicle control (water), **(B)** 6 mg/m^3 and **(C)** 12 mg/m^3 SiO_2 NP treated groups. The micrographs show progressive increase in air space quantified by Mean Linear Intercept **(D)**. Mean Linear Intercept was measured by the line intersection method and calculated from 20 random fields of view per animal. The Mean Linear Intercept of both 6 mg/m^3 and 12 mg/m^3 SiO_2 NP treated animals was significantly increased when compared to vehicle control (water).

exposed to 12 mg/m^3 had significant increases in total cell counts, neutrophils, lymphocytes, eosinophils, and multinucleated macrophages. A significant increase in cell types other than macrophages indicates an acute inflammatory response at 24 h after the last exposure [28]. Increased neutrophils may have the ability to shift protease/antiprotease balance in the lung leading to tissue injury [29]. Total Protein (TP), Lactate Dehydrogenase (LDH) and Alkaline Phosphatase (ALP) were all significantly increased in the BALF of the group treated with 12 mg/m^3 SiO_2 NPs. Total protein elevations can be attributed to injury of the alveolar-capillary barrier [30]. Increased LDH, a cytoplasmic enzyme, confirms the loss of cellular membrane integrity with an increased ALP, being a measure of damage to the alveolar epithelium [28, 31].

To date, the literature does not report any histologic changes comparable to those observed in this study. Lungs exposed to crystalline silica NPs have shown airway inflammation, collagen deposition and fibrosis [32, 33]. Histopathological examination of pulmonary tissue sections in the current study shows damaged alveolar walls with increased airspace size, quantified by Mean Linear Intercept. The observed increase in airspace size is attributed to cell death and subsequent alveolar wall destruction, resembling histologic features of emphysemic lungs [34]. Lung tissue sections stained using the TUNEL method have a significant increase in TUNEL positive cells present in the 12 mg/m^3 treated animal group. Kong et al, (2020) found increase TUNEL positive cells alongside caspase activation to confirm apoptosis occurring in mice [35].

Destruction of the alveolar septal tissue is a characteristic of emphysema [36]. Scanning Electron Microscopy (SEM) micrographs of the 12 mg/m^3 group show thinning of the

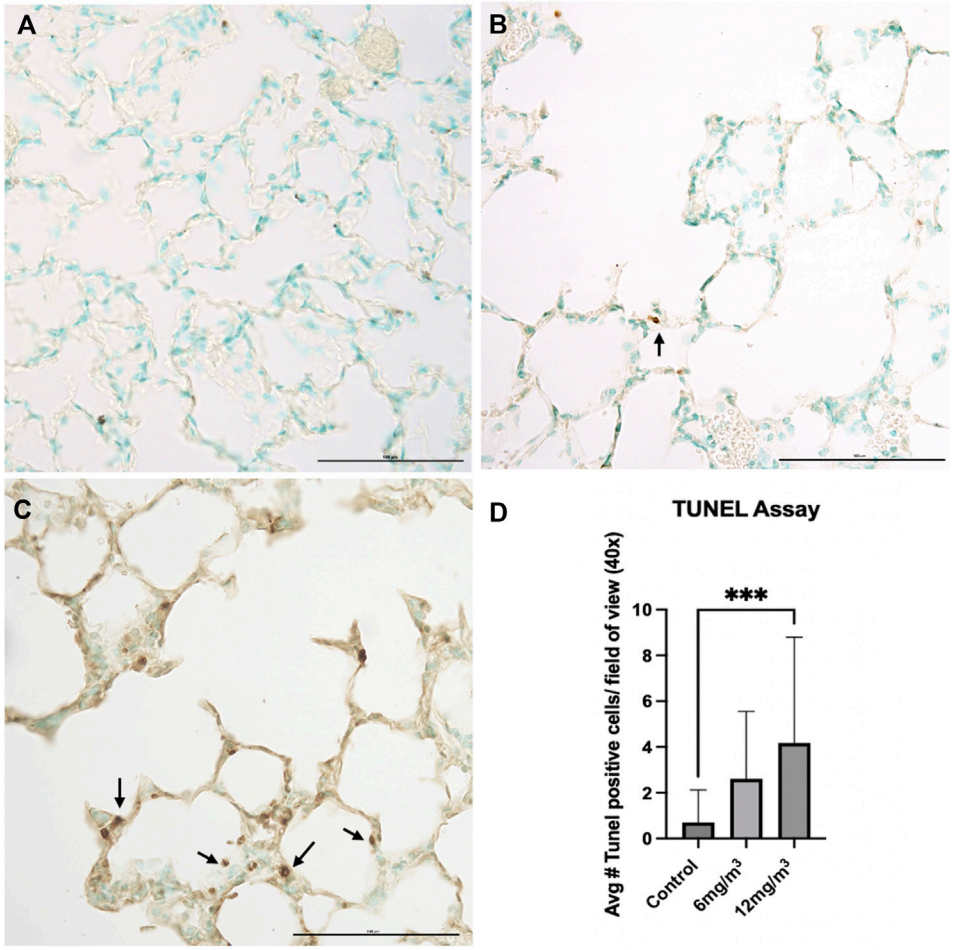

FIGURE 5
The photomicrographs are of formalin fixed tissue sections from the lungs of **(A)** vehicle control (water), **(B)** 6 mg/m^3 and **(C)** 12 mg/m^3 SiO_2 NP treated groups. The TUNEL Assay-stained tissue sections for TUNEL positive cells (apoptotic bodies). The micrographs show an increase with increased concentration of NPs with a concomitant increase in the number of apoptotic bodies. Arrows indicate apoptotic bodies. **(D)** A histogram of the count from the TUNEL assays shows a significant increase in TUNEL positive cells in the high concentration SiO_2 NP treated animals compared to vehicle control (water). The average TUNEL positive cells was based on calculated results of 20 random fields of view.

interalveolar septa, with increase in holes within the alveolar walls [37]. Lung sections from TEM images of the 12 mg/m^3 treated animals showed, apoptotic bodies, damaged interstitial cells, and SiO_2 NPs. Mitochondria appear unchanged showing tightly packed cristae with parallel alignment, higher matrix density, and visible matrix dense granules as opposed to injured mitochondria that would show increases in intermembrane spaces and shape alterations [38]. No change to Type I or II pneumocytes was found in the 12 mg/m^3 treated animals. Kantari and Walczak [39] found that the process of caspase 3 cleavage by caspase 8 can be blocked by XIAP (X-linked inhibitor of apoptosis) in Type II pneumocytes, that suggests while apoptosis is occurring in other cells, it may not be occurring in Type II pneumocytes [39]. This may explain lack of pathology in Type II pneumocytes in the 12 mg/m^3 TEM micrographs. Interstitial regions within the 12 mg/m^3 treated animals had visible apoptotic bodies with SiO_2 NPs present.

To confirm that the mechanism of apoptosis was activated, Cytochrome C, Caspases 9, 8 and 3 were measured. Cytochrome C and Caspase 9 levels did not change, while Caspases 3, and 8 were significantly increased in the 12 mg/m^3 group when compared to controls. Based on the literature crystalline silica has been found to increase Caspase 3, 9 and Cytochrome C release that supports an intrinsic pathway [40]. Results from the current study suggest an extrinsic pathway of apoptosis is the primary mechanism for cell death occurring after exposure to amorphous SiO_2 NPs. The extrinsic pathway is typically initiated by activation of cell surface receptors. Macrophages and neutrophils present after exposure to SiO_2 NPs will phagocytize the NPs leading to interactions that produce inflammatory factors such as TNF-α

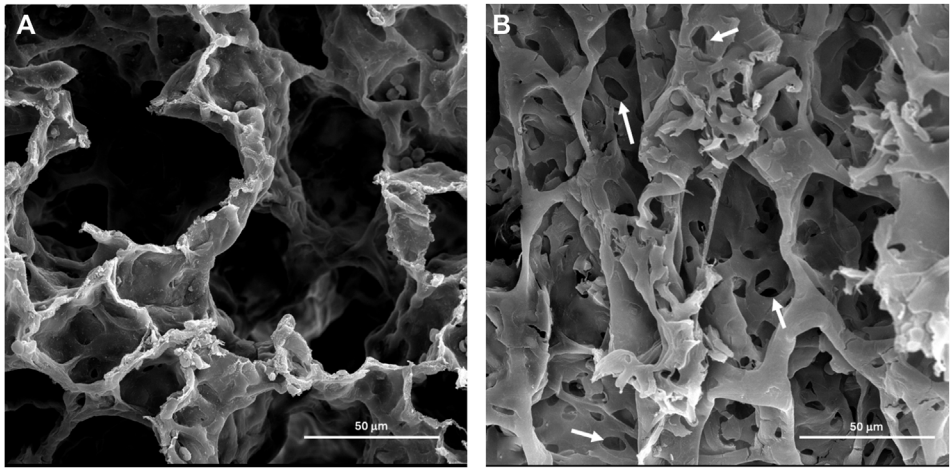

FIGURE 6
Representative scanning electron micrographs (SEM) of lung tissue from control and treated animals fixed in 3% glutaraldehyde and processed as described in methods. **(A)** The photomicrograph is from the lungs of a vehicle control (water) animal that shows typical architecture of the alveoli. **(B)** The lung tissue of an animal treated with 12 mg/m^3 shows an atypical architecture of the alveoli with increased holes within the alveoli wall marked by arrows.

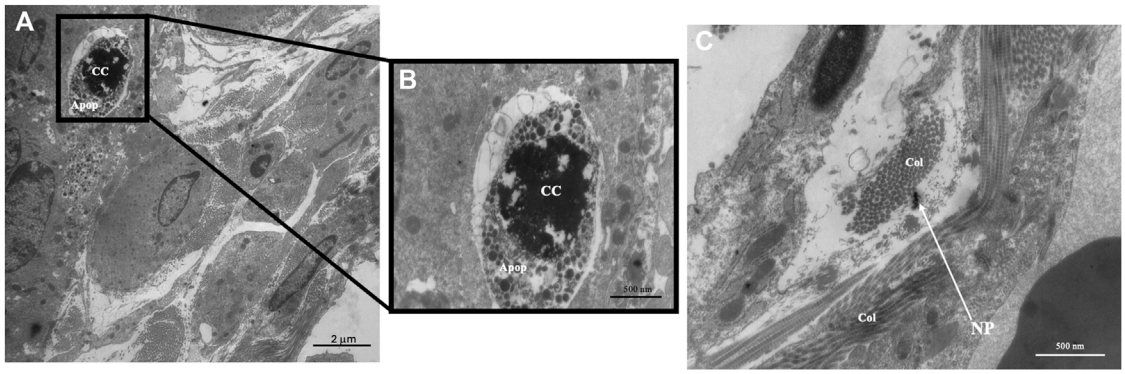

FIGURE 7
Representative transmission electron micrographs (TEM) of lung tissue from control and treated animals fixed in 3% glutaraldehyde and processed as described in methods. TEM photomicrographs of an interstitial region from a 12 mg/m^3 treated animal showing **(A)** apoptotic bodies and the presence of collagen, original magnification ×5,000. **(B)** An enlargement of the region of apoptotic bodies, original magnification ×20,000. **(C)** An interstitial region showing the presence of collagen and SiO_2 NPs, original magnification ×20,000. Key: Apoptotic Bodies (Apop), Chromatin Condensation (CC), Collagen (Col), Nanoparticles (NP).

[41]. When TNF-α is released, it can bind to a transmembrane receptor to initiate apoptosis leading to Caspase 8 and eventual Caspase 3 cleavage [42].

The lack of change in Caspase 9 and Cytochrome C may be attributed to an increase in HSP70, that can block mitochondrial translocation, activation of Bax, and prevent mitochondrial membrane permeabilization, Cytochrome C release, and Caspase 9 cleavage [43, 44]. Results from the current study including increased TNF-α, Caspase 3, 8, HSP70 along with no change in Caspase 9 or Cytochrome C levels support both the activation of the extrinsic pathway while eliminating the intrinsic pathway as the mechanism of apoptosis [43, 44].

The data from this study suggests that after exposure to amorphous SiO_2 NPs inflammatory cells such as macrophages, neutrophils, eosinophils, and lymphocytes are recruited. As these inflammatory cells are activated, they begin to release cytokines and proteases [45]. Elastic fibers, that act to maintain alveolar wall integrity, require balance between elastase and anti-elastase, while an imbalance can lead to tissue damage and resulting air space enlargement [45]. Once activated, neutrophils can release neutrophil elastase (NE), that is normally neutralized by alpha-1-antiprotease (A1AP) [45]. When inflammation is present the balance between NE and A1AP can be altered leading to destruction of lung tissue by unopposed NE breaking down

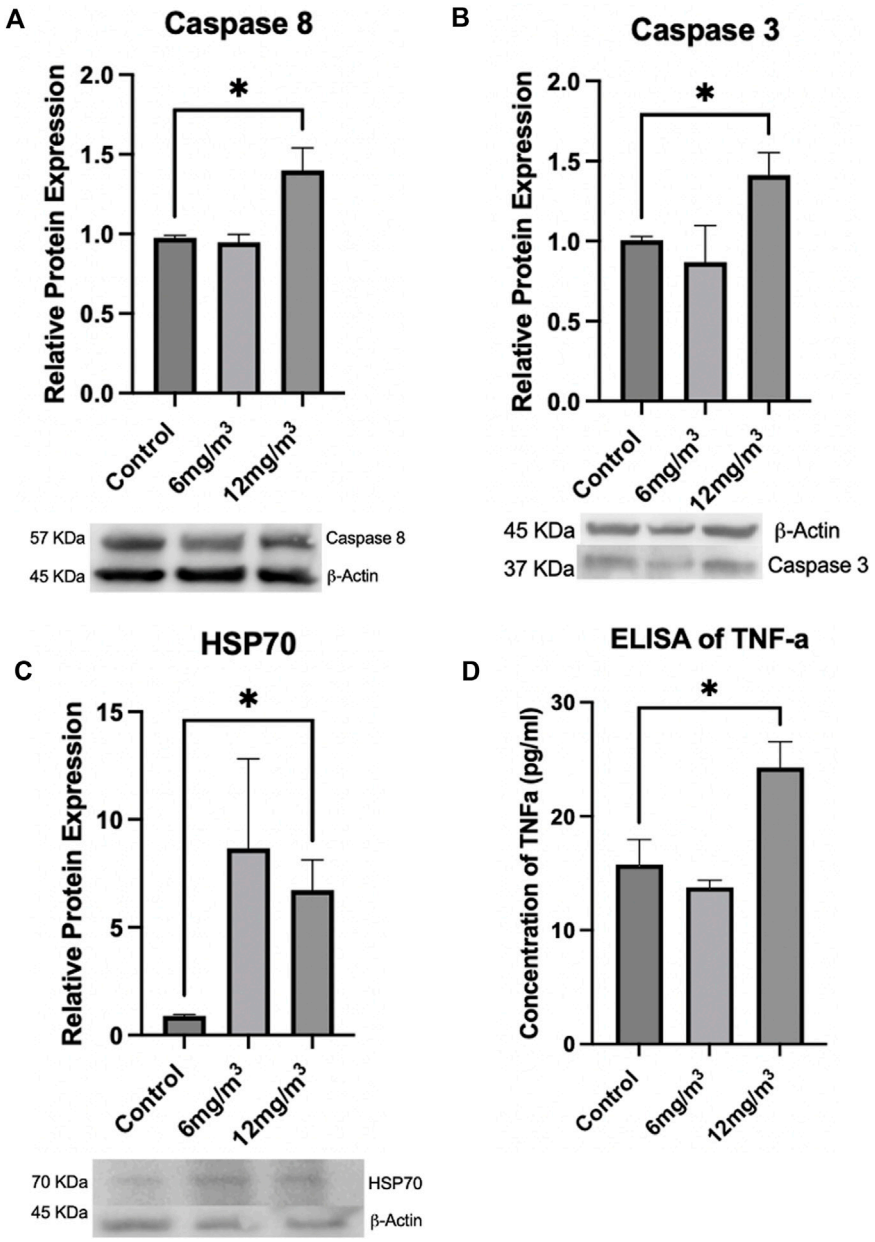

FIGURE 8
To determine if apoptosis was occurring, Caspases 8, 3, HSP70 and TNF-α were measured via Western Blot or ELISA. **(A)** Caspase 8 and **(B)** Caspase 3 were significantly increased in the 12 mg/m^3 treated group when compared to vehicle control (water). **(C)** HSP70, a marker of cellular stress, was measured by Western Blot and was significantly increased in the high concentration group when compared to vehicle control (water). **(D)** An ELISA of TNF-α levels was significantly increased in the high concentration treated group when compared to vehicle control (water). For Western Blots and ELISAs n = 4.

elastin in the lung septa [45]. It may be possible that resulting inflammation from exposure to amorphous SiO_2 NPs triggers such an imbalance in protease-antiprotease balance leading to resulting TUNEL positive cells, elevated apoptotic markers, increased airspace (reported by increased MLI) and increased hole size and number within the alveolar walls, along with thinning of the alveolar septa seen in SEM. Damage to lung tissue found in this study is comparable to emphysemic lung architecture, that is reported as abnormal permanent dilation of airspaces [45].

The current study investigated the toxicity to amorphous SiO_2 NPs in the lungs of Golden Syrian Hamsters. The study found amorphous SiO_2 NPs induce cell death through an extrinsic mechanism of apoptosis. The data from Golden Syrian Hamsters suggest that internalization of amorphous

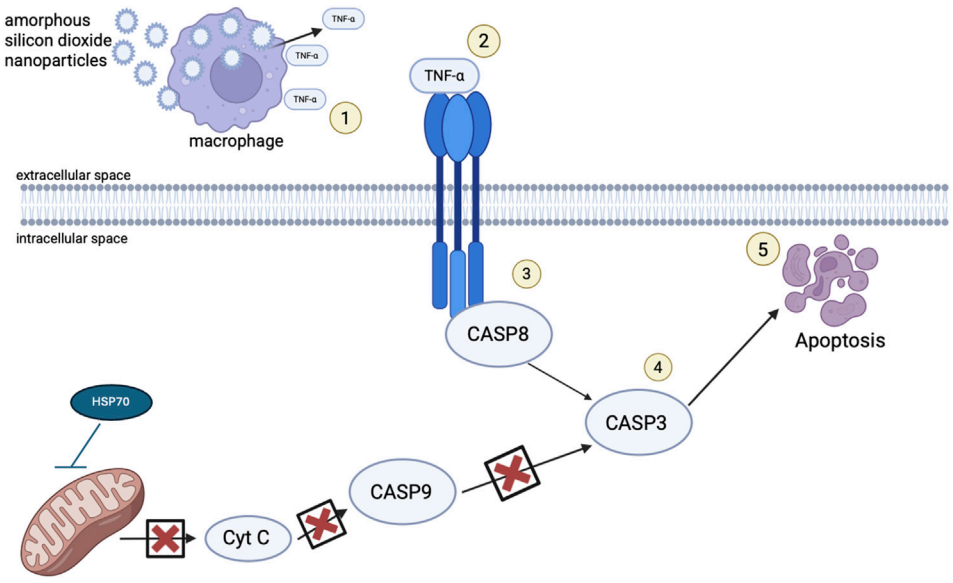

FIGURE 9
Schematic representation of the proposed mechanism of injury following exposure to SiO_2 NPs. (1) After exposure to SiO_2 NPs through inhalation, the NPs flow through the respiratory tract until they reach the alveoli where they are met by macrophages and neutrophils and they are phagocytized. During particle overload, and lack of mucociliary clearance, macrophages signal an inflammatory response, cytokines such as HSP70 and TNF-α are released and react, activating cell death receptors (2). TNF-α binds to death receptors transversing the cellular membrane activating procaspase 8 (3) with such recruitment leading to cleavage of caspase 3 (4) and cell death (5).

SiO_2 NPs by macrophages and neutrophils may lead to the generation of TNF-α, that will bind to a transmembrane receptor, that in turn will signal the death receptor cleavage of Caspase 8 and Caspase 3 to initiate apoptosis. As this extrinsic mechanism is occurring, HSP70 is acting against the intrinsic pathway, protecting the mitochondrial membrane from permeabilizing. Resulting apoptosis may then allow for hole formation and their enlargement within the alveoli septa, seen in SEM micrographs, which allows mechanical stress to cause alveolar wall breaks, as seen by increased air space size, and quantified by mean linear intercept. Figure 9 provides a mechanistic summary.

Author contributions

RR carried out all experimentation. RR and JC designed the experiments and analyzed the data. All authors contributed to the article and approved the submitted version.

Data availability

The original contributions presented in the study are included in the article/Supplementary Material, further inquiries can be directed to the corresponding author.

Ethics statement

The animal study was approved by St. John's University Institutional Animal Care and Use Committee. The study was conducted in accordance with the local legislation and institutional requirements.

Funding

The author(s) declared that financial support was received for this work and/or its publication. The research was funded by St. John's University, Queens, NY, United States.

Conflict of interest

The author(s) declared no potential conflicts of interest with respect to the research, authorship, and/or publication of this article.

Generative AI statement

The author(s) declared that generative AI was not used in the creation of this manuscript.

Any alternative text (alt text) provided alongside figures in this article has been generated by Frontiers with the support of artificial intelligence and reasonable efforts have been made to ensure accuracy, including review by the authors wherever possible. If you identify any issues, please contact us.

Supplementary material

The Supplementary Material for this article can be found online at: https://www.ebm-journal.org/articles/10.3389/ebm.2026.10793/full#supplementary-material

References

1. House JE, House KA. Chapter 12 - silicon, germanium, tin, and lead. In: *Descriptive inorganic chemistry*. London: Academic Press is an imprint of Elsevier (2016). p. 177–96. doi:10.1016/B978-0-12-804697-5.00012-9

2. Hamilton RFJ, Thakur SA, Holian A. Silica binding and toxicity in alveolar macrophages. *Free Radic Biol Med* (2008) **44**(7):1246–58. doi:10.1016/j.freeradbiomed.2007.12.027

3. Mostovenko E, Canal CG, Cho M, Sharma K, Erdely A, Campen MJ, et al. Indirect mediators of systemic health outcomes following nanoparticle inhalation exposure. *Pharmacol Ther* (2022) **235**:108120. doi:10.1016/j.pharmthera.2022.108120

4. Huang Y, Li P, Zhao R, Zhao L, Liu J, Peng S, et al. Silica-based nanoparticles: biomedical applications and toxicity. *Biomed Pharmacother* (2022) **151**:113053. doi:10.1016/j.biopha.2022.113053

5. Costantini LM, Gilberti RM, Knecht DA. The phagocytosis and toxicity of amorphous silica. *PLOS ONE* (2011) **6**(2):e14647–7. doi:10.1371/journal.pone.0014647

6. Tavares LP, Libreros S, Bitounis D, Nshimiyimana R, Demokritou P, Serhan CN, et al. SiO_2 nanoparticles as disruptors of endogenous resolution mechanisms of inflammatory responses that exacerbate pneumonia. *Sci Rep* (2025) **15**(1):6398. doi:10.1038/s41598-025-89700-y

7. Wang M, Li J, Dong S, Cai X, Simaiti A, Yang X, et al. Silica nanoparticles induce lung inflammation in mice via ROS/PARP/TRPM2 signaling-mediated lysosome impairment and autophagy dysfunction. *Part Fibre Toxicol* (2020) **17**(1):23. doi:10.1186/s12989-020-00353-3

8. Iyer R, Hamilton R, Li L, Holian A. Silica-induced apoptosis mediated via scavenger receptor in human alveolar macrophages. *Toxicol Appl Pharmacol* (1996) **141**(1):84–92. doi:10.1006/taap.1996.0263

9. Phalen RF, Mannix RC, Drew RT. Inhalation exposure methodology. *Environ Health Perspect* (1984) **56**:23–34. doi:10.1289/ehp.845623

10. Vrijhof H, Pulinckx S. *Technical report no. 122. Poorly soluble particles/lung overload – ECETOC*. Brussels: ECETOC (2021). Available online at: https://www.ecetoc.org/publication/tr-122-poorly-soluble-particles-lung-overload/ (Accessed July 30, 2025).

11. Oyabu T, Morimoto Y, Izumi H, Yoshiura Y, Tomonaga T, Lee BW, et al. Comparison between whole-body inhalation and nose-only inhalation on the deposition and health effects of nanoparticles. *Environ Health Prev Med* (2015) **21**(1):42–8. doi:10.1007/s12199-015-0493-z

12. Kwon RY, Youn SM, Choi SJ. Oral excretion kinetics of food-additive silicon dioxides and their effect on *in vivo* macrophage activation. *Int J Mol Sci* (2024) **25**:1614–4. doi:10.3390/ijms25031614

13. Hayes JA, Christensen TG, Snider GL. The hamster as a model of chronic bronchitis and emphysema in man. *Lab Anim Sci* (1977) **27**(5 Pt 2):762–70. Available online at: https://pubmed.ncbi.nlm.nih.gov/592728 (Accessed July 30, 2025).

14. Nakashima JM, Levin JR, Hyde DM, Giri SN. Repeated exposures to enzyme-generated oxidants cause alveolitis, epithelial hyperplasia, and fibrosis in hamsters. *Am J Pathol* (1991) **139**(6):1485–99. Available online at: https://pubmed.ncbi.nlm.nih.gov/1750514 (Accessed July 30, 2025).

15. Bijlani KH, Sukhija HR, Cantor JO, Cerreta JM. Pulmonary inflammation induced by single walled carbon nanotubes in golden Syrian hamsters. *J Anal Pharm Res* (2016) **2**(3):1–13. doi:10.15406/japlr.2016.02.00021

16. Prajapati MV, Adebolu OO, Morrow BM, Cerreta JM. Evaluation of pulmonary response to inhaled tungsten (IV) oxide nanoparticles in golden Syrian hamsters. *Exp Biol Med* (2016) **242**(1):29–44. doi:10.1177/1535370216665173

17. Michita RT, Mysorekar IU. Golden Syrian hamsters as a model for revisiting the role of biological sex differences in SARS-CoV-2 infection. *mBio* (2021) **12**:14. doi:10.1128/mBio.01848-21

18. Bednash JS, Kagan VE, Englert JA, Farkas D, Tyurina YY, Tyurin VA, et al. Syrian hamsters as a model of lung injury with SARS-CoV-2 infection: pathologic, physiologic, and detailed molecular profiling. *Transl Res* (2021) **240**:1–17. doi:10.1016/j.trsl.2021.10.007

19. Huber EA, Cerreta JM. Mechanisms of cell injury induced by inhaled molybdenum trioxide nanoparticles in golden Syrian hamsters. *Exp Biol Med* (2022) **247**(23):2067–80. doi:10.1177/15353702221104033

20. Lomphithak T, Fadeel B. Die hard: cell death mechanisms and their implications in nanotoxicology. *ToxicolSciences* (2023) **192**(2):141–54. doi:10.1093/toxsci/kfad008

21. Ketelut-Carniero N, Fitzgerald KA. Apoptosis, pyroptosis, and necroptosis—oh my! the many ways a cell can die. *J Mol Biol* (2022) **434**(4):167378. doi:10.1016/j.jmb.2021.167378

22. Harbeck RJ. Immunophenotyping of bronchoalveolar lavage lymphocytes. *Clin Diagnos Labor Immunol* (1998) **5**(3):271–7. doi:10.1128/CDLI.5.3.271-277.1998

23. Crowley G, Kwon S, Caraher EJ, Haider SH, Lam R, Batra P, et al. Quantitative lung morphology: semi-automated measurement of mean linear intercept. *BMC Pulm Med* (2019) **19**(1):206. doi:10.1186/s12890-019-0916-6

24. Lee JH, Ju JE, Kim BI, Pak PJ, Choi E-K, Lee H-S, et al. Rod-shaped iron oxide nanoparticles are more toxic than sphere-shaped nanoparticles to murine macrophage cells. *Environ Toxicol Chem* (2014) **33**(12):2759–66. doi:10.1002/etc.2735

25. Cohen J, Deloid G, Pyrgiotakis G, Demokritou P. Interactions of engineered nanomaterials in physiological media and implications for *in vitro* dosimetry. *Nanotoxicology* (2013) **7**(4):417–31. doi:10.3109/17435390.2012.666576

26. Öztürk K, Kaplan M, Calis S. Effects of nanoparticle size, shape, and zeta potential on drug delivery. *Intl J Pharm* (2024) **666**:124799. doi:10.1016/j.ijpharm.2024.124799

27. *Test no. 403: acute inhalation toxicity*. Paris: OECD. (2024). Available online at: https://www.oecd.org/en/publications/2009/09/test-no-403-acute-inhalation-toxicity_g1gh2927.html (Accessed August 14, 2025).

28. Srinvias A, Rao PJ, Selvam G, Murthy PB, Reddy PN. Acute inhalation toxicity of cerium oxide nanoparticles in rats. *Toxicol Lett* (2011) **205**(2):105–15. doi:10.1016/j.toxlet.2011.05.1027

29. Quint JK, Wedzicha JA. The neutrophil in chronic obstructive pulmonary disease. *J Allergy Clin Immunol* (2007) **119**(5):1065–71. doi:10.1016/j.jaci.2006.12.640

30. Muller J, Huaux F, Moreau N, Mission P, Heilier JF, Delos M, et al. Respiratory toxicity of multi-wall carbon nanotubes. *Toxicol Appl Pharmacol* (2005) **207**(3):221–31. doi:10.1016/j.taap.2005.01.008

31. Capelli A, Lusuardi M, Cerutti CG, Donner CF. Lung alkaline phosphatase as a marker of fibrosis in chronic interstitial disorders. *Am J Respir Crit Care Med* (1997) **155**(1):249–53. doi:10.1164/ajrccm.155.1.9001320

32. Kumari S, Singh R. Protective effects of intranasal curcumin on silica-induced lung damage. *Cytokine* (2022) **157**:155949. doi:10.1016/j.cyto.2022.155949

33. Ban J, Liu F, Zhang Q, Chang S, Zeng X, Chen J. Macrophage-derived exosomal lncRNA MSTRG.91634.7 inhibits fibroblasts activation by targeting PINK1 in silica-induced lung fibrosis. *Toxicol Lett* (2023) **372**:36–44. doi:10.1016/j.toxlet.2022.10.004

34. Augusti A, Cosío B. Chronic obstructive pulmonary disease | emphysema, general. In: Laurent G, Shapiro S, editors. *Encyclopedia of respiratory medicine*. London: Elsevier (2006). p. 448–57. doi:10.1016/B0-12-370879-6/00074-0

35. Kong Q, Wu X, Qiu Z, Huang Q, Xia Z, Song X. Protective effect of dexmedetomidine on acute lung injury *via* the upregulation of tumour necrosis factor-α-induced protein-8-like 2 in septic mice. *Inflammation* (2020) **43**(3):833–46. doi:10.1007/s10753-019-01169-w

36. Vlahovic G, Russell ML, Mercer RR, Crapo JD. Cellular and connective tissue changes in alveolar septal walls in emphysema. *Am J Respir Crit Care Med* (1999) **160**(6):2086–92. doi:10.1164/ajrccm.160.6.9706031

37. Congiu T, Demontis R, Cau F, Piras M, Fanni D, Geroasa C, et al. Scanning electron microscopy of lung disease due to COVID-19 - a case report and a review of the literature. *Eur Rev Medi Pharmacol Sci* (2021) **25**(24):7997–8003. doi:10.26355/eurrev_202112_27650

38. Delgado-Buenrostro NL, Freyre-Fonseca V, Cuéllar CM, Sánchez-Pérez Y, Gutierrez-Cirlos EB, Cabellos-Avelar T, et al. Decrease in respiratory function and electron transport chain induced by airborne particulate matter (PM10) exposure in lung mitochondria. *Toxicol Pathol* (2013) **41**(4):628–38. doi:10.1177/0192623312463784

39. Kantari C, Walczak H. Caspase-8 and bid: caught in the act between death receptors and mitochondria. *Biochim Biophys Acta* (2011) **1813**(4):558–63. doi:10.1016/j.bbamcr.2011.01.026

40. Ahamed M. Silica nanoparticles-induced cytotoxicity, oxidative stress and apoptosis in cultured A431 and A549 cells. *Hum Exp Toxicol* (2013) **32**(2):186–95. doi:10.1177/0960327112459206

41. Medrano-Bosch M, Moreno-Lanceta A, Melgar-Lesmes P. Nanoparticles to target and treat macrophages: the Ockham's concept? *Pharmaceutics* (2021) **13**(9):1340. doi:10.3390/pharmaceutics13091340

42. Guicciardini ME, Gores GJ. Life and death by death receptors. *FASEB J* (2009) **23**(6):1625–37. doi:10.1096/fj.08-111005

43. Stankiewicz AR, Lachapelle G, Foo CP, Radicioni SM, Mosser DD. Hsp70 inhibits heat-induced apoptosis upstream of mitochondria by preventing bax translocation. *J Biol Chem* (2005) **280**(46):38729–39. doi:10.1074/jbc.M509497200

44. Yang X, Wang J, Zhou Y, Wang Y, Wang S, Zhang W. Hsp70 promotes chemoresistance by blocking bax mitochondrial translocation in ovarian cancer cells. *Cancer Lett* (2012) **321**(2):137–43. doi:10.1016/j.canlet.2012.01.030

45. Pahal P, Avula A, Afzal M. *Emphysema*. Treasure Island (FL): StatPearls Publishing (2025). Available online at: https://www.ncbi.nlm.nih.gov/books/NBK482217/# (Accessed August 14, 2025).

EBM Experimental Biology and Medicine

TYPE Original Research
PUBLISHED 14 January 2026
DOI 10.3389/ebm.2025.10776

OPEN ACCESS

*CORRESPONDENCE
Ling-Jun Zhu,
lingjun__zhu@163.com
Youlong Zhu,
zhuyoulong1987@126.com

†These authors have contributed equally to this work

RECEIVED 29 July 2025
REVISED 06 December 2025
ACCEPTED 17 December 2025
PUBLISHED 14 January 2026

CITATION
Kong F, Feng J, Shan H, Zhu Y and Zhu L-J (2026) Machine learning-based comprehensive analysis of m6A RNA methylation regulators in colorectal cancer: implications for prognosis, immune microenvironment, and immunotherapy response.
Exp. Biol. Med. 250:10776.
doi: 10.3389/ebm.2025.10776

Machine learning-based comprehensive analysis of m6A RNA methylation regulators in colorectal cancer: implications for prognosis, immune microenvironment, and immunotherapy response

Feifei Kong[1,2†], Jiawei Feng[3†], Haixia Shan[2], Youlong Zhu[4*] and Ling-Jun Zhu[1*]

[1]Department of Oncology, The First Affiliated Hospital of Nanjing Medical University, Nanjing, China, [2]Department of Oncology, The Affiliated Hospital of Xuzhou Medical University, Xuzhou, Jiangsu, China, [3]Department of Thyroid Surgery, The Third Affiliated Hospital of Soochow University, Changzhou First People's Hospital, Changzhou, Jiangsu, China, [4]Department of Gastrointestinal Surgery, Southeast University Affiliated Xuzhou Central Hospital, Xuzhou, Jiangsu, China

Abstract

N6-methyladenosine (m6A) RNA methylation regulators have been implicated in colorectal cancer (CRC) progression. However, systematic evaluation using multiple machine learning approaches for prognostic prediction remains limited. This study aimed to develop and validate machine learning models for CRC prognosis based on m6A regulators and assess their potential for immunotherapy response prediction. We analyzed 1,047 CRC patients from TCGA and GEO databases (70% training, 30% validation). Twenty machine learning algorithms were systematically evaluated, with LASSO regression selecting optimal features from 27 m6A regulators. SHAP analysis provided model interpretability. Immune microenvironment characterization and immunotherapy response prediction were performed using established computational methods. LASSO regression selected eight m6A regulators (IGF2BP2, METTL3, HNRNPA2B1, METTL14, YTHDF2, VIRMA, FTO, ALKBH5) for model construction. Among 20 algorithms tested, Random Forest achieved optimal performance (training AUC = 0.895, validation AUC = 0.847). SHAP analysis identified IGF2BP2 (mean |SHAP| = 0.42) and METTL3 (mean |SHAP| = 0.36) as primary contributors to risk prediction. Risk stratification showed significant survival differences (HR = 2.41, 95% CI: 1.73–3.36, $p < 0.001$). Low-risk patients demonstrated enhanced immune infiltration with higher $CD8^+$ T cells (17.8% vs. 10.2%, $p < 0.001$) and better predicted immunotherapy response rates (36.5% vs. 20.3%, $p = 0.006$). Our systematic machine learning analysis demonstrates that m6A regulators can

effectively predict CRC prognosis and immunotherapy response. The eight-gene signature provides a practical tool for clinical risk assessment and treatment decision-making.

KEYWORDS

colorectal cancer, immunotherapy, m6A methylation, machine learning, SHAP

Impact statement

This study addresses the need for reliable prognostic tools in colorectal cancer by systematically evaluating machine learning approaches for m6A-based risk stratification. While m6A modifications are increasingly recognized in cancer biology, their clinical application remains limited by methodological inconsistencies. We advance the field by providing the first comprehensive comparison of 20 ML algorithms for m6A-based CRC prognosis, establishing a standardized framework for future studies. Our integration of SHAP analysis addresses the critical barrier of model interpretability in clinical settings. The resulting 8-gene signature demonstrates potential utility for patient stratification and preliminary evidence for immunotherapy response prediction. This work provides the research community with a validated methodology for developing m6A-based biomarkers and offers clinicians a potential tool for risk assessment. The findings contribute to the growing understanding of m6A's role in CRC progression and immune regulation, supporting further investigation into epigenetic-based therapeutic strategies.

Introduction

Colorectal cancer (CRC) remains the third most common malignancy worldwide, with over 1.9 million new cases and more than 900,000 deaths annually reported in 2024 [1]. Despite significant advances in surgical techniques, chemotherapy, and targeted therapies, the 5-year survival rate for metastatic CRC remains approximately 14%, highlighting the urgent need for improved prognostic tools and personalized treatment strategies [2]. CRC's diverse molecular subtypes and treatment responses require sophisticated predictive models to capture this complexity.

N6-methyladenosine (m6A) represents the most abundant internal chemical modification of eukaryotic mRNAs, accounting for approximately 0.1–0.4% of all adenosines in cellular mRNA [3]. This reversible modification regulates various aspects of RNA metabolism, including stability, translation efficiency, nuclear export, and localization [4]. The m6A modification is dynamically regulated by three categories of proteins: "writers" (methyltransferases such as METTL3, METTL14, WTAP), "readers" (binding proteins including YTHDF1/2/3, IGF2BP1/2/3, HNRNPC), and "erasers" (demethylases including FTO and ALKBH5) [5].

Accumulating evidence demonstrates that m6A dysregulation is causally involved in cancer initiation, progression, metastasis, and therapeutic resistance [6, 7]. In CRC specifically, recent mechanistic studies have elucidated the pathogenic roles of m6A regulators. Wang et al. demonstrated that HES1 promotes aerobic glycolysis through IGF2BP2-mediated GLUT1 m6A modification, driving CRC progression via m6A-dependent metabolic reprogramming [8]. Zhou et al. revealed that METTL3-mediated m6A modification promotes metastasis through REG1α stabilization and Wnt/β-catenin pathway activation, establishing a direct link between epigenetic modification and tumor progression [9]. Most recently, Qiao et al. showed that FTO demethylase targeting induces ferroptotic cell death through SLC7A11/GPX4 downregulation, highlighting therapeutic vulnerabilities [10]. METTL3 overexpression has been shown to promote CRC cell proliferation and metastasis through multiple mechanisms, including JAK1/STAT3 signaling activation and STC2 axis regulation [11, 12]. Conversely, enhanced m6A modification through demethylase inhibition has been associated with increased chemosensitivity and ferroptosis induction in CRC cells [13]. However, the comprehensive prognostic value of m6A regulators and their relationship with the tumor immune microenvironment in CRC remains incompletely understood.

Machine learning has transformed biomedical research and precision oncology by analyzing complex datasets to identify patterns and make predictions [14]. Unlike traditional statistical methods, machine learning algorithms can capture non-linear relationships and complex interactions between variables, making them suitable for analyzing the intricate regulatory networks of m6A modifications. However, the "black box" nature of complex machine learning models poses a significant barrier to clinical adoption, as physicians require transparent, interpretable predictions to make informed treatment decisions [15]. SHapley Additive exPlanations (SHAP), a unified framework based on cooperative game theory, has emerged as widely adopted method for model interpretation by quantifying each feature's contribution to individual predictions [16]. SHAP analysis has demonstrated robust performance across diverse domains including transportation systems, autonomous vehicle security [17], maritime risk assessment [18], and critically, biomedical applications. In healthcare, SHAP has been successfully applied to predict sepsis outcomes [19], interpret deep learning models in radiology, and identify key genetic drivers in cancer prognosis.

The method's model-agnostic nature and consistency with human intuition make it particularly valuable for translating complex computational models into clinically actionable insights.

Previous studies have primarily focused on individual m6A regulators or utilized limited machine learning approaches for CRC prognosis prediction. To our knowledge, no study has comprehensively evaluated 20 different machine learning algorithms for m6A-based prognostic modeling in CRC, nor has any study systematically investigated the relationship between m6A-based risk stratification and immunotherapy response prediction.

In this study, we aimed to: (1) develop and validate a comprehensive computational framework incorporating 20 machine learning algorithms for m6A-based CRC prognosis prediction using m6A regulators; (2) identify key m6A genes contributing to prognosis using LASSO feature selection; (3) provide model interpretability through SHAP analysis; (4) investigate the relationship between m6A-based risk stratification and immune microenvironment characteristics; and (5) evaluate the predictive value for immunotherapy response using established computational biomarkers. This work provides a hypothesis-generating framework to guide future experimental validation and clinical trials. Our findings provide a robust framework for personalized risk assessment and treatment selection in CRC patients. The overall study design and analytical workflow are illustrated in Figure 1.

Materials and methods

Study design and data sources

This retrospective study followed the Transparent Reporting of a multivariable prediction model for Individual Prognosis Or Diagnosis (TRIPOD) guidelines. We utilized publicly available gene expression and clinical data from The Cancer Genome Atlas (TCGA) COAD/READ cohorts and Gene Expression Omnibus (GEO) datasets (GSE39582).

Data accessibility

TCGA COAD:[1]
TCGA READ:[2]
GEO GSE39582:[3]
IMvigor210:[4]

1 https://portal.gdc.cancer.gov/projects/TCGA-COAD
2 https://portal.gdc.cancer.gov/projects/TCGA-READ
3 https://www.ncbi.nlm.nih.gov/geo/query/acc.cgi?acc=GSE39582
4 http://research-pub.gene.com/IMvigor210CoreBiologies/

The combined dataset comprised 1,047 CRC patients with complete gene expression profiles and clinical follow-up data, representing one of the largest cohorts utilized for m6A-based prognostic modeling in CRC. This sample size substantially exceeds the minimum requirements for stable machine learning model development and provides adequate statistical power for our analyses.

The dataset was divided into training (n = 733, 70%) and validation (n = 314, 30%) cohorts using stratified random sampling to maintain balanced outcome distribution. Data from TCGA COAD/READ and GEO dataset GSE39582 were first combined and then randomly split, with the training cohort used for model development, feature selection, and hyperparameter optimization via 5-fold cross-validation, while the validation cohort served as an independent holdout set for unbiased performance evaluation. The inclusion/exclusion criteria and screening process are detailed in Figure 2. All data were obtained from public repositories with appropriate ethical approvals from the original studies, and this secondary analysis was exempt from additional institutional review board approval.

m6A regulators and data preprocessing

We identified 27 m6A regulators through systematic literature review and functional annotation databases, comprising 8 writers (METTL3, METTL14, WTAP, VIRMA, RBM15, RBM15B, ZC3H13, ZCCHC4), 4 erasers (FTO, ALKBH5, CBLL1, ELAVL1), and 15 readers (YTHDC1, YTHDC2, YTHDF1-3, HNRNPC, FMR1, LRPPRC, HNRNPA2B1, IGFBP1-3, IGF2BP1-3).

Gene expression data underwent sequential preprocessing: log2 transformation, quantile normalization using the preprocessCore R package, and Z-score standardization within each dataset. Multi-source data integration employed Combat batch correction (sva R package version 3.42.0). Quality control removed genes with >20% missing values, followed by k-nearest neighbors imputation (k = 5) using the VIM R package. Clinical variables included age at diagnosis, gender, tumor stage (AJCC 8th edition), tumor location, microsatellite instability status, and survival outcomes (overall survival time and vital status).

Feature selection and model development

LASSO regression with 10-fold cross-validation identified prognostically relevant m6A regulators using the glmnet R package (version 4.1-4). The optimal lambda parameter was selected using the one standard error rule (lambda.1se) with random seed set to 123 for reproducibility. Twenty machine learning algorithms were implemented in Python 3.8 using scikit-learn (version 1.0.2), XGBoost (version 1.6.1), LightGBM (version 3.3.2), and CatBoost (version 1.0.6). Hyperparameter optimization employed 5-fold stratified cross-

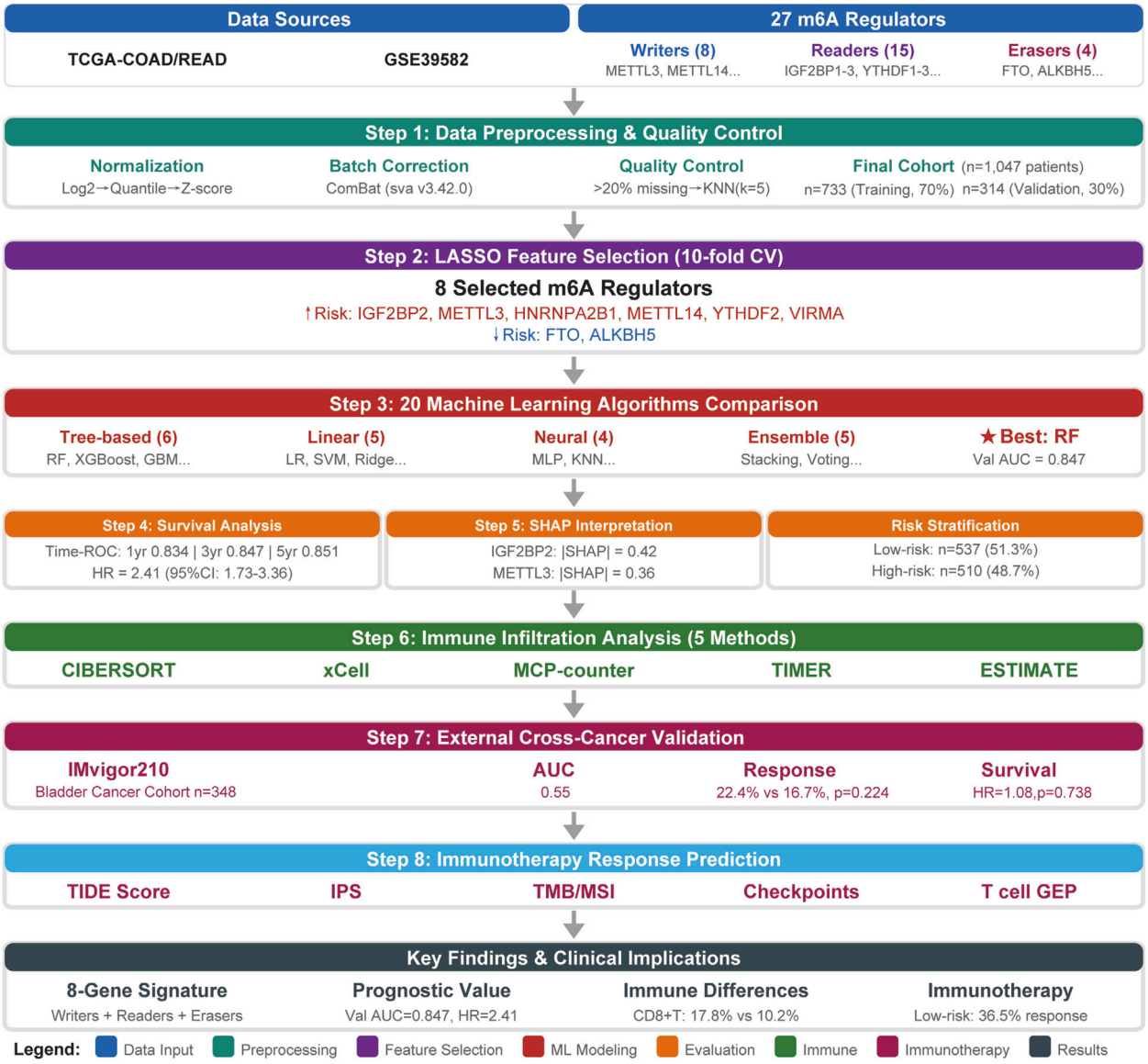

FIGURE 1
Comprehensive study workflow and analytical framework. The flowchart illustrates the complete analytical pipeline from data acquisition through clinical translation. (1) multi-cohort data acquisition (TCGA, GEO, validation cohorts); (2) data preprocessing and quality control; (3) feature selection via LASSO (27→8 m6A regulators); (4) machine learning model development with 20 algorithms; (5) model interpretation using SHAP analysis; (6) comprehensive validation across survival, immune microenvironment, and therapeutic response dimensions; (7) external validation in independent immunotherapy cohorts; and (8) development of clinical translation tools.

validation with grid search (random_state = 42). Class imbalance was addressed using SMOTE from the imbalanced-learn package (version 0.8.1) with random_state = 42.

Model evaluation and interpretability

Model performance was assessed using AUC-ROC as the primary metric, complemented by AUC-PR, accuracy, sensitivity, specificity, precision, F1-score, and Matthews correlation coefficient calculated using scikit-learn metrics. Model calibration was evaluated using Hosmer-Lemeshow test (scipy.stats) and calibration plots.

We selected SHAP (SHapley Additive exPlanations) as our primary interpretability framework based on several key advantages. First, SHAP is grounded in cooperative game theory with solid mathematical foundations, uniquely satisfying three desirable properties: local accuracy,

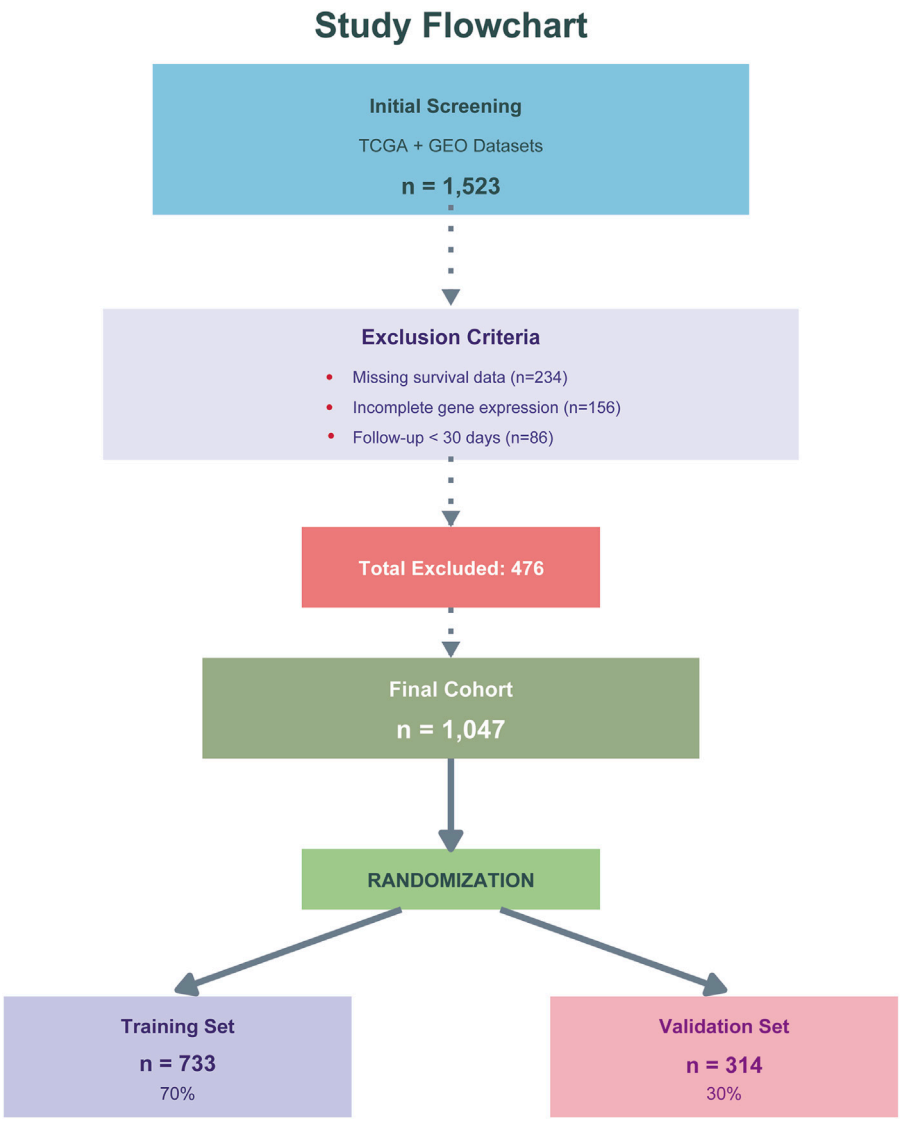

FIGURE 2
Study design and patient flow diagram. Flowchart showing patient selection from TCGA COAD/READ and GEO (GSE39582) databases. Of 1,523 initially screened patients, 476 were excluded due to missing survival data (n = 234), incomplete gene expression (n = 156), or follow-up <30 days (n = 86). The final cohort (n = 1,047) was randomly divided into training (n = 733, 70%) and validation (n = 314, 30%) sets.

missingness, and consistency [15, 16]. Second, SHAP provides both individual-level explanations and global interpretability through aggregated SHAP values, which is critical for personalized medicine. Third, TreeExplainer enables computationally efficient calculation of exact SHAP values for tree-based models in polynomial time, making it feasible for clinical deployment. Finally, SHAP has been extensively validated in healthcare applications and demonstrates high physician acceptance due to its alignment with clinical reasoning patterns.

SHAP framework (version 0.40.0) provided model interpretability through TreeExplainer for tree-based models and KernelExplainer for others, generating feature importance rankings, waterfall plots, and interaction analyses for the optimal model.

Risk stratification and survival analysis

Risk scores were calculated as weighted linear combinations of selected m6A regulators using LASSO coefficients: Risk Score = $\sum(\beta_i \times \text{Gene}_i)$. Optimal cutoffs were determined via maximally selected rank statistics using the maxstat R package with minprop = 0.1 and maxprop = 0.9. Survival analysis

employed Kaplan-Meier curves with log-rank tests (survival R package), Cox proportional hazards regression (coxph function), time-dependent ROC analysis using the timeROC R package for 1-, 3-, and 5-year predictions, concordance index (Harrell's C-index), and restricted mean survival time (survRM2 R package).

Immune microenvironment characterization

Tumor immune microenvironment was characterized using established algorithms: CIBERSORT (22 immune cell types) with LM22 signature matrix and 1,000 permutations, ESTIMATE algorithm for immune and stromal scores, MCP-counter for 10 immune and stromal populations, quanTIseq for immunotherapy-relevant cell types, and EPIC for immune and cancer cell fraction estimation. All analyses were performed using respective R packages with default parameters. Immune checkpoint genes (PDCD1, CD274, CTLA4, LAG3, HAVCR2, TIGIT) expression levels were extracted and log2-transformed. Immune phenotypes were classified as immune-inflamed ($CD8^+$ T cells > median and immune score > median), immune-excluded (moderate immune infiltration), or immune-desert (both $CD8^+$ T cells and immune score < median).

Immunotherapy response prediction

Immunotherapy response potential was evaluated using established computational methods. Tumor mutational burden (TMB) was calculated as the total number of nonsynonymous mutations per megabase from somatic mutation data. Microsatellite instability (MSI) status was determined using MSIsensor algorithm with default parameters (≥3.5 classified as MSI-high). Neoantigen load was predicted using NetMHCpan 4.0 for HLA class I binding prediction with binding affinity threshold <500 nM. TIDE score was calculated using the TIDE web portal[5]. Immunophenoscore (IPS) was calculated based on four categories of genes (effector cells, immunosuppressive cells, MHC molecules, and checkpoints) using established methodology. T cell-inflamed gene expression profile (GEP) was calculated using the 18-gene signature with weighted sum approach.

Cross-cancer validation

To evaluate the generalizability of our m6A risk model across different cancer types, we performed an independent cross-cancer validation using the IMvigor210 bladder cancer cohort. The IMvigor210 dataset comprises 348 patients with metastatic urothelial carcinoma who received atezolizumab (anti-PD-L1) immunotherapy, with available gene expression data, survival outcomes, and treatment response information. Gene expression data were log2-transformed and Z-score normalized. The eight m6A regulators from our CRC-derived model were mapped to the bladder cancer expression matrix. Risk scores were calculated using the fixed LASSO coefficients derived from the CRC training cohort, without any re-training. Patients were stratified into high-risk and low-risk groups based on the median risk score.

Statistical analysis

All statistical analyses were performed using R (version 4.2.0) and Python (version 3.8). Continuous variables were compared using Student's t-test or Mann-Whitney U test based on normality assessed by Shapiro-Wilk test. Categorical variables were compared using chi-square test or Fisher's exact test. Survival differences were assessed using log-rank test. Statistical significance was set at $P < 0.05$. Multiple testing correction was applied using Benjamini-Hochberg false discovery rate when appropriate. All computational analyses were performed with reproducible seeds to ensure result reproducibility.

Complete analysis code, detailed parameter settings, software environment specifications, and step-by-step workflow documentation are provided in the Supplementary Material (Supplementary Material S1, Supplementary Tables S1, S2). All analyses were performed with random seed = 42 to ensure reproducibility.

Results

Baseline characteristics

The study cohort comprised 1,047 CRC patients with a median age of 66 years [interquartile range (IQR): 57–74 years]. The training cohort (n = 733) included 392 males (53.5%) and 341 females (46.5%), while the validation cohort (n = 314) consisted of 171 males (54.5%) and 143 females (45.5%). Baseline characteristics were well-balanced between cohorts (Table 1).

Feature selection of m6A regulators for prognostic model construction

LASSO regression with 10-fold cross-validation was applied to identify prognostically relevant m6A regulators from the initial 27-gene panel. The optimal penalty parameter (λ* =

5 http://tide.dfci.harvard.edu/

TABLE 1 Baseline characteristics of study cohorts.

Characteristic	Training Set (n = 733)	Validation Set (n = 314)	P-value
Age, median (IQR)	66 (57–74)	67 (58–75)	0.542
Gender, n (%)			0.812
Male	392 (53.5%)	171 (54.5%)	
Female	341 (46.5%)	143 (45.5%)	
TNM Stage, n (%)			0.753
Stage I	127 (17.3%)	52 (16.6%)	
Stage II	276 (37.7%)	115 (36.6%)	
Stage III	243 (33.2%)	108 (34.4%)	
Stage IV	87 (11.9%)	39 (12.4%)	
Tumor Location, n (%)			0.834
Right colon	284 (38.7%)	125 (39.8%)	
Left colon	271 (37.0%)	112 (35.7%)	
Rectum	178 (24.3%)	77 (24.5%)	
MSI Status, n (%)			0.689
MSI-H	89 (12.1%)	41 (13.1%)	
MSS/MSI-L	644 (87.9%)	273 (86.9%)	
Adjuvant Chemotherapy, n (%)	423 (57.7%)	186 (59.2%)	0.674
Death Events, n (%)	200 (27.3%)	86 (27.4%)	0.973
Follow-up Time, median (IQR), months	32.5 (18.2–54.3)	31.8 (17.5–53.6)	0.721

0.0342) was determined using the minimum cross-validation error plus one standard error criterion (Figures 3A,B).

Eight m6A regulators were selected for prognostic model construction (Figure 3C). Six genes showed positive coefficients, indicating adverse prognostic associations: IGF2BP2 (0.412), METTL3 (0.356), HNRNPA2B1 (0.298), METTL14 (0.245), YTHDF2 (0.189), and VIRMA (0.167). Two genes exhibited negative coefficients, suggesting protective effects: FTO (−0.284) and ALKBH5 (−0.156).

The selected regulators encompassed all three functional categories of m6A machinery: writers (METTL3, METTL14, VIRMA), readers (IGF2BP2, HNRNPA2B1, YTHDF2), and erasers (FTO, ALKBH5), indicating comprehensive representation of the m6A regulatory system in prognostic prediction.

Machine learning model performance evaluation

Twenty machine learning algorithms were systematically evaluated using the eight-gene m6A signature for prognostic prediction. ROC curve analysis demonstrated that most models achieved satisfactory predictive performance, with distinct performance tiers emerging across the algorithmic spectrum (Figure 4A).

Performance stratification revealed that 2 models achieved excellent performance (AUC >0.84), 7 models demonstrated good performance (AUC 0.80–0.84), 6 models showed fair performance (AUC 0.75–0.80), and 5 models exhibited poor performance (AUC <0.75) (Figure 4B).

Among all evaluated algorithms, Random Forest (RF) demonstrated superior overall performance with the highest AUC of 0.887 (training) and 0.857 (validation), followed by XGBoost (XGB, AUC = 0.885/0.841) and Support Vector Machine (SVM, AUC = 0.874/0.851) (Figure 4C). The RF model exhibited excellent calibration (Hosmer-Lemeshow p = 0.342) and maintained robust performance across multiple evaluation metrics.

Comprehensive performance assessment using radar chart analysis confirmed RF's superiority across key metrics including AUC, accuracy, F1 score, sensitivity, and specificity, with XGB and SVM showing comparable but slightly inferior performance profiles (Figure 4D). Based on these results, the Random Forest model was selected as the optimal algorithm for subsequent prognostic model development and validation (Table 2, Figure 4).

SHAP analysis reveals key feature contributions to risk prediction

To understand which m6A regulators drove these predictions, we performed SHAP analysis to quantify individual feature contributions. SHAP analysis identified distinct contribution patterns of m6A regulators to risk prediction (Figure 5A). IGF2BP2 emerged as the most

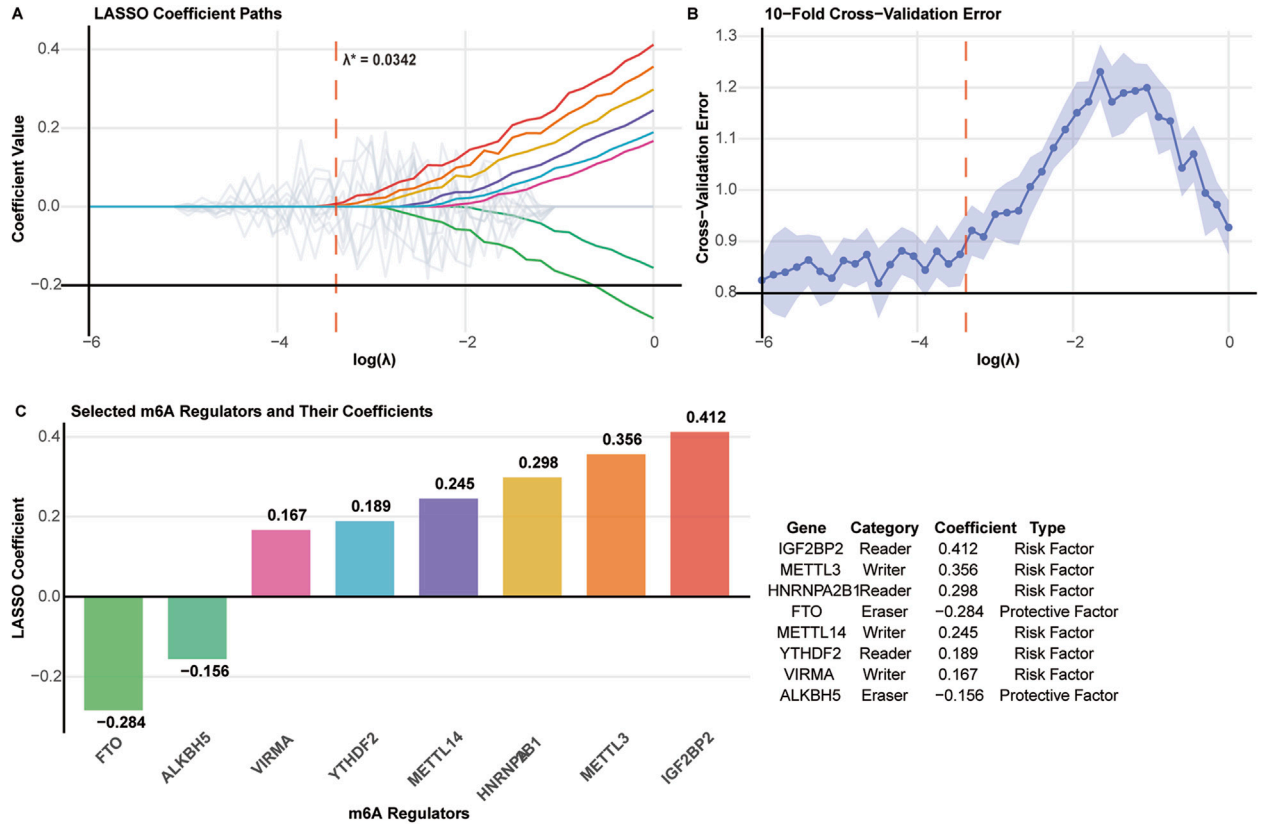

FIGURE 3
Feature selection of m6A regulators using LASSO regression. **(A)** LASSO coefficient paths for 27 m6A regulators. The optimal λ* = 0.0342 is indicated by the vertical dashed line. **(B)** Cross-validation error plot with minimum error and one standard error rule (λ.1se) marked. **(C)** Eight selected m6A regulators with their LASSO coefficients, functional categories, and prognostic types.

influential predictor (mean |SHAP| = 0.42), followed by METTL3 (0.36), FTO (0.28), and HNRNPA2B1 (0.25). YTHDF2, VIRMA, and ALKBH5 demonstrated lower but significant contributions to model performance.

Waterfall plot analysis revealed differential feature effects on risk prediction (Figure 5B). IGF2BP2 and METTL3 consistently contributed to increased mortality risk, while FTO exhibited protective effects with higher expression associated with better outcomes. Interaction analysis (Figure 5C) identified significant synergistic effects between METTL3 and IGF2BP2 (interaction strength: 0.23), moderate interactions between HNRNPA2B1 and YTHDF2 (0.18), and negative interactions between FTO and ALKBH5 (−0.21), suggesting cooperative protective mechanisms. Notably, METTL3 and IGF2BP2 showed synergistic interaction (interaction strength: 0.23), suggesting a cooperative mechanism: METTL3 deposits m6A marks that create high-affinity binding sites for IGF2BP2, thereby enhancing oncogenic mRNA stability.

The model stratified 1,047 patients into low-risk (n = 537, 51.3%) and high-risk (n = 510, 48.7%) groups with distinct mortality rates (15.7% vs. 27.3%). Kaplan-Meier analysis revealed significant survival differences (Figure 5D): median survival was not reached for low-risk patients versus 68.4 months for high-risk patients. Five-year survival rates were 78.2% and 54.3%, respectively (HR = 2.18, 95% CI: 1.54–3.09, $p < 0.001$).

Multivariate Cox regression confirmed independent prognostic significance after adjusting for age, TNM stage, and MSI status (HR = 2.18, 95% CI: 1.54–3.09, $p < 0.001$) (Figure 5E). Time-dependent ROC analysis demonstrated sustained predictive performance (Figure 5F): 1-year AUC = 0.834, 3-year AUC = 0.847, and 5-year AUC = 0.851, indicating excellent discriminative ability across different time horizons.

Enhanced immune infiltration characterizes low-risk tumor microenvironments

CIBERSORT analysis revealed distinct immune infiltration patterns between risk groups (Figure 6A). Low-risk tumors had

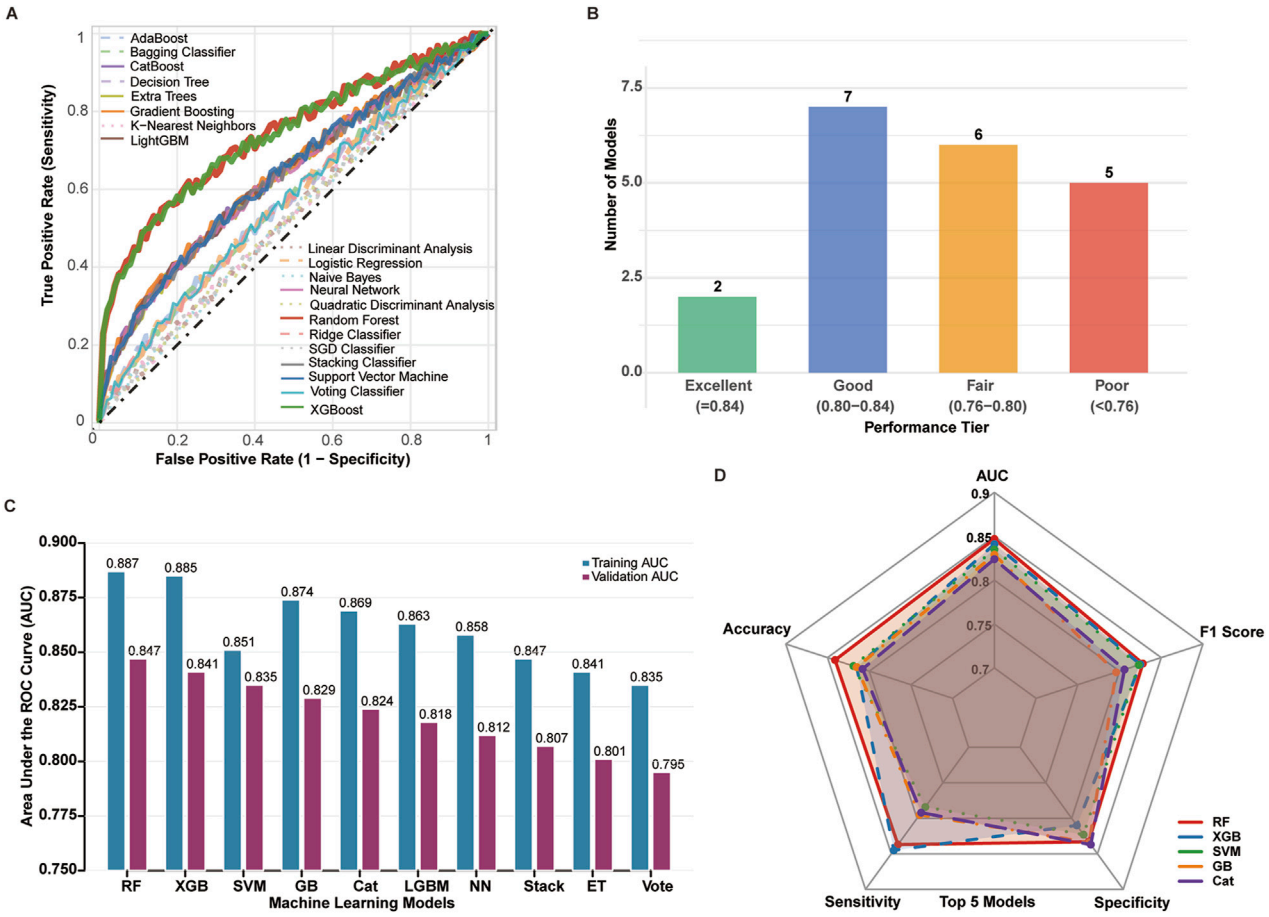

FIGURE 4
Comprehensive performance evaluation of 20 machine learning algorithms across training (n = 733) and validation (n = 314) cohorts. **(A)** ROC curves for all 20 algorithms evaluated on the independent validation cohort (TCGA + GEO, n = 314). Each curve represents a distinct algorithm, with Random Forest (red), XGBoost (blue), and SVM (green) highlighted. Diagonal dashed line indicates random classifier (AUC = 0.5). **(B)** Distribution of algorithm performance tiers in validation cohort. Models categorized as: Excellent (AUC >0.84, n = 2), Good (AUC 0.80–0.84, n = 7), Fair (AUC 0.75–0.80, n = 6), and Poor (AUC <0.75, n = 5). **(C)** Comparison of training (TCGA + GEO, n = 733, light bars) versus validation (n = 314, dark bars) AUC values for top 10 algorithms. Error bars represent 95% confidence intervals calculated by 1,000 bootstrap iterations. **(D)** Radar plot comparing six evaluation metrics (AUC, accuracy, F1-score, sensitivity, specificity, MCC) for top 5 algorithms in validation cohort. All performance metrics calculated on validation cohort using optimal hyperparameters determined through 5-fold cross-validation on training data.

higher $CD8^+$ T cells (17.2% vs. 10.1%, $p < 0.001$), activated $CD4^+$ memory T cells (15.3% vs. 9.2%, $p < 0.001$), and follicular helper T cells (6.8% vs. 3.1%, $p < 0.01$). High-risk tumors showed higher regulatory T cells (9.1% vs. 5.4%, $p < 0.001$) and M2 macrophages (12.7% vs. 8.2%, $p < 0.001$).

To further characterize immune cell interactions, correlation network analysis demonstrated markedly different organizational patterns between risk groups (Figure 6B). Low-risk tumors displayed positive correlations among effector immune populations, while high-risk tumors exhibited fragmented correlation networks. Radar plot analysis (Figure 6C) showed low-risk tumors had higher proportions of cytotoxic and helper populations.

ESTIMATE algorithm analysis showed low-risk tumors had higher immune scores (2,487 ± 642 vs. 1823 ± 521, $p < 0.001$) and lower stromal scores (1,124 ± 387 vs. 1,456 ± 429, $p < 0.001$) (Figure 6D). Heatmap analysis (Figure 6E) showed immune cell distributions across individual samples, with low-risk cases having higher levels of $CD8^+$ T cells, activated dendritic cells, and M1 macrophages.

Immunotherapy biomarker analysis reveals enhanced therapeutic potential in low-risk tumors

Comprehensive immunotherapy biomarker assessment demonstrated superior therapeutic indicators in low-risk patients (Figure 7A). Low-risk tumors exhibited significantly higher neoantigen burden (287 ± 124 vs. 198 ± 89, $p < 0.001$),

TABLE 2 Detailed performance comparison of 20 machine learning models.

Model	Training AUC	Validation AUC	Accuracy	Sensitivity	Specificity	F1-Score	MCC
Random Forest	0.895	0.847	0.819	0.826	0.815	0.783	0.621
XGBoost	0.887	0.841	0.812	0.814	0.811	0.776	0.609
Support Vector Machine	0.879	0.835	0.806	0.802	0.808	0.768	0.595
Gradient Boosting	0.872	0.829	0.799	0.791	0.804	0.759	0.582
CatBoost	0.868	0.824	0.794	0.784	0.801	0.753	0.573
LightGBM	0.861	0.818	0.787	0.779	0.793	0.745	0.561
Neural Network	0.854	0.812	0.781	0.767	0.789	0.737	0.549
Stacking Classifier	0.849	0.807	0.775	0.761	0.783	0.729	0.538
Extra Trees	0.843	0.801	0.769	0.755	0.777	0.721	0.526
Voting Classifier	0.837	0.795	0.763	0.749	0.771	0.713	0.514
AdaBoost	0.831	0.789	0.756	0.743	0.764	0.705	0.502
Logistic Regression	0.824	0.782	0.749	0.737	0.757	0.696	0.489
Bagging Classifier	0.818	0.776	0.743	0.731	0.751	0.688	0.477
Ridge Classifier	0.812	0.769	0.736	0.725	0.744	0.679	0.464
Decision Tree	0.805	0.762	0.729	0.719	0.737	0.671	0.451
Linear Discriminant Analysis	0.798	0.755	0.722	0.713	0.729	0.662	0.438
K-Nearest Neighbors	0.791	0.748	0.715	0.707	0.721	0.653	0.425
SGD Classifier	0.784	0.741	0.708	0.701	0.713	0.644	0.412
Quadratic Discriminant Analysis	0.777	0.734	0.701	0.695	0.705	0.635	0.399
Naive Bayes	0.769	0.726	0.693	0.689	0.696	0.626	0.385

tumor mutational burden (14.2 ± 7.3 vs. 9.7 ± 5.1 mutations/Mb, $p < 0.001$), and microsatellite instability-high frequency (18.6% vs. 9.8%, $p < 0.001$). T cell-inflamed gene expression profiles were elevated while TIDE scores indicated reduced immune dysfunction signatures. Immunophenoscore (IPS, a composite metric integrating effector cells, immunosuppressive cells, MHC molecules, and checkpoint expression) and T cell-inflamed gene expression profile (GEP, an 18-gene signature predicting anti-PD-1 response) scores were significantly elevated in low-risk patients.

Paradoxically, low-risk tumors demonstrated higher immune checkpoint expression across all major inhibitory receptors (Figures 7B,C): CTLA-4 (6.14 vs. 4.32), PD-1 (5.82 vs. 3.91), PD-L1 (4.27 vs. 2.87), LAG-3 (5.21 vs. 3.84), TIGIT (5.03 vs. 3.78), and TIM-3 (4.87 vs. 3.52) (all $p < 0.001$). This upregulation pattern suggests adaptive immune resistance mechanisms in response to enhanced T cell activation.

The m6A risk score demonstrated robust predictive capacity (AUC = 0.724) compared to PD-L1 expression (AUC = 0.598) and tumor mutational burden (AUC = 0.651) (Figure 7D). Integrated prediction analysis revealed 64.2% of low-risk patients as potential responders versus 35.8% of high-risk patients (OR: 2.24, 95% CI: 1.69–2.97, $p = 0.006$) (Figure 7E).

Cross-cancer validation in bladder cancer

The cross-cancer validation revealed limited transferability of the CRC-derived model to bladder cancer. Supplementary Figure S1A displays the model coefficients for eight m6A regulators applied to the bladder cancer cohort. Among these, IGF2BP2 (0.412), METTL3 (0.356), HNRNPA2B1 (0.298), METTL14 (0.245), YTHDF2 (0.189), and VIRMA (0.167) exhibited positive coefficients indicating risk-associated effects, while ALKBH5 (−0.156) and FTO (−0.284) showed negative coefficients suggesting protective roles. For immunotherapy response prediction, the model achieved an AUC of 0.550 (95% CI: 0.469–0.631), indicating near-random discrimination performance (Supplementary Figure S1B). Supplementary Figure S1C illustrates the distribution of risk scores across the bladder cancer cohort stratified by immunotherapy response status. The

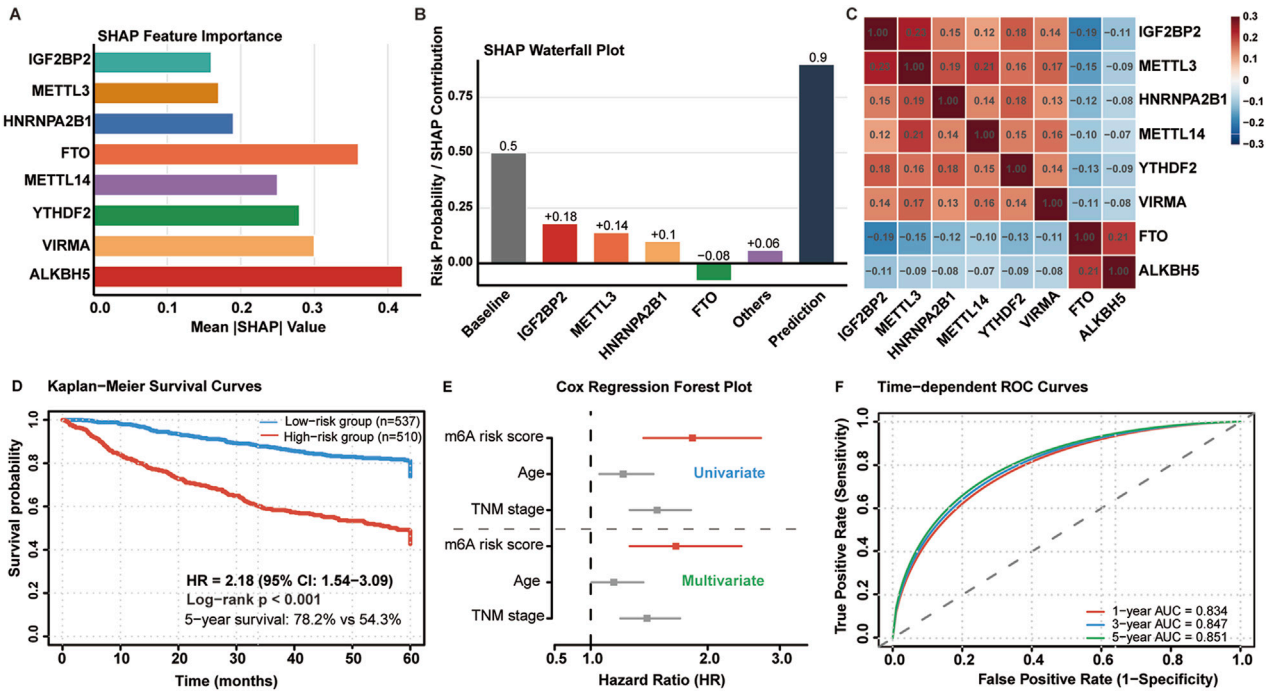

FIGURE 5
Model interpretation and survival analysis. **(A)** SHAP feature importance ranking for eight m6A regulators. **(B)** SHAP waterfall plot showing individual feature contributions to risk prediction. **(C)** SHAP interaction heatmap revealing feature dependencies. **(D)** Kaplan-Meier survival curves for risk groups (HR = 2.18, 95% CI: 1.54–3.09, p < 0.001). **(E)** Forest plot from multivariate Cox regression. **(F)** Time-dependent ROC curves at 1-, 3-, and 5-year intervals.

waterfall plot reveals substantial overlap between responders and non-responders across the entire risk score spectrum, with no clear separation pattern observed at the median cutoff. The response rates showed no significant difference between risk groups: 22.4% in the high-risk group versus 16.7% in the low-risk group (p = 0.224) (Supplementary Figure S1D). Survival analysis demonstrated no significant prognostic stratification (log-rank p = 0.738; HR = 1.08, 95% CI: 0.67–1.74) (Supplementary Figure S1E). These findings suggest that the prognostic and predictive value of m6A regulatory patterns exhibits substantial cancer-type specificity.

Differential pathway activation defines risk group molecular phenotypes

Gene Set Enrichment Analysis revealed distinct molecular programs between risk groups (Figure 8A). High-risk tumors demonstrated significant enrichment of cell cycle pathways: E2F targets (NES = 2.18), G2M checkpoint (NES = 1.94), MYC targets V1 (NES = 1.87), and DNA repair (NES = 1.76) (all FDR <0.005). Epithelial-mesenchymal transition (NES = 1.68) and mTORC1 signaling were additionally activated.

Conversely, low-risk tumors enriched immune surveillance pathways: interferon-gamma response (NES = −2.09), interferon-alpha response (NES = −1.96), allograft rejection (NES = −1.83), and inflammatory response (NES = −1.71) (all FDR <0.005). IL6-JAK-STAT3 signaling and complement pathways were concurrently activated.

Pathway interaction networks (Figure 8B) revealed tightly coordinated cell cycle modules in high-risk tumors, with E2F-MYC-cyclin regulatory circuits forming central hubs. Low-risk networks demonstrated interferon-centered immune activation, connecting antigen presentation and inflammatory response pathways.

Individual gene analysis confirmed pathway-level observations (Figure 8C). High-risk patients showed elevated proliferation markers (PCNA, CDC20, CCNE1) and reduced immune genes (TAP1, HLA-DRA, IRF1). Low-risk patients exhibited enhanced antigen presentation machinery (HLA-DRA, TAP1), immune checkpoints (CD274), and interferon-responsive elements (CXCL10, STAT1, IRF1).

Subgroup analysis confirms universal prognostic validity

Comprehensive subgroup analysis demonstrated consistent prognostic performance across all clinical stratifications with no

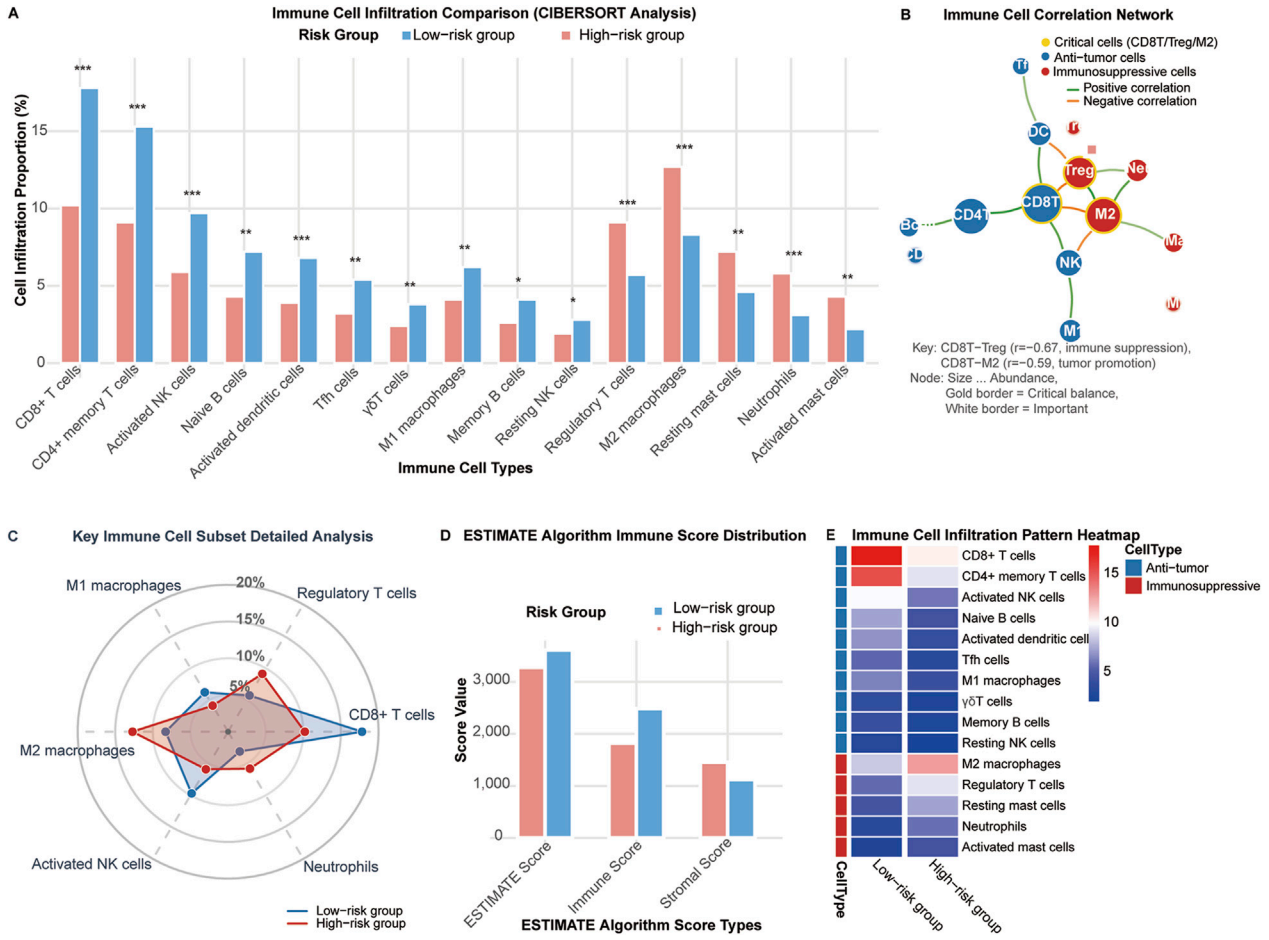

FIGURE 6
Differential immune cell infiltration between m6A risk groups across combined training and validation cohorts (n = 1,047). **(A)** CIBERSORT-estimated proportions of 22 immune cell types stratified by m6A risk group. Cell types ordered by absolute difference between groups. Statistical significance by Mann-Whitney U test with Benjamini-Hochberg correction: *p < 0.05, **p < 0.01, ***p < 0.001. **(B)** Correlation network analysis of immune cell populations within each risk group. Nodes represent cell types sized by mean proportion. Edges indicate significant correlations (|r| >0.3, p < 0.01). **(C)** Radar plot comparing key immune subsets between risk groups. **(D)** ESTIMATE algorithm-derived immune scores (left) and stromal scores (right) by risk group. **(E)** Heatmap of immune cell abundance across individual patient samples.

significant heterogeneity (interaction test: P = 0.384) (Figure 9). The m6A risk score maintained robust prognostic value independent of tumor stage: Stage I-II (HR = 2.31, 95% CI: 1.42–3.76, p < 0.001) and Stage III-IV (HR = 2.24, 95% CI: 1.51–3.32, p < 0.001).

Prognostic significance persisted across microsatellite instability status: MSS/MSI-L (HR = 2.19, 95% CI: 1.54–3.11, p < 0.001) and MSI-H (HR = 2.67, 95% CI: 1.23–5.81, p = 0.013). Age stratification revealed consistent performance in patients <65 years (HR = 2.48, 95% CI: 1.56–3.94, p < 0.001) and ≥65 years (HR = 2.15, 95% CI: 1.43–3.23, p < 0.001). Treatment context analysis showed maintained prognostic value regardless of chemotherapy administration, confirming broad clinical applicability across diverse patient populations and treatment scenarios.

Discussion

This study represents the most comprehensive machine learning analysis of m6A RNA methylation regulators for colorectal cancer prognosis. Our 8-gene signature effectively captures the core regulatory network of m6A modification, with IGF2BP2 emerging as the primary prognostic determinant. As an m6A reader that stabilizes oncogenic transcripts, IGF2BP2's prominence aligns with its established role in cancer progression, as demonstrated by Weng et al. through CRISPR-Cas9 knockout experiments showing that IGF2BP2 depletion inhibited CRC cell proliferation and tumor growth by reducing the stability of m6A-modified MYC transcripts [20]. Similarly, the secondary importance of METTL3, the primary m6A writer, reflects its multifaceted

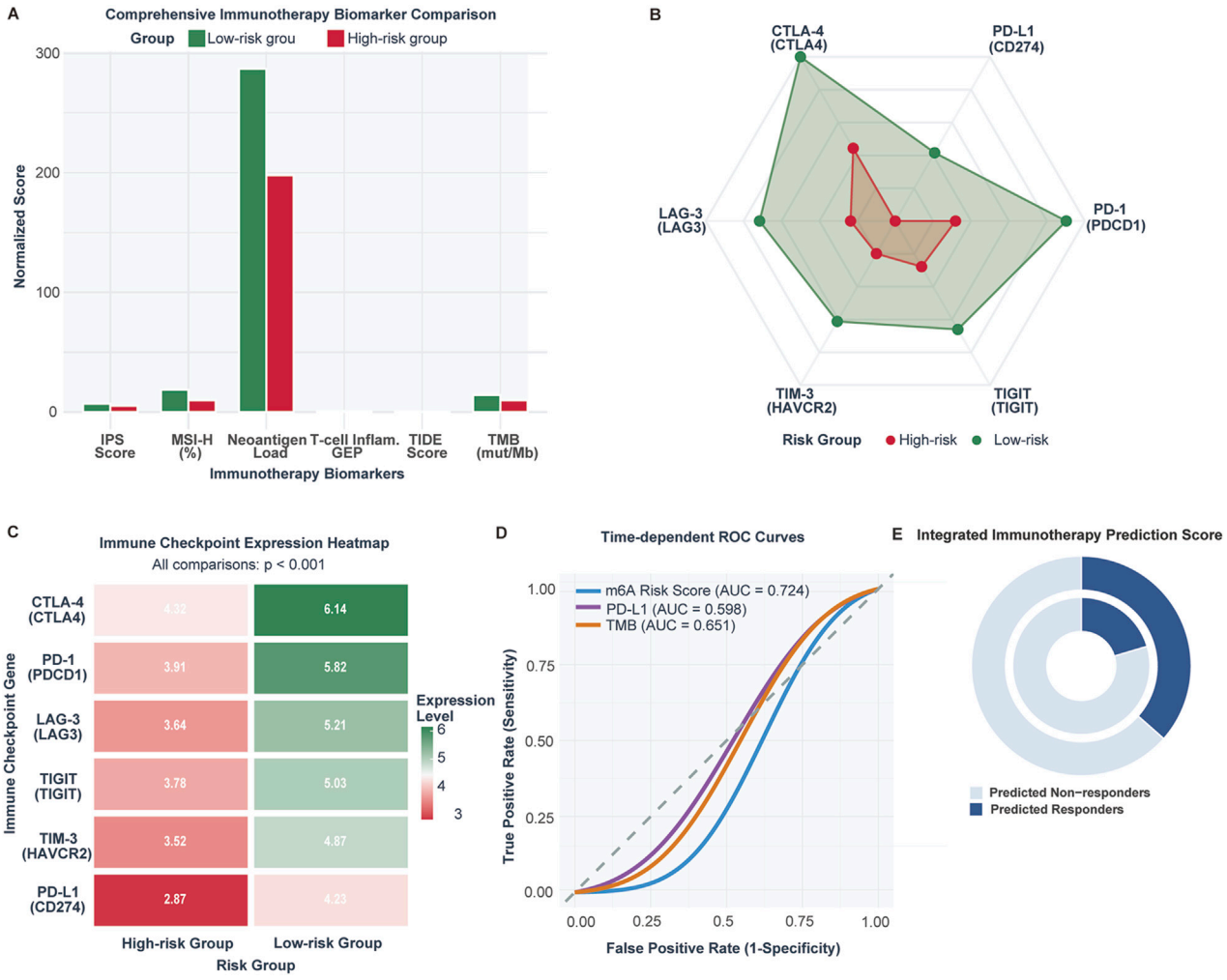

FIGURE 7
Immunotherapy response biomarkers and predictive capacity comparison between m6A risk groups (n = 1,047 CRC patients; validation cohort n = 298 IMvigor210 patients). **(A)** Comparison of established immunotherapy biomarkers between low-risk and high-risk CRC patients including TMB, neoantigen load, MSI-high frequency, TIDE score, Immunophenoscore (IPS), and T cell-inflamed GEP. **(B)** Radar plot of immune checkpoint expression levels in low-risk versus high-risk tumors. **(C)** Heatmap of checkpoint gene expression across individual samples. **(D)** ROC curve comparison for immunotherapy response prediction: m6A risk score (AUC = 0.698), PD-L1 (AUC = 0.621), TMB (AUC = 0.683). **(E)** Predicted immunotherapy response rates: 36.5% in low-risk vs. 20.3% in high-risk (OR = 2.24, p = 0.006).

oncogenic functions; Li et al. confirmed that METTL3 promotes CRC progression through m6A-dependent stabilization of glycolytic genes (HK2, GLUT1) [21] and tumor stemness maintenance through SOX2 stabilization [22]. Conversely, FTO's role in CRC appears context-dependent, with Chen et al. demonstrating that FTO regulates genomic stability through demethylation of DNA damage response genes, consistent with our finding of higher TMB in high-FTO patients [10, 23]. These experimental validations from independent laboratories provide strong biological plausibility for our computational findings.

SHAP analysis revealed how individual m6A regulators contribute to prognosis prediction. Notably, METTL3 and IGF2BP2 showed synergistic interaction (interaction strength: 0.23), suggesting a cooperative mechanism: METTL3 deposits m6A marks that create high-affinity binding sites for IGF2BP2, thereby enhancing oncogenic mRNA stability. This finding is supported by recent mechanistic studies showing that IGF2BP proteins preferentially bind to m6A-modified transcripts in specific sequence contexts. Conversely, the antagonistic interaction between FTO and ALKBH5 (interaction strength: −0.21) indicates functional redundancy in m6A demethylation, where the presence of either eraser can partially compensate for the loss of the other. This redundancy may explain why single-agent therapies targeting individual m6A erasers have shown limited efficacy.

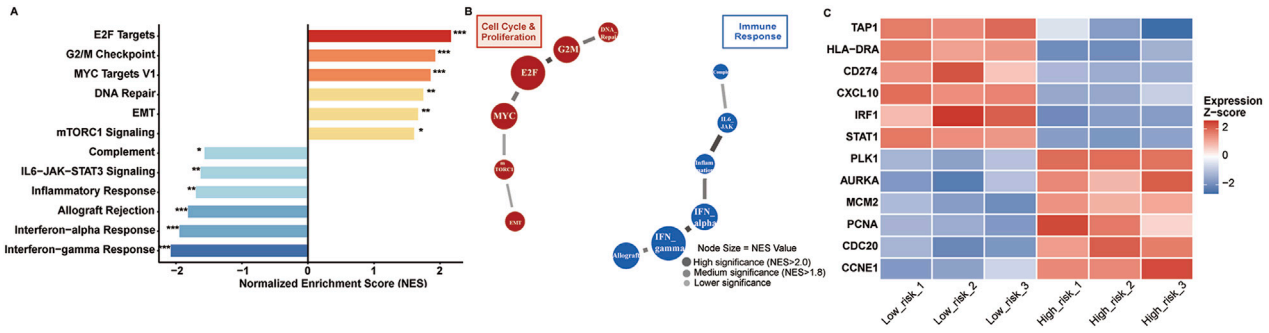

FIGURE 8
Pathway enrichment analysis. **(A)** GSEA results showing enriched pathways in high-risk (red) versus low-risk (blue) tumors. Significance: *p < 0.05, **p < 0.01, ***p < 0.001. **(B)** Pathway interaction network with node size indicating NES values. **(C)** Heatmap of representative genes from enriched pathways across risk groups. Expression values are Z-score normalized.

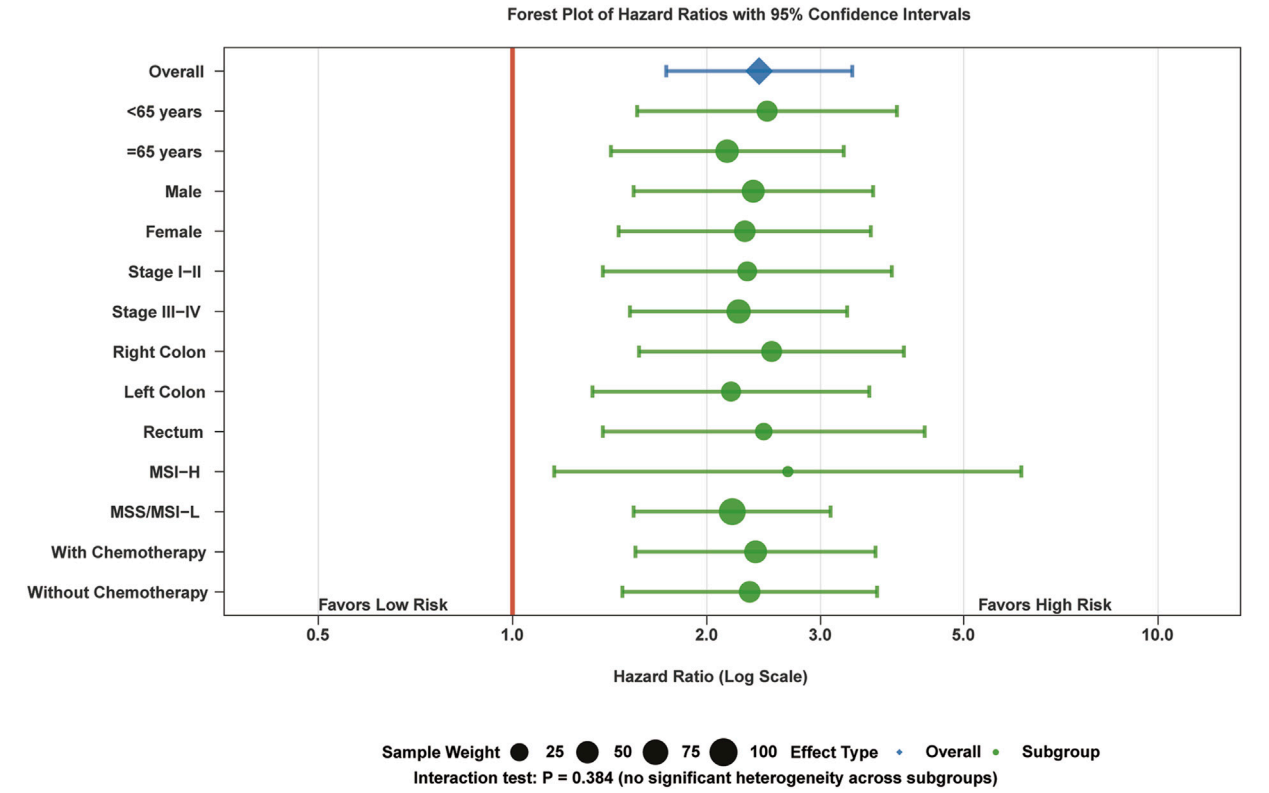

FIGURE 9
Subgroup analysis of prognostic validity. Forest plot showing hazard ratios with 95% confidence intervals across clinical subgroups. Circle size indicates sample weight. The m6A risk score maintained consistent prognostic significance across all subgroups (interaction test: P = 0.384). The vertical red line at HR = 1.0 represents no effect.

Our comprehensive immune profiling analysis revealed significant differences in $CD8^+$ T cell infiltration between low-risk (17.8%) and high-risk (10.2%) groups. This significant difference can be attributed to multiple mechanisms. First, m6A modifications significantly affect the stability and translation of chemokine mRNAs, particularly CXCL9 and CXCL10, which are critical for $CD8^+$ T cell recruitment to the tumor microenvironment. Second, m6A modifications regulate antigen presentation through YTHDF1-mediated control of lysosomal cathepsins

in dendritic cells, thereby influencing the cross-presentation of tumor antigens and subsequent $CD8^+$ T cell priming [24]. Furthermore, m6A modifications directly impact T cell exhaustion by regulating the expression of PD-1 and other exhaustion markers on tumor-infiltrating lymphocytes [25]. In summary, m6A modifications influence anti-tumor immunity through multiple interconnected mechanisms.

The increased regulatory T cell infiltration in high-risk patients (9.1% vs. 5.7%) supports the establishment of an immunosuppressive microenvironment mediated by m6A dysregulation. Tong et al. have demonstrated that METTL3 promotes Treg differentiation and function through m6A modification of FOXP3 mRNA, providing a mechanistic basis for the enhanced immunosuppression observed in high-risk tumors [26]. Collectively, these findings suggest that m6A modifications regulate immune mechanisms that determine tumor immune evasion and patient prognosis.

The strong association between m6A risk scores and immunotherapy biomarkers has immediate clinical implications. Low-risk patients showed higher tumor mutational burden (14.2 vs. 9.7 mutations/Mb), increased MSI-H frequency (18.6% vs. 9.8%), elevated neoantigen counts (287 vs. 198), and favorable TIDE scores (−0.42 vs. 0.31). These findings suggest that m6A-based risk stratification could guide immunotherapy selection, with the 1.8-fold higher predicted response rate in low-risk patients (36.5% vs. 20.3%) being clinically meaningful and comparable to established biomarkers like PD-L1 expression [27]. The relationship between m6A modification and immunotherapy response has been extensively studied. Bao et al. demonstrated that m^6A-reader YTHDF1 modulates tumor immune microenvironment and sensitizes CRC to PD-1 blockade through m^6A-dependent regulatory pathways [28]. Furthermore, recent studies have shown that factors affecting the tumor microenvironment, including epigenetic modifications, influence immune checkpoint inhibitor efficacy [29]. Bagchi et al. comprehensively reviewed mechanisms of immunotherapy resistance, highlighting epigenetic regulation as an emerging therapeutic target [30]. These findings support our observation that m6A-based risk stratification captures immune biology beyond conventional biomarkers like TMB and PD-L1 expression.

The limited performance of our CRC-derived m6A model in the IMvigor210 bladder cancer cohort (AUC = 0.550) highlights the cancer-type specificity of m6A regulatory mechanisms. Several factors may explain this finding: (1) the tumor microenvironment differs substantially between CRC, which occurs in an immunologically active mucosal environment with extensive microbiome interactions, and urothelial carcinoma, which develops in a distinct epithelial context with different immune cell compositions [31]; (2) the downstream targets of key regulators such as IGF2BP2 and METTL3 may vary based on tissue-specific transcriptome landscapes [32]; and (3) the treatment context differs significantly, as the IMvigor210 cohort received atezolizumab monotherapy whereas our CRC model was developed using patients who received diverse treatment regimens. These findings underscore the importance of cancer-type-specific biomarker development and suggest that m6A-based prognostic models should be developed and validated within specific cancer types rather than applied universally across malignancies.

Machine learning has transformed biomedical research and precision oncology. Recent studies have demonstrated ML's power in integrating multiomics data for cancer prediction. Lei et al. developed an immunogenic cell death-related gene expression signature that enabled robust molecular subtyping and prognostic stratification in CRC [33]. Wu et al. applied spatial transcriptomics with ML to map the immune landscape of colorectal liver metastases at single-cell resolution, revealing previously unrecognized immune-tumor interactions [34]. These advances underscore the potential of ML-driven biomarker discovery when combined with mechanistic biological insights. Our machine learning model addresses key implementation barriers. The 8-gene signature uses existing platforms like qRT-PCR and NanoString. SHAP analysis provides clear explanations for individual predictions. Risk stratification helps guide treatment decisions for adjuvant therapy and immunotherapy.

Our findings suggest several m6A-targeting strategies. METTL3 inhibitors like STM2457 show promise in preclinical studies [35]. For IGF2BP2, PROTACs offer a promising protein degradation approach, though specific degraders are still being developed [36]. FTO inhibitors targeting demethylase activity show therapeutic potential [37]. Combining m6A modulators with immunotherapy may create synergistic effects. Different risk groups have distinct pathway patterns that suggest additional targets. High-risk patients with activated E2F and MYC pathways may benefit from CDK4/6 inhibitors or BET bromodomain inhibitors [38, 39].

Our m6A-based framework demonstrates superior performance compared to existing prognostic models: Oncotype DX Colon (C-index ~0.68), ColoPrint (AUC ~0.66), and CMS classification. The superior performance (AUC = 0.847) reflects comprehensive algorithm evaluation, fundamental cellular process focus, and enhanced interpretability through SHAP analysis.

Several limitations should be acknowledged. First, as a retrospective computational study, our findings require prospective validation and experimental confirmation in independent cohorts before clinical implementation. Second, although SHAP analysis was employed to enhance model interpretability, we did not develop practical clinical decision-support tools; the construction of a nomogram or web-based calculator integrating clinical variables with the m6A risk score will be pursued in future studies to facilitate clinical

implementation. Third, our cohorts predominantly comprised Western populations, warranting validation in ethnically diverse groups. Fourth, the limited cross-cancer transferability (AUC = 0.550 in bladder cancer) indicates that our model may require cancer-type-specific recalibration. Fifth, bulk RNA sequencing data cannot capture intratumoral heterogeneity; integration with single-cell approaches would provide deeper insights. Sixth, immunotherapy response predictions were based on computational surrogates rather than real-world treatment outcomes. Finally, deep learning algorithms were excluded to prioritize clinical interpretability, though future studies with larger datasets could explore these approaches. Despite these limitations, our comprehensive framework provides a foundation for future experimental validation and clinical translation.

While our m6A-based framework demonstrates superior performance compared to existing prognostic models, the true measure of its clinical utility lies in its ability to address unmet needs in colorectal cancer management. The comprehensive evaluation of m6A regulation represents a fundamental advance in understanding cancer biology, but translating these insights into improved patient care remains the ultimate challenge.

Author contributions

FK performed the machine learning analysis, SHAP interpretation, and drafted the manuscript. JF conducted the immune infiltration analysis and pathway enrichment studies. HS performed data preprocessing and quality control. YZ contributed to the clinical data interpretation and statistical analysis. LJ-Z conceived and designed the study, supervised the research, and critically revised the manuscript. All authors contributed to the article and approved the submitted version.

Data availability

The datasets supporting the conclusions of this article are publicly available. TCGA COAD/READ data can be accessed at https://portal.gdc.cancer.gov/, and GEO validation data (GSE39582) are available at https://www.ncbi.nlm.nih.gov/geo/query/acc.cgi?acc=GSE39582. Complete analysis code, detailed parameter settings, software environment specifications, and step-by-step workflow documentation are provided in the Supplementary Materials (Supplementary Material S1, Supplementary Tables S1, S2). All analyses were performed with random seed = 42 to ensure reproducibility. The analysis code and processed data are available from the corresponding author upon reasonable request. All software packages and versions used are detailed in the Methods section.

Ethics statement

This study utilized publicly available, de-identified datasets from The Cancer Genome Atlas (TCGA), Gene Expression Omnibus (GEO), and the IMvigor210 clinical trial cohort (NCT02108652). All original studies obtained appropriate ethical approvals and informed consent, with the IMvigor210 trial conducted in accordance with Good Clinical Practice guidelines and the Declaration of Helsinki. As this research involved secondary analysis of anonymized data with no direct patient contact or identifiable information, it was deemed exempt from additional IRB approval per the Common Rule (45 CFR 46.104). All data were accessed through public repositories in accordance with their data use agreements.

Funding

The author(s) declared that financial support was received for this work and/or its publication. This work was supported by Project supported by the Affiliated Hospital of Xuzhou Medical University (2023ZL08).

Acknowledgements

We thank the TCGA Research Network and GEO contributors for making data publicly available.

Conflict of interest

The author(s) declared no potential conflicts of interest with respect to the research, authorship, and/or publication of this article.

Generative AI statement

The author(s) declared that generative AI was used in the creation of this manuscript. We declare that generative AI was used in the preparation of this manuscript. Specifically, we used AI-based reference management tools to assist with the formatting and organization of the bibliography according to journal guidelines. All references were manually verified for accuracy and completeness. No AI tools were used for generating, editing, or modifying the scientific content, data analysis, or interpretation of results in this manuscript. The authors have thoroughly reviewed all AI-assisted formatting and take full responsibility for the accuracy and integrity of all content in this publication.

Any alternative text (alt text) provided alongside figures in this article has been generated by Frontiers with the support of artificial intelligence and reasonable efforts have been made to ensure accuracy, including review by the authors wherever possible. If you identify any issues, please contact us.

Supplementary material

The Supplementary Material for this article can be found online at: https://www.ebm-journal.org/articles/10.3389/ebm.2025.10776/full#supplementary-material

References

1. Bray F, Laversanne M, Sung H, Ferlay J, Siegel RL, Soerjomataram I, et al. Global cancer statistics 2022: GLOBOCAN estimates of incidence and mortality worldwide for 36 cancers in 185 countries. *CA Cancer J Clin* (2024) **74**(3):229–63. doi:10.3322/caac.21834

2. Siegel RL, Miller KD, Wagle NS, Jemal A. Cancer statistics, 2023. *CA Cancer J Clin* (2023) **73**(1):17–48. doi:10.3322/caac.21763

3. Dominissini D, Moshitch-Moshkovitz S, Schwartz S, Salmon-Divon M, Ungar L, Osenberg S, et al. Topology of the human and mouse m6A RNA methylomes revealed by m6A-seq. *Nature* (2012) **485**(7397):201–6. doi:10.1038/nature11112

4. Roundtree IA, Evans ME, Pan T, He C. Dynamic RNA modifications in gene expression regulation. *Cell* (2017) **169**(7):1187–200. doi:10.1016/j.cell.2017.05.045

5. Yang Y, Hsu PJ, Chen YS, Yang YG. Dynamic transcriptomic m6A decoration: writers, erasers, readers and functions in RNA metabolism. *Cell Res* (2018) **28**(6): 616–24. doi:10.1038/s41422-018-0040-8

6. Liao JN, Ni WJ, Wu PH, Yang YD, Yang Y, Long W, et al. Switching from messenger RNAs to noncoding RNAs, METTL3 is a novel colorectal cancer diagnosis and treatment target. *World J Gastrointest Oncol* (2025) **17**(5):104076. doi:10.4251/wjgo.v17.i5.104076

7. Sun W, Su Y, Zhang Z. Characterizing m6A modification factors and their interactions in colorectal cancer: implications for tumor subtypes and clinical outcomes. *Discov Onc* (2024) **15**:457. doi:10.1007/s12672-024-01298-1

8. Wang J, Zhu M, Zhu J, Li J, Zhu X, Wang K, et al. HES1 promotes aerobic glycolysis and cancer progression of colorectal cancer via IGF2BP2-mediated GLUT1 m6A modification. *Cell Death Discov* (2023) **9**:411. doi:10.1038/s41420-023-01707-4

9. Zhou M, He J, Li Y, Jiang L, Ran J, Wang C, et al. N6-methyladenosine modification of REG1α facilitates colorectal cancer progression via β-catenin/MYC/LDHA axis mediated glycolytic reprogramming. *Cell Death Dis* (2023) **14**(8):557. doi:10.1038/s41419-023-06067-6

10. Qiao Y, Su M, Zhao H, Liu H, Wang C, Dai X, et al. Targeting FTO induces colorectal cancer ferroptotic cell death by decreasing SLC7A11/GPX4 expression. *J Exp Clin Cancer Res* (2024) **43**(1):108. doi:10.1186/s13046-024-03032-9

11. Sun Y, Gong W, Zhang S. METTL3 promotes colorectal cancer progression through activating JAK1/STAT3 signaling pathway. *Cell Death Dis* (2023) **14**(12): 827. doi:10.1038/s41419-023-06287-w

12. Su Q, Wang K, Liao R, Zhang H, Wang B. Dissecting the METTL3/STC2 axis in colorectal cancer: implications for drug resistance and metastasis. *Cell Biol Toxicol* (2025) **41**(1):100. doi:10.1007/s10565-025-10043-5

13. Wang F, Sun Z, Zhang Q, Yang H, Yang G, Yang Q, et al. Curdione induces ferroptosis mediated by m6A methylation via METTL14 and YTHDF2 in colorectal cancer. *Chin Med* (2023) **18**:122. doi:10.1186/s13020-023-00820-x

14. Rajkomar A, Dean J, Kohane I. Machine learning in medicine. *N Engl J Med* (2019) **380**(14):1347–58. doi:10.1056/NEJMra1814259

15. Lundberg SM, Lee SI. A unified approach to interpreting model predictions. *Adv Neural Inf Process Syst* (2017) **30**:4765–74.

16. Lundberg SM, Erion G, Chen H, DeGrave A, Prutkin JM, Nair B, et al. From local explanations to global understanding with explainable AI for trees. *Nat Mach Intell* (2020) **2**(1):56–67. doi:10.1038/s42256-019-0138-9

17. Saharuna Z, Ahmad T, Ijtihadie RM. SHAP-based feature selection and MASV-weighted SMOTE for enhanced attack detection in VANETs. *Vehicular Commun* (2025) **56**:100970. doi:10.1016/j.vehcom.2025.100970

18. Wu ZZ, Wang SZ, Li LY, Suo Y. An interpretable ship risk model based on machine learning and SHAP interpretation technique. *Ocean Eng* (2025) **335**: 121686. doi:10.1016/j.oceaneng.2025.121686

19. Lauritsen SM, Kristensen M, Olsen MV, Larsen MS, Lauritsen KM, Jørgensen MJ, et al. Explainable artificial intelligence model to predict acute critical illness from electronic health records. *Nat Commun* (2020) **11**(1):3852. doi:10.1038/s41467-020-17431-x

20. Huang H, Weng H, Sun W, Qin X, Shi H, Wu H, et al. Recognition of RNA N6-methyladenosine by IGF2BP proteins enhances mRNA stability and translation. *Nat Cell Biol* (2018) **20**(3):285–95. doi:10.1038/s41556-018-0045-z

21. Shen C, Sheng Y, Zhu AC, Ma Y, Xu P, Tian X, et al. m6A-dependent glycolysis enhances colorectal cancer progression. *Mol Cancer* (2020) **19**(1):72. doi:10.1186/s12943-020-01190-w

22. Li T, Hu PS, Zuo Z, Lin JF, Li X, Wu QN, et al. METTL3 facilitates tumor progression *via* an m6A-IGF2BP2-dependent mechanism in colorectal carcinoma. *Mol Cancer* (2019) **18**(1):112. doi:10.1186/s12943-019-1038-7

23. Ruan DY, Li T, Wang YN, Meng Q, Li Y, Yu K, et al. FTO downregulation mediated by hypoxia facilitates colorectal cancer metastasis. *Oncogene* (2021) **40**: 5168–81. doi:10.1038/s41388-021-01916-0

24. Han D, Liu J, Chen C, Dong L, Liu Y, Chang R, et al. Anti-tumour immunity controlled through mRNA m6A methylation and YTHDF1 in dendritic cells. *Nature* (2019) **566**(7743):270–4. doi:10.1038/s41586-019-0916-x

25. Yang S, Wei J, Cui YH, Park G, Shah P, Deng Y, et al. m6A mRNA demethylase FTO regulates melanoma tumorigenicity and response to anti-PD-1 blockade. *Nat Commun* (2019) **10**:2782. doi:10.1038/s41467-019-10669-0

26. Tong J, Cao G, Zhang T, Sefik E, Amezcua Vesely MC, Broughton JP, et al. m6A mRNA methylation sustains Treg suppressive functions. *Cell Res* (2018) **28**(2): 253–6. doi:10.1038/cr.2018.7

27. Doroshow DB, Bhalla S, Beasley MB, Sholl LM, Kerr KM, Gnjatic S, et al. PD-L1 as a biomarker of response to immune-checkpoint inhibitors. *Nat Rev Clin Oncol* (2021) **18**(6):345–62. doi:10.1038/s41571-021-00473-5

28. Bao Y, Zhai J, Chen H, Wong CC, Liang C, Ding Y, et al. Targeting m6A reader YTHDF1 augments antitumour immunity and boosts anti-PD-1 efficacy in colorectal cancer. *Gut* (2023) **72**(8):1497–509. doi:10.1136/gutjnl-2022-328845

29. Liang Y, Wang L, Ma P, Ju D, Zhao M, Shi Y. Enhancing anti-tumor immune responses through combination therapies: epigenetic drugs and immune checkpoint inhibitors. *Front Immunol* (2023) **14**:1308264. doi:10.3389/fimmu.2023.1308264

30. Bagchi S, Yuan R, Engleman EG. Immune checkpoint inhibitors for the treatment of cancer: clinical impact and mechanisms of response and resistance. *Annu Rev Pathol* (2021) **16**:223–49. doi:10.1146/annurev-pathol-042020-042741

31. Guo XW, Lei RE, Zhou QN, Zhang G, Hu BL, Liang YX. Tumor microenvironment characterization in colorectal cancer to identify prognostic and immunotherapy genes signature. *Sci Rep* (2021) **11**(1):15201. doi:10.1186/s12885-023-11277-4

32. Zhou Y, Huang Y, Dai T, Chen CW, Liu D. The role of insulin-like growth factor 2 mRNA-binding proteins (IGF2BPs) as m6A readers in cancer. *Int J Biol Sci* (2022) **18**(7):2744–58. doi:10.7150/ijbs.70458

33. Lei J, Fu J, Wang T, Guo Y, Gong M, Xia T, et al. Molecular subtype identification and prognosis stratification by an immunogenic cell death-related gene expression signature in colorectal cancer. *Expert Rev Anticancer Ther* (2024) **24**(7):635–47. doi:10.1080/14737140.2024.2320187

34. Wu Y, Yang S, Ma J, Chen Z, Song G, Rao D, et al. Spatiotemporal immune landscape of colorectal cancer liver metastasis at single-cell level. *Cancer Discov* (2022) **12**(1):134–53. doi:10.1158/2159-8290.CD-21-0316

35. Yankova E, Blackaby W, Albertella M, Rak J, De Braekeleer E, Tsagkogeorga G, et al. Small-molecule inhibition of METTL3 as a strategy against myeloid leukaemia. *Nature* (2021) **593**(7860):597–601. doi:10.1038/s41586-021-03536-w

36. Liu H, Qin S, Liu C, Gao Z, Jia S, Cao L, et al. Regulatory mechanisms and therapeutic implications of insulin-like growth factor 2 mRNA-binding proteins, the emerging crucial m6A regulators of tumors. *Theranostics* (2023) **13**(13):4247–65. doi:10.7150/thno.86528

37. Huang Y, Su R, Sheng Y, Dong L, Dong Z, Xu H, et al. Small-molecule targeting of oncogenic FTO demethylase in acute myeloid leukemia. *Cancer Cell* (2019) **35**(4):677–91.e10. doi:10.1016/j.ccell.2019.03.006

38. Schiavon G, Hrebien S, Garcia-Murillas I, Cutts RJ, Pearson A, Tarazona N, et al. Analysis of ESR1 mutation in circulating tumor DNA demonstrates evolution during therapy for metastatic breast cancer. *Sci Transl Med* (2015) **7**(313):313ra182. doi:10.1126/scitranslmed.aac7551

39. Delmore JE, Ber GC, Yang Z, Rahl PB, Shi J, Jacobs HM, et al. BET bromodomain inhibition as a therapeutic strategy to target c-Myc. *Cell* (2011) **146**(6):904–17. doi:10.1016/j.cell.2011.08.017

EBM Experimental Biology and Medicine

TYPE Original Research
PUBLISHED 13 February 2026
DOI 10.3389/ebm.2026.10745

OPEN ACCESS

*CORRESPONDENCE
Homood M. As Sobeai,
hassobeai@ksu.edu.sa

RECEIVED 09 July 2025
REVISED 11 January 2026
ACCEPTED 27 January 2026
PUBLISHED 13 February 2026

CITATION
Alhudaithi SS, Salih MHR, AlHusseini ZH, Almufadhili SM, Alelayani N, Bakheit AH, Alkahtani HM, Asiri HH, Alshamrani AA, Alhoshani AR, Alotaibi MR and As Sobeai HM (2026) Poliovirus receptor (PVR) expression as a predictor of relapse in colorectal cancer: bioinformatics and virtual screening. *Exp. Biol. Med.* 251:10745. doi: 10.3389/ebm.2026.10745

Poliovirus receptor (PVR) expression as a predictor of relapse in colorectal cancer: bioinformatics and virtual screening

Sulaiman S. Alhudaithi[1], Muhamed Hamza R. Salih[2], Zaid H. AlHusseini[2], Sarah M. Almufadhili[2], Noura Alelayani[2], Ahmed H. Bakheit[3], Hamad M. Alkahtani[3], Hanadi H. Asiri[3], Ali A. Alshamrani[2], Ali R. Alhoshani[2], Moureq R. Alotaibi[2] and Homood M. As Sobeai[2]*

[1]Department of Pharmaceutics, College of Pharmacy, King Saud University, Riyadh, Saudi Arabia, [2]Department of Pharmacology and Toxicology, College of Pharmacy, King Saud University, Riyadh, Saudi Arabia, [3]Department of Pharmaceutical Chemistry, College of Pharmacy, King Saud University, Riyadh, Saudi Arabia

Abstract

Colorectal cancer (CRC) is one of the most frequently diagnosed malignancies worldwide. Despite advancements in CRC treatment strategies in recent years, disease recurrence remains a major problem; relapsed patients have a poorer prognosis and higher mortality risk. Several factors have been associated with CRC relapse. However, the role of immune checkpoints in CRC recurrence remains elusive. In this work, we aimed to investigate immune checkpoint genes correlated with recurrence in CRC, evaluate their potential as prognostic biomarkers, and identify promising immune checkpoint inhibitors through molecular docking and molecular dynamics simulations. Clinical, genetic, and epigenetic data of relapsed and relapse-free CRC patients in the Cancer Genome Atlas were retrieved from the cBioportal database and evaluated. Subsequently, molecular docking and molecular dynamics simulations studies were conducted to identify suitable poliovirus receptor (*PVR*)/TIGIT binders. *PVR* is a ligand for TIGIT and competes with CD226. The crystal structure used for docking was obtained from the Protein Data Bank (PDB ID: 3UDW). Using this investigative approach, clinical parameters data revealed that among immune checkpoint genes, the *PVR* gene was significantly upregulated in relapsed patients. That upregulation was strongly correlated with diagnosis age, Aneuploidy, fraction genome alterations, and mutation count. Furthermore, free survival analysis showed that patients exhibiting elevated *PVR* levels were 2.16 times more likely to relapse than those with low *PVR* expression (p = 0.039). Virtual screening identified 106 natural compounds as potential binders at the *PVR*/TIGIT interface. Molecular docking and molecular dynamics simulations identified three binders that exhibit favorable interactions with *PVR*, with ZINC001848443492 emerging

as the most promising. The results underscore the potential role of *PVR* as a prognostic biomarker for relapse in CRC. Future studies, including TIGIT-PVR blockade assays and assessments of the impact of predicted PVR/TIGIT interface binders on T cell function, are necessary to validate this study's findings.

KEYWORDS

colorectal cancer, poliovirus receptor, prognostic biomarker, relapse, virtual screening

Impact statement

Poliovirus receptor (PVR) upregulation has been associated with relapse in many malignancies, such as lung and cervical cancer. However, the association between PVR overexpression and colorectal cancer (CRC) recurrence has not been established. This work demonstrates, for the first time, a correlation between PVR gene upregulation and relapse in CRC patients. It also reveals that certain clinical and genetic factors were associated with high PVR levels. Our study also showed that CRC patients overexpressing PVR were more susceptible to recurrence. In addition, three natural compound inhibitors that effectively target PVR were discovered through molecular docking and dynamics simulations, introducing promising therapeutic candidates for preventing relapse. These findings advance the field by unveiling the role of PVR in CRC recurrence and providing a rationale for the preclinical assessment of the identified immune checkpoint inhibitors, thereby opening new avenues for novel treatment strategies that could improve patient outcomes and reduce relapse rates.

Introduction

Colorectal cancer (CRC) is the third most prevalent malignancy and a leading cause of cancer-related deaths worldwide [1, 2]. The five-year survival rate of CRC in the localized stage is over 85%; however, in the distant stage of CRC, the rate drops dramatically to less than 20% [3]. CRC metastasizes primarily to the liver and, to a lesser extent, to the lungs, brain, and peritoneum [4]. Liver metastasis develops in 20%–50% of CRC patients, significantly deteriorating their prognosis and greatly contributing to the poor survival rates in the advanced stages [5, 6]. Current treatment strategies for CRC are diverse and tailored based on stage, cancer type, and patient genetic profile. Strategies include surgery (for resectable

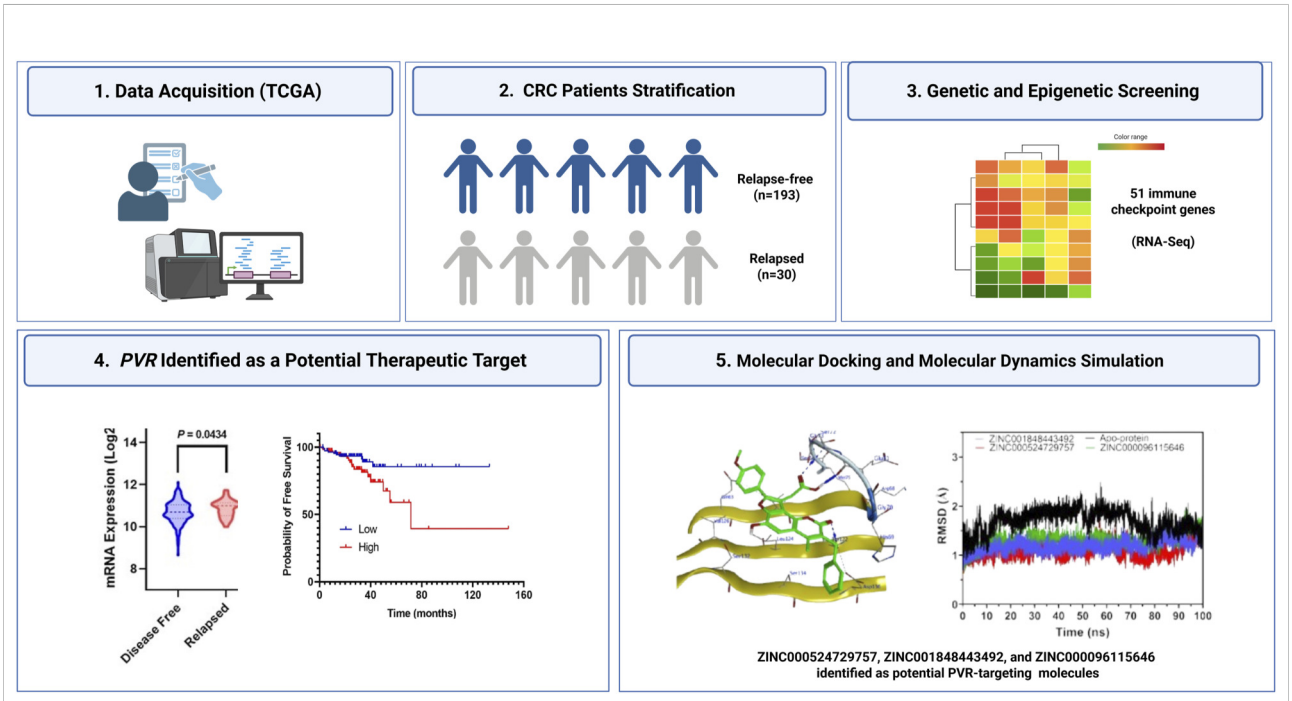

GRAPHICAL ABSTRACT

tumors), chemotherapy, targeted therapy, and immunotherapy [4, 7].

The tumor microenvironment (TME) in CRC is complex and besides cancer cells, it includes blood vessels, resident and infiltrating immune cells of myeloid origin such as dendritic cells (DC) and tumor-associated macrophages (TAMs), as well as lymphoid populations like T helper 1 (Th1), T regulatory (Treg), and $CD8^+$ cytotoxic T cells, along with natural killer (NK) cells. In addition, the TME encompasses stromal cells and their associated extracellular matrix (ECM) proteins [8]. Solid tumor evasion is mediated, in part, by tumor-induced cytotoxic T cell exhaustion through upregulation of co-inhibitory molecule expression [9]. ICIs have emerged as an efficacious immunotherapeutic strategy for CRC, and they act by targeting immune checkpoint axes such as PD-1-PD-L1/PD-L2 and CTLA4-CD80/CD86, reversing T cell exhaustion, and thereby improving the adaptive antitumor response [10]. Notably, tumors with microsatellite instability (MSI-H)/deficient mismatch repair (dMMR) respond better to PD-1/PD-L1 immunotherapy, compared to tumors with microsatellite stability (MSS) or proficient mismatch repair (pMMR)/low microsatellite-instability (MSI-L) [11]. However, ICIs targeting the PD-1-PD-L1 are effective only in tumors that highly express co-inhibitory molecules like PD-L1 [12, 13]. Further, resistance to those therapies has emerged as a formidable challenge in cancer treatment [14, 15]. Other immune checkpoints, such as LAG3, VISTA, and poliovirus receptor (PVR), have also been investigated as molecular targets for cancer therapy [16–18]. PVR is a pleiotropic protein, highly expressed in certain tumors. It acts as a ligand for T cell immunoreceptor with Ig and immunoreceptor tyrosine-based inhibitory motif, ITIM, domains (TIGIT), CD96, and to a lesser extent, CD226, and upon its interaction with the inhibitory receptors (CD96 and TIGIT), transmits a negative signal to T cell activation [19, 20]. *PVR* upregulation has been associated with tumor progression in lung, pancreatic, and cervical cancers [19, 21]. Moreover, in CRC, *PVR* is highly expressed, and its elevated levels are correlated with poor prognosis [19, 22]. To date, no FDA-approved ICI targets the PVR-TIGIT axis. Therefore, a therapeutic strategy targeting PVR/TIGIT represents an unmet clinical need in CRC, particularly in MSS and pMMR/MSI-L patients. Despite substantial advances in CRC treatment over the recent decades, the survival rates, particularly in advanced stages, remain poor and recurrence rates continue to be a significant concern.

Although many patients undergo curative tumor resection/treatment, the malignancy tends to recur within a few years in some populations [23]. Recurrence occurs in approximately 30% of patients with stage I-III and can reach up to 65% in those with stage IV [23]. Notably, CRC patients who experience recurrence within 5 years following surgery/treatment have a substantially increased risk of mortality [24]. Various clinical and molecular characteristics have been associated with CRC recurrence, including genetic and epigenetic factors, tumor features, and treatment-related factors [25–27]. The most frequently mutated genes in CRC patients are *APC*, *TP53*, *KRAS*, and *PIK3CA* [28], and these genes are also prevalent in CRC patients who developed tumor relapse after undergoing curative surgery. A study by Lan et al. demonstrated that *KRAS* gene is the most frequently mutated in both early and late recurrence of colon cancer, followed by mutations in *TP53*, *PIK3CA*, and *ABC*. In rectal cancer, however, *TP53* mutations were the most common among patients with recurrent CRC [27]. Epigenetic factors, including *CDKN2A* hypermethylation and methylation of *HPP1* and *HLTF* have also been widely linked to an elevated risk of recurrence and tumor progression in CRC patients [29]. Tumor-related factors associated with relapse in CRC include the cancer stage; with more advanced stages, the probability of recurrence increases [23, 24]. The likelihood of relapse is also influenced by the type of CRC malignancy; rectal cancer has higher recurrence rates compared to colon cancer [30].

The study aimed to unveil potential prognostic biomarkers and identify molecular targets that may be suitable for alternative therapeutic approaches in CRC. In this work, we analyzed data from CRC patients to identify novel genes associated with recurrence, with a particular emphasis on immune checkpoint genes. In addition, molecular docking and molecular dynamics simulations were conducted to identify potential binders/hits targeting the immune checkpoint axis of interest.

Materials and methods

Study design and data collection

Clinical, genetic, and epigenetic data related to CRC patients (n = 223) of the Cancer Genome Atlas (TCGA) [31] were extracted and analyzed using cBioProtal database (https://www.cbioportal.org/, 14 January 2023) [32–34]. Patients were allocated into two groups based on relapse status: patients who had undergone recurrence (n = 30) and relapse-free subjects (n = 193).

Clinical characteristics, genetic, and epigenetic factors assessment

Data of clinical characteristics (cancer type, stage, diagnosis age, weight, gender, and vital status), Genetic factors (mutations, aneuploidy, buffa hypoxia, and MSI MANTIS), and epigenetic factors (methylation status) from both relapsed and relapse-free CRC patients were examined statistically using Student's t-test (continuous variables) and Chi-square/Fisher's Exact test

(Categorical variables). Differences with *P* values <0.05 indicate statistical significance.

Immune checkpoint genes screening

To screen for upregulated immune checkpoint (ICP) genes among relapsed CRC patients relative to relapse-free patients, RNA-Sequencing (RNA-Seq) data were utilized. The expression of 51 genes including ICPs, human leukocyte antigen (HLA), cell adhesion, and co-stimulatory genes in all patients was assessed. Expression data were presented as normalized mean $\log_2$ values ±SEM. Log2 ratios of expression values in the replace-free group relative to the relapsed group were computed. Statistical significance between the two cohorts was assessed using Student's t-test. Differences of *P* value <0.05 were considered statistically significant.

Genetic alteration and methylation status examinations

To explore the mechanisms behind the upregulation of candidate ICP genes, both genetic factors (somatic mutations and putative copy number alterations [PCNA]) and epigenetic modifications (methylation status) were assessed. Somatic mutations analyzed included missense, inframe, and truncated mutations. PCNA analysis identified amplifications and deletions in the examined ICP genes. The $\log_2$ ratio was calculated. Statistical significance was assessed using a two-sided Fisher's Exact test, with a significance threshold of $p < 0.05$. For methylation status, the average methylation levels of the ICP genes were calculated for each cohort, and the $\log_2$ ratio was determined. A Student's t-test was used to evaluate the statistical significance of differences in methylation levels.

Correlation assessment between clinical parameters and the upregulated ICP gene expression

Clinical parameters, including cancer type, stage, diagnosis age, weight, gender, vital status, mutations count, aneuploidy score, buffa hypoxia score, MSI MANTIS, associated with the upregulated immune checkpoint genes in CRC patients were evaluated. Student's t-test was utilized to determine statistical significance ($p < 0.05$) between data from relapsed and relapse-free patients. Pearson correlation coefficient (r) was also used to identify the correlation between the stated factors and the upregulated immune checkpoint genes. The upregulated genes were further analyzed in relation to MSI status (MSI-high vs. MSI-low) to determine whether the observed associations were MSI-dependent.

Survival studies

To investigate the influence of upregulated immune checkpoint genes on overall and free survival, Kaplan–Meier survival analyses were employed and curves were generated based on RNA-Seq data for individual gene expressions. Patients were stratified into two cohorts based on the upregulated gene expression levels, with the mean expression value serving as the threshold: one group exhibited high gene expression (≥median), while the other showed low expression (<median). In addition, we evaluated the impact of MSI MANTIS score on disease-free survival to determine whether MSI status influences relapse risk. The statistical significance between these cohorts was assessed by calculating hazard ratios (HRs) and corresponding P-values from the Log-rank (Mantel-Cox) test. GraphPad Prism 9.1 was used for data analysis. The association between the candidate ICP genes and disease-free survival was validated in an independent large study, GSE39582, which comprises 566 primary colon tumors profiled by transcriptomic analysis using the Affymetrix Human Genome U133 Plus 2.0 Array [35]. The Kaplan–Meier figures of the validating dataset were generated using KM plotter [36].

Virtual screening

Ligand preparation

The crystal structure of the human TIGIT/PVR complex (PDB ID: 3UDW) [37] was retrieved from the Protein Data Bank (https://www.rcsb.org/). During preprocessing, all non-protein atoms, including water molecules, were excluded from the structure. The three-dimensional conformation of PVR (chain C of the 3UDW structure) was utilized for subsequent computational docking studies.

A dataset comprising 80,617 natural product compounds was obtained at no cost from the ZINC20database (https://zinc.docking.org/substances/subsets/natural-products/). Before screening, the compounds were processed using RDKit tools to remove salts and perform complex structural refinements, ensuring their chemical integrity and accurate representation of their molecular structure.

Protein preparation and site finder

For molecular docking studies, the three-dimensional conformation of PVR (chain C) from 3UDW, which represents the complex of human TIGIT bound to the PVR/CD155 D1 domain, was selected. The structure was solved by X-ray diffraction at a resolution of 2.90 Å, providing moderate-quality atomic coordinates suitable for molecular docking and interface analysis. The structure contains chains corresponding to TIGIT (chains A and B) and PVR/CD155 (chains C and D), forming the native receptor–ligand interface. Preprocessing involved the removal of all non-protein atoms, including

water molecules, followed by structure optimization using the Molecular Operating Environment (MOE 2024.06) software (Chemical Computing Group ULC, Montreal, QC, Canada).

The TGIT/PVR complex structure used for docking was obtained from the Protein Data Bank (PDB ID: 3UDW) and imported into MOE for preprocessing. Initial inspection of the structural integrity and stereochemistry was performed using the Structure Preparation tool (MOE | Compute | Prepare | Structure Preparation). The identified issues included incomplete termini, protonation inconsistencies, partial charge warnings, and minor steric clashes, as summarized in the MOE diagnostics (e.g., Termini = 3, HCount = 1, Charge = 1, Protonate3D = 112, Clash = 1). To resolve these issues, the Correct function within the Structure Preparation panel was applied to automatically address missing atoms, standardize residue names, repair incomplete termini, and resolve alternate locations.

Following structural correction, the Protonate 3D tool (MOE | Compute | Prepare | Protonate 3D) was used to assign the optimal protonation states of all ionizable residues at physiological pH, in accordance with local hydrogen-bonding patterns and electrostatic environments. Hydrogens were added, and the hydrogen-bonding network was optimized. Partial charges were then assigned using MOE's Partial Charges module to ensure proper electrostatic representation for subsequent docking and molecular mechanics refinement.

To relieve local steric clashes and minimize crystallographic strain while maintaining the overall native conformation, a tethered energy minimization step was performed. Minimization was carried out using the Energy Minimize panel with positional restraints applied to backbone heavy atoms to prevent major deviations from the crystal structure. This procedure corrected minor geometric distortions, resolved the detected steric clash, and yielded an energetically optimized receptor conformation suitable for docking. No missing loops were reported for 3UDW; therefore, loop reconstruction was not required. The binding site was identified by selecting residues within a 4.5 Å radius, guided by reference data, and the binding pocket for small molecule binders was determined using the Site Finder module in MOE.

Active sites in PVR

The identified β-sheets (Arg68–Leu64 and Phe125–Tyr121) and loop region (His69–Met75) in the PVR receptor represent critical structural elements involved in its interaction with the TIGIT protein. These regions form part of the binding interface and are positioned at the surface of the immunoglobulin-like domain, enabling direct contact with TIGIT. Therefore, the active sites of PVR responsible for binding are located within these specific loop and sheet regions. The TIGIT-PVR interface is formed through a highly complementary lock-and-key arrangement involving residues located primarily on the C′C″ loop and FG loop of the IgV domains of both molecules. The AX_6G motif (residues 76–83 in PVR and 66–74 in TIGIT), located on the C′C″ loop, forms a conserved hydrophobic pocket that functions as the "lock." This concave pocket is capped by the terminal residue of the motif and provides a structurally rigid anchoring site. Opposing this, the FG loop contributes the corresponding "key" element, defined by the T(F/Y)P motif—residues 127–129 in PVR and 112–114 in TIGIT—where an aromatic residue (F128 in PVR or Y113 in TIGIT) inserts directly into the hydrophobic lock pocket of the partner molecule. These complementary topologies on symmetric corners of the interface constitute the core of the TIGIT-PVR binding specificity.

Additional stabilizing contacts arise from the conserved (V/I)(S/T)Q motif—residues 61–63 in PVR and 54–56 in TIGIT—which further supports intermolecular packing across the β-sheet interface (A′GFCC′C″ region). Collectively, these residues bury approximately 1,600 $Å^2$ of surface area and define the dominant hotspots governing the TIGIT/PVR interaction. Notably, the same residues form the binding surface exploited by poliovirus, highlighting the functional significance and evolutionary conservation of this interaction site [37, 38].

Molecular docking of small molecules targeting PVR

The crystal structure of the TIGIT-PVR complex (PDB ID: 3UDW) was utilized as a structural basis for identifying small molecules capable of effectively disrupting TIGIT-PVR interactions. Key residues located at the interaction interface between TIGIT and PVR were recognized as critical for mediating their binding, and this region was chosen as the primary target for molecular docking. Ligand placement was performed using the Triangle Matcher method, and the initial poses were evaluated using the London dG scoring function, which estimates the binding free energy based on empirical terms and hydrophobic contact potentials. For each ligand, 30 preliminary poses were generated and ranked according to their London dG scores. The top poses were subsequently subjected to refinement using the Rigid Receptor protocol, during which the GBVI/WSA dG scoring function was applied to rescore and estimate the binding affinity. GBVI/WSA dG combines the Generalized Born Volume Integral implicit solvation model with Weighted Surface Area terms to provide a more accurate approximation of binding free energy during refinement. From this stage, 10 refined poses were retained. Together, the London dG (primary scoring) and GBVI/WSA dG (refinement scoring) functions provided a consensus evaluation of ligand binding, ensuring both rapid screening and more physically grounded energy estimation. As detailed in the screening protocol, the PVR domain underwent structural refinement, 3D protonation, and optimization. Additionally, energy minimization was applied to 80,617 natural product compounds from the ZINC database (https://zinc.docking.org/substances/subsets/natural-products) using MOE software. From those, 29,308 molecules

that complied with Lipinski's rule of five and had molecular weights between 250 and 550 Da were selected. Based on predicted binding modes, 166 compounds were identified to interact specifically with the PVR interface. Subsequent molecular docking was performed, and compounds showing docking scores (S-values) of ≤−10 were prioritized for further consideration.

Molecular dynamics simulation studies

Molecular dynamics (MD) simulations were conducted using Nanoscale Molecular Dynamics (NAMD) software (version 3.0) [39]. These simulations involved both the PVR protein alone and its complexes with the ligands ZINC000096115646, ZINC001848443492, and ZINC000524729757. Initial energy minimization of each ligand–PVR complex was carried out using the MOE software suite (version 2024.10). Complex configuration files were created through CHARMM-GUI [40], and the systems were parameterized using the CHARMM General Force Field (CGenFF) [41, 42]. The all-atom additive CHARMM36 force field was applied to construct the topologies of the ligand–PVR complexes. Solvation was performed using the TIP3P water model [43]. Following this, the system—comprising the complexes, ions, and solvent—underwent energy equilibration and a minimization step of 10,000 iterations. The MD simulation was then run for 1,000,000 steps, including a production phase of 125,000 steps. The equilibration period was set to 250 ps using the NVT ensemble, whereas production runs were carried out under the NPT ensemble for 100 ns. Finally, the stability of both the unbound PVR and its complexes was evaluated using VMD software [44] through the analysis of root-mean-square deviation (RMSD), root-mean-square fluctuation (RMSF), and radius of gyration (Rg) [45, 46].

Results

Clinical characteristics and genetic features of the enrolled patients

Patients' clinical data and their genetic profiles were collected and allocated into two groups based on relapse status: i) Relapse-free and ii) relapsed. Results (Table 1) showed that CRC type, stage, patient's age at diagnosis, and weight, were not associated with recurrence status. Interestingly, nearly twice as many male CRC patients experienced recurrence compared to females, while no gender differences were observed in relapse-free subjects. However, such differences were not statistically significant (p = 0.09). Vital status, on the other hand, was markedly correlated with relapse; the mortality rate in the relapsed group was significantly higher compared to the relapse-free cohort ($p < 0.0001$).

In addition, genetic data indicated that the average aneuploidy score was marginally higher in the relapsed cohort, whereas the mean MSI MANTIS score was slightly lower. No significant differences in the other genetic factors were observed between the two study groups (Table 1). Details of the clinical characteristics and the genetic factors are listed in Supplementary Table S1.

Immune checkpoints and other cell surface proteins gene expression in relapsed and relapse-free subjects

RNA-Seq data of the enrolled CRC patients were retrieved and analyzed to screen for ICIs associated with disease recurrence. Alterations in other genes, including HLA, cell adhesion, and co-stimulatory genes, were also investigated. Among the examined ICIs, *PVR* was significantly correlated with CRC recurrence (Figure 1C). *NECTIN2* (also known as Poliovirus receptor-related 2, PVRL2) expression is slightly elevated in patients who experienced recurrence compared to the relapse-free group ($p < 0.2$) (Figure 1D). In contrast, the expression of *CD274* (PD-L1) and *PDCD1* (PD-1) genes was relatively higher in relapse-free subjects (Supplementary Table S2). Nevertheless, except for *PVR*, no significant differences in immune checkpoint gene profiles were detected between the relapsed and the relapse-free group (Figure 1; Supplementary Table S2).

Antigenic peptides, including cancer antigens, are presented to CD4 + T cells in the context of HLA class II molecules, such mechanism is crucial for T cell activation and function [47]. CD4 + T helper 1 cells promote cytotoxic T cell differentiation and proliferation, thereby enhancing the adaptive antitumor response [47, 48]. RNA-Seq datasets revealed that *HLA-DRA* (a type of HLA class II molecules) gene expression was significantly lower in the relapsed CRC group relative to the relapse-free group (Supplementary Figure S1A). Other *HLA* class II types, including HLA-DRB1, HLA-DMA, HLA-DMB, HLA-DQA1, and HLA-DPA1, were also downregulated in the relapsed cohort relative to the relapse-free group; however, such differences did not reach statistical significance (p = 0.08–0.15) (Supplementary Figure S1). These data suggest that the antigen presentation capacity is reduced in the relapsed CRC patients compared to relapse-free subjects, which in turn may compromise the antitumorigenic functions of T cells.

Genetic alteration and methylation status of identified upregulated ICP genes

The genetic alteration, including somatic mutation and PCNA, and methylation status in the upregulated ICP genes, *PVR*, were examined. No significant somatic mutations or abnormal PCNA were detected in *PVR* in the relapsed group relative to the relapse-free group (Supplementary Table S3). In

TABLE 1 Clinical characteristics and genetic factors of relapse-free and relapsed CRC patients.

Factor	Relapse-free n = 193 (86.55%)	Relapsed n = 30 (13.45%)	*P* value
Cancer type	Rectal adenocarcinoma = 36 (69.43%) Colon adenocarcinoma = 134 (18.65%) Mucinous adenocarcinoma of the colon and Rectum = 23 (11.92%)	Rectal adenocarcinoma = 6 (76.67%) Colon adenocarcinoma = 23 (20.00%) Mucinous adenocarcinoma of the colon and rectum = 1 (3.33%)	0.369
Stage	I = 48 (24.87%) II = 81 (41.97%) III = 57 (29.53%) IV = 0 (0.00%) Unknown = 7 (3.63%)	I = 4 (13.33%) II = 15 (50.00%) III = 10 33.33%) IV = 0 (0.00%) Unknown = 1 (3.33%)	0.370
Diagnosis age (years)	64.97 ± 0.88	65.57 ± 2.47	0.809
Weight (kgs)	78.43 ± 2.23	82.03 ± 4.23	0.371
Gender	Female = 96 (49.74%) Male = 97 (50.26)	Female = 10 (33.33%) Male = 20 (66.67%)	0.094
Vital status	**Living = 184 (95.34%)** **Deceased = 9 (4.66%)**	**Living = 21 (70.00%)** **Deceased = 9 (30.00%)**	**<0.0001**
MSI MANTIS score	0.42 ± 0.02	0.39 ± 0.04	0.050
Mutation count	Positive = 5 (4.59%) Negative = 91 (83.49%) Unknown = 13 (11.93%)	Positive = 7 (7.86%) Negative = 67 (75.28%) Unknown = 15 (16.85%)	0.356
Aneuploidy score	11.35 ± 0.58	14.43 ± 1.56	0.055
Buffa hypoxia score	18.77 ± 1.34	19.29 ± 3.34	0.879
Fraction genome alteration	0.23 ± 0.01	0.27 ± 0.03	0.225

Values are mean ± SE or frequencies, as appropriate. P < 0.05 was considered statistically significant. Significant values are in bold.

addition, hypermethylation of *PVR* was observed in the relapsed group compared to the disease-free cohort; however, the comparison did not result in statistical significance ($p = 0.127$, Supplementary Table S4). It is worth mentioning that *APC (70.2%), TP53 (55.1%), TNN (49.5%), KRAS (41.9%), and PIK3CA (31.8%)*, were the most frequently mutated genes in our cohort, with no significant difference between the relapse-free and relapsed groups (Supplementary Table S5).

Correlation between clinical parameters and the upregulated immune checkpoint gene expression

The potential correlation between *PVR* gene expression and CRC patients' clinical and genetic factors was assessed. Amongst all the evaluated clinical factors, the patient's age at diagnosis was the only factor strongly correlated with elevated *PVR* gene expression (Table 2), *PVR* upregulation was more common in younger patients than in older subjects. Genetic data, on the other hand, revealed several factors associated with upregulated *PVR* levels (Table 2). Aneuploidy and fraction genome alterations were positively correlated with *PVR* upregulation ($p = 0.017$ and $p = 0.005$, respectively), whereas mutation count was negatively correlated ($p = 0.04$). These data indicate that *PVR* elevation is somewhat associated with the "nature" of genetic alteration rather than the "number" of mutations. MSI status (high vs. low) did not significantly influence *PVR* expression (Supplementary Figure S2A). No significant correlations were detected between *PVR* increased gene expression and any of the other evaluated factors, including cancer type, stage, weight, gender, vital status, and buffa hypoxia score (Table 2).

Survival analysis

Considering the correlation between *PVR* gene overexpression and recurrence identified in this study, and the established association between relapse and survival outcomes observed both here and in previous work [24], we were prompted to further elucidate the association between *PVR* and relapse in CRC and also explore the relationship between *PVR* gene expression and survival outcomes. Thus, both overall and free survival analyses were performed and the survival data from the high-*PVR* patients' group were compared with low-*PVR* patients' group data. Kaplan–Meier analysis showed that overall survival was not significantly impacted by *PVR* genetic levels in CRC patients (Supplementary Figure S3). However, disease-free survival investigation showed that patients with tumors expressing high *PVR* had higher relapse rates (Hazard ratio: 2.016 $P = 0.039$)

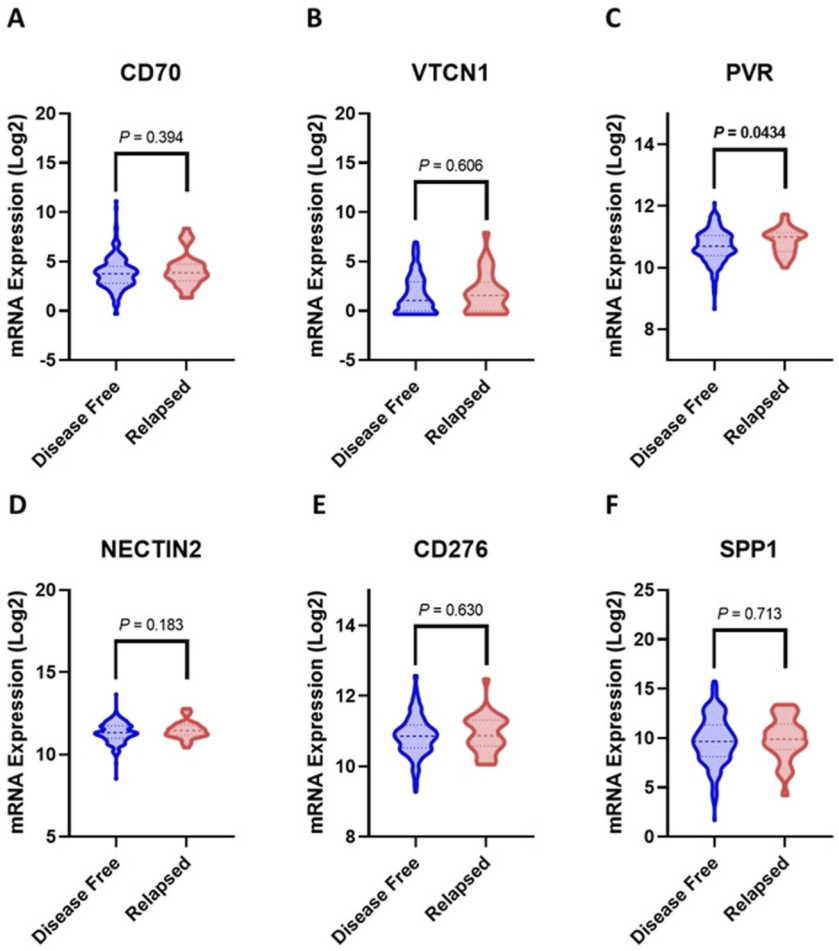

FIGURE 1
Upregulated Immune checkpoint genes in relapsed CRC patients relative to disease-free. **(A)** *CD70*, **(B)** *VTCN1*, **(C)** *PVR*, **(D)** *NECTIN2*, **(E)** *CD276*, **(F)** *SPP1*. The mean and 95% confidence interval values are represented by bold and light intermittent lines, respectively. Statistical significance was determined by Student's t-test.

(Figure 2). These results were validated in the GSE39582 cohort (Supplementary Figure S4). *PVR* expression was significantly associated with disease-free survival, with patients exhibiting high *PVR* expression showing a higher risk of relapse compared with those with low *PVR* expression (HR = 1.46, 95% CI: 1.08–1.97; p = 0.013). These results independently support our findings and further substantiate the prognostic relevance of *PVR* for relapse risk. In addition, we conducted survival analyses stratified by MSI status. Patients were classified as MSI-high or MSI-low, and no significant difference in disease-free survival was observed between the two groups (Supplementary Figure S2B).

Docking of compounds 1–166 with PVR

The molecular docking analysis identified three natural product ligands—ZINC000096115646, ZINC001848443492, and ZINC000524729757—that display favourable binding interactions with the PVR receptor at its TIGIT-binding interface (Figure 3).

ZINC000096115646 forms multiple hydrogen bonds with residues GLU71, SER72, and THR122 in chain C of PVR, contributing to a cumulative binding energy (E) of −1.6 kcal/mol and an S-value of −11.02 kcal/mol. Notably, its hydrogen bond with GLU71 (2.82 Å) and a π-H interaction with LEU124 (4.02 Å) suggest a stable and well-oriented binding pose within the active site region (Figure 3A; Table 3).

ZINC001848443492 also engages key residues at the PVR–TIGIT interface, including GLU71, THR122, and SER72. A strong hydrogen donor interaction with GLU71 (2.73 Å) is associated with a significant interaction energy of −6.5 kcal/mol, which likely contributes substantially to its overall docking score of −10.56 kcal/mol (Figure 3B; Table 3).

ZINC000524729757 forms a hydrogen bond with SER134 and a π-H interaction with THR122. Although the individual interaction energies are modest

TABLE 2 Clinical and genetic factors and their correlation with PVR upregulation.

Factor	Pearson correlation coefficient (r)	*P* value
Cancer type	-	0.063
Stage	-	0.083
Diagnosis age	**−0.133**	**0.049**
Weight	0.107	0.267
Gender	-	0.636
Vital status	-	0.99
Mutation count	**−0.147**	**0.040**
Aneuploidy score	**0.161**	**0.017**
Buffa hypoxia score	0.084	0.349
Fraction genome alteration	**0.191**	**0.005**
MSI MANTIS score	−0.126	0.071

P < 0.05 was considered statistically significant using Pearson correlation coefficient. Significant values are in bold.

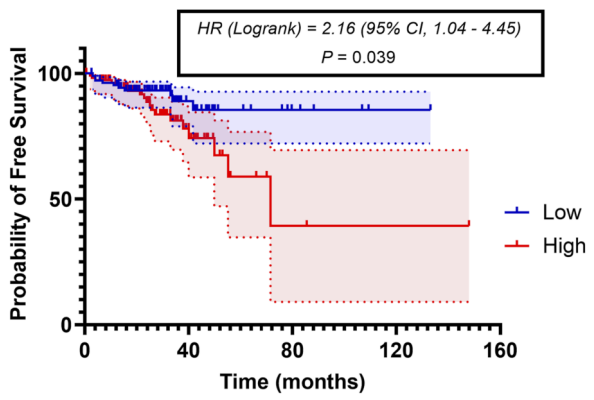

FIGURE 2
Free survival curves for patients with low *PVR* expression (blue) and patients with high *PVR* expression (red). The median gene expression value was used as the cut-off to stratify patients into the two cohorts, high and low. Hazard ratio (HR) and *p*-value were calculated using the log-rank test. The shaded area around each curve represents 95% confidence interval.

(−1.4 and −0.9 kcal/mol, respectively), the overall binding remains favorable with an S-value of −10.26 kcal/mol. These interactions indicate a stable association near the receptor's binding interface (Figure 3C; Table 3).

Molecular dynamics simulation

The Molecular Dynamics (MD) simulation results, as depicted in the provided Root Mean Square Deviation (RMSD) plot over a 100 ns timeframe (Figure 4A), compare the structural stability of the poliovirus receptor (PVR/CD155) in its apo form with its complexes bound to three compounds: ZINC000096115646, ZINC001848443492, and ZINC000524729757. The RMSD values, with means of 1.58 Å for the apo-protein, 1.50 Å for ZINC000096115646, 1.32 Å for ZINC001848443492, and 1.20 Å for ZINC000524729757, indicate that ligand binding generally stabilizes PVR, with ZINC000524729757 showing the lowest mean RMSD, suggesting the strongest stabilizing effect. The standard deviations (0.137 Å for apo-protein, 0.149 Å for ZINC000096115646, 0.117 Å for ZINC001848443492, and 0.178 Å for ZINC000524729757) reveal varying dynamic behaviors, with ZINC001848443492 exhibiting the most consistent structure (lowest STD) and ZINC000524729757 showing the greatest fluctuations, potentially due to a dynamic or less rigid binding mode.

RMSF plot in Figure 4B illustrates the flexibility of the poliovirus receptor (PVR/CD155) residues over a 100 ns MD simulation, comparing the apo-protein form with complexes bound to ZINC000524729757 (red), ZINC001848443492 (blue), and ZINC000096115646 (green). The RMSF values, which indicate per-residue fluctuations, show that the apo-protein (black) exhibits a baseline level of flexibility, while the ligand-bound states display varying degrees of stabilization or increased motion depending on the compound. ZINC000524729757 shows the highest peaks (reaching ~2 Å), suggesting significant local flexibility, possibly due to dynamic interactions or partial destabilization of certain regions, whereas ZINC001848443492 and ZINC000096115646 exhibit more moderate fluctuations (peaking around 1–1.5 Å), indicating better constraint of PVR's structure.

The MD simulation results for the radius of gyration (Rg) in Figure 4C and Solvent Accessible Surface Area (SASA) in Figure 4D over a 100 ns timeframe provide insights into the compactness and surface exposure of the poliovirus receptor

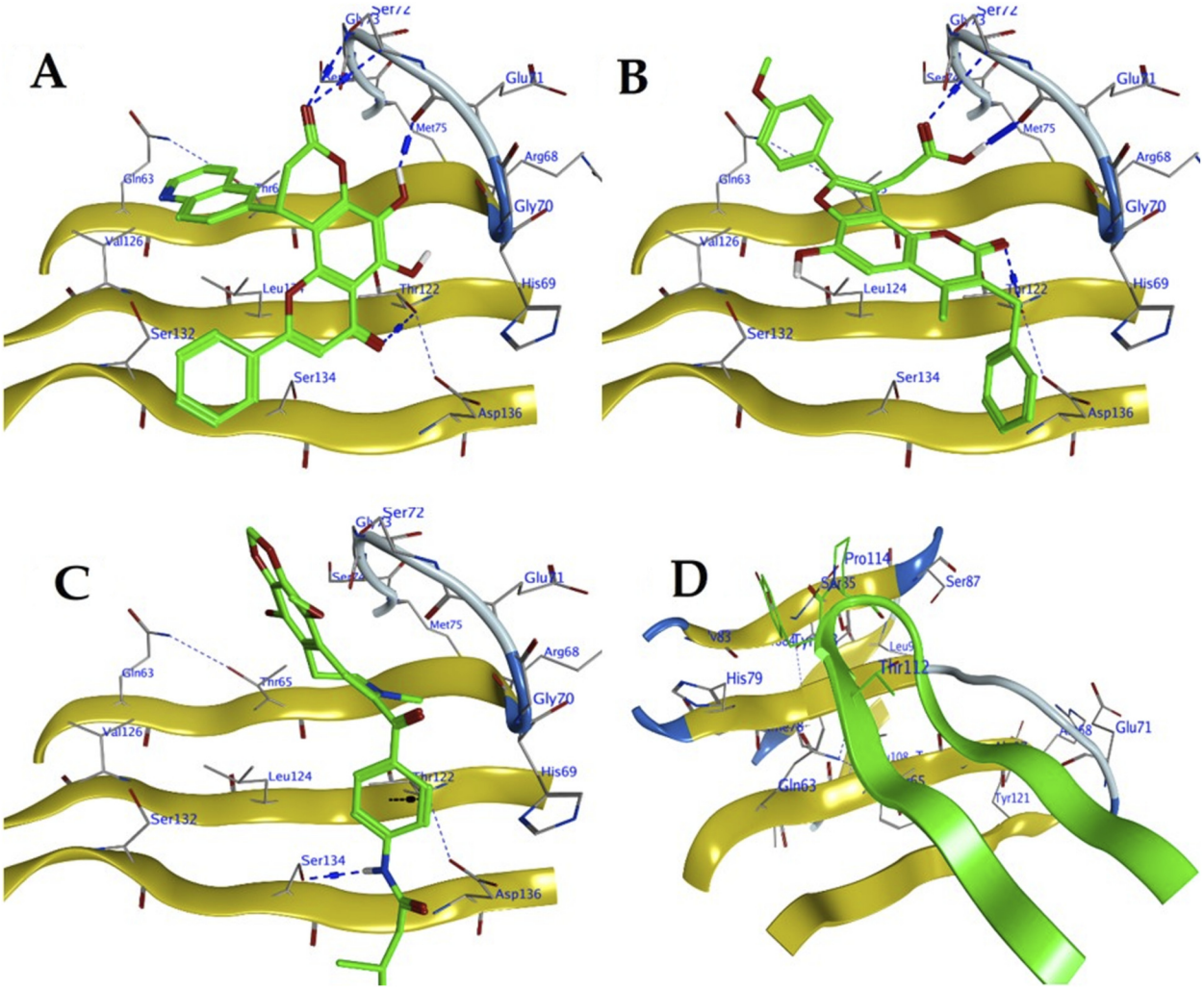

FIGURE 3
Molecular docking representations of the active site of the poliovirus receptor (PVR/CD155) interacting with **(A)** ZINC000096115646, **(B)** ZINC001848443492, **(C)** ZINC000524729757, and **(D)** TIGIT, highlighting key binding residues and interactions. The yellow ribbons depict the PVR structure, while green structures represent the ligands or TIGIT, with specific amino acid residues (e.g., Ser132, Glu70, His187) and hydrogen bonds (blue dashed lines) illustrating the binding interfaces.

(PVR/CD155) in its apo form and when bound to ZINC000524729757, ZINC001848443492, and ZINC000096115646. The Rg values, which measure the protein's compactness, show mean values ranging from 14.482 Å (ZINC001848443492) to 14.566 Å (ZINC000096115646), with the apo-protein at 14.534 Å, indicating that ligand binding slightly alters PVR's compactness, with ZINC001848443492 promoting the most compact structure and ZINC000096115646 the least. The low standard deviations (0.062–0.077 Å) and narrow ranges between maximum (14.785–14.804 Å) and minimum (14.225–14.334 Å) Rg values suggest stable compactness across all systems, with minimal fluctuations, implying that these compounds do not significantly disrupt PVR's overall fold, though ZINC001848443492 appears to enhance compactness slightly more effectively.

The SASA results in Figure 4D complement this analysis, with mean values ranging from 7,006 Å^2 (apo-protein) to 7,104 Å^2 (ZINC000096115646), indicating that ligand binding generally increases surface exposure, with ZINC000096115646 showing the highest mean SASA, suggesting greater solvent accessibility possibly due to conformational changes or less tight binding. The standard deviations (122.6–151.5 Å^2) and ranges between maximum (7,419–7,722 Å^2) and minimum (6,529–6,675 Å^2) SASA values reflect moderate variability, with ZINC001848443492 exhibiting the lowest STD (122.6 Å^2), indicating more consistent surface exposure.

TABLE 3 The molecular docking interactions between selected natural product ligands and the PVR receptor at the TIGIT-binding interface.

Compound	Ligand	Receptor	Interaction	Distance	E (kcal/mol)	S (kcal/mol)
ZINC000096115646	O 27	O GLU 71 (C)	H-donor	2.82	−1.6	−11.02
	O 1	CA SER 72 (C)	H-acceptor	3.51	−0.8	
	O 1	OG SER 72 (C)	H-acceptor	2.99	−1.1	
	O 34	OG1 THR 122 (C)	H-acceptor	3.33	−0.8	
	6-ring	CD2 LEU 124 (C)	pi-H	4.02	−1.2	
ZINC001848443492	O 52	O GLU 71 (C)	H-donor	2.73	−6.5	−10.56
	O 42	OG1 THR 122 (C)	H-acceptor	3.23	−0.6	
	O 51	CA SER 72 (C)	H-acceptor	3.53	−0.9	
ZINC000524729757	N 38	OG SER 134 (C)	H-donor	3.1	−1.4	−10.26
	6-ring	OG1 THR 122 (C)	pi-H	3.47	−0.9	

Discussion

CRC is one of the top-ranked malignancies in terms of diagnosis and mortality worldwide [49, 50]. Surgical resection of tumor cells with subsequent adjuvant chemotherapy has long been the gold standard protocol to eliminate CRC [51, 52]. However, disease recurrence plays a pivotal role in increased mortality rates and reduced overall survival in CRC patients [30]. Latest estimates indicate that more than 30% of patients with stage II or III CRC experience recurrence [53, 54]. To date, according to the American Society of Clinical Oncology (ASCO) panel, the accurate definition of 'high-risk' relapsed patients remains elusive, as some stage II diagnosed patients and supposedly at higher risk do not experience relapse, whereas some patients with average risk do [55, 56]. Therefore, there is an urgent need to explore reliable predictive molecular biomarkers to accurately identify CRC patients with a higher risk of relapse to help guide treatment decisions.

Over the years, an accumulating number of studies have demonstrated the unprecedented ability of cancer cells to evade destruction by immune cells, which was recently recognized as an independent hallmark of cancer [57]. Tumor cells can suppress immune response signaling in the TME by either downregulating the activity of stimulatory immunoreceptors or upregulating the activity of inhibitory immunoreceptors, also known as "immune checkpoints" [13]. These molecules are expressed on various immune and cancer cells and serve as gatekeepers to prevent overactivation of the immune system [58]. Elevated levels of immune checkpoint genes have been reported in CRC patients and were associated with poorer clinical outcomes [59–61]. However, the role of these checkpoints in CRC therapy failure and disease relapse remains elusive. Interestingly, a recent study showed that PLCG2 is associated with immune evasion and disease progression in CRC and that PLCG2 knockdown enhanced the efficacy of ICI therapy [62]. In this study, we sought to identify immune checkpoint gene-expression signatures at diagnosis and evaluate their utilization as prognostic biomarkers and potential predictors of CRC relapse. We further investigated the genetic and epigenetic mechanisms underlying the differential expression of immune checkpoint genes in relapsed CRC patients compared with their relapse-free counterparts. Bioinformatic analysis of the RNA-sequencing dataset revealed that the immune checkpoint gene, *PVR*, is significantly upregulated in CRC-relapsed patients relative to relapse-free patients. These results suggest that high *PVR* gene expression might have contributed to the intrinsic resistance that the relapsed cohort exhibited, which may have led to the failure of therapy. Furthermore, our data identified several clinical parameters to be significantly associated with elevated levels of *PVR* in CRC-relapsed patients, including diagnosis age, aneuploidy score, and fraction genome alteration. These parameters might be prognostic factors in identifying patients who might have elevated *PVR* expression and a higher risk of relapse.

PVR is a molecule predominantly expressed on myeloid cells and on some cancer cells [63]. Several lines of evidence reported the overexpression of *PVR* in numerous carcinomas, including CRC [22, 64–66]. Higher levels of *PVR* have been strongly associated with disease recurrence in several malignancies, including hepatocellular carcinoma [67], squamous cell lung carcinoma [68], cervical adenocarcinoma [69], and soft tissue sarcomas [70]. In accordance with those studies, our study is the first to demonstrate a significant correlation between elevated expression of the *PVR* gene and the incidence of CRC relapse. Similar to the previously published studies [19], we report that higher expression of *PVR* was strongly associated with shorter free survival times compared with the low-expression cohort.

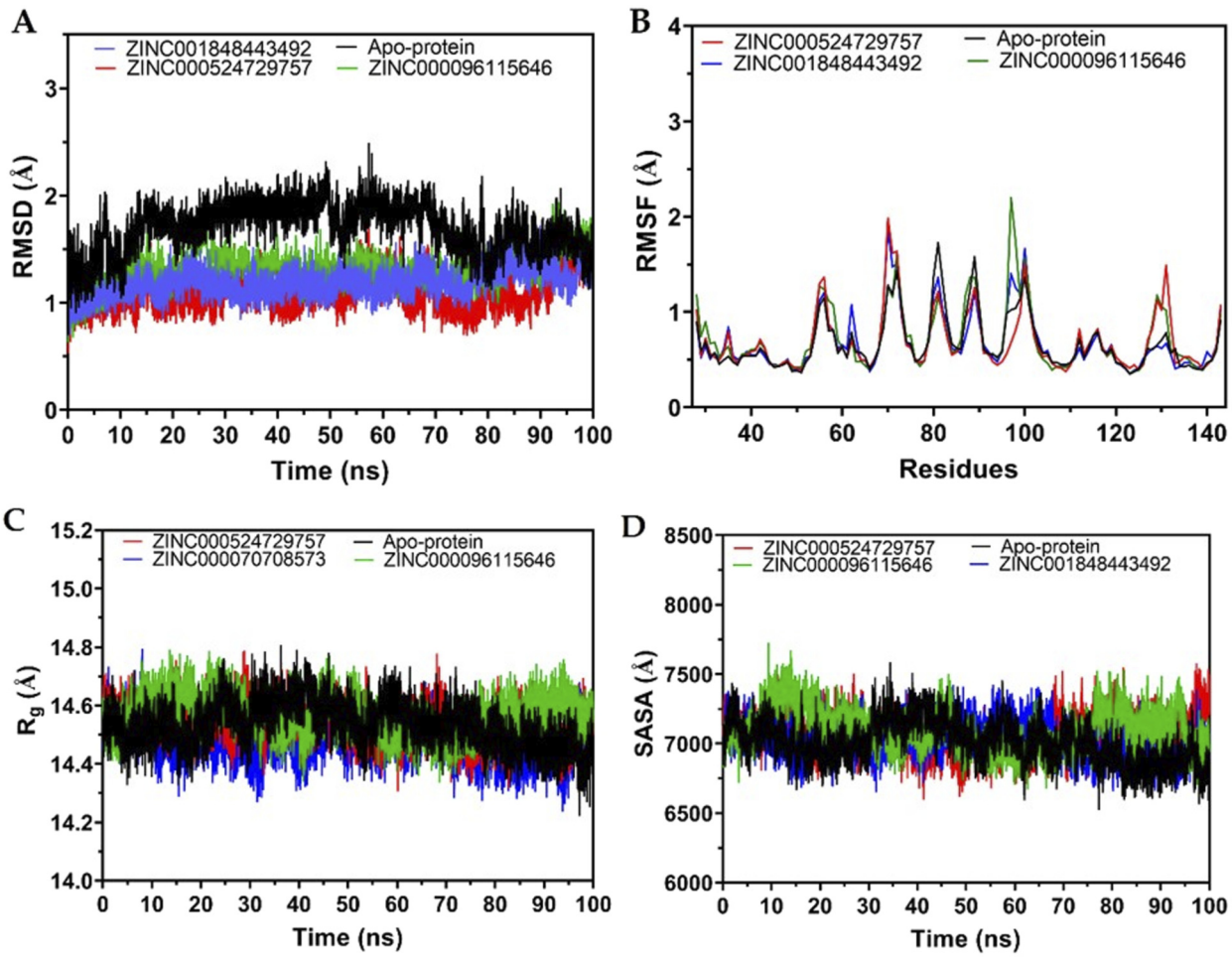

FIGURE 4
Molecular Dynamics simulation analyses of the poliovirus receptor (PVR/CD155) over 100 ns. **(A)** RMSD (Root Mean Square Deviation) plots comparing the structural stability of PVR in its apo form (black) and when bound to ZINC000096115646 (blue), ZINC001848443492 (red), and ZINC000524729757 (green). **(B)** RMSF (Root Mean Square Fluctuation) plots illustrating per-residue flexibility for the apo-protein (black) and complexes with ZINC000524729757 (red), ZINC001848443492 (blue), and ZINC000096115646 (green). **(C)** Radius of gyration (Rg) plots assessing compactness for the apo-protein (black) and complexes with ZINC000524729757 (red), ZINC000070708573 (blue), and ZINC000096115646 (green). **(D)** SASA (Solvent Accessible Surface Area) plots indicating solvent exposure for the apo-protein (black) and complexes with ZINC000524729757 (red), ZINC000096115646 (green), and ZINC001848443492 (blue).

These findings have been validated in another large CRC cohort [35], which independently confirmed the prognostic relevance of *PVR* for relapse risk. Furthermore, *PVR* expression was examined according to the MSI MANTIS score (MSI-high vs. MSI-low). We observed no statistically significant difference in *PVR* expression between the MSI-high and MSI-low groups, suggesting that *PVR* expression is MSI-independent. These findings reveal the essential role of PVR in immune-mediated disease relapse.

We analyzed the genetic and epigenetic anomalies of the relapsed patients compared to the relapse-free patients to understand the potential mechanism by which *PVR* was upregulated in the relapsed cohort. No significant mutations or PCNA alterations were found in the relapsed cohort relative to relapse-free cohorts. Although *PVR* was hypermethylated in the recurrence group compared to the non-recurrence group, it failed to reach statistical significance. These data indicate that the upregulation in *PVR* is driven by the mechanisms governing *PVR* gene expression rather than genetic abnormalities. Future mechanistic studies investigating the regulatory factors of *PVR* gene activity in relapsed CRC patients are highly warranted.

Over the last decade, the therapeutic approach of targeting immune-regulating proteins, also known as immunotherapy, to treat solid and non-solid cancers has grown exponentially [71–73]. Of the 11 ICIs approved by the US Food and Drug Administration (FDA), only two have gained accelerated approval to treat patients with metastatic DNA dMMR or MSI-H CRC. Nivolumab (Anti-PD-1) monotherapy or in

combination with ipilimumab (anti-CLTA-4) in CRC adult and pediatric patients >12 years old, whose disease has progressed following treatment with at least one agent, including fluoropyrimidine, oxaliplatin, and irinotecan, have shown improved overall response rate (ORR) and duration of response (DOR) [74, 75]. In addition, several ongoing clinical trials are evaluating the safety and efficacy of many ICIs, including Sintilimab and Dostarlimab for the treatment of various types of CRC [76]. Evidence suggests that existing ICIs are poorly effective in the pMMR or MSS CRC population [77]. The landscape of immunotherapy in malignancy is rapidly evolving. Thus, future studies are warranted to explore new targets for treating CRC patients with diverse genetic backgrounds. Since MSS/pMMR CRC largely remains resistant to PD-1/PD-L1 and CTLA-4-based ICIs, and because the TIGIT-PVR axis suppresses CD226 co-stimulation, pharmacologic targeting of PVR, especially when combined with those ICIs, may help convert ICI-refractory pMMR/MSS disease into a responsive state. To our knowledge, our study is the first to show a correlation between PVR upregulation and the development of relapse in CRC patients, and the first to establish the need for further studies to investigate the impact of concomitant ICI use on preventing CRC relapse after complete remission.

Our work was extended to identify natural product ligands targeting PVR by using molecular docking. All three identified ligands demonstrated strong binding affinity, as indicated by their docking scores (S-values), which were ≤−10 kcal/mol, a commonly accepted threshold for significant interaction.

RMSD data suggest that the compounds influence PVR's conformational dynamics differently, with ZINC000524729757 providing the most significant stabilization despite higher variability, possibly indicating a strong yet flexible interaction, while ZINC001848443492 offers a more rigid and stable binding pose. The apo-protein's higher mean RMSD (1.58 Å) reflects its intrinsic flexibility without ligand constraints, with an initial adjustment period (0–20 ns) before stabilization (Figure 4A). The reduced RMSD in ligand-bound states highlights the role of these compounds in influencing the active site of PVR. This modulation could affect its natural interactions, such as with TIGIT. However, a more detailed analysis of the binding residues or energetics would be necessary to gain a better understanding of these molecular interactions.

Observations from RMSF data suggest that while all compounds influence PVR's dynamics, ZINC000524729757 may induce greater conformational variability, potentially reflecting a less rigid binding mode, whereas ZINC001848443492 and ZINC000096115646 provide more consistent stabilization, aligning with their roles in modulating PVR's active site interactions.

The SASA results suggest that while all compounds influence PVR's surface properties, ZINC001848443492 maintains a more stable and compact interaction, potentially correlating with its observed lower Rg, whereas ZINC000096115646 may induce a more exposed and less compact conformation, impacting PVR's interaction dynamics at the active site.

Validating our findings should include binding assays such as surface plasmon resonance (SPR) to assess the binding of our candidate hits to TGIT-PVR, as well as fluorescence-based binding blockade assays to evaluate the efficacy of the candidate compounds in blocking TGIT-PVR interaction [78, 79]. Future research should also explore the impact of TGIT-PVR blockade on $CD8^+$ T cell activation, NK cell cytotoxicity, immune cell infiltration, cytokine expression, and tumor burden and recurrence using CRC murine models. The clinical implications of our findings should be cautiously interpreted, given the few limitations of our study. For instance, the reported *PVR* expressions in our study are relative between the CRC-relapsed patients and relapse-free ones. We cannot extrapolate these observations to other subgroups, including early- and late-relapsing patients. Furthermore, we had no control over the inclusion and exclusion criteria of this study's participating subjects, given that the first part of this study is a secondary analysis of published data sets. The type and length of the initiated chemotherapy, concurrent use of other medications, patient genetic background, time of relapse after a complete remission, and the definition of complete remission are confounders that could have impacted the observed difference between the two cohorts. The fact that this study proposes the concurrent use of ICIs with chemotherapy in PVR-expressing CRC patients as a prophylactic measure to prevent disease relapse is a critical strength of this work.

Our study identifies PVR as a potential drug target and serves as a sturdy foundation for future studies to answer several unresolved questions. In addition to the importance of validating our findings presented in this study, the impact of chemotherapy on the PVR levels, the association between highly-expressed PVR with the timing of relapse after a complete remission, and the role of PVR expression levels with the mortality rates remain open questions that are warranted to be answered.

Conclusion

In this work, a correlation between the immune checkpoint *PVR* and relapse in CRC was established. RNA-Seq dataset showed that *PVR* is significantly upregulated in relapsed patients compared to relapse-free individuals. Such elevated *PVR* gene levels in patients experiencing recurrence were accompanied by relatively lower levels in genes involved in antigen presentation, and this was specifically observed in HLA-DRA. Further investigation to explore the clinical and genetic factors associated with increased *PVR* gene expression in relapsed CRC patients revealed that

diagnosis age, Aneuploidy, fraction genome alterations, and mutation count were strongly correlated with *PVR* upregulation. Furthermore, free survival analysis indicated that patients with tumors highly expressing *PVR* were more susceptible to recurrence compared to *PVR*-low expression patients, verifying the initial screening via RNA-seq analysis. All three natural product PVR/TIGIT interface binders exhibited strong binding affinity, with docking scores (S-values) of ≤−10 kcal/mol and stable interactions with critical residues, including Glu71, Thr122, and Ser72. Among them, ZINC001848443492 emerged as the most promising candidate due to its balanced performance, showing a strong hydrogen bond with GLU71, a docking score of −10.56 kcal/mol, and the most consistent structural behavior during molecular dynamics simulations—evidenced by the lowest RMSD, minimal fluctuation (RMSF), and enhanced compactness and surface stability. Taken together, these findings suggest that *PVR* may work as a prognostic biomarker for recurrence risk in CRC, and that ZINC001848443492 holds potential as a lead compound for the further development of TIGIT-PVR immune checkpoint inhibitors for CRC treatment.

Author contributions

Conceptualization, SSA and HMAS; methodology, SSA, MS, ZA, AB, HMA, HHA, and HMAS; validation, AAA, HMA, ARA, and MA; formal analysis, SSA, AB, HHA, AAA, ARA, MA, and HMAS; investigation, MS, ZA, SMA, and NA; data curation, SSA, MS, ZA, SMA, NA, and AB; writing—original draft, SSA, AB, and AAA; writing—review and editing, all authors; supervision, HMAS; project administration, HMAS; funding acquisition, SSA. All authors contributed to the article and approved the submitted version.

Data availability

The datasets analyzed in this study are publicly available at the cBioportal database (Available online: https://www.cbioportal.org/study/summary?id=coadread_tcga_pan_can_atlas_2018) (accessed on 14 January 2023). All analyses are reported in the paper, in the main figures and tables, or in the Supplementary Material.

Ethics statement

The data used in this study are publicly available from cBioPortal and are de-identified; therefore, no ethical approval was required for this study.

Funding

The author(s) declared that financial support was received for this work and/or its publication. This work was supported by Ongoing Research Funding Program number (ORF-2025-598), King Saud University, Riyadh, Saudi Arabia.

Conflict of interest

The author(s) declared no potential conflicts of interest with respect to the research, authorship, and/or publication of this article.

Generative AI statement

The author(s) declared that generative AI was not used in the creation of this manuscript.

Any alternative text (alt text) provided alongside figures in this article has been generated by Frontiers with the support of artificial intelligence and reasonable efforts have been made to ensure accuracy, including review by the authors wherever possible. If you identify any issues, please contact us.

Supplementary material

The Supplementary Material for this article can be found online at: https://www.ebm-journal.org/articles/10.3389/ebm.2026.10745/full#supplementary-material

SUPPLEMENTARY FIGURE S1
Downregulated HLA class II molecules genes in relapsed CRC patients relative to disease-free. **(A)** HLA-DRA, **(B)** HLA-DRB1, **(C)** HLA-DMA, **(D)** HLA-DMB, **(E)** HLA-DQA1, **(F)** HLA-DPA1. The mean and 95% confidence interval values are represented by bold and light intermittent lines, respectively. Statistical significance was determined by Student's t-test.

SUPPLEMENTARY FIGURE S2
PVR expression profile and disease-free survival according to MSI status. **(A)** Log2 PVR expression in MSI-high patients relative to MSI-low patients. The mean and 95% confidence interval values are represented by bold and light intermittent lines, respectively. Statistical significance was determined by Student's t-test. **(B)** Free survival curves for MSI-low patients (blue) and MSI-high patients (red). The median gene expression value was used as the cut-off to stratify patients into the two cohorts, high and low. Hazard ratio (HR) and p-value were calculated using the log-rank test. The shaded area around each curve represents 95% confidence interval.

SUPPLEMENTARY FIGURE S3
Kaplan–Meier overall survival curve for patients with low PVR expression (blue) and patients with high PVR expression (red). The median gene expression value was used as the cut-off to stratify patients into the two cohorts, high and low. Hazard ratio (HR) and p-value were calculated using the log-rank test.

SUPPLEMENTARY FIGURE S4
Kaplan–Meier free survival curve for patients with low PVR expression (black) and patients with high PVR expression (red) in the validation dataset, GSE39582. The number at risk of relapse is shown under the curves. The median gene expression value was used as the cut-off to stratify patients into the two cohorts. Hazard ratio (HR) and p-value were calculated using the log-rank test. The figure was generated using KM plotter [36].

SUPPLEMENTARY TABLE S1
Clinical characteristics analysis.

SUPPLEMENTARY TABLE S2
Expression of various genes in relapse-free and relapsed CRC patients.

SUPPLEMENTARY TABLE S3
Genetic alteration.

SUPPLEMENTARY TABLE S4
The methylation status of various genes in relapse-free and relapsed CRC patients.

SUPPLEMENTARY TABLE S5
Most frequently mutated genes in the CRC cohort.

SUPPLEMENTARY TABLE S6
Clinical and genetic characteristics of patients with low *PVR* expression and patients with high *PVR* expression.

References

1. WHO. Colorectal cancer (2024). Available online at: https://www.who.int/news-room/fact-sheets/detail/colorectal-cancer (Accessed October 13, 2024).

2. Colorectal Cancer Statistics. How common is colorectal cancer? Available online at: https://www.cancer.org/cancer/types/colon-rectal-cancer/about/key-statistics.html (Accessed October 13, 2024).

3. Colorectal Cancer Survival Rates. Colorectal cancer prognosis. Available online at: https://www.cancer.org/cancer/types/colon-rectal-cancer/detection-diagnosis-staging/survival-rates.html (Accessed October 13, 2024).

4. Colon Cancer Treatment, by Stage. How to treat Colon cancer. Available online at: https://www.cancer.org/cancer/types/colon-rectal-cancer/treating/by-stage-colon.html (Accessed October 13, 2024).

5. Zhou H, Liu Z, Wang Y, Wen X, Amador EH, Yuan L, et al. Colorectal liver metastasis: molecular mechanism and interventional therapy. *Sig Transduct Target Ther* (2022) **7**:1–25. doi:10.1038/s41392-022-00922-2

6. Martin J, Petrillo A, Smyth EC, Shaida N, Khwaja S, Cheow H, et al. Colorectal liver metastases: current management and future perspectives. *World J Clin Oncol* (2020) **11**:761–808. doi:10.5306/wjco.v11.i10.761

7. Rectal Cancer Treatment, by Stage. How to treat rectal cancer. Available online at: https://www.cancer.org/cancer/types/colon-rectal-cancer/treating/by-stage-rectum.html (Accessed October 13, 2024).

8. Janeeh AS, Bajbouj K, Rah B, Abu-Gharbieh E, Hamad M. Interplay between tumor cells and immune cells of the colorectal cancer tumor microenvironment: Wnt/β-catenin pathway. *Front Immunol* (2025) **16**:1587950. doi:10.3389/fimmu.2025.1587950

9. Raskov H, Orhan A, Christensen JP, Gögenur I. Cytotoxic CD8+ T cells in cancer and cancer immunotherapy. *Br J Cancer Nat Publishing Group* (2021) **124**:359–67. doi:10.1038/s41416-020-01048-4

10. Chow A, Perica K, Klebanoff CA, Wolchok JD. Clinical implications of T cell exhaustion for cancer immunotherapy. *Nat Rev Clin Oncol* (2022) **19**:775–90. doi:10.1038/s41571-022-00689-z

11. Cui G. The mechanisms leading to distinct responses to PD-1/PD-L1 blockades in colorectal cancers with different MSI statuses. *Front Oncol* (2021) **11**:573547. doi:10.3389/fonc.2021.573547

12. Schmid P, Adams S, Rugo HS, Schneeweiss A, Barrios CH, Iwata H, et al. Atezolizumab and nab-paclitaxel in advanced triple-negative breast cancer. *New Engl J Med* (2018) **379**:2108–21. doi:10.1056/NEJMoa1809615

13. He X, Xu C. Immune checkpoint signaling and cancer immunotherapy. *Cell Res. Nat Publishing Group* (2020) **30**:660–9. doi:10.1038/s41422-020-0343-4

14. Fares CM, Van Allen EM, Drake CG, Allison JP, Hu-Lieskovan S. Mechanisms of resistance to immune checkpoint blockade: why does checkpoint inhibitor immunotherapy not work for all patients? *Am Soc Clin Oncol Educ Book* (2019) **39**:147–64. doi:10.1200/EDBK_240837

15. Kula A, Dawidowicz M, Mielcarska S, Kiczmer P, Skiba H, Krygier M, et al. Overexpression and role of HHLA2, a novel immune checkpoint, in colorectal cancer. *Int J Mol Sci* (2023) **24**:5876. doi:10.3390/ijms24065876

16. Qin S, Xu L, Yi M, Yu S, Wu K, Luo S. Novel immune checkpoint targets: moving beyond PD-1 and CTLA-4. *Mol Cancer* (2019) **18**:155. doi:10.1186/s12943-019-1091-2

17. Marin-Acevedo JA, Dholaria B, Soyano AE, Knutson KL, Chumsri S, Lou Y. Next generation of immune checkpoint therapy in cancer: new developments and challenges. *J Hematol and Oncol* (2018) **11**:39. doi:10.1186/s13045-018-0582-8

18. Borgeaud M, Sandoval J, Obeid M, Banna G, Michielin O, Addeo A, et al. Novel targets for immune-checkpoint inhibition in cancer. *Cancer Treat Rev* (2023) **120**:102614. doi:10.1016/j.ctrv.2023.102614

19. Murakami D, Matsuda K, Iwamoto H, Mitani Y, Mizumoto Y, Nakamura Y, et al. Prognostic value of CD155/TIGIT expression in patients with colorectal cancer. *PLoS ONE* (2022) **17**:e0265908. doi:10.1371/journal.pone.0265908

20. Ou X, Yin J, Shi F, Zhao Y, Zhou Q, Yuan K, et al. CD155-TIGIT/CD96/CD226 immune checkpoint axis interacting with tumor-infiltrating lymphocytes to exhibit diverse prognostic effects on breast cancer: a cohort study. *Front Immunol* (2025) **16**:1649078. doi:10.3389/fimmu.2025.1649078

21. Murakami K, Ganguly S. The nectin family ligands, PVRL2 and PVR, in cancer immunology and immunotherapy. *Front Immunol* (2024) **15**:1441730. doi:10.3389/fimmu.2024.1441730

22. Masson D, Jarry A, Baury B, Blanchardie P, Laboisse C, Lustenberger P, et al. Overexpression of the CD155 gene in human colorectal carcinoma. *Gut* (2001) **49**:236–40. doi:10.1136/gut.49.2.236

23. van der Stok EP, Spaander MCW, Grünhagen DJ, Verhoef C, Kuipers EJ. Surveillance after curative treatment for colorectal cancer. *Nat Rev Clin Oncol* (2017) **14**:297–315. doi:10.1038/nrclinonc.2016.199

24. Balboa-Barreiro V, Pértega-Díaz S, García-Rodríguez T, González-Martín C, Pardeiro-Pértega R, Yáñez-González-Dopeso L, et al. Colorectal cancer recurrence and its impact on survival after curative surgery: an analysis based on multistate models. *Dig Liver Dis* (2024) **56**:1229–36. doi:10.1016/j.dld.2023.11.041

25. Wang L, Shen X, Wang Z, Xiao X, Wei P, Wang Q, et al. A molecular signature for the prediction of recurrence in colorectal cancer. *Mol Cancer* (2015) **14**:22. doi:10.1186/s12943-015-0296-2

26. Wang Y, Jatkoe T, Zhang Y, Mutch MG, Talantov D, Jiang J, et al. Gene expression profiles and molecular markers to predict recurrence of dukes' B Colon cancer. *JCO* (2004) **22**:1564–71. doi:10.1200/JCO.2004.08.186

27. Lan Y-T, Chang S-C, Lin P-C, Lin C-C, Lin H-H, Huang S-C, et al. Clinicopathological and molecular features of patients with early and late recurrence after curative surgery for colorectal cancer. *Cancers (Basel)* (2021) **13**:1883. doi:10.3390/cancers13081883

28. Koncina E, Haan S, Rauh S, Letellier E. Prognostic and predictive molecular biomarkers for colorectal cancer: updates and challenges. *Cancers (Basel)* (2020) **12**:319. doi:10.3390/cancers12020319

29. Jung G, Hernández-Illán E, Moreira L, Balaguer F, Goel A. Epigenetics of colorectal cancer: biomarker and therapeutic potential. *Nat Rev Gastroenterol Hepatol* (2020) **17**:111–30. doi:10.1038/s41575-019-0230-y

30. Nors J, Iversen LH, Erichsen R, Gotschalck KA, Andersen CL. Incidence of recurrence and time to recurrence in stage I to III colorectal cancer: a nationwide Danish cohort study. *JAMA Oncol* (2024) **10**:54–62. doi:10.1001/jamaoncol.2023.5098

31. NCI. The cancer genome atlas program (TCGA) - NCI (2022). Available online at: https://www.cancer.gov/ccg/research/genome-sequencing/tcga (Accessed December 24, 2024).

32. Ceramil E, Gao J, Dogrusoz U, Gross BE, Sumer SO, Aksoy BA, et al. The cBio cancer genomics portal: an open platform for exploring multidimensional cancer genomics data. *Cancer Discov* (2012) **2**:401–4. doi:10.1158/2159-8290.CD-12-0095

33. Gao J, Aksoy BA, Dogrusoz U, Dresdner G, Gross B, Sumer SO, et al. Integrative analysis of complex cancer genomics and clinical profiles using the cBioPortal. *Sci Signal* (2013) **6**:pl1. doi:10.1126/scisignal.2004088

34. de Bruijn I, Kundra R, Mastrogiacomo B, Tran TN, Sikina L, Mazor T, et al. Analysis and visualization of longitudinal genomic and clinical data from the AACR project GENIE biopharma collaborative in cBioPortal. *Cancer Res* (2023) **83**:3861–7. doi:10.1158/0008-5472.CAN-23-0816

35. Marisa L, de Reyniès A, Duval A, Selves J, Gaub MP, Vescovo L, et al. Gene expression classification of Colon cancer into molecular subtypes: characterization, validation, and prognostic value. *Plos Med* (2013) **10**:e1001453. doi:10.1371/journal.pmed.1001453

36. Győrffy B. Integrated analysis of public datasets for the discovery and validation of survival-associated genes in solid tumors. *Innovation (Camb)* (2024) **5**:100625. doi:10.1016/j.xinn.2024.100625

37. Stengel KF, Harden-Bowles K, Yu X, Rouge L, Yin J, Comps-Agrar L, et al. Structure of TIGIT immunoreceptor bound to poliovirus receptor reveals a cell-cell adhesion and signaling mechanism that requires cis-trans receptor clustering. *Proc Natl Acad Sci U S A*. (2012) **109**:5399–404. doi:10.1073/pnas.1120606109

38. Samanta D, Guo H, Rubinstein R, Ramagopal UA, Almo SC. Structural, mutational and biophysical studies reveal a canonical mode of molecular recognition between immune receptor TIGIT and nectin-2. *Mol Immunol* (2017) **81**:151–9. doi:10.1016/j.molimm.2016.12.003

39. Phillips JC, Hardy DJ, Maia JDC, Stone JE, Ribeiro JV, Bernardi RC, et al. Scalable molecular dynamics on CPU and GPU architectures with NAMD. *J Chem Phys* (2020) **153**:044130. doi:10.1063/5.0014475

40. Jo S, Cheng X, Islam SM, Huang L, Rui H, Zhu A, et al. CHARMM-GUI PDB manipulator for advanced modeling and simulations of proteins containing nonstandard residues. *Adv Protein Chem Struct Biol* (2014) **96**:235–65. doi:10.1016/bs.apcsb.2014.06.002

41. Yu W, He X, Vanommeslaeghe K, MacKerell AD. Extension of the CHARMM general force field to sulfonyl-containing compounds and its utility in biomolecular simulations. *J Comput Chem* (2012) **33**:2451–68. doi:10.1002/jcc.23067

42. Vanommeslaeghe K, Hatcher E, Acharya C, Kundu S, Zhong S, Shim J, et al. CHARMM general force field: a force field for drug-like molecules compatible with the CHARMM all-atom additive biological force fields. *J Comput Chem* (2010) **31**:671–90. doi:10.1002/jcc.21367

43. Boonstra S, Onck PR, Giessen Ed. CHARMM TIP3P water model suppresses peptide folding by solvating the unfolded state. *J Phys Chem B* (2016) **120**:3692–8. doi:10.1021/acs.jpcb.6b01316

44. Humphrey W, Dalke A, Schulten K. VMD: visual molecular dynamics. *J Mol Graphics* (1996) **14**:33–8. doi:10.1016/0263-7855(96)00018-5

45. Bakheit AH, Saquib Q, Ahmed S, Ansari SM, Al-Salem AM, Al-Khedhairy AA. Covalent inhibitors from Saudi medicinal plants target RNA-dependent RNA polymerase (RdRp) of SARS-CoV-2. *Viruses* (2023) **15**:2175. doi:10.3390/v15112175

46. Dahhas MA, Alkahtani HM, Malik A, Almehizia AA, Bakheit AH, Ansar SA, et al. Screening and identification of potential MERS-CoV papain-like protease (PLpro) inhibitors; steady-state kinetic and molecular dynamic studies. *Saudi Pharm J* (2023) **31**:228–44. doi:10.1016/j.jsps.2022.12.007

47. Speiser DE, Chijioke O, Schaeuble K, Münz C. CD4+ T cells in cancer. *Nat Cancer. Nature Publishing Group* (2023) **4**:317–29. doi:10.1038/s43018-023-00521-2

48. Kravtsov DS, Erbe AK, Sondel PM, Rakhmilevich AL. Roles of CD4+ T cells as mediators of antitumor immunity. *Front Immunol* (2022) **13**:972021. doi:10.3389/fimmu.2022.972021

49. Siegel RL, Giaquinto AN, Jemal A. Cancer statistics, 2024. *CA: A Cancer J Clinicians* (2024) **74**:12–49. doi:10.3322/caac.21820

50. Morgan E, Arnold M, Gini A, Lorenzoni V, Cabasag CJ, Laversanne M, et al. Global burden of colorectal cancer in 2020 and 2040: incidence and mortality estimates from GLOBOCAN. *Gut* (2023) **72**:338–44. doi:10.1136/gutjnl-2022-327736

51. Yoshino T, Argilés G, Oki E, Martinelli E, Taniguchi H, Arnold D, et al. Pan-Asian adapted ESMO clinical practice guidelines for the diagnosis treatment and follow-up of patients with localised colon cancer. *Ann Oncol* (2021) **32**:1496–510. doi:10.1016/j.annonc.2021.08.1752

52. McQuade RM, Stojanovska V, Bornstein JC, Nurgali K. Colorectal cancer chemotherapy: the evolution of treatment and new approaches. *Curr Med Chem* (2017) **24**:1537–57. doi:10.2174/0929867324666170111152436

53. Matsuoka T, Yashiro M. Precision medicine for gastrointestinal cancer: recent progress and future perspective. *World J Gastrointest Oncol* (2020) **12**:1–20. doi:10.4251/wjgo.v12.i1.1

54. Oki E, Ando K, Taniguchi H, Yoshino T, Mori M. Sustainable clinical development of adjuvant chemotherapy for Colon cancer. *Ann Gastroenterological Surg* (2022) **6**:37–45. doi:10.1002/ags3.12503

55. Benson AB, Hamilton SR. Path toward prognostication and prediction: an evolving matrix. *J Clin Oncol* (2011) **29**:4599–601. doi:10.1200/JCO.2011.37.8646

56. O'Connor ES, Greenblatt DY, LoConte NK, Gangnon RE, Liou J-I, Heise CP, et al. Adjuvant chemotherapy for stage II colon cancer with poor prognostic features. *J Clin Oncol* (2011) **29**:3381–8. doi:10.1200/JCO.2010.34.3426

57. Hanahan D. Hallmarks of cancer: new dimensions. *Cancer Discov* (2022) **12**:31–46. doi:10.1158/2159-8290.CD-21-1059

58. Meng L, Wu H, Wu J, Ding P, He J, Sang M, et al. Mechanisms of immune checkpoint inhibitors: insights into the regulation of circular RNAS involved in cancer hallmarks. *Cell Death Dis. Nature Publishing Group* (2024) **15**:1–26. doi:10.1038/s41419-023-06389-5

59. Saleh R, Taha RZ, Toor SM, Sasidharan Nair V, Murshed K, Khawar M, et al. Expression of immune checkpoints and T cell exhaustion markers in early and advanced stages of colorectal cancer. *Cancer Immunol Immunother* (2020) **69**:1989–99. doi:10.1007/s00262-020-02593-w

60. Elashi AA, Sasidharan NV, Taha RZ, Shaath H, Elkord E. DNA methylation of immune checkpoints in the peripheral blood of breast and colorectal cancer patients. *Oncoimmunology* (2019) **8**:e1542918. doi:10.1080/2162402X.2018.1542918

61. Sasidharan Nair V, Toor SM, Taha RZ, Shaath H, Elkord E. DNA methylation and repressive histones in the promoters of PD-1, CTLA-4, TIM-3, LAG-3, TIGIT, PD-L1, and galectin-9 genes in human colorectal cancer. *Clin Epigenetics* (2018) **10**:104. doi:10.1186/s13148-018-0539-3

62. Zhou X, Lin J, Shao Y, Zheng H, Yang Y, Li S, et al. Targeting PLCG2 suppresses tumor progression, orchestrates the tumor immune microenvironment and potentiates immune checkpoint blockade therapy for colorectal cancer. *Int J Biol Sci* (2024) **20**:5548–75. doi:10.7150/ijbs.98200

63. Meng F, Xiang M, Liu Y, Zeng D. TIGIT/PVR axis regulates anti-tumor immunity in hematologic malignancies. *Ann Hematol* (2025) **104**:1415–26. doi:10.1007/s00277-025-06304-2

64. Sloan KE, Eustace BK, Stewart JK, Zehetmeier C, Torella C, Simeone M, et al. CD155/PVR plays a key role in cell motility during tumor cell invasion and migration. *BMC Cancer* (2004) **4**:73. doi:10.1186/1471-2407-4-73

65. Inozume T, Yaguchi T, Furuta J, Harada K, Kawakami Y, Shimada S. Melanoma cells control antimelanoma CTL responses *via* interaction between TIGIT and CD155 in the effector phase. *J Invest Dermatol* (2016) **136**:255–63. doi:10.1038/JID.2015.404

66. Nishiwada S, Sho M, Yasuda S, Shimada K, Yamato I, Akahori T, et al. Clinical significance of CD155 expression in human pancreatic cancer. *Anticancer Res.* (2015) **35**:2287–97.

67. Liu W-F, Quan B, Li M, Zhang F, Hu K-S, Yin X. PVR-A prognostic biomarker correlated with immune cell infiltration in hepatocellular carcinoma. *Diagnostics (Basel)* (2022) **12**:2953. doi:10.3390/diagnostics12122953

68. Lee JB, Hong MH, Park SY, Chae S, Hwang D, Ha S-J, et al. Overexpression of PVR and PD-L1 and its association with prognosis in surgically resected squamous cell lung carcinoma. *Sci Rep* (2021) **11**:8551. doi:10.1038/s41598-021-87624-x

69. Murakami T, Takasawa A, Takasawa K, Akimoto T, Aoyama T, Magara K, et al. Aberrant expression of junctional adhesion molecule-a contributes to the malignancy of cervical adenocarcinoma by interaction with poliovirus receptor/CD155. *Cancer Sci* (2020) **112**:906. doi:10.1111/cas.14734

70. Atsumi S, Matsumine A, Toyoda H, Niimi R, Iino T, Sudo A. Prognostic significance of CD155 mRNA expression in soft tissue sarcomas. *Oncol Lett* (2013) **5**:1771–6. doi:10.3892/ol.2013.1280

71. Salik B, Smyth MJ, Nakamura K. Targeting immune checkpoints in hematological malignancies. *J Hematol Oncol* (2020) **13**:111. doi:10.1186/s13045-020-00947-6

72. Kaushik I, Ramachandran S, Zabel C, Gaikwad S, Srivastava SK. The evolutionary legacy of immune checkpoint inhibitors. *Semin Cancer Biol* (2022) **86**:491–8. doi:10.1016/j.semcancer.2022.03.020

73. Sun Q, Hong Z, Zhang C, Wang L, Han Z, Ma D. Immune checkpoint therapy for solid tumours: clinical dilemmas and future trends. *Signal Transduct Target Ther* (2023) **8**:320. doi:10.1038/s41392-023-01522-4

74. Overman MJ, McDermott R, Leach JL, Lonardi S, Lenz H-J, Morse MA, et al. Nivolumab in patients with metastatic DNA mismatch repair-deficient or microsatellite instability-high colorectal cancer (CheckMate 142): an open-label, multicentre, phase 2 study. *Lancet Oncol* (2017) **18**:1182–91. doi:10.1016/S1470-2045(17)30422-9

75. Overman MJ, Lonardi S, Wong KYM, Lenz H-J, Gelsomino F, Aglietta M, et al. Durable clinical benefit with nivolumab plus ipilimumab in DNA mismatch

repair-Deficient/Microsatellite instability-high metastatic colorectal cancer. *J Clin Oncol* (2018) **36**:773–9. doi:10.1200/JCO.2017.76.9901

76. Kelly P. Immune checkpoint blockade therapies for colorectal cancer: current strategies and emerging approaches. *JCO Oncol Adv*. doi:10.1200/OA-24-00077

77. Zhao W, Jin L, Chen P, Li D, Gao W, Dong G. Colorectal cancer immunotherapy-recent progress and future directions. *Cancer Lett* (2022) **545**: 215816. doi:10.1016/j.canlet.2022.215816

78. Um YJ, Kwak D, Kim SY, Chang HJ, Yum SH, Hwang J, et al. Enhancing anti-tumor immunity through TIGIT blockade and tumor-directed targeting in pancreatic cancer. *Int Immunopharmacology* (2025) **167**:115653. doi:10.1016/j.intimp.2025.115653

79. Lü X, Wei X, Wang C, Tang M, Jin Y, Fan S, et al. Identification of the therapeutic potential of novel TIGIT/PVR interaction blockers based advanced computational techniques and experimental validation. *Biophysical Chem* (2025) **318**:107383. doi:10.1016/j.bpc.2024.107383

EBM Experimental Biology and Medicine

TYPE Original Research
PUBLISHED 21 January 2026
DOI 10.3389/ebm.2025.10687

OPEN ACCESS

*CORRESPONDENCE
Santosh Kumar,
ksantosh@uthsc.edu

†These authors have contributed equally to this work

RECEIVED 02 June 2025
REVISED 24 November 2025
ACCEPTED 19 December 2025
PUBLISHED 21 January 2026

CITATION
Sinha N, Hiser L, Godse S, Zhou L, Shynykul Z, Risley C, Cory T and Kumar S (2026) HIV-HPV interactions via extracellular vesicles among tobacco smokers and nonsmokers.
Exp. Biol. Med. 250:10687.
doi: 10.3389/ebm.2025.10687

HIV-HPV interactions via extracellular vesicles among tobacco smokers and nonsmokers

Namita Sinha[1†], Laree Hiser[2†], Sandip Godse[1], Lina Zhou[1], Zhanserik Shynykul[1], Carolann Risley[2], Theodore Cory[3] and Santosh Kumar[1*]

[1]Department of Pharmaceutical Sciences, College of Pharmacy, The University of Tennessee, Health Science Center, Memphis, TN, United States, [2]Department of Cell and Molecular Biology, School of Nursing, Cancer Center and Research Institute, School of Medicine, The University of Mississippi Medical Center, Jackson, MS, United States, [3]Department of Clinical Pharmacy and Translational Sciences, College of Pharmacy, The University of Tennessee, Health Science Center, Memphis, TN, United States

Abstract

Human Immunodeficiency Virus (HIV) and Human Papillomavirus (HPV) co-infections are significantly prevalent, especially among African Americans (AA), a situation further compounded by the prevalence of tobacco smoking. Extracellular vesicles (EVs) are integral to the mechanisms of viral pathogenesis, as they are pivotal in the modulation of immune responses and the inflammatory process. This research study examines the varying concentrations of EVs, their associated biomarkers, and the cytokine/chemokine profiles present in plasma obtained from individuals infected with HIV and those coinfected with HIV and HPV, with particular emphasis on the ramifications of smoking behavior. Our findings revealed that HIV infection markedly elevates EV formation and modifies their protein composition, whereas HPV co-infection does not significantly augment EV levels but does influence the specific cytokine packaging. Notably, monocyte chemoattractant protein-1 (MCP-1 or CCL2) and Regulated upon Activation, Normal T cell Expressed and presumably Secreted (RANTES or CCL5) exhibited substantial enrichment in EVs derived from individuals coinfected with HIV and HPV, implying a potential role of EVs in immune modulation related to viral persistence. Importantly, smoking was found to affect EV characteristics, resulting in an increase in EV size and the packaging of inflammatory mediators, such as MCP-1 and interleukin-18 (IL-18), from plasma into EVs in HIV- and/or HIV+HPV-infected samples. This observation suggests that oxidative stress induced by smoking may intensify immune dysregulation through modifications in EV-mediated cytokine signaling pathways. Nevertheless, smoking did not exhibit a significant impact on the expression of EV marker proteins or the overall levels of EVs. These outcomes underscore the intricate interactions between HIV, HPV, and/or smoking in influencing the

immune milieu via EVs. Further comprehensive understanding of the role of EVs in the context of these viral infections could yield valuable insights into potential biomarkers for disease progression and new therapeutic strategies.

KEYWORDS

HIV, HPV, tobacco smokers, extracellular vesicles, inflammation

Impact statement

Despite notable progress in the management of HIV through the implementation of antiretroviral therapies, the incidence rates and prevalence of HIV-associated neurocognitive disorders (HAND) continue to escalate, with a disproportionate impact on African Americans (AA). Furthermore, human papillomavirus (HPV), a highly endemic sexually transmitted infection, exacerbates the overall disease burden, particularly amongst individuals with compromised immune systems. Epidemiological data indicates a bidirectional interplay between HIV and HPV infections, potentially mediated by oxidative stress and inflammatory mechanisms. Tobacco consumption, which is notably higher among individuals living with HIV, further intensifies immune suppression, oxidative stress, and inflammatory responses, thereby facilitating disease progression. Extracellular vesicles (EVs) act as pivotal mediators of intercellular communication and may influence the pathogenesis of both HIV and HPV. This investigation examines potential HIV-HPV interactions via EVs by measuring the variations in the levels of EVs and their associated oxidative stress biomarkers and inflammatory cytokines and chemokines in individuals coinfected with HIV and HPV, with a particular focus on smokers.

Introduction

Despite considerable progress in the management of Human Immunodeficiency Virus (HIV) facilitated by antiretroviral therapies, rates of infection persist in an upward trajectory both on a global scale and within the United States [1]. Notably, African Americans (AA) or Black people are disproportionately affected by HIV infections, and due to HIV-related conditions, they experience relatively high mortality. Recent data from the Centers for Disease Control and Prevention (CDC) indicate that although AA constitute 12% of the overall population in the United States, they account for 44% of newly diagnosed HIV infections [2]. Furthermore, HIV-associated neurocognitive disorders (HAND), particularly mild and asymptomatic forms, affect an estimated 50% of individuals living with HIV [3, 4]. Given that over half of the HIV-positive population is aged 50 and older, the prevalence of HAND is expected to rise in the coming years [5].

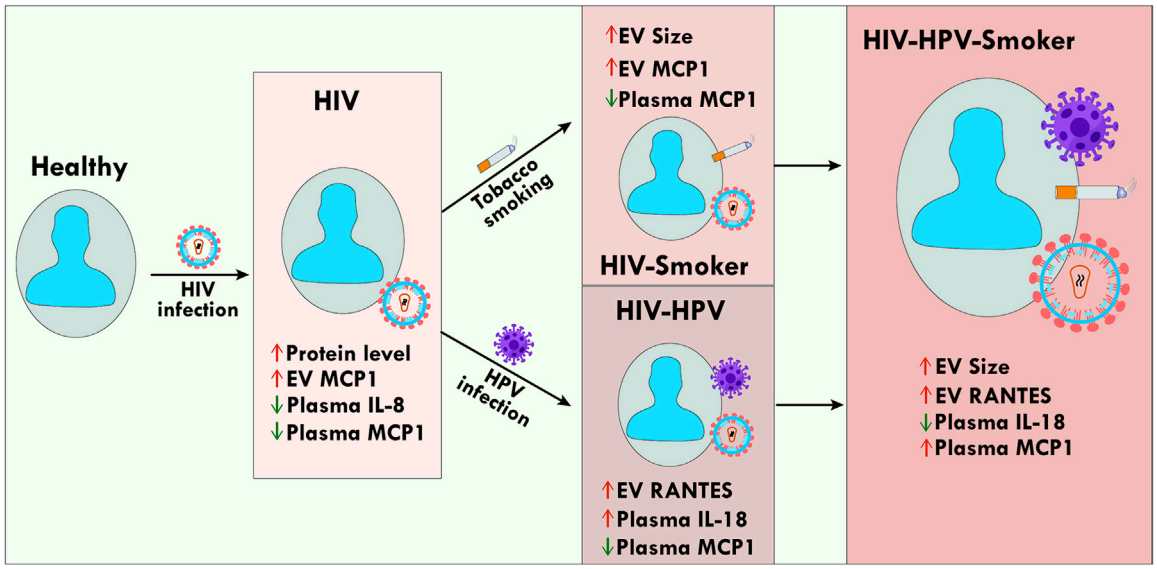

GRAPHICAL ABSTRACT

Human papillomavirus (HPV) is the most common sexually transmitted pathogen that causes anogenital cancers, with approximately 80% of people having acquired an HPV infection by age 50. Similar to HIV infection, the prevalence of anogenital HPV is also higher in AA than Caucasian Americans [6]. When HPV infection persists, it can lead to the development of anogenital and other cancers [7, 8]. Among more than 100 types of HPV, the most prevalent high risk types of HPV are HPV16 and 18 [7–9], which have been detected in ~70% of cervical cancers [8, 10].

Epidemiological data suggest that the risk of HIV infection is increased by ~2-fold in patients who are infected by HPV, and the risk of HPV infection is also increased in HIV seropositive patients [11–14]. It is possible that crosstalk exists between HPV- and HIV-infected cells, since HPV infection strongly correlates with immunosuppression, which is the hallmark of HIV infection. Therefore, investigation of biological interactions between HPV- and HIV-infected cells is important towards finding effective interventions for patients with this comorbidity. Previously, we have shown that supernatants from HPV-infected cells increase HIV replication via cytochrome P450 (CYP) and oxidative stress pathways when applied to HIV-infected cells *in vitro* [15].

Tobacco smoking is more prevalent in people living with HIV compared to the general population [16]. It is well established that cigarette smoke and tobacco constituents differentially regulate immune activation, inflammation, and oxidative stress [7, 8], leading to HIV pathogenesis [9–14]. Our own studies [17–19] have confirmed this. Persistent HIV pathogenesis in tobacco users exacerbates HAND [15–17]. Similarly, tobacco smoking, including second-hand smoking, is associated with a high risk of HPV infection and HPV-related pathogenesis, including cervical cancer [20, 21]. Further this study has shown that the combination of HPV and cigarette smoke promotes superoxide dismutase 2 (SOD2) alterations, leading to increased DNA damage and HPV pathogenesis. An epidemiological study also shows an association between CYP1A1, which activates tobacco constituents, and an increased susceptibility for HPV-induced precancer in the uterine cervix [22]. Recently, we have shown the role of inflammatory pathways via tumor necrosis factor α (TNF-α), nuclear factor kappa-light-chain-enhancer of activated B cells (NF-κB), and interleukin-6 (IL-6) in smoking-induced HPV pathogenesis, including HPV16 E6/E7 oncogenes and epithelial-mesenchymal transition markers in cervical cancer cells [23].

Literature reports and our studies [24] suggest that redox balance and oxidative stress are promoting factors in HPV-initiated pathogenesis [25, 26]. HPV infection can modulate the host cell redox homeostasis to favor infection and possibly alter cellular metabolism to enhance HIV pathogenesis [24–28]. Furthermore, increased inflammatory markers found in women with persistent HPV infection could lead to decreased immune functions and increased inflammation [29, 30], which are hallmarks of HIV pathogenesis.

Extracellular vesicles (EVs) play a significant role in the progression and modulation of both HIV and HPV infections, resulting in cellular pathogenesis including cervical cancers, by facilitating intercellular communication between infected and uninfected cells [18, 19, 31]. Upon HIV infection, EVs derived from infected cells can carry viral proteins, RNA, and oxidative and inflammatory mediators enhancing viral spread, immune activation, and chronic inflammation [20] (PMID: 38655385). Recent studies have shown that EVs in HIV-infected cells can package specific biomolecules including miRNA and oxidative and inflammatory agents upon exposure to drugs of abuse including tobacco smoking [21, 22]. Similarly, upon HPV infection, EVs can transport viral oncogenes such as E6 and E7, contributing to immune evasion and cancer progression, particularly in cervical and head and neck cancers [23–25].

It is conceivable that EVs that are differentially packed with components of the oxidative stress pathway, such as antioxidant enzymes (AOEs) and inflammatory cytokines and chemokines derived from HPV-infected cells, are circulated in plasma so that the contents are delivered to HIV-infected cells. The enhanced levels of oxidative stress and inflammation may thus contribute to enhanced HIV pathogenesis in HPV+HIV coinfected cells. EVs are small nanovesicles that can package and transport diverse biological cargo, such as proteins, mRNA, and miRNA, to distant cells, thus serving both as diagnostic biomarkers [32, 33] and as potential therapeutic targets [34]. We have shown elevated levels of HPV cell-derived EVs containing CYP1A1, CYP2A6, SOD1, and HPV oncoproteins (HPV16 E6) [24].

In this study, our objective is to examine differential levels of EVs and EV biomarkers, particularly oxidative stress and inflammatory cytokines/chemokines, in plasma derived from healthy, HIV-positive, and HIV+HPV-positive subjects. Our hypothesis is that the levels of EVs and EV components will differ in plasma derived from HIV+HPV-positive subjects compared to subjects infected with only HIV or neither virus. We further hypothesize that these EV components will differ in HIV+HPV-positive subjects who are tobacco smokers compared to nonsmokers. Since HIV and HPV are more prevalent in the AA population, and HPV is more prevalent in women, we examined the levels of plasma EV and their components in AA women, comparing smokers to nonsmokers.

Materials and methods

Sample and study design

We conducted a case-control study by recruiting participants from five distinct groups: healthy nonsmokers, HIV-positive nonsmokers, HIV and HPV coinfected nonsmokers, HIV-positive smokers, and HIV and HPV coinfected smokers (Table 1). Written informed consent was obtained from all participants, and institutional review board approval was

TABLE 1 Sample characteristics.

Description	Age	CD4 counts (cells/mm^3)	Smoking status	HIV status	HPV status
Healthy nonsmoker (n = 6)	24–65		Never smoked cigarettes	Negative	Negative
HIV$^+$/HPV$^-$ nonsmoker (n = 6)	30–55	739 ± 269	Never smoked cigarettes	Positive	Negative
HIV$^+$/HPV$^+$ nonsmoker (n = 5)	35–64	694 ± 314	Never smoked cigarettes	Positive	Positive
HIV$^+$/HPV$^-$ smoker (n = 6)	45–68	754 ± 254	Currently smoke cigarettes some days of the week	Positive	Negative
HIV$^+$/HPV$^+$ smoker (n = 5)	29–65	813 ± 213	Currently smoke cigarettes some days of the week	Positive	Positive

secured at each site—The University of Tennessee Health Science Center and The University of Mississippi Medical Center. The study sample consisted of 5-6 AA women in each group ranging between 29 and 68 years of age (Table 1). Apparently, neither HPV coinfection nor smoking appeared to significantly impact CD4 counts, likely due to the controlled viral load since they were on ART (Table 1). The HIV viral load was ≤21 copies/mL with two exceptions: one participant in the HIV$^+$/HPV$^-$ group had a viral load of 36 copies/mL and another one in the HIV$^+$/HPV$^+$ group had a viral load of 586 copies/mL. Since they were on ART, the HIV viral load was undetectable in most women: 4 of 6 in the HIV$^+$/HPV$^-$ group who had never smoked, 3 of 4 HIV$^+$/HPV$^-$ ever smokers, 3 of 5 HIV$^+$/HPV$^+$ nonsmokers, and 2 of 5 in the HIV$^+$/HPV$^+$ ever smoker group.

For EV characterization and Western blot analysis, we used samples from four randomly selected subjects per group, and for cytokine and chemokine analysis, samples from five to six subjects per group were analyzed. In this study, we did not recruit a group with HPV infection alone or a healthy smoker group because our goal was to determine how HPV infection, with or without tobacco smoking, alters EV constituents specifically within the context of HIV infection.

A chart review was conducted to determine inclusion and exclusion criteria for participants' recruitment. The inclusion criteria were: (A) Healthy group—generally healthy individuals, as determined by a standard history and physical exam, with no evidence of HPV on an anal and/or cervical Papanicolaou (Pap) test within the last 3 months and a negative HIV test within the last 6 months; (B) HIV$^+$/HPV$^-$—HIV-positive individuals with a manageable CD4 count (>400 cells/μL) based on the CDC's 2008 Stage II HIV-1 classification, drawn within the past 3 months, and negative for high-risk HPV on an anal or cervical Pap test within the past 3 months; (C) HIV$^+$/HPV$^+$—HIV-positive individuals with a manageable CD4 count tested within the past 3 months and positive for a high-risk HPV type based on an anal or cervical Pap smear within the past 3 months; and (D) Smoker groups—individuals who currently smoke cigarettes every day of the week or on some days of the week. The exclusion criteria included children, pregnant or lactating women, current or former smokers in the nonsmoker group, and individuals diagnosed with tuberculosis or hepatitis A, B, or C.

Isolation and characterization of plasma EVs

Buffy coats or blood samples from freshly drawn blood were processed to isolate plasma. Approximately 50 mL of blood was collected in 3 vacutainer tubes with potassium EDTA using a 21-gauge needle. Centrifugation at 750 × *g* for 10 min at 4 °C was performed within 15 min of blood collection, and plasma was collected and stored at −80 °C within 3 h of blood draw. EVs were freshly extracted from plasma (50 μL) specimens utilizing a modified methodology derived from previously established protocols [26, 34, 35], employing a commercially available precipitation reagent (Invitrogen Catalog number 4484450). The method yields EVs with minimal plasma, including HIV particles, or cellular contaminations, which are not likely to interfere with our analysis. Initially, plasma underwent filtration through a 0.22 μm filter followed by centrifugation at 10,000 x *g* for a duration of 20 min to eliminate larger particulates. The resultant supernatant was combined with 0.5 volumes of phosphate-buffered saline (PBS) and 0.2 volumes of the exosome precipitation reagent, then incubated at ambient temperature for 10 min, followed by centrifugation at 10,000 x *g* for 5 min to obtain the EV pellet. The EV pellet was resuspended in 100 μL RIPA buffer or PBS as needed for the subsequent experiments. We measured the size and zeta potential of EVs by dynamic light scattering using a Zetasizer Nano-ZS (Malvern Instruments Inc, Malvern, UK).

Western blot analysis

Isolated EVs were lysed with RIPA buffer including protease inhibitors, and protein concentration was determined using the Pierce BCA Protein Assay Kit (ThermoFisher Scientific, Cat. No. 23225). Equal protein amounts (10 μg) were loaded on polyacrylamide gels, electrophoresed, and transferred onto PVDF membranes. Membranes were blocked in LI-COR blocking buffer for one hour and incubated overnight at 4 °C with primary antibodies specific to CD63 (1:500, Cat. No. 25682-1-AP, Proteintech), CD9 (1:500, Cat. No. 60232-1-1g, Proteintech), Alix (1:500, Cat. No. sc-53538, Santa Cruz Biotechnology), IL-6 (1:400, Cat. No. 21865-1-AP, Proteintech), IL-18 (1:400, Cat. No. 10663-1-AP, Proteintech), MCP-1 (1:400, Cat. No. 66272-1-1g, Proteintech),

SOD1 (1:1000, Cat No. sc-101523, Santa Cruz Biotechnology), or catalase (1:500, Cat. No. 21260-1-AP, Proteintech). After washing, membranes were incubated with IRDye-conjugated secondary antibodies (1:10,000, Cat. No. 926-32211 for anti-mouse and 926-68072 for anti-rabbit, LI-COR Biosciences) for one hour at room temperature in the dark. Protein bands were visualized using the LI-COR Scanner and quantified using LI-COR Image Studio Software (v5.2, LI-COR Biosciences).

Multiplex ELISA

Cytokine and chemokine concentrations, encompassing both pro-inflammatory and anti-inflammatory mediators, were evaluated in plasma-derived EVs and plasma utilizing a tailored human 9-Plex ProcartaPlex™ multiplex immunoassay (ThermoFisher Scientific) [27, 28]. The method yields minimal EV cytokines/chemokines contamination from plasma samples, which is not likely to interfere with our analysis. A 50 µL plasma sample and equivalent amount of EVs isolated from 50 µL plasma were used for ELISA. Samples and standards were incubated in a magnetic 96-well enzyme-linked immunoassay (ELISA) plate for one hour at ambient temperature, followed by a series of washing steps. The quantification of cytokine and chemokine concentrations was carried out according to the assay protocols, and the resulting concentrations were reported in pg/mL. EV packaging efficiency was calculated by dividing the cytokine/chemokine value in EVs by the corresponding plasma (free cytokines/chemokines) plus EV cytokine/chemokine values and multiplying by 100 (EV packaging = EV packaging (%) = [EV / (plasma + EV)] × 100. Plasma samples used for ELISA (50 µL, without detergent treatment) contained both free and EV-associated cytokines/chemokines, but only free cytokines/chemokines were quantified. For simplicity, we write this as plasma cytokines/chemokines in results and discussion. In contrast, EV pellets were resuspended in a detergent-containing buffer, allowing release of EV-encapsulated cytokines/chemokines. Some degree of cross-contamination is possible. For example, plasma cytokines/chemokines may contain EV surface cytokines/chemokines, or EV cytokines/chemokines may carry cytokines/chemokines from plasma fraction. Although the absolute percentage of cytokines/chemokines packaged within EVs may therefore be imprecise, the relative comparison of EV packaging among different groups remains valid.

Statistical analysis

All outcomes are shown as the mean ± standard error of the mean (SEM) from n = ≥4 subjects per group. Comparisons of statistical data between experimental groups were conducted using one-way ANOVA with Tukey's post-hoc test applied for multiple comparisons. A p-value of less than 0.05 was considered statistically significant, with significance levels denoted as follows: $^{*}p < 0.05$, $^{**}p < 0.01$, $^{***}p < 0.001$, $^{****}p < 0.0001$.

Results

Characterization of plasma EVs from healthy nonsmokers and HIV and HIV+HPV individuals in nonsmoker and smoker groups

Our results demonstrated that the total plasma-derived EV protein levels were significantly elevated in the HIV-positive, nonsmoker group (Figure 1A, $^{*}p < 0.05$) compared to the healthy control. However, the presence of HPV co-infection in the HIV-positive nonsmoker group did not result in a further increase in EV protein levels. Similarly, in both the HIV-positive and the HIV+HPV-positive smoker groups, tobacco smoking did not lead to a further increase in EV protein levels. Although these groups showed a pattern of increase in EV protein levels compared to healthy groups, the increase was not statistically significant. Thus, HIV infection is the primary driver of elevated EV protein levels, whereas HPV co-infection or smoking does not contribute to further increases. Smoking markedly decreased the plasma EV protein levels in both HIV-positive and HIV+HPV-positive individuals, although the results were not statistically significant.

The zeta potential of plasma EVs remained unchanged across all experimental groups, including HIV-positive and HIV+HPV-positive nonsmoker and smoker groups, indicating a consistent surface charge distribution relative to the healthy control (Figure 1B). This suggests that neither HIV nor HPV co-infection, alone or in combination with smoking, significantly altered the electrostatic properties of EVs.

The plasma EV size exhibited notable differences across groups (Figures 1C,D). Compared to the healthy control (42.65 ± 2.60 nm), the HIV-positive (59.13 ± 9.012 nm) and HIV+HPV-positive (50.57 ± 1.61 nm) nonsmoker groups showed a modest increase in EV size, but they were not statistically significant. More pronounced differences were observed in the smoker subgroups, where the HIV-positive smoker group (62.77 ± 1.17 nm) had significantly larger EVs than the control, and the HIV+HPV-positive smoker group (78.97 ± 2.77 nm) displayed the most substantial increase (Figures 1C,D). Statistical comparisons indicate that the HIV+HPV-positive smoker group exhibited a significantly larger EV size than both the HIV-positive and HIV+HPV nonsmoker groups. The finding that smoking in the context of HIV and HPV co-infection contributes to a significant increase in EV size suggests potential alterations in EV biogenesis or cargo composition (Figures 1C,D). There is mixed correlation between EV protein levels (Figure 1A) and EV size (Figures 1C,D) for most groups suggest that the increase in EV protein levels could be a result of either increased EV size or increased EV numbers. Compared to healthy individuals,

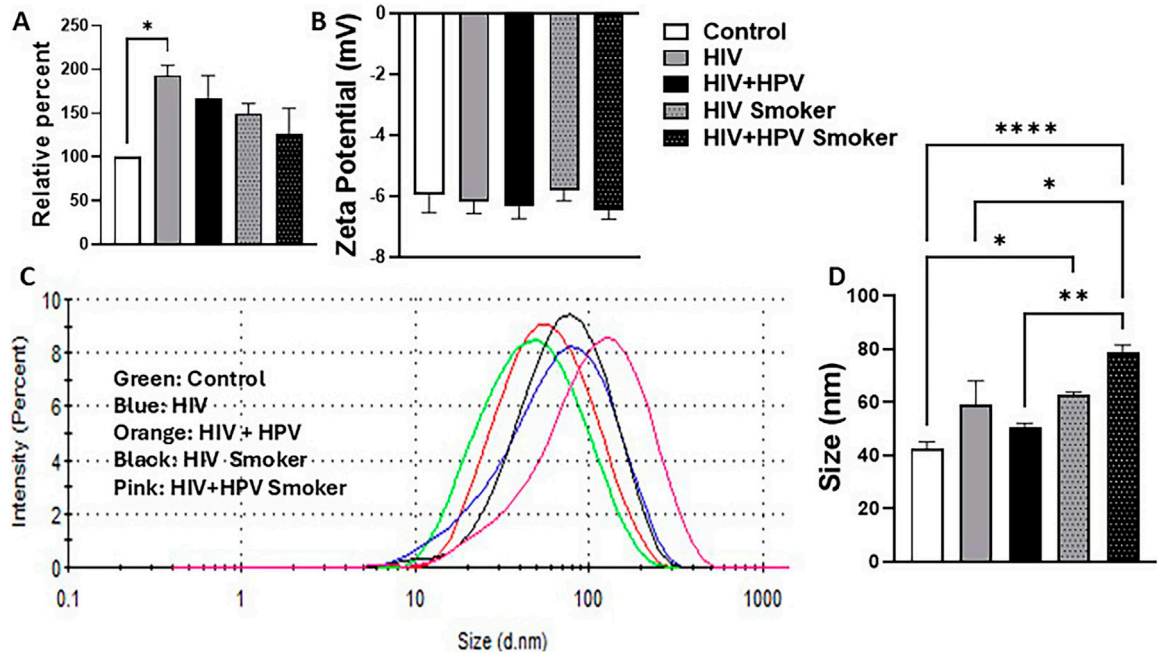

FIGURE 1
Characterization of plasma EVs from healthy nonsmokers and HIV and HIV+HPV individuals in nonsmoker and smoker groups. EVs were isolated using filtration and precipitation as described in Materials and Methods. EVs were characterized using. **(A)** Quantification of total EV proteins presented as relative percent, **(B)** Zeta potential, **(C)** Size distribution (intensity-weighted), and **(D)** Mean size. The EV proteins were quantified using Pierce BCA Protein Assay Kit, and the size and zeta potential of EVs were measured and analyzed using the dynamic light scattering (DLS) method. Statistical analysis was performed by one-way ANOVA with Tukey's *post hoc* test. Values are shown as mean ± SEM (n = 4/group). *$p < 0.05$, **$p < 0.01$, ****$p < 0.0001$.

HIV-positive non-smokers exhibited an increase in EV protein levels without a significant change in EV size. In contrast, among HIV-HPV coinfected individuals, smokers showed an increase in EV size compared to nonsmokers, without a corresponding change in EV protein levels.

Relative levels of plasma-derived EV negative and positive marker proteins in healthy nonsmokers and HIV and HIV+HPV individuals in nonsmoker and smoker groups

EV negative marker proteins (actin, calnexin, and GAPDH) and EV marker proteins (CD63, CD9, and Alix) were examined in plasma samples from the five different groups. Western blot analysis was performed to verify the existence or non-existence of these markers in the EV fractions, affirming the legitimacy of the isolated vesicles (Figure 2). As expected, while actin, calnexin, and GAPDH were present in positive control (cellular fractions), these proteins were absent or negligible in EV fractions of all the groups (Figures 1A,B). In comparison to the healthy nonsmokers, HIV infection resulted in a marked increase in CD63 and CD9, but not Alix levels in EVs in the HIV-positive and HIV+HPV-positive nonsmoker groups, suggesting that HIV infection could alter EV composition (Figure 2C). However, the changes did not reach statistical significance. On the other hand, compared to HIV-positive nonsmoker groups, the levels of none of the EV marker proteins were substantially altered in HIV and HIV+HPV-positive smoker groups (Figure 2D). These findings indicate that although HIV and HPV infections may affect EV cargo by enhancing CD63 and CD9, smoking does not additionally modify these changes. It should be noted that because two separate Western blots were performed for the same HIV non-smoker samples in Figure 2A vs. Figure 2B and Figure 2C vs. Figure 2D, the observed differences in protein band intensities are attributable to inter-blot variability. Similarly, since these are two different blots, we cannot compare results between Figure 2C,D. These situations apply to the subsequent analysis in Figures 3, 4.

Relative levels of plasma-derived EV antioxidant enzymes in healthy nonsmokers and HIV and HIV+HPV individuals in nonsmoker and smoker groups

Next, we examined the levels of the common plasma EV oxidative stress marker proteins, SOD1 and catalase, using Western blot analysis (Figures 3A,B). These antioxidant

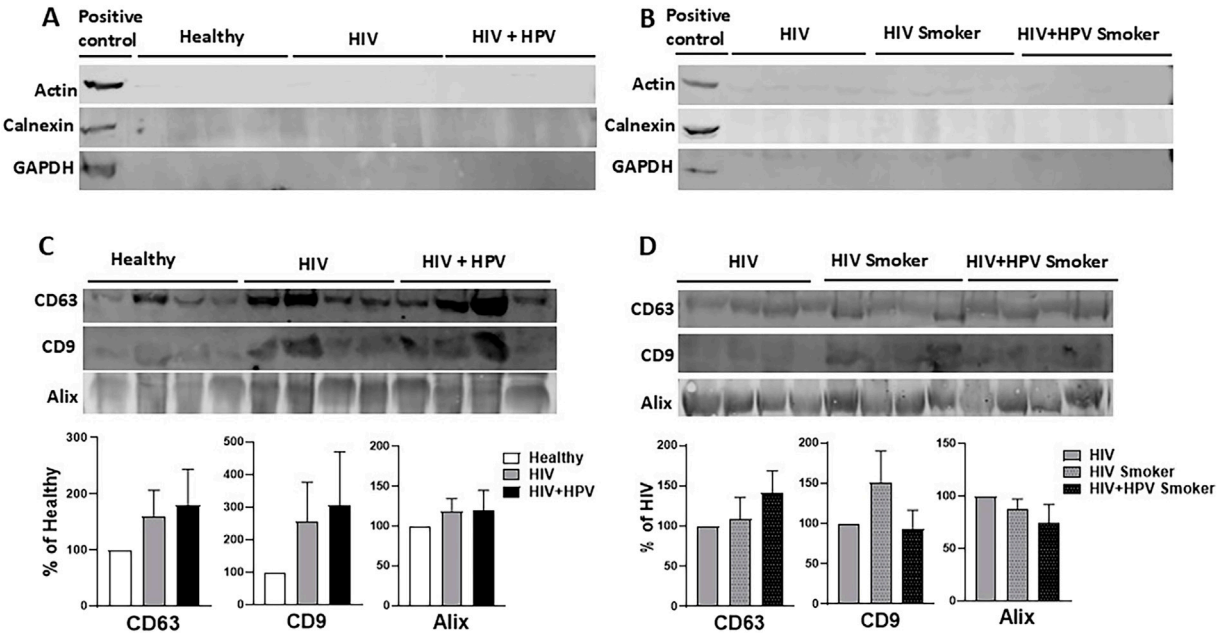

FIGURE 2
Relative levels of plasma-derived EV negative and positive marker proteins. **(A)** Analysis of EV negative marker proteins actin, calnexin, and GAPDH from plasma-derived EVs in healthy, HIV, and HIV+HPV nonsmoker groups. **(B)** Analysis of EV negative marker proteins actin, calnexin, and GAPDH from plasma-derived EVs in HIV nonsmoker and HIV and HIV+HPV smoker groups. **(C)** Analysis of EV marker proteins CD63, CD9, and Alix from plasma-derived EVs in healthy, HIV, and HIV+HPV nonsmoker groups. **(D)** Analysis of EV marker proteins CD63, CD9, and Alix from plasma-derived EVs in HIV nonsmoker and HIV and HIV+HPV smoker groups. Western blot of EV marker proteins and their quantitative analyses were performed as described in Materials and Methods. Values are expressed as mean ± SEM (*n* = 4/group).

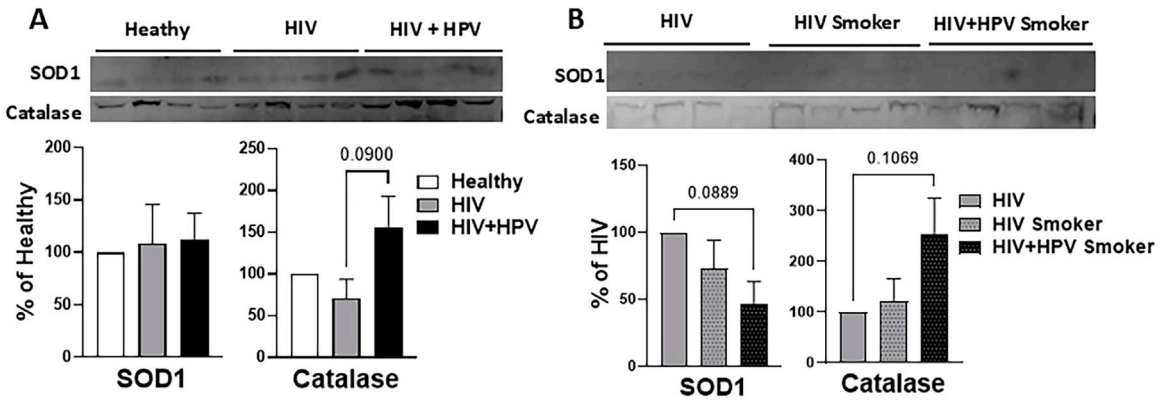

FIGURE 3
Relative levels of plasma-derived EV antioxidant enzymes. **(A)** Analysis of SOD1 and catalase from plasma-derived EVs in healthy, HIV, and HIV+HPV nonsmoker groups. **(B)** Analysis of SOD1 and catalase from plasma-derived EVs in HIV nonsmoker and HIV and HIV+HPV smoker groups. Western blot of EV SOD1 and catalase and their quantitative analysis were performed as described in Materials and Methods. Statistical analysis was performed by one-way ANOVA with Tukey's *post hoc* test. Values are expressed as mean ± SEM (n = 4/group). Because no comparisons reached statistical significance at $p < 0.05$, actual p-values ≤0.1 are reported.

enzymes (AOEs) can detoxify oxidants and reduce oxidative stress. Their presence in plasma EVs suggests that AOEs originating from one tissue or organ could lead to altered oxidative stress in distant recipient tissues or organs via systemic circulation. Although not statistically significant, the levels of EV catalase appear to increase in HIV+HPV nonsmokers in comparison to healthy controls (Figure 3A). Our results also showed that compared to healthy

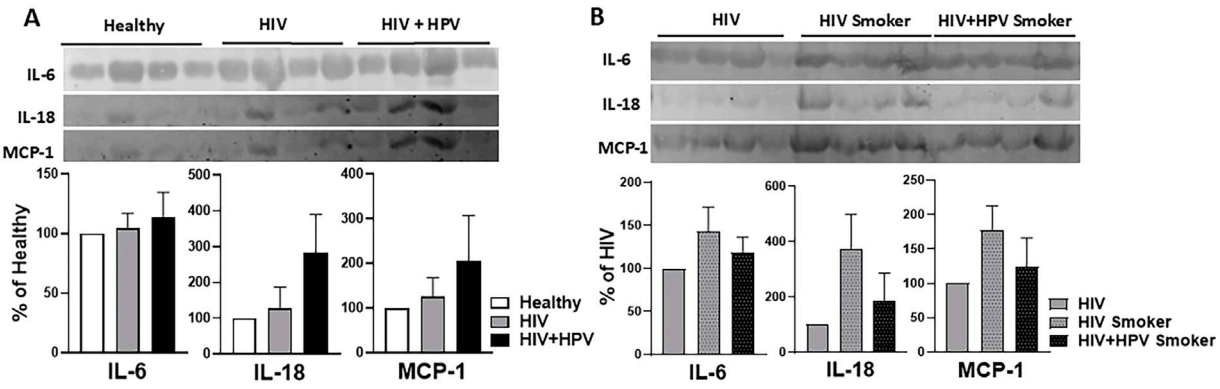

FIGURE 4
Relative levels of plasma-derived EV cytokines and chemokines. **(A)** Analysis of cytokines IL-6 and IL-18 and chemokine MCP-1 from plasma-derived EVs in healthy, HIV, and HIV+HPV in nonsmoker groups. **(B)** Analysis of cytokines IL-6 and IL-18 and chemokine MCP-1 from plasma-derived EVs in HIV nonsmoker and HIV and HIV+HPV smoker groups. Western blot of EV cytokines and chemokines and their quantitative analysis were performed as described in Materials and Methods. Statistical analysis was performed by one-way ANOVA with Tukey's *post hoc* test. Values are expressed as mean ± SEM (n = 4/group). No comparisons reached statistical significance at $p < 0.05$.

nonsmokers with HIV, SOD1 and catalase had opposite trends; SOD1 decreased, and catalase increased in both the HIV and HIV+HPV smoker groups, although the results were not statistically significant (Figure 3B). These findings suggest that while HIV+HPV coinfections impact catalase levels in nonsmokers, both HIV and HIV+HPV infections impact both SOD1 and catalase in smokers.

Relative levels of plasma-derived EV cytokines and chemokines in healthy nonsmokers and HIV and HIV+HPV individuals in nonsmoker and smoker groups

Similarly, important proinflammatory interleukins (IL-6 and IL-18) and a chemokine [monocyte chemoattractant protein-1 MCP-1 (also known as CCL2)] linked to EVs, were examined in plasma EV samples using Western blot analysis (Figure 4). Their involvement in inflammatory signaling and presence in EVs could suggest systemic immune activation and modified intercellular communication in relation to HIV and HPV infections, especially upon tobacco smoking.

Compared to healthy nonsmokers, HIV+HPV coinfection resulted in a marked increase in the levels of IL-18 and MCP-1, but not IL-6, in plasma EVs in the HIV+HPV-positive nonsmoker group (Figure 4A). However, the changes did not reach statistical significance. Similarly, although not statistically significant, the levels of these EV cytokines and chemokines were markedly increased in HIV-positive and slightly increased in HIV+HPV-positive smoker groups compared to the HIV nonsmoker group (Figure 4B). These findings suggest that while HIV+HPV coinfection may only increase EV cytokine and chemokine levels in nonsmoking groups, HIV infection may increase these levels in smoking groups.

Relative cytokine and chemokine distributions between plasma and plasma-derived EVs in healthy and HIV and HIV+HPV individuals

Furthermore, we used the ELISA method to carry out the measurement and analysis of several plasma and EV-associated cytokines and chemokines, which are considered important in the context of HIV and HPV infections. In this analysis, we combined nonsmoker and smoker groups to assess the impact of HIV and HIV+HPV infections on EV and plasma cytokines/chemokines, regardless of smoking status. The analysis may offer insights into the packaging of plasma EV cytokines and chemokines and their possible function in immune activation and inflammation via intercellular communication upon HIV and HIV+HPV coinfections (Figure 5).

The IL-6 could not be detected by ELISA in this study. In comparison to the healthy nonsmokers, EV IL-8 exhibited an upward trend in both HIV and HIV+HPV infections, while plasma IL-8 was significantly decreased (Figures 5A,B). This may suggest a transfer of IL-8 from plasma to EVs, with a total packaging efficiency of 15–30% upon HIV and HIV+HPV coinfections, respectively. IL-18 displayed a rising trend in EV packaging in both HIV and HIV+HPV groups relative to healthy controls (Figure 5C). Interestingly, a significant increase in plasma IL-18 was observed in HIV+HPV coinfected compared to HIV. It is possible that overall IL-18 level is

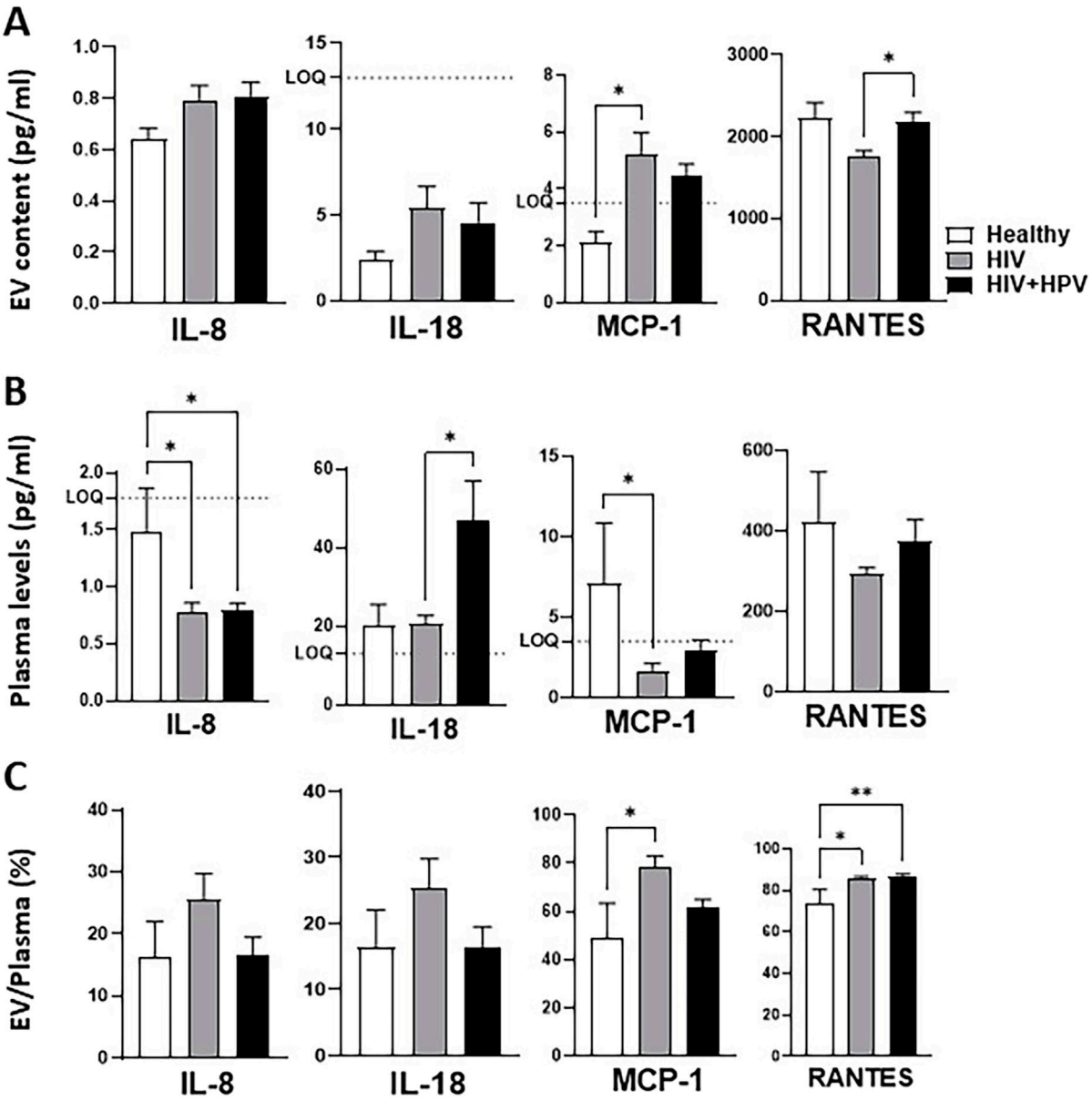

FIGURE 5
Relative cytokines and chemokines distributions between plasma and plasma-derived EVs in healthy, HIV, and HIV+HPV individuals. **(A)** Analysis of cytokines and chemokines in plasma-derived EVs of Healthy, HIV, and HIV+HPV. **(B)** Analysis of cytokines and chemokines in plasma of Healthy, HIV, and HIV+HPV. **(C)** Ratio of EV and plasma cytokines and chemokines in healthy, HIV, and HIV+HPV. Cytokine and chemokine levels were measured using a human 9-Plex ProcartaPlex™ multiplex immunoassay as described in Materials and Methods. The EV packaging efficiency was calculated by dividing the EV cytokine or chemokine values with that of plasma plus EV cytokine or chemokine values, multiplied by EV packaging (%) = [EV / (plasma + EV)] × 100. The ELISA measures only soluble or free plasma cytokines and chemokines. Statistical analysis was performed by one-way ANOVA with Tukey's *post hoc* test. Values are expressed as mean ± SEM (n = 5–6/group). *$p < 0.05$.

upregulated upon HIV and/or HIV+HPV infections, thereby increasing its levels in both EV and plasma. The total EV packaging efficiency of IL-18 was assessed at 15–25%, without a significant change in EV IL-18 packaging in any of the groups.

For the chemokine MCP-1, compared to healthy controls, a significant increase in EV protein was noted in the HIV group, and no further change was detected in the HIV+HPV group (Figure 5A). Conversely, compared to healthy controls, plasma MCP-1 concentrations were significantly and markedly decreased in individuals infected with HIV and HIV+HPV groups, respectively (Figure 5B). The total packaging efficiency of MCP-1 was 50% in healthy controls and was significantly and

markedly increased in HIV (75%) and HIV+HPV (60%) groups, respectively (Figure 5C).

A significant rise in another chemokine RANTES, also known as CCL5, was seen in EVs of individuals coinfected with HIV and HPV when compared to the HIV-only group, whereas plasma RANTES did not vary significantly across the groups (Figures 5A,B). Perhaps HPV rescues the effect of HIV infection with regards to RANTES. Importantly, the total packaging efficiency of RANTES, a chemotactic factor for inflammatory and immune cells, in healthy controls was 75%, and was significantly increased in both HIV and HIV+HPV groups (85%) (Figure 5C).

Overall, these results show that proinflammatory cytokines IL-8 and IL-18 and chemokines RANTES and MCP-1 show a general trend of increased packaging in EVs and decreased levels in plasma in HIV-positive and/or HIV+HPV. Importantly, the high packaging percentage for RANTES and MCP-1 along with their increased packaging in HIV and/or HIV+HPV groups suggests a potential role for these chemoattractants in EV-mediated cell-cell interactions in HIV and/or HPV infected populations.

Relative cytokine and chemokine distributions between plasma and plasma-derived EVs in HIV and HIV+HPV individuals in nonsmoker and smoker groups

The analysis of plasma cytokines and chemokines and EV-associated proinflammatory cytokines and chemokines was carried out in HIV and HIV+HPV groups, and they were compared between nonsmoker and smoker groups (Figure 6). We also analyzed EV packaging percentage of cytokines and chemokines in HIV and HIV+HPV individuals between nonsmoker and smoker groups.

The IL-6 could not be detected by ELISA in this study. One of the challenges of the IL-8 measurement was that the cytokine levels were below the lower level of quantification (LLQ), suggesting low detection sensitivity. Nevertheless, the analysis suggests that the levels of EV IL-8, plasma IL-8, and its packaging percentage (EV/plasma) did not significantly change in smokers compared to nonsmokers, irrespective of their infection status (HIV and/or HIV+HPV) (Figure 6). The analysis also showed a relatively high packaging (about 50%) across the groups (Figure 6C).

Similarly, compared to HIV infection, there was no significant change in EV IL-18 packaging by either HIV+HPV coinfection or smoking (Figure 6C). Interestingly, compared to HIV alone, HIV+HPV coinfections significantly increased plasma IL-18 in nonsmokers and markedly decreased the IL-18 plasma levels in smokers (Figure 6B). The overall packaging of IL-18 is relatively low (15–25%), compared to IL-8 packaging (about 50%), without a significant change between the groups (Figure 6C).

There was a significant and marked increase in EV MCP-1 packaging by HIV and HIV+HPV, respectively, in smokers compared to nonsmokers (Figure 6A). The increased EV packaging of MCP-1 in smoker groups, especially for HIV individuals, appears to be correlated with a significant decrease in the levels of MCP-1 in plasma. Interestingly, compared to HIV alone, HIV+HPV coinfections significantly decrease plasma MCP-1 in nonsmokers, but significantly increase plasma MCP-1 in smokers (Figure 6B). Similar to IL-18 and RANTES, the overall packaging of MCP-1 is also high (60–75%) across the groups, without a significant change between the groups (Figure 6C).

Similarly, the analysis showed a trend in increase in EV RANTES packaging by HIV+HPV coinfections, especially in smokers compared to nonsmokers and/or HIV alone. However, the plasma levels across the group were unaltered (Figures 6A,B). As expected, the EV packaging percentage was very high (>80%) in all the groups with no further increase in smokers for either HIV or HIV+HPV groups (Figure 6C).

Overall, the differential packaging of these cytokines and chemokines in EVs may indicate their role in modulating inflammation and immune responses under varying conditions. For example, MCP-1 shows increased packaging into EVs in smokers, and IL-18 appears to have the opposite trend, at least for HIV+HPV coinfections in nonsmokers vs. smokers (Figure 6A).

Discussion

Tobacco smoking is a recognized risk factor that aggravates the progression of both HIV and HPV, with a notably higher prevalence of smoking found in individuals with HIV than in the general population [29], [36]. Previous research, including our findings, has shown that cigarette smoke and components of tobacco lead to differential immune regulation, inflammation, and oxidative stress; particularly, increased inflammation and oxidative stress speed up HIV progression and worsen HAND [35], [9–14], [27, 28], [30–32]. Likewise, tobacco consumption has been closely associated with heightened vulnerability to HPV infection and more severe HPV-related diseases, such as cervical cancer [23]. Cigarette smoke has been demonstrated to cause changes in SOD2, which results in heightened DNA damage and fosters HPV-related cancer development [37]. Moreover, the activation of cytochrome P450 enzymes, especially CYP1A1, boosts the metabolic activation of carcinogens from tobacco, heightening the vulnerability to premalignant alterations in HPV-infected cells [38]. Considering that both HIV and HPV pathogenesis involve immune dysfunction and oxidative stress, it is reasonable to suggest that tobacco exposure exacerbates these pathogenic processes via EVs, which act as carriers for

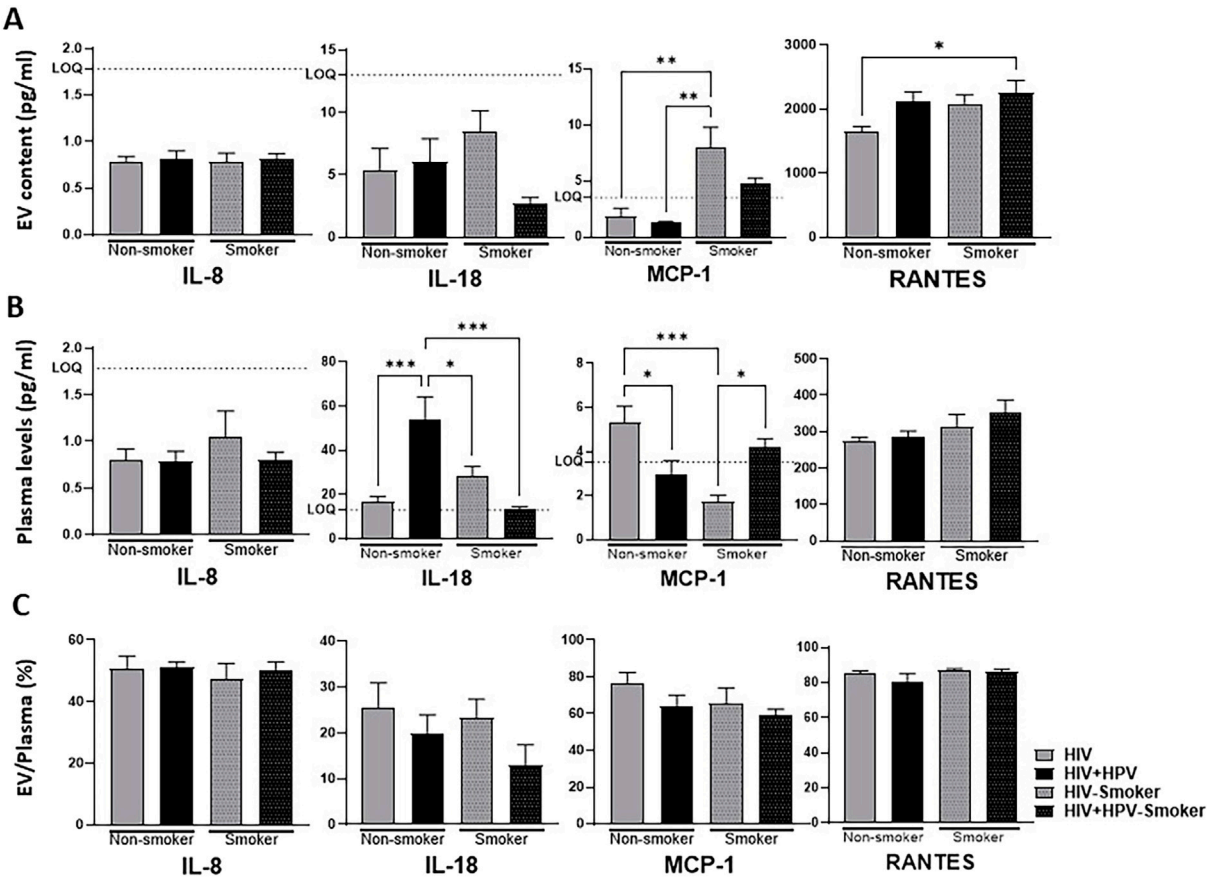

FIGURE 6
Relative cytokine and chemokine distributions between plasma and plasma-derived EVs in HIV and HIV+HPV individuals in nonsmoker and smoker groups. **(A)** Analysis of cytokines and chemokines in plasma-derived EVs of HIV and HIV+HPV individuals in nonsmoker and smoker groups. **(B)** Analysis of cytokines and chemokines in plasma of HIV and HIV+HPV individuals in nonsmoker and smoker groups. **(C)** Ratio of EV and plasma cytokines and chemokines in HIV and HIV+HPV individuals in nonsmoker and smoker groups. Cytokine and chemokine levels were measured using human 9-Plex ProcartaPlex™ multiplex immunoassay as described in Materials and Methods. The EV packaging efficiency was calculated by dividing the EV cytokines/chemokines values with that of plasma plus EV cytokines/chemokines values, multiplied by 100 (EV/(plasma+EV)x100). The ELISA measure soluble or free plasma cytokines/chemokines. Statistical analysis was performed by one-way ANOVA with Tukey's *post hoc* test. Values are expressed as mean ± SEM (n = 5–6/group). *$p < 0.05$, **$p < 0.01$, ***$p < 0.001$.

inflammatory mediators and molecules associated with oxidative stress.

The findings of our research suggest that HIV infection is a significant factor in raising EV protein levels, while coinfection with HPV and smoking do not lead to additional increases. These results are consistent with earlier studies, which have shown that HIV infection results in heightened EV secretion, probably because the virus takes control of the exosomal biogenesis pathway to promote viral spread and immune modulation [39, 40]. The absence of increased EV protein levels in individuals coinfected with HPV indicates that HPV does not independently influence EV secretion in relation to HIV. This aligns with earlier research indicating that HPV mainly affects the composition of EV cargo rather than the total production of EVs [41]. Additionally, the consistent zeta potential observed in all experimental groups indicates that the surface charge of EVs does not vary with infection status, aligning with previous studies demonstrating that EVs preserve their electrostatic characteristics for effective cellular uptake [42]. Nonetheless, EV size showed distinct variations, especially in smokers, with HIV and HPV coinfected smokers experiencing the largest rise. This indicates that smoking could affect EV biogenesis or change the molecular makeup of EVs. Earlier research has indicated that components of tobacco, such as nicotine and polycyclic aromatic hydrocarbons, increase EV secretion and modify their cargo by inducing oxidative stress and inflammation [43]. The significant rise in EV size among smokers coinfected with HIV and HPV may indicate a heightened inflammatory response, possibly leading to an acceleration in disease progression.

Examination of EV marker proteins emphasizes how HIV alters EV composition, as shown by elevated CD63 and CD9 levels in those infected with HIV, consistent with current

research [40]. The tetraspanins CD63 and CD9 are often upregulated in EVs from HIV-infected cells, likely contributing to viral spread and evasion of the immune response [44]. HPV coinfection did not increase levels of CD63 and CD9, indicating that HPV does not significantly influence EV tetraspanin-associated cargo. This discovery aligns with earlier research indicating HPV's capability to modify EV composition, specifically regarding the inclusion of oncogenic proteins, rather than impacting EV marker proteins [40]. Furthermore, the level of Alix, an essential factor in EV biogenesis, was consistent in all groups, suggesting that neither HIV nor HPV interferes with the basic mechanism of EV formation. Smoking had no effect on EV marker expression, which contradicts certain studies suggesting that oxidative stress from smoking might change EV profiles [43]. The absence of alterations in EV marker levels among smokers indicates that although smoking might enhance EV size, it does not affect EV biogenesis or markers associated with tetraspanins. These results emphasize the intricate nature of EV-mediated interactions in HIV and HPV infections, underscoring the differing impact of viral infections and external influences like smoking on EV traits. Additional studies are required to clarify how smoking-related modifications in EV size could relate to functional changes in EV cargo and their effects on disease progression.

The effect of coinfection with HIV and HPV on EV-related inflammatory cytokines and chemokines offers important insights into systemic immune activation and cell-to-cell communication. Our results indicate that although HIV infection by itself or together with HPV does not substantially change IL-6, IL-18, or MCP-1 levels in EVs, there is a noticeable trend towards heightened IL-18 and MCP-1 levels in individuals infected with HIV, particularly in those also infected with HPV. This finding is consistent with earlier research indicating that coinfection with HIV and HPV leads to heightened inflammatory responses, mainly through pathways associated with IL-18 and MCP-1, which play roles in monocyte attraction and immune activation [43]. Nevertheless, the lack of notable IL-6 upregulation indicates that HIV and HPV might selectively influence inflammatory cytokines via EVs, likely emphasizing pathways linked to chronic inflammation and immune dysfunction over acute-phase responses [42]. Interestingly, smoking seemed to reduce this inflammatory response, as IL-18 and MCP-1 levels in the smoker groups did not follow the same patterns seen in nonsmokers. This discovery indicates that oxidative stress linked to tobacco might inhibit or change the packaging of cytokines within EVs, which could interfere with immune signaling and lead to immune dysregulation in smokers coinfected with HIV and HPV [44].

Additional examination of cytokine distribution in plasma and EVs indicated a notable change in inflammatory mediators like IL-8, RANTES, and MCP-1, showing greater incorporation into EVs among HIV and HIV+HPV coinfected individuals, whereas plasma concentrations of these cytokines were significantly diminished. This indicates that viral infections could promote the entrapment of inflammatory cytokines within EVs, potentially serving as a regulatory mechanism to manage excessive systemic inflammation. Consistent with our findings, earlier studies demonstrate that EV-mediated cytokine transport is vital for regulating immune responses in chronic infections [45]. The notable rise in EV-related RANTES in individuals coinfected with HIV and HPV, while maintaining stable plasma levels, underscores the possible function of EVs in specifically modulating chemokine signaling, potentially aiding in the recruitment of immune cells to sites of infection. Furthermore, the noted rise in MCP-1 packaging efficiency in HIV and HIV+HPV groups (50–80%) corroborates previous findings suggesting that MCP-1 plays a crucial role in monocyte trafficking during HIV infection [40]. The results indicate that the compartmentalization of cytokines into EVs may serve as a method through which HIV and HPV influence immune signaling to avoid detection by the immune system or to promote viral persistence. Overall, our research emphasizes the significance of EVs in influencing inflammatory responses during HIV and HPV coinfections and points out the necessity for additional studies on their effects on disease advancement and possible therapeutic interventions.

The distinct packaging of proinflammatory cytokines in EVs, along with their plasma concentrations in individuals coinfected with HIV and HPV, underscores an essential mechanism in immune modulation and the development of viral diseases. Our results indicate that IL-8, MCP-1, IL-18, and RANTES show heightened encapsulation in EVs, while their plasma concentrations are markedly lower in individuals coinfected with HIV and HPV. The noted transition of IL-8 from plasma to EVs, demonstrating a packaging efficiency of 15–30%, implies that EVs could serve as reservoirs for inflammatory cytokines, promoting intercellular communication and boosting local immune responses while curbing systemic inflammation. This aligns with earlier research suggesting that EV-mediated cytokine transport contributes to immune cell recruitment and activation in chronic infections, such as HIV [46]. Significantly, RANTES showed the highest packaging efficiency (75–80%), especially in individuals coinfected with HIV and HPV, aligning with findings that associate RANTES with immune cell movement and inflammation during HIV infection [47]. The significant rise in MCP-1 packaging in HIV and HIV+HPV coinfections reinforces its involvement in monocyte recruitment and ongoing immune activation, a key feature of HIV pathogenesis [48]. The change in cytokine distribution implies that EVs are crucial in controlling inflammation in individuals infected with HIV and HIV+HPV by capturing cytokines from the plasma, potentially altering their biological impact on immune balance and disease advancement.

The influence of smoking on EV-mediated cytokine behavior in HIV and HIV+HPV infections highlights its

role in altering inflammatory responses. In contrast to IL-8, which stayed the same, both RANTES and MCP-1 displayed elevated levels in smokers, while MCP-1 demonstrated a shift from plasma into EVs without affecting its packaging efficiency. These results are consistent with earlier studies that emphasize smoking's contribution to chronic inflammation and immune system dysfunction in individuals with HIV [49]. The noted decrease in plasma IL-18 among smokers, coupled with no significant rise in EV-associated IL-18, indicates that smoking might either inhibit IL-18 production or promote its removal, thus altering inflammatory pathways in a manner distinct from that of nonsmokers. Previous research has demonstrated that cigarette smoke triggers oxidative stress and modifies cytokine release, which may clarify these inconsistencies [50]. Moreover, the rise in RANTES levels found in smokers, in both plasma and EVs, indicates that smoking boosts chemokine signaling, possibly worsening immune cell recruitment and leading to ongoing inflammation. Since RANTES is vital in HIV pathogenesis by facilitating viral replication and immune activation, these results emphasize the necessity for additional research on smoking-related alterations in EV-mediated inflammatory signaling regarding HIV and HPV coinfections. Our research collectively offers new perspectives on the roles of EV-mediated intercellular interactions leading to altered inflammation upon HIV and HIV+HPV infections, especially in tobacco smokers.

In summary, smoking seemed to change EV properties, enlarging EV size and changing cytokine distribution, particularly leading to a significant transfer of MCP-1 and IL-18 from plasma into EVs. The results suggest that the EVs are essential in regulating inflammatory signaling and immune responses in individuals coinfected with HIV and HPV, while smoking may additionally affect these interactions. Our results show that HIV infection notably boosts EV secretion and modifies cytokine composition, with greater incorporation of proinflammatory factors like IL-8, RANTES, and MCP-1, while decreasing their levels in plasma. This indicates that EVs function as storage for inflammatory cytokines, possibly promoting localized immune activation and restricting systemic inflammation.

Limitations of the study

The major limitations of this study include a relatively small sample size and the absence of smoker-only and HPV-only control groups. The absence of smoker-only and HPV-only groups restrict interpretation of HPV-specific and smoking-specific effects. For example, the study doesn't assert that smoking amplifies HPV effects; instead, it concludes that smoking modulates EV properties and cargo within HIV and HIV+HPV infected groups. Our study cannot distinguish biological interactions from behavioral co-occurrence. The observed smoking-HPV association may reflect shared behavioral factors, but not as proof that smoking biologically amplifies HPV effects. Additionally, all subjects had well-controlled HIV through antiretroviral treatment, which may have masked the potential effects of HPV coinfection and tobacco smoking. As a pilot study, the primary goal was to explore whether HPV and smoking further influence EV biogenesis and EV-associated inflammatory responses in individuals with HIV. Based on the findings presented above, a larger follow-up study is currently underway, which will include smoker-only and HPV-only control groups. The future study will also incorporate a longitudinal component, potentially recruiting newly HIV-infected individuals who have not yet initiated antiretroviral therapy, particularly among HPV-infected and smoker populations.

Author contributions

SK designed and conceived the idea. NS, TC, LH, CR, SG, amd LZ performed experiments. NS, LZ, and SG analyzed the data and prepared the figures. ZS wrote the first draft of the manuscript. SK reviewed and edited the manuscript. All authors contributed to the article and approved the submitted version.

Author disclaimer

The content is solely the responsibility of the authors and does not necessarily represent the official views of the National Institutes of Health.

Data availability

The raw data supporting the conclusions of this article will be made available by the authors, without undue reservation.

Ethics statement

The studies involving humans were approved by Institutional Review Board from The University of Tennessee Health Science Center and The University of Mississippi Medical Center. The studies were conducted in accordance with the local legislation and institutional requirements. The participants provided their written informed consent to participate in this study.

Funding

The author(s) declared that financial support was received for this work and/or its publication. This work was supported by the CORNET award of the University of Tennessee Health Science Center and University of Mississippi Medical Center. This research was also supported by the National Institutes of Health grant U54GM115428 to Carolann Risley and AG081140 to SK.

Acknowledgements

We acknowledge Aubri Hickman for participant selection and consenting participants, and Sydney Reaves for assistance with data management at the University of Mississippi Medical Center. We also acknowledge Crystal Walker from the College of Nursing, University of Tennessee Health Science Center, and Nathan Summer at the Adult Special Care, Regional One Hospital, to help with subject recruitment. Finally, we also acknowledge Dr. Ahmed Rakib for his assistance in preparing the graphical abstract.

Conflict of interest

The author(s) declared no potential conflicts of interest with respect to the research, authorship, and/or publication of this article.

Generative AI statement

The author(s) declared that generative AI was not used in the creation of this manuscript.

Any alternative text (alt text) provided alongside figures in this article has been generated by Frontiers with the support of artificial intelligence and reasonable efforts have been made to ensure accuracy, including review by the authors wherever possible. If you identify any issues, please contact us.

References

1. Beyrer C, Ratevosian J, Gelderblom H, Rosenberg NE. The HIV/AIDS pandemic: where are we now? *AIDS* (2025) **39**:1497–504. doi:10.1097/QAD.0000000000004308

2. Mehta H, Nazzal K, Sadikot RT. Cigarette smoking and innate immunity. *Inflamm Res* (2008) **57**:497–503. doi:10.1007/s00011-008-8078-6

3. Singh SP, Kalra R, Puttfarcken P, Kozak A, Tesfaigzi J, Sopori ML. Acute and chronic nicotine exposures modulate the immune system through different pathways. *Toxicol Appl Pharmacol* (2000) **164**:65–72. doi:10.1006/taap.2000.8897

4. Sopori M. Effects of cigarette smoke on the immune system. *Nat Rev Immunol* (2002) **2**:372–7. doi:10.1038/nri803

5. Sgambato JA, Jones BA, Caraway JW, Prasad GL. Inflammatory profile analysis reveals differences in cytokine expression between smokers, moist snuff users, and dual users compared to non-tobacco consumers. *Cytokine* (2018) **107**:43–51. doi:10.1016/j.cyto.2017.11.013

6. Hodge-Bell KC, Lee KM, Renne RA, Gideon KM, Harbo SJ, McKinney WJ. Pulmonary inflammation in mice exposed to mainstream cigarette smoke. *Inhal Toxicol* (2007) **19**:361–76. doi:10.1080/08958370601144076

7. Arimilli S, Schmidt E, Damratoski BE, Prasad GL. Role of oxidative stress in the suppression of immune responses in peripheral blood mononuclear cells exposed to combustible tobacco product preparation. *Inflammation* (2017) **40**:1622–30. doi:10.1007/s10753-017-0602-9

8. van der Vaart H, Postma DS, Timens W, ten Hacken NH. Acute effects of cigarette smoke on inflammation and oxidative stress: a review. *Thorax* (2004) **59**:713–21. doi:10.1136/thx.2003.012468

9. Ande A, McArthur C, Kumar A, Kumar S. Tobacco smoking effect on HIV-1 pathogenesis: role of cytochrome P450 isozymes. *Expert Opin Drug Metab Toxicol* (2013) **9**:1453–64. doi:10.1517/17425255.2013.816285

10. Valiathan R, Miguez MJ, Patel B, Arheart KL, Asthana D. Tobacco smoking increases immune activation and impairs T-cell function in HIV infected patients on antiretrovirals: a cross-sectional pilot study. *PLoS One* (2014) **9**:e97698. doi:10.1371/journal.pone.0097698

11. Sajja RK, Rahman S, Cucullo L. Drugs of abuse and blood-brain barrier endothelial dysfunction: a focus on the role of oxidative stress. *J Cereb Blood Flow Metab* (2016) **36**:539–54. doi:10.1177/0271678X15616978

12. Steel HC, Venter WDF, Theron AJ, Anderson R, Feldman C, Kwofie L, et al. Effects of tobacco usage and antiretroviral therapy on biomarkers of systemic immune activation in HIV-infected participants. *Mediators Inflamm* (2018) **2018**:8357109. doi:10.1155/2018/8357109

13. Mu Y, Patters BJ, Midde NM, He H, Kumar S, Cory TJ. Tobacco and antiretrovirals modulate transporter, metabolic enzyme, and antioxidant enzyme expression and function in polarized macrophages. *Curr HIV Res* (2018) **16**:354–63. doi:10.2174/1570162X17666190130114531

14. Amegashie EA, Sikeola RO, Tagoe EA, Paintsil E, Torpey K, Quaye O. Oxidative stress in people living with HIV: are diverse supplement sources the solution? *Health Sci Rep* (2025) **8**:e70824. doi:10.1002/hsr2.70824

15. Persidsky Y, Gendelman HE. Mononuclear phagocyte immunity and the neuropathogenesis of HIV-1 infection. *J Leukoc Biol* (2003) **74**:691–701. doi:10.1189/jlb.0503205

16. Pereira Hslmn CF. The blood-brain barrier in HIV-Associated dementia. *NeuroAids* (2000) **3**.

17. Nottet HS. Interactions between macrophages and brain microvascular endothelial cells: role in pathogenesis of HIV-1 infection and blood - brain barrier function. *J Neurovirol* (1999) **5**:659–69. doi:10.3109/13550289909021294

18. Saleem M, Chang CW, Qadeer A, Asiri M, Alzahrani FM, Alzahrani KJ, et al. The emerging role of extracellular vesicles in viral transmission and immune evasion. *Front Immunol* (2025) **16**:1634758. doi:10.3389/fimmu.2025.1634758

19. Dong S, Zhang Y, Wang Y. Role of extracellular vesicle in human papillomavirus-associated cervical cancer. *J Cancer Res Clin Oncol* (2023) **149**:16203–12. doi:10.1007/s00432-023-05374-x

20. Tang Z, Lu Y, Dong JL, Wu W, Li J. The extracellular vesicles in HIV infection and progression: mechanisms, and theranostic implications. *Front Bioeng Biotechnol* (2024) **12**:1376455. doi:10.3389/fbioe.2024.1376455

21. Kaddour H, Kopcho S, Lyu Y, Shouman N, Paromov V, Pratap S, et al. HIV-infection and cocaine use regulate semen extracellular vesicles proteome and miRNAome in a manner that mediates strategic monocyte haptotaxis governed by miR-128 network. *Cell Mol Life Sci* (2021) **79**(5):5. doi:10.1007/s00018-021-04068-2

22. Haque S, Kodidela S, Gerth K, Hatami E, Verma N, Kumar S. Extracellular vesicles in smoking-mediated HIV pathogenesis and their potential role in biomarker discovery and therapeutic interventions. *Cells* (2020) **9**:864. doi:10.3390/cells9040864

23. Acevedo-Sanchez V, Rodriguez-Hernandez RM, Aguilar-Ruiz SR, Torres-Aguilar H, Romero-Tlalolini MLA. Extracellular vesicles in cervical cancer and HPV infection. *Membranes (Basel)* (2021) **11**:453. doi:10.3390/membranes11060453

24. Chen X, Liu Y, Luo X, Pan T, Zhang T, Hu L, et al. HPV16 E6-induced M2 macrophage polarization in the cervical microenvironment *via* exosomal miR-204-5p. *Sci Rep* (2024) **14**:23725. doi:10.1038/s41598-024-74399-0

25. Harden ME, Munger K. Human papillomavirus 16 E6 and E7 oncoprotein expression alters microRNA expression in extracellular vesicles. *Virology* (2017) **508**:63–9. doi:10.1016/j.virol.2017.05.005

26. Kodidela S, Wang Y, Patters BJ, Gong Y, Sinha N, Ranjit S, et al. Proteomic profiling of exosomes derived from plasma of HIV-infected alcohol drinkers and cigarette smokers. *J Neuroimmune Pharmacol* (2020) **15**:501–19. doi:10.1007/s11481-019-09853-2

27. Kodidela S, Ranjit S, Sinha N, McArthur C, Kumar A, Kumar S. Cytokine profiling of exosomes derived from the plasma of HIV-infected alcohol drinkers and cigarette smokers. *PLoS One* (2018) **13**:e0201144. doi:10.1371/journal.pone.0201144

28. Haque S, Kodidela S, Sinha N, Kumar P, Cory TJ, Kumar S. Differential packaging of inflammatory cytokines/chemokines and oxidative stress modulators in U937 and U1 macrophages-derived extracellular vesicles upon exposure to tobacco constituents. *PLoS One* (2020) **15**:e0233054. doi:10.1371/journal.pone.0233054

29. Rahmanian S, Wewers ME, Koletar S, Reynolds N, Ferketich A, Diaz P. Cigarette smoking in the HIV-infected population. *Proc Am Thorac Soc* (2011) **8**:313–9. doi:10.1513/pats.201009-058WR

30. Ranjit S, Kumar S. Recent advances in cancer outcomes in HIV-positive smokers. *F1000Res* (2018) **7**:F1000 Faculty Rev-718. doi:10.12688/f1000research.12068.1

31. Ande A, McArthur C, Ayuk L, Awasom C, Achu PN, Njinda A, et al. Effect of mild-to-moderate smoking on viral load, cytokines, oxidative stress, and cytochrome P450 enzymes in HIV-infected individuals. *PLoS One* (2015) **10**:e0122402. doi:10.1371/journal.pone.0122402

32. Kumar A, Sinha N, Kodidela S, Zhou L, Singh UP, Kumar S. Effect of benzo(a)pyrene on oxidative stress and inflammatory mediators in astrocytes and HIV-infected macrophages. *PLoS One* (2022) **17**:e0275874. doi:10.1371/journal.pone.0275874

33. Rao P, Ande A, Sinha N, Kumar A, Kumar S. Effects of cigarette smoke condensate on oxidative stress, apoptotic cell death, and HIV replication in human monocytic cells. *PLoS One* (2016) **11**:e0155791. doi:10.1371/journal.pone.0155791

34. van Niel G, D'Angelo G, Raposo G. Shedding light on the cell biology of extracellular vesicles. *Nature Reviews Molecular Cell Biology* (2018) **19**(4):213–228.

35. Kumar A, Sinha N, Haque S, Kodidela S, Wang T, Martinez AG, Chen H, Kumar S. Nicotine self-administration with menthol and audiovisual cue facilitates differential packaging of CYP2A6 and cytokines/chemokines in rat plasma extracellular vesicles. *Scientific reports* (2021) **11**:1–13.

36. Jiang C, Chen Q, Xie M. Smoking increases the risk of infectious diseases: A narrative review. *Tob Induc Dis* (2020) **18**:60.

37. Carrillo-Beltrán D, Osorio JC, Blanco R, Oliva C, Boccardo E, Aguayo F. Interaction between cigarette smoke and human papillomavirus 16 E6/E7 oncoproteins to induce SOD2 expression and DNA damage in head and neck cancer. *Int J Mol Sci* (2023) **24**(8):6907.

38. Ande A, McArthur C, Kumar A, Kumar S. Tobacco smoking effect on HIV-1 pathogenesis: role of cytochrome P450 isozymes. *Expert Opin Drug Metab Toxicol* (2013) **9**(11):1453–64.

39. Koppensteiner H, Brack-Werner R, Schindler M. Macrophages and their relevance in human immunodeficiency virus type I infection. *Retrovirology* (2016) **13**(1):1–14.

40. Arenaccio C, Anticoli S, Manfredi F, Chiozzini C, Olivetta E, Federico M. Role of exosomes in HIV infection and pathogenesis. *Biomedicines* (2022) **10**(2):361.

41. Maugeri M, Nawaz M, Papadimitriou A, Angerfors A, Camponeschi A, Na M, et al. Linkage between HPV infection and exosomal cargo in cervical cancer: a comprehensive analysis. *Proteomics Clin Appl* (2019) **13**(2):e1800072.

42. Urbanelli L, Magini A, Buratta S, Brozzi A, Sagini K, Polchi A, et al. Signaling pathways in exosomes biogenesis, secretion and fate. *Genes* 2019;**10**(2):91–43.

43. Caruso S, Venza I, Visalli G, Facciolà A, Malara N, Vita G, et al. Tobacco smoking and HPV: the role of oxidative stress, inflammatory pathway activation, and cellular senescence in the pathogenesis of HPV-related diseases. *Int J Mol Sci* (2020) **21**(11):3800.

44. de Carvalho JV, de Castro RO, da Silva EZ, Silveira PP, da Silva-Júnior IF. Exosomes from HIV-infected cells reinforce viral infection and impair antiviral immune responses. *Front Microbiol* (2021) **12**:735225.

45. Kumar MA, Baba SK, Sadida HQ, Marzooqi SA, Jerobin J, Altemani FH, et al. Extracellular vesicles as tools and targets in therapy for diseases. *Signal Transduct Target Ther* (2024) **9**(1):27.

46. Carpintero-Fernández P, Fafián-Labora J, O'Loghlen A, Rodríguez-Navarro JA. Extracellular vesicles in aging and chronic inflammation: a case for senescence-associated EVs in age-related diseases. *J Extracell Vesicles* (2020) **9**(1):1710428.

47. Harding C, Heuser J, Stahl P. Exosomes: looking back three decades and into the future. *J Cell Biol* (2021) **211**(4):769–80. doi:10.1083/jcb.202011014

48. Ribeiro CM, Vargas MR, Hollenbach AD. Regulation of immune cell function by extracellular vesicles and their implications in HIV-1 infection. *Front Immunol* (2019) **10**:2446. doi:10.3389/fimmu.2019.02446

49. Kelesidis T, Kendall MA, Yang OO, Hodis HN, Currier JS. Cigarette smoking and HIV: independent predictors of immune activation in HIV-1 infection. *AIDS* (2020) **34**(5):735–44.

50. Shirazi F, Vasudevan S, Zhang H, Yuan J. The impact of cigarette smoke on immune cell activation and cytokine profiles in HIV-infected individuals. *Int J Mol Sci* (2022) **23**(9):4890. doi:10.3390/ijms23094890

EBM Experimental Biology and Medicine

TYPE Review
PUBLISHED 06 February 2026
DOI 10.3389/ebm.2026.10712

OPEN ACCESS

*CORRESPONDENCE
Yu-Chi Liu,
liuchiy@gmail.com

†These authors have contributed equally to this work

RECEIVED 19 June 2025
REVISED 04 January 2026
ACCEPTED 26 January 2026
PUBLISHED 06 February 2026

CITATION
Shanmathi AV, Yu M, Liu C, Lee IXY, Tong L and Liu Y-C (2026) Electrotherapy in the management of neuropathic corneal pain: narrative review.
Exp. Biol. Med. 251:10712.
doi: 10.3389/ebm.2026.10712

Electrotherapy in the management of neuropathic corneal pain: narrative review

A. V. Shanmathi[1†], Mingyi Yu[2†], Chang Liu[2], Isabelle Xin Yu Lee[2], Louis Tong[3,4,5] and Yu-Chi Liu[2,4,5*]

[1]Trinity College Dublin, University of Dublin, Dublin, Ireland, [2]Regenerative Therapy Group, Singapore Eye Research Institute, Singapore, Singapore, [3]Ocular Surface Research Group, Singapore Eye Research Institute, Singapore, Singapore, [4]Department of Cornea and External Eye Disease, Singapore National Eye Centre, Singapore, Singapore, [5]Ophthalmology and Visual Sciences Academic Clinical Program, Duke-NUS Medical School, Singapore, Singapore

Abstract

Neuropathic corneal pain (NCP) is a debilitating condition resulting from corneal nerve damage or dysfunction, leading to persistent ocular pain, discomfort and hypersensitivity. Conventional therapy with eye drops often provides inadequate relief, necessitating the need for alternative therapeutic approaches. This review explores the role of electrotherapy in managing NCP, including its mechanisms, clinical efficacy, and potential integration into multimodal treatment strategies. We examine current evidence on various electrotherapy modalities such as transcutaneous electrical nerve stimulation, neurostimulation, and microcurrent stimulation. These electrotherapies have the potential to modulate pain pathways, promote nerve regeneration, and restore corneal homeostasis. Emerging studies suggest electrotherapy may alleviate NCP by altering neural signaling and reducing hyperalgesia. Integrating electrotherapy into existing pain management strategies may enhance the outcomes for patients with refractory NCP. However, its clinical application remains limited by a lack of standardized protocols and robust clinical trials. Although electrotherapy presents a promising and non-invasive option for NCP management, further research is needed to optimize the treatment parameters and optimal duration, assess the long-term efficacy, and establish guidelines for clinical use.

KEYWORDS

corneal nerve dysfunction, hyperalgesia, nerve regeneration, neuropathic corneal pain, ocular pain management, transcutaneous electrical nerve stimulation

Impact statement

Neuropathic corneal pain (NCP) poses a significant clinical challenge with limited effective treatment options, affecting patients' quality of life for its persistent ocular discomfort unresponsive to conventional therapies of dry eye. This comprehensive review advances the field by evaluating electrotherapy modalities, including transcutaneous

electrical nerve stimulation, neurostimulation, and microcurrent stimulation as novel therapeutic approaches for NCP management. It provides critical new insights by synthesizing current evidence on the mechanisms of action of electrotherapy in promoting corneal nerve regeneration and modulating pain pathways, establishing a foundation for evidence-based clinical applications. This synthesis has a direct impact on clinical practice by identifying gaps in current treatment protocols and proposing standardized approaches for integrating electrotherapy into multimodal pain management strategies. This review aims to provide clinicians and researchers with necessary guidance for optimizing therapeutic outcomes, establishing a roadmap for future clinical trials and treatment protocol development, ultimately advancing the standard of care for patients suffering from this debilitating condition.

Introduction

Neuropathic pain is defined by The International Association for the Study of Pain (IASP) as "pain caused by a lesion or disease of the somatosensory nervous system". When it occurs in the cornea, it is referred to as neuropathic corneal pain (NCP). It causes patients to experience eye pain in the absence of any painful stimulus [1]. The cornea has a dense network of nerves in the body, making the cornea one of the most potent in pain generation in the body [2]. Small Aδ and C nerve fibers, which are part of the sensory and autonomic nervous systems, make up 70–90% of corneal nerves [2]. Coupled to the vital sensory function they hold, corneal nerves also sustain the functional integrity of the ocular surface by releasing trophic substances that support corneal homeostasis and by stimulating brainstem circuits that trigger reflex tear production and blinking [3].

Clinical features and mechanisms of neuropathic corneal pain

Etiology and origins of neuropathic corneal pain

NCP can be classified based on its underlying etiologies. Systemic causes of NCP include diabetes, systemic autoimmune diseases, medication-induced neuropathy (e.g., chemotherapy), and trigeminal neuralgia. Ocular causes include herpes simplex keratitis, dry eye disease (DED), refractive surgery, and ocular trauma [4]. In addition, NCP can be categorized based on the level of nervous system involvement, namely peripheral or central NCP [5]. Common causes of peripheral NCP include refractive surgery [6], chronic dry eye [7], and herpetic keratitis [8]. Peripheral sensitization occurs as a result of abnormal regeneration of corneal nociceptors and nerve fibers following corneal nerve injuries. Central sensitization results from elevated excitatory neurotransmitters due to chronic inflammation and, potentially, rewiring of pain perception pathways, which intensifies the perception of pain. Its common causes include small-fiber polyneuropathy, fibromyalgia, and radiation keratopathy [9].

Associated comorbid conditions

NCP often coexists with conditions that affect pain perception and psychological well-being, such as depression, anxiety, fatigue, and sleep disturbances. These conditions are not causative factors but represent comorbidities that can influence the severity and impact of NCP. Moreover, NCP may be linked to comorbidities including anxiety, depression, and chronic pain syndrome such as migraine [10].

Clinical presentations

Symptoms experienced by patients with NCP are described as dryness, burning sensation and hyperalgesia which are usually worsened by extreme temperatures, light (photoallodynia) and dry wind. Our group has identified that burning and light sensitivity are the two most common symptoms in NCP [11]. More focus is diverted to understanding the pathophysiology of pain which transitions from a protective physiological reflex to a more persistent and chronic condition [9].

Despite patients frequently reporting pain or pain-like symptoms, standard ophthalmological examinations often do not reveal objective or visible findings. This discrepancy can lead to delayed diagnosis and even many patients being misdiagnosed with dry eye disease (DED), which is a multifactorial condition characterized by an imbalance in tear film homeostasis and ocular symptoms, with tear film instability and hyperosmolarity, ocular surface inflammation and damage, and neurosensory abnormalities playing etiological roles [12]. Importantly, NCP and DED are not mutually exclusive and may coexist, or one may be a precursor or a sequel. These two conditions share partial overlap in symptomatology and underlying pathophysiological mechanisms. DED patients present with a range of symptoms including ocular dryness, burning, aching and tenderness, overlapping considerably with the symptom profile of NCP [7]. Additionally, neuroinflammation response is suggested to contribute to the pathogenesis of both conditions [7]. Due to the mismatch between the severity of symptoms and observable signs, patients' symptoms are often dismissed as "psychological" or "functional," leaving them feeling ignored and neglected, worsening their condition [10]. In terms of quality of life, Chin et al reported that patients with NCP had significantly worse quality of life on the majority of the items in the Ocular Pain Assessment Survey and Ocular Surface Disease Index

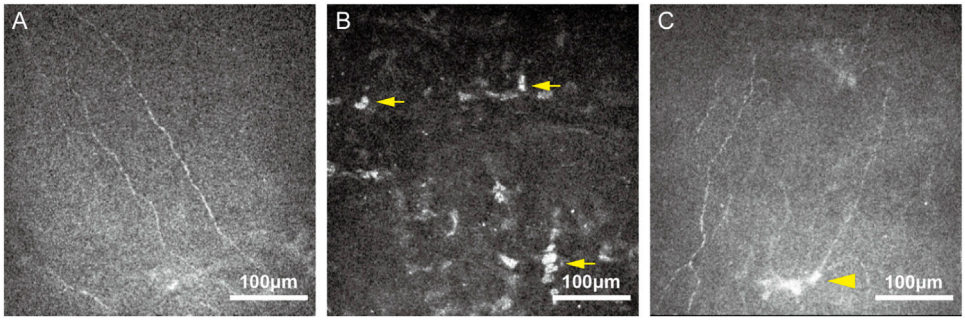

FIGURE 1
Representative *in vivo* confocal microscopy (IVCM) images from patients with NCP. **(A)** Decreased corneal nerve density and nerve fiber fractal dimension. **(B)** Activated keratocytes (arrows), appeared as patchy areas of increased stromal reflectivity. **(C)** Microneuromas (arrowhead) manifested as irregularly shaped enlargements of terminal nerve endings with poorly defined margins and variable hyper-reflectivity.

questionnaires compared to those with DED, suggesting NCP is more debilitating than DED [10].

Although patients with NCP and DED share many common symptoms, the differentiating factors are imaging findings, proteomic patterns and clinical features which explain their distinct pathophysiologies. NCP is a neuropathic disorder with nerve dysfunction, corneal microneuromas, neuroinflammation, and pain that is disproportionate to clinical signs whereas DED is an inflammatory and tear film disorder accompanied with epithelial damage, immune activation, and symptoms that are correlating with objective findings. Microneuromas are the key differentiator and NCP patients exhibit higher numbers, larger area and larger perimeter of microneuromas than DED patients. NCP patients have elevated levels of tear proteome associated with neuronal activity and neuroinflammation whereas DED showed proteomic patterns dominated by inflammatory mediators [7]. Treatment wise, some patients with NCP do not respond to conventional treatments used to treat DED and thus differentiating them is essential to offer more effective treatment [13].

In vivo confocal microscopy (IVCM) imaging findings of neuropathic corneal pain

In-vivo confocal microscopy (IVCM) has been extensively used to visualize the corneal nerve plexus and corneal cells [14]. Through IVCM evaluation, decreased corneal nerve densities, decreased nerve fiber fractal dimension, increased corneal nerve fiber width, activated keratocytes, smaller corneal epithelial cell size, and an increased number, area and perimeter of micro neuromas in patients with NCP were identified (Figure 1) [11, 15]. Previous study suggested that the presence of microneuromas on IVCM could serve as a biomarker to distinguish NCP from DED, with high sensitivity and specificity [16]. However, recent evidence indicates that microneuromas can be observed not only in patients with NCP, but also in painless DED and even in healthy subjects [17]. From a diagnostic perspective, the mere presence of microneuromas therefore appears insufficient to indicate corneal neuropathic alterations. Quantitative microneuroma metrics, such as perimeter and area, may be required to improve diagnostic specificity [17].

Pathogenesis and pathways involved in neuropathic corneal pain

NCP is characterized by increased release of excitatory neurotransmitters at presynaptic terminals, ectopic firing of nerve fibers, nerve sprouting and rewiring, spontaneous generation of action potentials, abnormalities in signal conduction, and transformation of non-nociceptive sensory fibers into nociceptive ones [18]. Nociceptors are important for pain perception and can produce action potentials in response to thermal, mechanical, chemical, or polymodal stimuli [19]. The nociceptors are centrally connected to higher-order somatosensory pain pathways and the thalamus, where pain is perceived. Tissue damage and inflammation of the ocular surface cause peripheral axonal injuries and release of pro-inflammatory mediators, which lower the activation thresholds of ion channels in affected nerve endings. These sensitizing effects may spread to adjacent nociceptors, enhancing peripheral nociceptive signaling and ultimately leading to peripheral sensitization [20].

In addition to the ascending pathways that transmit pain signals, descending modulatory pathways also play a critical role in NCP by contributing to central sensitization and heightened pain perception [21]. Descending inhibitory activity is believed to originate from the reticular system and thalamus, activating

central gamma-aminobutyric acid (GABA) receptors, modulating interneurons, and ultimately altering ascending trigeminal pain signals. Normally, interneurons release inhibitory neurotransmitters that suppress nociceptive signaling [22]. However, persistent insult reduces the inhibitory effect of GABA on ascending pathways due to changes in chloride currents [23]. As a result, signals in the ascending pain pathways intensify, contributing to the perception of chronic pain [24]. Furthermore, descending modulation of the trigeminal nuclei can be either inhibitory or facilitatory. Inhibitory control predominates under physiological conditions, while a shift toward facilitatory modulation following tissue or nerve injury may contribute to the development of chronic pain [25].

Genetic polymorphisms can also affect corneal neurophysiology and inflammation by altering the expression of neurokines and neuromediators which influences the clinical presentation and severity of NCP. A recent report discovered a single nucleotide polymorphism (rs140293404), an intronic variant in the gene ENSG00000287251, that has met the genome-wide significance threshold for NCP [26]. Genetic polymorphisms may explain why some are more susceptible to NCP.

Continuous stimulation of corneal nerves causes the release of glutamate from presynaptic afferent neurons, which activates two types of glutamate receptors: N-methyl-D-aspartic acid receptors (NMDAR), responsive to strong stimuli, and α-amino-3-hydroxy-5-methyl-4-isoxazolepropionic acid receptors (AMPAR), sensitive to weaker signals [27]. The activation of NMDAR results in intense and prolonged neural responses [9]. Peripheral axonal injury induces the release of inflammatory mediators that decrease the threshold potentials of ion channels in nerve endings, intensifying neural responses. Moreover, mechanical stimuli in the cornea are transduced by Piezo2 channels, which are low-threshold mechanically activated channels expressed in trigeminal sensory neurons innervating the cornea [28]. Research indicates that Piezo2 contributes to various forms of mechanoreceptive sensitization, including mechanical allodynia induced by inflammatory responses or injury [29, 30]. In NCP, alterations in Piezo2 channel function may affect innate reflexes and cause mechanical hypersensitivity [31]. Recurrent dysregulation of Piezo2 signaling may facilitate nociceptive sensitization and influence long-term central nervous system responses even after the offending stimulus is removed [32]. A previous study using Piezo2 conditional knockout mice demonstrated that Piezo2 channels in corneal neurons are directly involved in corneal mechano-nociception [33]. However, systemic inhibition of Piezo2 for neuropathic pain relief is not feasible due to its essential role in mechanotransduction processes across multiple organs, including touch, proprioception, and interoception [33]. Despite this limitation, topical inhibition of Piezo2 in the cornea may represent a promising strategy to alleviate discomfort and pain associated with corneal mechanical irritation and warrants further investigation. Additionally, photophobia and photoallodynia are common symptoms in NCP. The presence of melanopsin expression in trigeminal neurons suggests the existence of a functional neural pathway that permits light to influence various sensory processes [34].

Neurotrophins released during neuroinflammation in NCP act as retrograde signaling molecules. Evidence from trigeminal ganglion studies demonstrate that neurotrophins can induce changes in ion channel expression and membrane excitability in sensory neurons. Although the specific role of neutrophils in NCP remains incompletely understood, findings extrapolated from peripheral nerve injury models indicates they may promote nerve depolarization and contribute to altered pain perception through modulation of neuronal properties [35]. Chronic neuropathic nerves may further lead to reorganization, resulting in more excitable and abnormal firing patterns [36]. Furthermore, recent research indicates that immune cells, including dendritic cells, release neuropeptides and neurokines that modulate neuronal excitability, contributing to peripheral sensitization [37]. These collectively exacerbate neuroinflammation, which perpetuates the cycle of NCP [38]. As time passes, sustained peripheral input may facilitate the development of central sensitization, where central neurons become increasingly responsive to similar levels of pain, resulting in heightened pain perception [39].

On a molecular level, neurokines like Interleukin- 1 Beta (IL-1β) and Tumour Necrosis Factor-Alpha (TNF-α) bind to receptors on corneal sensory afferents, modulating neuronal excitability and lowering thresholds for generation of action potential, thus, facilitating the release of neuropeptides such as substance P [37, 38]. Substance P directs immune cells to the terminals of nociceptors, where they release neurokines that contribute to neuropathic pain [40]. Substance P and Calcitonin Gene-Related Peptide (CGRP) have prolonged effects on corneal nociceptors and are strongly implicated in sensory hypersensitivity [35]. Neurokines and neurotrophic factors promote the reorganization and increased sprouting of peptidergic nerve fibers [41]. Additionally, nerve growth factor (NGF), a neurotrophin, increases in the tears of patients with NCP [11], altering the expression of transduction molecules in C- and Aδ-fibers, increasing their excitability [42, 43]. Our group further identified the significantly dysregulated tear proteins in NCP. Specifically, the levels of metallothionein-2, creatine kinase B-type, vesicle-associated membrane protein 2, neurofilament light polypeptide and myelin basic protein were significantly over-expressed [11].

Current management of neuropathic corneal pain

Treatment of NCP involves a complex, long-term and multi-step approach. Lubricants lower tear osmolarity and dilute pro-

TABLE 1 Current management strategies for neuropathic corneal pain.

Treatment	Mechanism of action
Lubricants	Lubricants dilute pro-inflammatory mediators and lower tear osmolarity [44]
Topical steroids	Topical steroids prevent leukocyte migration by inhibiting cytokine, prostaglandin, and leukotriene production [44]
Topical cyclosporine	Cyclosporine suppresses T-cell activation and reduces inflammatory cytokines [44]
Autologous serum tears (AST)	AST contains growth factors and anti-inflammatory components that promote corneal nerve regeneration and reduce pain and photoallodynia [45]
Cryopreserved amniotic membrane (PROKERA®)	Confers anti-inflammatory and neurotrophic effects [47]
Bandage contact lenses/scleral lenses	These lenses protect the ocular surface, reduce mechanical irritation, and promote healing [47]

inflammatory mediators, while topical steroids or cyclosporines have been a cornerstone in anti-inflammatory treatments due to their ability to inhibit the production of cytokines, prostaglandins, and leukotrienes. They also prevent leukocyte migration, contributing to their overall effectiveness in reducing inflammation [44]. Autologous serum tears (AST) have been shown to improve corneal nerve regeneration, relieve corneal pain and photoallodynia as they contain growth factors and anti-inflammatory components [45]. When symptoms of NCP are due to central sensitization, systemic pharmacotherapy such as tricyclic antidepressants, anticonvulsants, low-dose naltrexone, serotonin-norepinephrine inhibitors, sodium channel blockers and calcium channel ligands are used. They may also help in treating peripheral sensitization and speed up relief measures [46]. Other ocular treatments include cryopreserved amniotic membrane (PROKERA®, Bio-Tissue, Miami, FL) that confer anti-inflammatory and neurotropic effects and extended-wear soft bandage contact lenses or scleral lenses that protect the ocular surface and promote healing by reducing mechanical irritation [47]. Table 1 summarizes the current common management strategies for Neuropathic Corneal Pain and its mechanism of action.

In addition to the above-mentioned treatment, electrotherapy is an emerging option that utilises electrical stimulation (ES) to modulate pain and is being explored as a potential treatment for managing NCP via pain modulation, neuroplasticity and reduction of sensitization [48].

Electrotherapy as a therapeutic approach for neuropathic pain

Electrotherapy in peripheral neuropathic pain

Electrotherapy has been used in the treatment of peripheral neuropathic pain. It involves using electrical impulses to stimulate nerves in the affected area, helping in pain reduction and promoting healing [49]. The analgesic effects of electricity were attributed to the activation of the descending inhibitory pathway, increasing the production of endogenous opioids [50] and other neurochemical compounds such as serotonin [51], GABA [52], and adenosine [53]. The pain reduction could also be attributed to the gate-control theory proposed by Melzack and Wall, which states that pain is modulated by inhibiting small afferent nociceptive fibers through the activation of larger afferent fibers of the spinal cord [54]. This leads to the activation of inhibitory interneurons and reducing nociceptive signaling [55].

Among different electrotherapies, Transcutaneous Electrical Nerve Stimulation (TENS) is a widely used form that involves placing electrodes on the skin near the painful area that deliver low-frequency electrical impulses to stimulate the affected nerves. Previous studies suggest that TENS may reduce nociceptive signaling by decreasing nociceptor activity, modulating the expression of pain-related ion channels, thus inhibiting nociceptor neurotransmission [56]. β-endorphins and methionine-enkephalin levels, which interact with opioid receptors, increase after high-frequency TENS, which may contribute to reduced release of glutamate and substance P in the spinal cord [55].

In diabetic neuropathy, conventional treatments for painful diabetic neuropathy have essentially focused on drug therapies such as gabapentin, pregabalin, duloxetine, and tricyclic antidepressants. However, these drugs are associated with notable side effects involving dizziness, sedation, peripheral edema and anticholinergic effects including cardiac arrhythmias [9]. Despite these treatments, many patients experience persistent pain, incurring substantial indirect and direct economic costs [57]. ES is a potentially safer option due to its minimal contraindications and absence of known drug interactions [58]. Clinical studies reported that ES enhances peripheral cutaneous circulation, potentially through stimulation of sympathetic nerves [59]. Although improved cutaneous circulation has been associated with pain relief in neuropathic conditions [60, 61], the specific underlying mechanisms remain incompletely understood. Additionally, ES has been shown to increase vascular endothelial growth

factor (VEGF) levels. VEGF improved the microcirculation associated with neuropathy, which may enhance nerve function [62]. Other studies have demonstrated notable increases in beta-endorphin levels [63], heightened expression of CGRP [64], reduction in inflammatory markers [65], and increased NGF after ES [66]. ES also diminishes pain by inhibiting nociception at the presynaptic level within the dorsal horn, thereby preventing the central transmission of pain signals [67]. Kumar et al reported that TENS resulted in a reduction in pain and discomfort in 83% of patients, although the symptoms recurred approximately after 1 month upon termination of TENS [68]. However, a systematic review presented only a slight reduction in pain intensity favoring TENS. The considerable variation in treatment protocols, such as the intensity, frequency, and duration of TENS application, made it challenging to synthesize the research findings effectively [69].

In this review, we aim to explore the role of electrotherapy in the management of NCP, focusing on its underlying mechanisms, efficacy, and clinical applications. We evaluate current evidence, highlight emerging technologies, and discuss future directions for integrating electrotherapy into clinical practice.

Search strategy and selection criteria

An electronic literature search was conducted on the PubMed database to explore the effects of electrotherapy in the management of NCP. The search utilized a combination of the following terms: "(Electrotherapy OR Electrical Stimulation OR TENS OR Neuromodulation)" AND "(Neuropathic Corneal Pain OR Keratoneuralgia OR Corneal Neuropathy OR Corneal Pain OR Neuropathic Ocular Pain)" AND" (Management OR Treatment OR Intervention)". Methods of stimulation such as transcranial direct current are not within the scope of this narrative review because it is unclear which pain pathways are involved. The search spanned from the database's inception to December 18, 2024, with no filters applied. The initial search yielded 179 references published between 1955 and 2024. Articles of various study types, including clinical trials, meta-analyses, randomized controlled trials, reviews, and systematic reviews, relevant to the application of electrotherapy in NCP, were included after duplicate removal. Exclusion criteria included non-English articles and those without full-text availability. Following the application of inclusion and exclusion criteria and a screening of titles and abstracts for relevance, 45 references were deemed suitable for further review (Figure 2). Full-text versions of these articles were assessed for eligibility. Additional relevant studies identified through cross-referencing were incorporated to provide a broader discussion, encompassing the application of electrotherapy in neuropathic pain.

Electrotherapy in neuropathic corneal pain

Recent advancements in neurostimulation technologies have led to improved outcomes in reducing chronic corneal pain, particularly in cases where conventional treatments have proven ineffective. Hence, electrotherapy has emerged as a treatment option for managing NCP, offering a potential alternative to traditional pharmacological treatments or as adjunct therapy together with conventional therapy. By delivering targeted ES to affected nerves, this therapy aims to modulate pain signals and potentially promote nerve regeneration [70].

Transcutaneous trigeminal ganglion stimulation

The pain signals from the cornea are transmitted via the trigeminal nerve, which connects with second-order neurons in the trigeminal subnucleus caudalis. These neurons send signals to the thalamus, where they link with third-order neurons that extend to the sensorimotor cortex and paralimbal region, both of which play a role in the emotional experience of pain [71]. Pain management may be improved by targeting different points along these pathways. A single case report described the use of transcutaneous trigeminal ganglion stimulation in a patient who developed severe NCP following laser-assisted *in situ* keratomileusis (LASIK). An electrode array was implanted into the trigeminal ganglion through the left foramen ovale, in which an electrode was inserted and positioned toward the V1 branch of the trigeminal ganglion. Intraoperative testing with the patient awakes confirmed paresthesia in the V1 region without causing corneal anesthesia. Despite unilateral stimulation, the patient reported immediate relief from bilateral pain. Symptom relief was maintained for 8 months but the pain re-emerged when the electrode leads migrated [72]. While these observations provide preliminary evidence suggesting that trigeminal ganglion stimulation may have effectiveness on the treatment of NCP, the evidence limited to a single case. Further studies are required to establish the safety, efficacy, and clinical applicability of this approach. Additionally, as an anecdotal observation, it lacks a control group to compare the outcomes of the neuromodulatory treatments with other treatment modalities or a placebo. Without such a comparison, it is challenging to ascertain whether the observed outcomes were directly due to the treatments or influenced by other factors, such as the natural variation of symptoms over time or psychological elements affecting the perception of pain. The report mentions complications such as the migration of the electrode and catheter, which required additional procedures and revisions. These complications suggest that whilst the treatments may provide short-term benefits, they may also carry risks of failure or require further interventions. It is also important to note that the effectiveness of these treatments may rely on the expertise of the healthcare team and the availability of specific

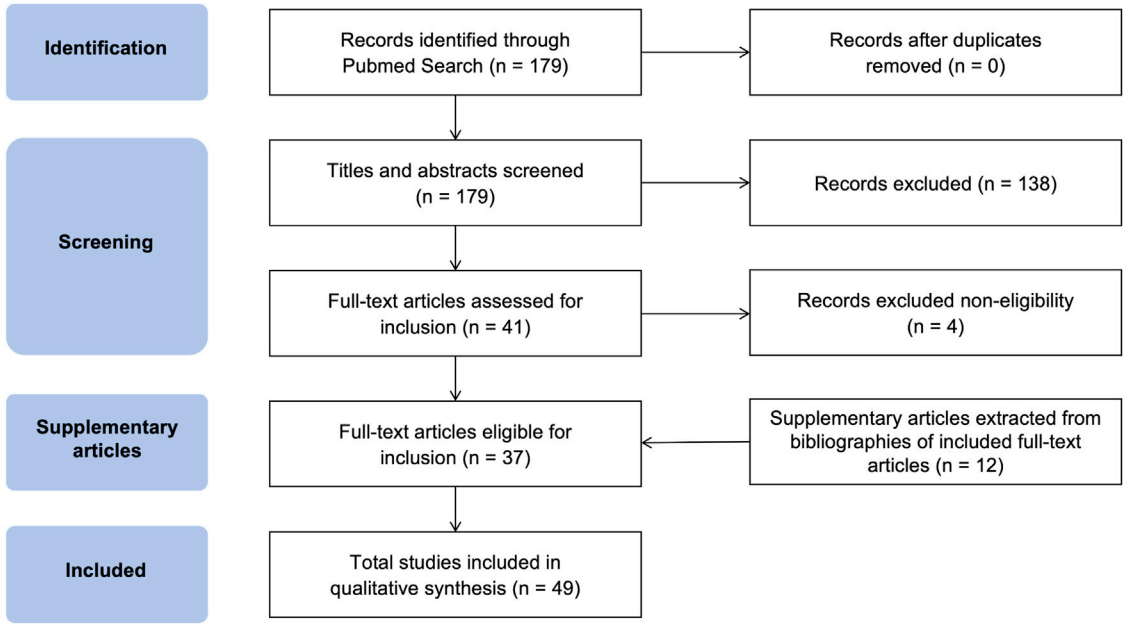

FIGURE 2
Flow diagram of the literature selection process for the present review.

equipment, which could limit the broader applicability. Moreover, the durability of symptom relief and the long-term safety profile remain uncertain, which warrants long-term follow-up studies. Consequently, the clinical applicability of trigeminal ganglion stimulation for NCP remains limited, and further well-designed, controlled studies are required before its therapeutic role can be defined.

Transcutaneous electrical stimulation

The pain modulation effects of electrotherapy in NCP may result from its nerve-stimulating effects. A study focused on determining the effect of transcutaneous electrical stimulation (TES) on corneal nerve regeneration in rabbits that underwent superficial lamellar keratectomy (SLK) [73]. TES was administered for 28 days following the corneal nerve injury secondary to SLK. Corneal sensitivity was measured, and changes in the corneal tissue were observed through Western blotting, real-time polymerase chain reaction (PCR), and immunofluorescence in which proteins involved in corneal nerve regeneration and wound healing were evaluated. Compared to post-treatment day 1, corneal sensitivity increased on day 7 in both the control group and the 2-Hz and 20-Hz treatment groups. Notably, the corneal sensitivity in the 2-Hz and 20-Hz groups (both 1.5 ± 0.0 cm) was significantly higher than that in the control group (0.8 ± 0.3 cm) on day 7. Western blotting showed that the expression of SPRR1A, a regeneration-associated protein, was significantly increased in the 2-Hz group on days 1 and 7 compared to the control and 20-Hz groups. PCR results showed a significant increase in NGF on day 1 in the 2-Hz group compared to the other groups. Furthermore, immunofluorescence demonstrated notable nerve regeneration, with a significantly higher density of subbasal nerve plexus and nerve terminal in the 2-Hz group. These results collectively suggest that TES promoted corneal nerve regeneration and enhanced corneal sensitivity in the SLK rabbit model. However, this study only tested only two frequencies (2 Hz and 20 Hz) of ES. Although corneal nerve regeneration was assessed, the authors did not directly measure pain or other subjective symptoms.

In another randomized clinical study, TES improved corneal nerve sensitivity 3 months after LASIK, potentially by promoting accelerated regeneration of corneal nerves [74]. Among the total of 40 eyes from 20 patients, one eye was randomly assigned to receive 60 min of TES at 20 Hz, while the other eye served as a control. Corneal sensitivity was assessed using the Cochet-Bonnet esthesiometer at four peripheral and five central locations within the LASIK flap, both preoperatively and at multiple postoperative intervals (1 day, 1 week, 1 month, and 3 months). Notably, this study focused on postoperative corneal nerve sensitivity and regeneration and did not include direct assessments of pain severity or TES-induced pain relief.

It has been proposed that ES promotes nerve and tissue regeneration via an increased calcium influx into neurons. When ES was applied to cultured dorsal root ganglion neurons, it significantly enhanced neurite outgrowth [75]. Similar to peripheral nerve injuries, corneal nerves also rely on calcium-

dependent processes for regeneration. Blocking calcium waves—whether by inhibiting voltage-gated calcium channels or calcium release from intracellular stores like the endoplasmic reticulum—has been shown to impair nerve regeneration. ES is hypothesized to increase retrograde calcium signals, thereby activating nerve repair [76]. ES might also decrease the time needed for corneal nerve fibers to reconnect to their target areas, potentially reducing the chronic pain associated with delayed regeneration in NCP [75]. While the functional recovery of corneal nerves due to ES has been demonstrated, direct evidence pertaining to structural recovery and the physiological mechanisms involved remains ambiguous and requires further research.

Transcutaneous electrical nerve stimulation

More recently, Zayan et al presented the use of TENS for managing chronic ocular pain. Fourteen patients with chronic ocular pain who had previously received treatments such as topical medications and oral analgesics that provided insufficient relief were recruited [77]. These patients received TENS treatment for a minimum of 3 months, with a median duration of use being 6.5 months. All patients were able to integrate TENS into their ocular pain management regimen. The parameters such as pulse width, amplitude, and frequency were adjusted to each patient's comfort level. Patients were instructed to use the TENS device up to three times daily, adjusting the intensity to their comfort. The device operated at pre-set frequencies of 5000/5100 Hz, creating a 100 Hz beat frequency. Four electrodes were placed near the trigeminal nerve branches on the forehead and temple. Patients adjusted the intensity by increasing the signal until they no longer felt pain, then lowering it slightly. This process was repeated on the right side first, followed by the left. Patients initially reported a median device usage of 14.0 times per week (range: 3 – 21). However, their usage decreased to a median of 3.0 times per week as they began experiencing the benefits by the time of the last follow-up. The findings suggested that TENS therapy resulted in significant, long-lasting pain reduction in most of the study patients, where 90% patients indicated a subjective reduction in pain. Pain intensity was reduced by about 27.4%. None of the patients reported experiencing any adverse effects. This study provides preliminary evidence for TENS as a treatment for NCP, with the potential to complement pharmacological therapies. It opens avenues for further research into the long-term efficacy of TENS in NCP. However, concerning the treatment protocol, patients used the TENS device at varying frequencies. Further studies on the optimal frequency, standardized protocol and long-term effectiveness of TENS are warranted for wider clinical applications. Moreover, participants were taking multiple systemic analgesics, which is a significant confounding factor that limits the ability to attribute the analgesic effects solely to TENS. Future studies with better control for the use of systemic analgesics may isolate the effects of TENS more clearly.

It is important to recognize that sympathetic efferent hyperactivity can often play a significant role in the development and persistence of neuropathic conditions, including NCP. TENS has been found to influence sympathetic activity through a sympatholytic effect, which may help explain its pain-relieving effects [78]. Unlike oral medications such as opioids and Nonsteroidal Anti-inflammatory Drugs that often present with systemic side effects, TENS may have fewer systemic side effects due to localized application. This is especially important for older patients with other comorbid conditions where one should be more cautious with the side effect profile of certain drugs.

Intranasal neurostimulation (ITNS)

Recently, ITNS has emerged as a novel electrotherapeutic approach targeting the neurophysiology of the lacrimal functional unit and has recently gained attention in the management of DED and ocular pain. TrueTear (Allergan, San Diego, CA), an ITNS device approved for the treatment of DED, delivers adjustable electrical pulses (up to 13 V or 5 mA at 30–60 Hz) to stimulate the anterior ethmoidal nerve, thereby activating the nasolacrimal reflex [70]. Clinical studies have demonstrated a favorable safety profile, with mild, self-limited nasal discomfort and occasional epistaxis being the most commonly reported adverse events [79]. Both animal and human studies further suggest that intranasal stimulation not only increases tear secretion but also promotes lipid and mucin release, supporting a more comprehensive restoration of tear film components [80, 81]. An interventional case series involving DED patients with ocular pain reported that ITNS significantly increased tear volume and reduced symptom severity, including dryness and ocular pain [82]. Notably, improvements in pain and dryness were not correlated with changes in tear volume, indicating that analgesic effects of ITNS may occur independently of tear production. ITNS is hypothesized to share mechanisms with TENS [83]. Stimulation of large-diameter Aβ fibers in the anterior ethmoidal nerve may presynaptically inhibit nociceptive input from small corneal C fibers at the level of the spinal trigeminal nucleus, thereby reducing pain perception in the somatosensory cortex. However, the study did not assess corneal nerve morphology, which may be relevant to the outcome of NCP. Additionally, only a single ITNS session was performed, and the durability and reproducibility of the treatment effects after multiple sessions require further investigation.

Another study enrolled patients with peripheral or mixed NCP and evaluated the effects of daily ITNS over a 90-day period [84]. The results indicated that ITNS could effectively alleviate pain symptoms, with a more pronounced reduction observed in patients reporting burning sensations. However, heterogeneity in treatment response was noted, as some patients appeared to develop tolerance to repeated treatment over time. Taken together, ITNS may present a

promising adjunct treatment for NCP and future prospective randomized trials are warranted.

Extranasal neurostimulation (EXNS)

EXNS is a targeted electrotherapy approach that stimulates the external nasal nerve, a terminal branch of the anterior ethmoidal nerve, which is an extraconal branch of the nasociliary nerve [85]. Although the external nasal nerve is initially regarded as a sensory nerve containing Ab fibers, it has been shown to stimulate tear production by activating the lacrimal functional unit [85]. According to the gate control theory, stimulation of these Aβ fibers via EXNS may inhibit pain signals transmitted by smaller-caliber Aδ and C fibers originating from the cornea [86]. This inhibition reduces the transmission of pain signals to second-order neurons in the trigeminal nucleus, ultimately decreasing the pain signals reaching the somatosensory cortex [83]. A pilot study investigating the efficacy of EXNS in patients with refractory peripheral or mixed NCP reported that following a single session of EXNS, patients had an average pain reduction of 54.88% as measured by the Visual Analog Scale (VAS) [87]. Subgroup analysis showed a 68.40% decrease in pain intensity for patients with peripheral NCP and a 43.61% reduction for those with mixed NCP. Moreover, 63.63% of NCP patients experienced at least a 50% improvement in pain, 9.09% had a 30–49.9% improvement, while 27.27% showed less than 30% improvement. However, there existed significant variation in the responses of patients in this study. These findings suggest that EXNS may serve as an adjuvant therapy to alleviate pain in NCP patients, especially those with a peripheral pain component. However, this study primarily assessed pain outcomes and did not evaluate changes in tear film parameters. Future research is needed to explore the long-term efficacy of EXNS, its impact on tear film quality, and whether it can enhance the effects of other treatments in managing NCP.

Scrambler therapy

Scrambler therapy is another non-invasive electrotherapeutic approach designed to remodulate aberrant pain signaling and has emerged as an option for the management of various forms of neuropathic pain, and its efficacy has been supported by multiple randomized and non-randomized clinical trials [88]. Scrambler therapy delivers constantly changing electrical signals across the affected dermatome(s) to substitute pathological "pain" information with synthetic "non-pain" signals. These signals engage peripheral nerve fiber endings, generate action potentials, and transmit altered sensory information to the spinal cord and brain [89]. This process is thought to modulate central pain processing, potentially through redistribution of cerebral blood flow from pain-related regions toward frontal inhibitory centers [89]. In addition, successful therapy has been associated with normalization of serum neuroinflammatory mediators, including NGF, suggesting a broader neuromodulatory and anti-inflammatory effect [90]. A typical treatment session lasts 30–45 min and may be repeated up to ten times or until adequate pain relief is achieved. In cases of pain recurrence, booster sessions (usually two to three treatments) can be administered and often result in a more sustained remission [88]. A case series involving 3 patients with unilateral NCP who were refractory to conventional topical and systemic treatments or experienced intolerable side effects demonstrated meaningful functional improvement and a reduced reliance on systemic analgesics, although complete pain resolution was not achieved [91]. These findings suggest that Scrambler therapy may be a potential treatment approach for NCP. All patients had pain associated with a documented extra-ocular trigeminal nerve injury, limiting the generalizability of these findings. Consequently, the effectiveness of Scrambler therapy in bilateral NCP or in cases arising directly from ocular surface disease remains uncertain and warrants further investigation. While Scrambler therapy may offer more durable pain modulation compared with conventional transcutaneous electrical nerve stimulation, its clinical use is constrained by the need for specialized equipment and trained providers, limiting accessibility. Table 2 summarizes the key findings of publications on the application of electrotherapy on NCP.

Discussion

Limitations and future directions

Electrotherapy is contraindicated in patients who are pregnant, epileptic, have cancer, or have cardiovascular disease. It is also contraindicated for those patients who have implanted electrical devices or have recently undergone radiotherapy due to unpredictable tissue response after radiotherapy [92]. Electrotherapy should also be avoided when skin is irritated, infected, bleeding or extremely sensitive [93]. This may narrow the number of patients who can be treated or participants for trials.

Currently, there are no standardized guidelines that exist for electrotherapy in NCP, causing a difference in the parameters used such as intensity, treatment duration and frequency. This makes the comparison of outcomes between studies much harder and hampers reproducibility. Insufficient stimulation may yield suboptimal outcomes, while excessive stimulation could result in adverse effects or diminishing returns. Determining the optimal dose of electrical therapy would be part of future research. Modification of ES according to the unique pathophysiology of corneal nerves may be necessary as it vastly differs from peripheral nerves.

In addition, the above-mentioned studies did not include a comparative arm, making it difficult to conclude whether the observed pain reduction was directly due to ES or attributed to

TABLE 2 The application of electrotherapy in the management of neuropathic corneal pain.

Study	Study type	Electrotherapy	Key findings	Conclusion
Sayegh et al. [72]	Case study	Percutaneous stimulation of the trigeminal ganglion in a 32-year-old woman with severe corneal neuropathic pain after LASIK	Complete symptom relief after electrode implantation, but pain recurred with lead migration	Trigeminal ganglion stimulation is effective for treating severe NCP in LASIK patients unresponsive to conventional therapies
Yoo et al. [73]	Experimental study	TES at 2-Hz & 20-Hz frequencies for 28 days on New Zealand white rabbits with corneal nerve damage induced by SLK	Increased corneal sensitivity in both TES groups with significant increase in SPRR1a, NGF and nerve regeneration observed in the 2-Hz group	TES promotes corneal nerve regeneration in the rabbit SLK model, with 2-Hz frequency being more effective than 20-Hz frequency, indicating potential for clinical applications in corneal nerve degeneration
Zayan et al. [77]	Retrospective study	Home use of TENS device in ten patients with chronic ocular pain unresponsive to conventional treatments	Overall pain intensity decreased by 27.4% post-treatment with no adverse events reported	Integration of TENS into the long-term management of ocular pain leads to improvements in overall pain intensity
Farhangi et al. [82]	Retrospective case series study	A single session of ITNS treatment in DED patients with ocular pain	ITNS significantly increased tear volume and reduced the severity of dryness and ocular pain symptom. Improvements in pain and dryness symptoms not correlated with in tear volume changes	ITNS may present a promising adjunct treatment for NCP and the analgesic effects of ITNS may occur independently of tear production
Olcucu et al. [84]	Prospective study	Daily ITNS treatment in patients with peripheral or mixed NCP over a 90-day period	ITNS reduced pain scores evaluated by ocular pain assessment survey, with a more pronounced reduction observed in patients reporting burning sensations	ITNS can be effective in relieving pain symptoms in most patients with peripheral and mixed NCP, in particular in patients with burning
Koseoglu et al. [87]	Retrospective pilot study	A single session of EXNS in patients with refractory peripheral or mixed NCP	NCP patients had an average pain reduction of 54.88%. Peripheral NCP patients reported a 68.40% pain reduction, while mixed NCP patients reported a 43.61% pain reduction	EXNS may serve as an adjuvant therapy to alleviate pain in NCP patients, especially those with a peripheral pain component
Karakus et al. [91]	Case series study	Scrambler therapy in 3 patients with unilateral NCP who were refractory to conventional treatments or experienced intolerable side effect	All patients had pian relief and a reduced reliance on systemic analgesics, although complete pain resolution was not achieved	Scrambler therapy may be a potential treatment approach for NCP. Its effectiveness in bilateral NCP or in cases arising directly from ocular surface disease warrants further investigation

LASIK, laser-assisted *in situ* keratomileusis; NCP, neuropathic corneal pain; TES, transcutaneous electrical stimulation; SLK, superficial lamellar keratectomy; SPRR1a, small proline-rich repeat protein 1A; NGF, nerve growth factor; TENS, transcutaneous electrical nerve stimulation; ITNS, intranasal neurostimulation; DED, dry eye disease; EXNS, extranasal neurostimulation.

spontaneous improvement or concurrent treatments. Future research should incorporate control groups to establish the cause-and-effect relationships concerning the efficacy of TENS.

Individual differences in the underlying etiology of NCP may also influence the effectiveness of electrical therapy. Factors such as baseline nerve damage, pain sensitivity, and response to treatment may lead to inconsistent outcomes. Moreover, most studies focus on short-term outcomes, with limited data on long-term efficacy and safety. It remains unclear whether the advantages of electrical therapy are sustained over time or require continuous treatment. The need for repeated sessions of electrotherapy over weeks or months may impose a logistical and financial burden on patients.

Furthermore, the use of electrotherapy requires specialized equipment and trained personnel, which may not be readily available in all healthcare settings, limiting its widespread adoption, particularly in low-resource settings and third-world countries. Reliance on subjective assessments, such as pain scores and patient-reported outcomes, may introduce bias. Objective measures, like corneal nerve imaging or electrophysiological data, are less frequently used, making it difficult to assess and adjust therapy dynamically.

Future directions can focus on investigating optimal parameters for various electrotherapy modalities such as TENS or trigeminal nerve stimulation. These can include intensity, duration, and frequency in respective patients to achieve maximal therapeutic outcomes. More effort should also be put in developing individualized electrotherapy regimens based on patient-specific factors so that it is catered to specific patient needs. The combined use of electrotherapy and pharmacological treatments should also be explored to maximize the efficacy of pain management.

Future studies should also aim to explore the molecular and cellular processes by which electrotherapy aids in pain alleviation and nerve regeneration. More detailed research into neurotrophic factors, such as BDNF and NGF, as well as calcium influx, could provide valuable insights. Moreover, follow-up studies can be performed to assess the lasting effects of electrotherapy in

chronic NCP management and potential symptom recurrence. The safety of electrotherapy over extended periods while focusing on potential adverse effects can also be assessed on each patient, but objectively quantifying pain level and comfort might be hard. Long-term studies, larger-scale, and comparative or randomized controlled trials are required.

Conclusion

Electrotherapy shows significant promise in the management of NCP. TENS has shown potential in reducing NCP severity, associated symptoms and improving corneal nerve function, indicating both symptomatic relief and recovery of nerves. The mechanism with which electrotherapy is used to treat peripheral neuropathic pain can be applied to NCP as well. Despite the promising results, challenges such as pain recurrence and the identification of optimal therapeutic parameters persist. The incorporation of electrotherapy into long-term management, especially for patients refractory to conventional treatments, warrants more research. While electrotherapy can emerge as a promising form of treatment in patients with NCP that offer benefits over current treatment, further research, including large-scale validation, clinical trials with control groups and longer follow-up period, and a deeper exploration of the molecular mechanisms involved, is critical to optimizing the safety and efficacy of electrotherapy in this clinical context.

Author contributions

AS contributed to literature search, drafting the manuscript, reviewing and editing. MY contributed to drafting the manuscript, reviewing and editing. LT contributed to reviewing and editing. CL and IL contributed to data curation. Y-CL contributed to conceptualization, funding acquisition, supervision, reviewing and editing. All authors contributed to the article and approved the submitted version.

Funding

The author(s) declared that financial support was received for this work and/or its publication. This work is supported by the Clinician Scientist Awards (MOH-CSAINV21jun-0001 and CSAINV24jul-0005), and Clinician Scientist individual research grant (CIRG24jul-0010), from the Singapore National Medical Research Council.

Conflict of interest

The author(s) declared no potential conflicts of interest with respect to the research, authorship, and/or publication of this article.

Generative AI statement

The author(s) declared that generative AI was not used in the creation of this manuscript.

Any alternative text (alt text) provided alongside figures in this article has been generated by Frontiers with the support of artificial intelligence and reasonable efforts have been made to ensure accuracy, including review by the authors wherever possible. If you identify any issues, please contact us.

References

1. Wong NSQ, Liu C, Lin MT, Lee IXY, Tong L, Liu YC. Neuropathic corneal pain after coronavirus disease 2019 (COVID-19) infection. *Diseases* (2024) **12**(2):37. doi:10.3390/diseases12020037

2. Muller LJ, Marfurt CF, Kruse F, Tervo TM. Corneal nerves: structure, contents and function. *Exp Eye Res* (2003) **76**(5):521–42. doi:10.1016/s0014-4835(03)00050-2

3. Marfurt CF, Cox J, Deek S, Dvorscak L. Anatomy of the human corneal innervation. *Exp Eye Res* (2010) **90**(4):478–92. doi:10.1016/j.exer.2009.12.010

4. Dieckmann G, Goyal S, Hamrah P. Neuropathic corneal pain: approaches for management. *Ophthalmology* (2017) **124**(11):S34–S47. doi:10.1016/j.ophtha.2017.08.004

5. Belmonte C, Nichols JJ, Cox SM, Brock JA, Begley CG, Bereiter DA, et al. TFOS DEWS II pain and sensation report. *Ocul Surf* (2017) **15**(3):404–37. doi:10.1016/j.jtos.2017.05.002

6. Teo CHY, Liu C, Lee IXY, Lin MTY, Liu F, Toh CJL, et al. Neuropathic corneal pain following refractive surgery: risk factors, clinical manifestations, imaging and proteomic characteristics. *Br J Ophthalmol* (2025) **109**(7):747–55. doi:10.1136/bjo-2024-325996

7. Cheng J, Liu C, Yu M, Lee IXY, Wang X, Hsu VWT, et al. Exploration of imaging and molecular biomarkers for differentiation of neuropathic corneal pain from dry eye syndrome. *Ocul Surf* (2025) **38**:230–41. doi:10.1016/j.jtos.2025.08.002

8. So WZ, Wong NSQ, Tan HC, Yu Lin MT, Yu Lee IX, Mehta JS, et al. Diabetic corneal neuropathy as a surrogate marker for diabetic peripheral neuropathy. *Neural Regen Res* (2022) **17**(10):2172–8. doi:10.4103/1673-5374.327364

9. Goyal S, Hamrah P. Understanding neuropathic corneal Pain--Gaps and current therapeutic approaches. *Semin Ophthalmol* (2016) **31**(1-2):59–70. doi:10.3109/08820538.2015.1114853

10. Chin JY, Tong L, Liu C, Lee IXY, Wong JHF, Wong RKT, et al. Quality of life and symptomatology in neuropathic corneal pain in comparison with dry eye syndrome. *Cornea.* (2024) **44**(7):825–31. doi:10.1097/ICO.0000000000003674

11. Liu C, Lin MT, Lee IXY, Wong JHF, Lu D, Lam TC, et al. Neuropathic corneal pain: tear proteomic and neuromediator profiles, imaging features, and clinical manifestations. *Am J Ophthalmol* (2024) **265**:6–20. doi:10.1016/j.ajo.2024.03.015

12. Bron AJ, de Paiva CS, Chauhan SK, Bonini S, Gabison EE, Jain S, et al. Tfos dews ii pathophysiology report. *The Ocular Surface* (2017) **15**(3):438–510. doi:10.1016/j.jtos.2017.05.011

13. Dieckmann G, Ozmen MC, Cox SM, Engert RC, Hamrah P. Low-dose naltrexone is effective and well-tolerated for modulating symptoms in patients with neuropathic corneal pain. *The Ocular Surface* (2021) **20**:33–8. doi:10.1016/j.jtos.2020.12.003

14. Liu YC, Lin MT, Mehta JS. Analysis of corneal nerve plexus in corneal confocal microscopy images. *Neural Regen Res* (2021) **16**(4):690–1. doi:10.4103/1673-5374.289435

15. Ross AR, Al-Aqaba MA, Almaazmi A, Messina M, Nubile M, Mastropasqua L, et al. Clinical and *in vivo* confocal microscopic features of neuropathic corneal pain. *Br J Ophthalmol* (2020) **104**(6):768–75. doi:10.1136/bjophthalmol-2019-314799

16. Moein HR, Akhlaq A, Dieckmann G, Abbouda A, Pondelis N, Salem Z, et al. Visualization of microneuromas by using *in vivo* confocal microscopy: an objective biomarker for the diagnosis of neuropathic corneal pain? *Ocul Surf* (2020) **18**(4): 651–6. doi:10.1016/j.jtos.2020.07.004

17. Guerrero-Moreno A, Liang H, Moreau N, Luzu J, Rabut G, Melik Parsadaniantz S, et al. Corneal nerve abnormalities in painful dry eye disease patients. *Biomedicines* (2021) **9**(10):1424. doi:10.3390/biomedicines9101424

18. Kocot-Kępska M, Zajączkowska R, Mika J, Wordliczek J, Dobrogowski J, Przeklasa-Muszyńska A. Peripheral mechanisms of neuropathic pain—the role of neuronal and non-neuronal interactions and their implications for topical treatment of neuropathic pain. *Pharmaceuticals* (2021) **14**(2):77. doi:10.3390/ph14020077

19. Van der Cruyssen F, Politis C. Neurophysiological aspects of the trigeminal sensory system: an update. *Rev Neurosciences* (2018) **29**(2):115–23. doi:10.1515/revneuro-2017-0044

20. Opree A, Kress M. Involvement of the proinflammatory cytokines tumor necrosis factor-alpha, IL-1 beta, and IL-6 but not IL-8 in the development of heat hyperalgesia: effects on heat-evoked calcitonin gene-related peptide release from rat skin. *J Neurosci* (2000) **20**(16):6289–93. doi:10.1523/JNEUROSCI.20-16-06289.2000

21. Puja G, Sonkodi B, Bardoni R. Mechanisms of peripheral and central pain sensitization: focus on ocular pain. *Front Pharmacol* (2021) **12**:764396. doi:10.3389/fphar.2021.764396

22. Yin Y, Yi MH, Kim DW. Impaired autophagy of GABAergic interneurons in neuropathic pain. *Pain Res Manag* (2018) **2018**:9185368. doi:10.1155/2018/9185368

23. Castro A, Li Y, Raver C, Chandra R, Masri R, Lobo MK, et al. Neuropathic pain after chronic nerve constriction may not correlate with chloride dysregulation in mouse trigeminal nucleus caudalis neurons. *Pain* (2017) **158**(7):1366–72. doi:10.1097/j.pain.0000000000000926

24. Rahman M, Okamoto K, Thompson R, Katagiri A, Bereiter DA. Sensitization of trigeminal brainstem pathways in a model for tear deficient dry eye. *Pain* (2015) **156**(5):942–50. doi:10.1097/j.pain.0000000000000135

25. Mills EP, Alshelh Z, Kosanovic D, Di Pietro F, Vickers ER, Macey PM, et al. Altered brainstem pain-modulation circuitry connectivity during spontaneous pain intensity fluctuations. *J Pain Res* (2020) **13**:2223–35. doi:10.2147/JPR.S252594

26. Huang JJ, Rodriguez DA, Slifer SH, Martin ER, Levitt RC, Galor A. Genome wide association study of neuropathic ocular pain. *Ophthalmol Sci* (2024) **4**(2): 100384. doi:10.1016/j.xops.2023.100384

27. Belin S, Maki BA, Catlin J, Rein BA, Popescu GK. Membrane stretch gates NMDA receptors. *J Neurosci* (2022) **42**(29):5672–80. doi:10.1523/JNEUROSCI.0350-22.2022

28. Woo S-H, Lukacs V, De Nooij JC, Zaytseva D, Criddle CR, Francisco A, et al. Piezo2 is the principal mechanotransduction channel for proprioception. *Nat Neuroscience* (2015) **18**(12):1756–62. doi:10.1038/nn.4162

29. Eijkelkamp N, Linley JE, Torres JM, Bee L, Dickenson AH, Gringhuis M, et al. A role for Piezo2 in EPAC1-dependent mechanical allodynia. *Nat Commun* (2013) **4**:1682. doi:10.1038/ncomms2673

30. Zhang M, Wang Y, Geng J, Zhou S, Xiao B. Mechanically activated piezo channels mediate touch and suppress acute mechanical pain response in mice. *Cell Rep* (2019) **26**(6):1419–31 e4. doi:10.1016/j.celrep.2019.01.056

31. Sonkodi B, Resch MD, Hortobágyi T. Is the sex difference a clue to the pathomechanism of dry eye disease? Watch out for the NGF-TrkA-Piezo2 signaling axis and the Piezo2 channelopathy. *J Mol Neurosci* (2022) **72**(8):1598–608. doi:10.1007/s12031-022-02015-9

32. Puja G, Sonkodi B, Bardoni R. Mechanisms of peripheral and central pain sensitization: focus on ocular. *Eye Pain: Etiology Ther Approaches* (2022): 78852468. doi:10.3389/fphar.2021.764396

33. Fernández-Trillo J, Florez-Paz D, Íñigo-Portugués A, González-González O, Del Campo AG, González A, et al. Piezo2 mediates low-threshold mechanically evoked pain in the cornea. *J Neurosci* (2020) **40**(47):8976–93. doi:10.1523/JNEUROSCI.0247-20.2020

34. Matynia A, Nguyen E, Sun X, Blixt FW, Parikh S, Kessler J, et al. Peripheral sensory neurons expressing melanopsin respond to light. *Front Neural Circuits* (2016) **10**:60. doi:10.3389/fncir.2016.00060

35. Asiedu K. Role of ocular surface neurobiology in neuronal-mediated inflammation in dry eye disease. *Neuropeptides* (2022) **95**:102266. doi:10.1016/j.npep.2022.102266

36. Guerrero-Moreno A, Baudouin C, Melik Parsadaniantz S, Réaux-Le Goazigo A. Morphological and functional changes of corneal nerves and their contribution to peripheral and central sensory abnormalities. *Front Cellular Neuroscience* (2020) **14**: 610342. doi:10.3389/fncel.2020.610342

37. Blanco-Vázquez M, Vázquez A, Fernández I, Novo-Diez A, Martínez-Plaza E, García-Vázquez C, et al. Inflammation-related molecules in tears of patients with chronic ocular pain and dry eye disease. *Exp Eye Res* (2022) **219**:109057. doi:10.1016/j.exer.2022.109057

38. Li B, Tian Y, Wang S. The correlation of cytokines and sensory hypersensitivity in mild dry eye patients characterized by symptoms outweighing signs. *Mol Vision* (2020) **26**:359–69.

39. Launay P-S, Reboussin E, Liang H, Kessal K, Godefroy D, Rostene W, et al. Ocular inflammation induces trigeminal pain, peripheral and central neuroinflammatory mechanisms. *Neurobiol Disease* (2016) **88**:16–28. doi:10.1016/j.nbd.2015.12.017

40. Ren K, Dubner R. Interactions between the immune and nervous systems in pain. *Nat Medicine* (2010) **16**(11):1267–76. doi:10.1038/nm.2234

41. Asiedu K. Neurophysiology of corneal neuropathic pain and emerging pharmacotherapeutics. *J Neurosci Res* (2024) **102**(1):e25285. doi:10.1002/jnr.25285

42. Khan N, Smith MT. Neurotrophins and neuropathic pain: role in pathobiology. *Molecules* (2015) **20**(6):10657–88. doi:10.3390/molecules200610657

43. Yang LWY, Mehta JS, Liu YC. Corneal neuromediator profiles following laser refractive surgery. *Neural Regen Res* (2021) **16**(11):2177–83. doi:10.4103/1673-5374.308666

44. de Paiva CS, Pflugfelder SC. Rationale for anti-inflammatory therapy in dry eye syndrome. *Arq Bras Oftalmol.* (2008) **71**(6 Suppl. l):89–95. doi:10.1590/s0004-27492008000700017

45. Anam A, Liu C, Tong L, Liu YC. Blood-derived eye drops for the treatment of corneal neuropathic pain. *J Ocul Pharmacol Ther* (2024) **40**(5):281–92. doi:10.1089/jop.2023.0155

46. Dworkin RH, O'Connor AB, Kent J, Mackey SC, Raja SN, Stacey BR, et al. Interventional management of neuropathic pain: NeuPSIG recommendations. *Pain* (2013) **154**(11):2249–61. doi:10.1016/j.pain.2013.06.004

47. Dimit R, Gire A, Pflugfelder SC, Bergmanson JP. Patient ocular conditions and clinical outcomes using a PROSE scleral device. *Cont Lens Anterior Eye* (2013) **36**(4): 159–63. doi:10.1016/j.clae.2013.02.004

48. Moisset X, Lanteri-Minet M, Fontaine D. Neurostimulation methods in the treatment of chronic pain. *J Neural Transm (Vienna)* (2020) **127**(4):673–86. doi:10.1007/s00702-019-02092-y

49. Chu X-L, Song X-Z, Li Q, Li YR, He F, Gu XS, et al. Basic mechanisms of peripheral nerve injury and treatment *via* electrical stimulation. *Neural Regeneration Research* (2022) **17**(10):2185–93. doi:10.4103/1673-5374.335823

50. Sabino GS, Santos CM, Francischi JN, De Resende MA. Release of endogenous opioids following transcutaneous electric nerve stimulation in an experimental model of acute inflammatory pain. *The Journal Pain* (2008) **9**(2):157–63. doi:10.1016/j.jpain.2007.09.003

51. Sluka KA, Lisi TL, Westlund KN. Increased release of serotonin in the spinal cord during low, but not high, frequency transcutaneous electric nerve stimulation in rats with joint inflammation. *Arch Physical Medicine Rehabilitation* (2006) **87**(8): 1137–40. doi:10.1016/j.apmr.2006.04.023

52. Maeda Y, Lisi T, Vance C, Sluka K. Release of GABA and activation of GABAA in the spinal cord mediates the effects of TENS in rats. *Brain Research* (2007) **1136**: 43–50. doi:10.1016/j.brainres.2006.11.061

53. Song Y, Guo Y, Zhao L, Chen S. Electroacupuncture alleviates inflammatory pain via adenosine suppression and its mediated substance P expression. *Arquivos de Neuro-Psiquiatria* (2020) **78**:617–23. doi:10.1590/0004-282X20200078

54. Melzack R, Wall PD. Pain mechanisms: a new theory. *Science* (1965) **150**(3699):971–9. doi:10.1126/science.150.3699.971

55. Vance CG, Dailey DL, Rakel BA, Sluka KA. Using TENS for pain control: the state of the evidence. *Pain Manag* (2014) **4**(3):197–209. doi:10.2217/pmt.14.13

56. Johnson M. Transcutaneous electrical nerve stimulation: mechanisms, clinical application and evidence. *Rev Pain* (2007) **1**(1):7–11. doi:10.1177/204946370700100103

57. Billington R. Consequences of neuropathic pain: quality-of-life issues and associated costs. *Am J Manag Care* (2006) **12**(9 Suppl. l):S263–8.

58. Sluka KA, Walsh D. Transcutaneous electrical nerve stimulation: basic science mechanisms and clinical effectiveness. *J Pain* (2003) **4**(3):109–21. doi:10.1054/jpai.2003.434

59. Chen CC, Johnson MI, McDonough S, Cramp F. The effect of transcutaneous electrical nerve stimulation on local and distal cutaneous blood flow following a prolonged heat stimulus in healthy subjects. *Clin Physiology Functional Imaging* (2007) **27**(3):154–61. doi:10.1111/j.1475-097X.2007.00731.x

60. Somers DL, Somers MF. Treatment of neuropathic pain in a patient with diabetic neuropathy using transcutaneous electrical nerve stimulation applied to the skin of the lumbar region. *Phys Therapy* (1999) **79**(8):767–75.

61. Forst T, Nguyen M, Forst S, Disselhoff B, Pohlmann T, Pfützner A. Impact of low frequency transcutaneous electrical nerve stimulation on symptomatic diabetic neuropathy using the new salutaris device. *Diabetes Nutrition and Metabolism* (2004) **17**(3):163–8.

62. Zhao M, Bai H, Wang E, Forrester JV, McCaig CD. Electrical stimulation directly induces pre-angiogenic responses in vascular endothelial cells by signaling through VEGF receptors. *J Cell Science* (2004) **117**(3):397–405. doi:10.1242/jcs.00868

63. Hughes JGS, Lichstein PR, Whitlock D, Harker C. Response of plasma beta-endorphins to transcutaneous electrical nerve stimulation in healthy subjects. *Phys Therapy* (1984) **64**(7):1062–6. doi:10.1093/ptj/64.7.1062

64. Ding L, Song T, Yi C, Huang Y, Yu W, Ling L, et al. Transcutaneous electrical nerve stimulation (TENS) improves the diabetic cytopathy (DCP) via up-regulation of CGRP and cAMP. *PLoS One* (2013) **8**(2):e57477. doi:10.1371/journal.pone.0057477

65. Zhou W-t, Ni Y-q, Jin Z-b, Zhang M, Wu Jh., Zhu Y, et al. Electrical stimulation ameliorates light-induced photoreceptor degeneration *in vitro via* suppressing the proinflammatory effect of microglia and enhancing the neurotrophic potential of müller cells. *Exp Neurology* (2012) **238**(2):192–208. doi:10.1016/j.expneurol.2012.08.029

66. ElZaridi F, Lennikov A, Cho K-S, Dartt DA, Yang M, Chen D. Electrical stimulation promotes growth of the corneal nerves. *Invest Ophthalmol and Vis Sci* (2023) **64**(8):5402.

67. DeSantana JM, Walsh DM, Vance C, Rakel BA, Sluka KA. Effectiveness of transcutaneous electrical nerve stimulation for treatment of hyperalgesia and pain. *Curr Rheumatol Rep* (2008) **10**(6):492–9. doi:10.1007/s11926-008-0080-z

68. Kumar D, Marshall HJ. Diabetic peripheral neuropathy: amelioration of pain with transcutaneous electrostimulation. *Diabetes Care* (1997) **20**(11):1702–5. doi:10.2337/diacare.20.11.1702

69. Gibson W, Wand BM, O'Connell NE. Transcutaneous electrical nerve stimulation (TENS) for neuropathic pain in adults. *Cochrane Database Syst Rev* (2017)(9). doi:10.1002/14651858.CD011976.pub2

70. Ni L, Yao Z, Zhao Y, Zhang T, Wang J, Li S, et al. Electrical stimulation therapy for peripheral nerve injury. *Front Neurol* (2023) **14**:1081458. doi:10.3389/fneur.2023.1081458

71. Brooks J, Tracey I. From nociception to pain perception: imaging the spinal and supraspinal pathways. *J Anat* (2005) **207**(1):19–33. doi:10.1111/j.1469-7580.2005.00428.x

72. Sayegh RR, Sweet JA, Miller JP, Hayek SM. Electrical stimulation of the trigeminal ganglion and intrathecal drug delivery systems for the management of corneal neuropathic pain. *Cornea* (2016) **35**(4):576–7. doi:10.1097/ICO.0000000000000751

73. Yoo Y-S, Park S, Eun P, Park YM, Lim DH, Chung T-Y. Corneal neuro-regenerative effect of transcutaneous electrical stimulation in rabbit lamellar keratectomy model. *Translational Vis Sci and Technology* (2022) **11**(10):17. doi:10.1167/tvst.11.10.17

74. Ghaffariyeh A, Peyman A, Puyan S, Honarpisheh N, Bagheri B, Peyman M. Evaluation of transcutaneous electrical simulation to improve recovery from corneal hypoesthesia after LASIK. *Graefe's Archive Clin Exp Ophthalmol* (2009) **247**(8):1133–8. doi:10.1007/s00417-009-1079-5

75. Yan X, Liu J, Huang J, Huang M, He F, Ye Z, et al. Electrical stimulation induces calcium-dependent neurite outgrowth and immediate early genes expressions of dorsal root ganglion neurons. *Neurochem Res* (2014) **39**(1):129–41. doi:10.1007/s11064-013-1197-7

76. Liu Y, Fox PM. The role of electrical stimulation in peripheral nerve regeneration: current evidence and future directions. *J Hand Surg Glob Online* (2024) **6**(5):718–21. doi:10.1016/j.jhsg.2024.01.022

77. Zayan K, Aggarwal S, Felix E, Levitt R, Sarantopoulos K, Galor A. Transcutaneous electrical nerve stimulation for the long-term treatment of ocular pain. *Neuromodulation* (2020) **23**(6):871–7. doi:10.1111/ner.13146

78. Liao CD, Tsauo JY, Liou TH, Chen HC, Rau CL. Efficacy of noninvasive stellate ganglion blockade performed using physical agent modalities in patients with sympathetic hyperactivity-associated disorders: a systematic review and meta-analysis. *PLoS One* (2016) **11**(12):e0167476. doi:10.1371/journal.pone.0167476

79. Cohn GS, Corbett D, Tenen A, Coroneo M, McAlister J, Craig JP, et al. Randomized, controlled, double-masked, multicenter, pilot study evaluating safety and efficacy of intranasal neurostimulation for dry eye disease. *Invest Ophthalmol and Vis Sci* (2019) **60**(1):147–53. doi:10.1167/iovs.18-23984

80. Brinton M, Kossler AL, Patel ZM, Loudin J, Franke M, Ta CN, et al. Enhanced tearing by electrical stimulation of the anterior ethmoid nerve. *Invest Ophthalmol and Vis Sci* (2017) **58**(4):2341–8. doi:10.1167/iovs.16-21362

81. Gumus K, Schuetzle KL, Pflugfelder SC. Randomized controlled crossover trial comparing the impact of sham or intranasal tear neurostimulation on conjunctival goblet cell degranulation. *Am Journal Ophthalmology* (2017) **177**:159–68. doi:10.1016/j.ajo.2017.03.002

82. Farhangi M, Cheng AM, Baksh B, Sarantopoulos CD, Felix ER, Levitt RC, et al. Effect of non-invasive intranasal neurostimulation on tear volume, dryness and ocular pain. *Br J Ophthalmol* (2020) **104**(9):1310–6. doi:10.1136/bjophthalmol-2019-315065

83. Mendell LM. Constructing and deconstructing the gate theory of pain. *Pain®* (2014) **155**(2):210–6. doi:10.1016/j.pain.2013.12.010

84. Olcucu O, Dieckmann G, Ozmen MC, Cox S, Liu G, Hamrah P. An exploratory, prospective, interventional, open-label, clinical trial with intranasal neurostimulation for ameliorating symptoms of neuropathic corneal pain. *Invest Ophthalmol and Vis Sci* (2024) **65**(7):2658.

85. Ji MH, Moshfeghi DM, Periman L, Kading D, Matossian C, Walman G, et al. Novel extranasal tear stimulation: pivotal study results. *Translational Vision Science and Technology* (2020) **9**(12):23. doi:10.1167/tvst.9.12.23

86. Moayedi M, Davis KD. Theories of pain: from specificity to gate control. *J Neurophysiology* (2013) **109**(1):5–12. doi:10.1152/jn.00457.2012

87. Koseoglu ND, Chen E, Tuwani R, Kompa B, Cox SM, Cuneyt Ozmen M, et al. Development and validation of a deep learning model for diagnosing neuropathic corneal pain *via in vivo* confocal microscopy. *Npj Digital Med* (2025) **8**(1):277. doi:10.1038/s41746-025-01577-3

88. Smith TJ, Wang EJ, Loprinzi CL. Cutaneous electroanalgesia for relief of chronic and neuropathic pain. *New Engl J Med* (2023) **389**(2):158–64. doi:10.1056/NEJMra2110098

89. Lee SY, Park C-H, Cho YS, Kim L, Yoo JW, Joo SY, et al. Scrambler therapy for chronic pain after burns and its effect on the cerebral pain network: a prospective, double-blinded, randomized controlled trial. *J Clin Med* (2022) **11**(15):4255. doi:10.3390/jcm11154255

90. Starkweather AR, Coyne P, Lyon DE, Elswick JR, An K, Sturgill J. Decreased low back pain intensity and differential gene expression following calmare®: results from a double-blinded randomized sham-controlled study. *Res Nursing and Health* (2015) **38**(1):29–38. doi:10.1002/nur.21632

91. Karakus S, Rajabalee N, Tunc U, Smith TJ. Scrambler therapy as a novel treatment for unilateral ocular neuropathic pain. *The Ocular Surface* (2024) **34**:122–3. doi:10.1016/j.jtos.2024.06.006

92. Radhakrishnan R, Sluka KA. Spinal muscarinic receptors are activated during low or high frequency TENS-induced antihyperalgesia in rats. *Neuropharmacology* (2003) **45**(8):1111–9. doi:10.1016/s0028-3908(03)00280-6

93. Almalty AR, Hamed SH, Jebril MY, Abdelnour HM. The effect of electrical stimulation on skin vulnerability to irritants. *Skin Res Technol* (2024) **30**(2):e13591. doi:10.1111/srt.13591

EBM Experimental Biology and Medicine

TYPE Original Research
PUBLISHED 21 January 2026
DOI 10.3389/ebm.2026.10800

OPEN ACCESS

*CORRESPONDENCE
Wenping Zhang,
zwpstudents@163.com

RECEIVED 27 August 2025
REVISED 05 December 2025
ACCEPTED 06 January 2026
PUBLISHED 21 January 2026

CITATION
Hou R, Zhang X, Zhang J and Zhang W (2026) Liposomes as carriers for garlic oil delivery to increase anti-inflammatory and antioxidant activities in mice with ALI.
Exp. Biol. Med. 251:10800.
doi: 10.3389/ebm.2026.10800

Liposomes as carriers for garlic oil delivery to increase anti-inflammatory and antioxidant activities in mice with ALI

Ruilin Hou[1], Xiaowei Zhang[2], Jiaming Zhang[2] and Wenping Zhang[1]*

[1]Drug/Medical Device Clinical Trial Institution Office, General Hospital of Ningxia Medical University, Yinchuan, Ningxia, China, [2]College of Pharmacy, Ningxia Medical University, Yinchuan, Ningxia, China

Abstract

ALI/ARDS are clinical syndromes with diverse etiological origins and are characterized by high mortality rates and a lack of specific therapeutic options. Garlic oil (GO) has been utilized in both culinary and medicinal applications for millennia. However, its complex chemical composition and inherent instability have limited further development and clinical application. We aimed to encapsulate GO within liposomes to increase its solubility and stability. The therapeutic efficacy of GO-loaded liposomes (GO-lips) against LPS-induced ALI was subsequently evaluated *in vivo*. A novel GO-lip formulation was developed, and its preparation process was optimized to ensure its stability and bioavailability. A murine model of LPS-induced ALI was established. The animals were randomly assigned to the normal control, LPS model, GO treatment, or GO-lip treatment group. Therapeutic outcomes were evaluated by lung tissue histopathology, inflammatory cytokine quantification and oxidative stress biomarker measurement. PCR and molecular dynamics simulations were used to verify the ALI treatment-related pathways influenced by GO-lips. We successfully developed GO-lips using a novel fabrication method. GO-lips demonstrated favorable physicochemical characteristics, with a mean particle diameter of 175 $\pm$ 3 nm, a PDI of 0.27 $\pm$ 0.02, and an encapsulation efficiency of 70.74 $\pm$ 2.11%. Compared with the LPS model group, the GO-lip treatment group exhibited significant protection against LPS-induced ALI. GO-lips demonstrated greater efficacy than free GO, as evidenced by the improved lung histopathology, reduced pulmonary edema, decreased inflammatory responses, and attenuated oxidative stress. PCR analysis demonstrated that GO-lips significantly protect mice primarily via Nrf2 pathway activation. These findings suggest that liposomal encapsulation of GO increases its anti-inflammatory and antioxidant activities, protecting against LPS-induced ALI. This research offers a

novel clinical therapeutic approach for ALI and contributes to foundational knowledge supporting the development and utilization of GO-derived formulations.

KEYWORDS

acute lung injury, garlic oil, inflammatory cytokines, liposomes, oxidative stress

Impact statement

Acute Lung Injury (ALI) and its more severe manifestation, Acute Respiratory Distress Syndrome (ARDS), represent prevalent and critical respiratory conditions characterized by high mortality rates. These disorders impose significant economic and psychological burdens on both patients and society. Currently, no effective treatment exists for ALI, and conventional glucocorticoid therapies are often accompanied by severe adverse effects. In the present study, garlic oil was administered using liposome-based nanodelivery technology, which serves to mitigate adverse drug reactions while simultaneously improving the therapeutic efficacy in the management of ALI.

Introduction

Acute lung injury (ALI) is a rapidly progressive and severe pulmonary disorder primarily caused by bacterial and viral infections. Clinically, ALI is characterized by an exaggerated inflammatory response both within the lungs and systemically, resulting in disruption of the pulmonary endothelial barrier, impaired alveolar fluid clearance, and widespread lung tissue damage. The acute nature of ALI often results in severe dyspnea within a short timeframe, and can rapidly progress to acute respiratory distress syndrome (ARDS) within hours [1, 2]. ALI has a high incidence rate, a considerable risk of complications, and substantial treatment costs, making it one of the most prevalent and critical conditions encountered in intensive care units [3]. The pathophysiology of ALI involves complex interplay among several interrelated mechanisms, such as dysregulated inflammatory responses, oxidative stress imbalance, epithelial–endothelial barrier disruption, and aberrant cellular apoptosis [4]. Collectively, these processes compromise the structural integrity of the alveolar–capillary barrier and impair pulmonary gas exchange. The intricacy of the interactions among inflammation, oxidative stress, and apoptosis highlights the complexity of ALI pathogenesis. Sustained inflammatory and oxidative challenges promote apoptosis in alveolar epithelial and endothelial cells, thereby hindering tissue repair and exacerbating barrier dysfunction. Notably, the NF-κB-mediated inflammatory signaling pathway and the Nrf2/ARE-mediated antioxidant pathway have been identified as principal molecular regulators of the progression of ALI [5]. These pathways operate in conjunction with intricate crosstalk among multiple signaling cascades. Consequently, biomarkers such as tumor necrosis factor-alpha (TNF-α), various interleukins, and malondialdehyde (MDA) are frequently employed for comprehensive, multidimensional assessment of ALI. This disease imposes considerable psychological and physiological burdens on patients and their families and poses a significant global health threat. Consequently, the development of novel, safe, and effective pharmacological therapies for ALI/ARDS is urgently needed.

Allium sativum L., commonly known as garlic, is an annual bulbous herb belonging to the Liliaceae family and originating from Central and South Asia. Historically, garlic has been utilized for millennia as a functional food, culinary spice, flavoring agent, and traditional medicinal plant. Despite its longstanding use in ethnomedicine, systematic investigations into its bioactive constituents have gained momentum only in recent decades [6]. The primary bioactive compounds in garlic are organosulfur compounds, which are also responsible for its characteristic pungent odor [7]. The key organosulfur constituents include diallyl sulfide (DAS), diallyl disulfide (DADS), and diallyl trisulfide (DATS), all of which demonstrate a wide range of pharmacological properties as shown in Figure 1 [8, 9]. Recent studies have extensively documented various physiological effects of garlic oil (GO), such as anti-atherosclerotic, antihypertensive, antibacterial, anticancer, and immunomodulatory effects, which are attributed predominantly to antioxidant and anti-inflammatory mechanisms [10]. However, the clinical application of GO is substantially limited by its complex chemical composition, poor solubility, instability, and pronounced pungency. Consequently, contemporary studies have concentrated on increasing the stability and bioavailability of garlic oil, attenuating its irritant properties, and optimizing its therapeutic and nutritional potential in clinical applications.

Liposomes (Lips) are nanoscale spherical vesicles that are composed primarily of phospholipids, cholesterol, and various auxiliary components; they are characterized by their nonimmunogenicity, low likelihood of causing allergic reactions, and high safety [11]. The PEG layer in GO loaded liposomes increases circulation time and provides a stealth sheath that stabilizes the drug delivery system in blood and in storage [12]. A good example of this approach is Doxil (a

liposomal drug formulation that is used to deliver chemotherapeutic doxorubicin into the cancer cells). Doxil was approved by the FDA in 1995 [13]. As a mature drug delivery system, liposomes are capable of encapsulating a diverse array of compounds ranging from small molecules to large biological macromolecules, and they have been shown to significantly increase drug delivery efficiency, therapeutic efficacy and effectively reducing the side effects of drugs across a broad spectrum of disease [14]. While, by exploiting the enhanced permeability and retention (EPR) effect, which is enabled by the increased pulmonary vascular permeability in ALI, Lips with particle sizes ranging from 100 to 200 nm can accumulate at sites of lung injury via vascular gaps. This accumulation facilitates an increase in the local concentration of the therapeutic agent [15]. Consequently, liposomes were chosen as the delivery system to generate experimental data supporting the commercialization of GO nanoformulations. In subsequent studies, we intend to develop GO nanomicelles and nanoemulsions.

In this study, for the first time, liposomes composed of DSPC, cholesterol, and DSPE-MPEG2000 were used to deliver GO to ameliorate lipopolysaccharide (LPS)-induced acute lung injury. Here, GO-loaded liposomes (GO-lips) were prepared, and their morphology, size, encapsulation efficiency, and stability were systematically characterized. Moreover, we conducted an in-depth investigation into the ability of GO-lips to increase the protective efficacy of GO against LPS-induced ALI. The findings revealed that the protective mechanism of GO-lips is facilitated through the activation of Nrf2, which subsequently promotes the upregulation of antioxidant gene expression. This cascade effectively mitigates oxidative stress-induced tissue damage and suppresses the ROS-mediated inflammatory cytokine storm in pulmonary tissues. This preliminary study provides further evidence that PEG-stabilized liposomes may serve as promising carriers for hydrophobic liquid drugs.

Materials and methods

Chemical reagents

The following compounds were used in this study: GO (Yuanye Co. Ltd., Shanghai, China; CAS: 8008-99-9), DSPC (CAS: 816-94-4), DSPE-MPEG2000 (CAS: 147867-65-0), cholesterol (CAS: 57-88-5), all procured from A.V.T. Co. Ltd. (Shanghai, China), chloroform (Chronchem Co. Ltd., Sichuan, China; CAS: 67-66-3), methanol (Thermo Fisher Scientific, USA; CAS: 67-56-1), formic acid (Macklin, Shanghai, China; CAS: 64-18-6), HEPES (Amresco, CAS: 7365-45-9), potassium phosphate monobasic (Guangnuo Co. Ltd., Shanghai, China; CAS: 7778-77-0), potassium phosphate dibasic (Damao Co. Ltd., Tianjin, China; CAS: 7758-11-4), and dimethyl sulfoxide (Biotopped, Beijing, China; CAS: 67-68-5).

Preparation and characterization of garlic oil-loaded PEG-stabilized liposomes

Preparation of garlic oil-loaded PEG-stabilized liposomes

Garlic oil-loaded PEG-stabilized liposomes (GO-lips) were prepared via the thin-film dispersion method with a DSPC: cholesterol: $MPEG_{2K}$-DSPE molar ratio of 0.151:0.099:0.014. Briefly, 114.98 mg of DSPC, 38.3 mg of DSPE-MPEG2000, and 38.29 mg of cholesterol were accurately weighed and transferred into a 50 mL round-bottom flask containing a dry magnetic stirrer. The mixture was thoroughly dissolved in chloroform, after which an aliquot of 10 μL of GO was added. During gentle stirring for 2 h, a homogeneous and transparent lipid mixture was formed, and precautions were taken to avoid splashing the mixture onto the flask walls. The organic solvent was subsequently removed by slow evaporation using a rotary evaporator under reduced pressure at 40 °C. During solvent volatilization, the phospholipid molecules assembled into a thin and compact drug-loaded lipid film on the surface of the flask. The experimental temperature was optimized on the basis of the physicochemical properties of phospholipids to ensure complete dissolution while minimizing the risk of thermal degradation, as excessive temperatures may promote phospholipid oxidation and hydrolysis, thereby compromising the quality of the resulting film. The product was sealed to maintain its dryness and stored at 4 °C for a period of more than 3 days.

Characterization of GO-loaded liposomes

The solution was dissolved in selected solvents and subjected to low-temperature ultrasonication to obtain liposomes. The mean particle size of the liposomes was determined using a Malvern Zetasizer Nano ZS90 (Malvern Nano ZS, Malvern, UK). Briefly, 1 mL of the GO-loaded liposome mixture was transferred into a dish and was subsequently analyzed using a Marvin laser particle size analyzer to determine the particle size distribution.

The morphology of the liposomes was characterized via transmission electron microscopy (TEM). Briefly, a single drop of the liposome sample was carefully deposited onto a copper grid coated with a carbon membrane. The samples were allowed to air dry at ambient temperature for 30 min to ensure complete evaporation of the solvent. The samples were subsequently imaged using a Hitachi H-600 transmission electron microscope operated at an accelerating voltage of 200 kV. Micrographs were acquired at a magnification of ×20,000 with an accelerating voltage of 200 kV.

GO-lip were dissolved in deionized water, HEPES buffer, or phosphate buffer (pH 5.8), and stability assessments were conducted at controlled temperatures (4 °C, room temperature, and 40 °C) to validate the encapsulation efficiency and stability. The GO concentration was quantitatively determined using high-performance liquid

chromatography (HPLC) after mixing with methanol at a 1:1 ratio. Following identification of the optimal solvent system, the micelles were reconstituted in deionized water and separated by centrifugation at 14,000 rpm for 10 min, which resulted in a precipitated phase containing encapsulated GO. The precipitate was subsequently resolubilized in DMSO through a sequential process involving 5 min of vortex mixing and 30 min of sonication, with this dissolution cycle repeated three times to ensure complete dissociation of the liposomes. Both the supernatant and the DMSO-dissolved precipitate fractions were mixed with an equal volume of methanol prior to HPLC analysis for precise determination of the encapsulation efficiency.

Animal experiments

All animal procedures were performed in strict accordance with the national standards for the care and use of laboratory animals as outlined in the Guidelines for Welfare and Ethical Review of Laboratory Animals (GB/T35892-2018, China). The study protocol was approved by the Animal Care and Use Committee of the General Hospital of Ningxia Medical University (approval number: KYLL-2025-0079). To establish the LPS-induced ALI model, 6- to 8-week-old male ICR mice were obtained from the Animal Experiment Center of Ningxia Medical University. The animals were housed under controlled conditions, which included a 12-h light/dark cycle, an ambient temperature of 22 ± 2 °C, and a relative humidity of 50% ± 10%. Prior to experimentation, the mice were provided *ad libitum* access to standard dry chow and tap water and were acclimated for 1 week. The mice were subsequently randomly assigned to one of four groups (n = 10 for each group): the control, LPS, LPS plus GO-liposome (50 mg/kg, administered 4 h post-LPS administration), and LPS plus GO (50 mg/kg, administered 4 h post-LPS administration) groups. LPS (O111:B4; Sigma–Aldrich, USA) was dissolved in precooled PBS (pH 7.4). 4 h after the intraperitoneal administration of 15 mg/kg LPS, the GO-loaded liposome formulation or GO was administered via tail vein injection at a dose of 50 mg/kg [16]. 2 h following the intravenous administration of GO, all mice were anesthetized using pentobarbital at a dosage of 60 mg/kg and subsequently euthanized humanely via CO_2 inhalation. In accordance with international ethical guidelines aimed at minimizing animal distress, lung tissues, blood samples, and bronchoalveolar lavage fluid (BALF) were systematically collected.

Evaluation of pulmonary edema via the wet/dry weight ratio and lung coefficient

After 6 h of modeling, the mice were euthanized, the left lung was harvested via thoracotomy, blotted dry with filter paper, and placed in a preweighed EP tube, after which the wet weight was recorded and labeled. The sample was subsequently dried in an oven at 80 °C for 48 h until complete dehydration was achieved, after which the dry weight was recorded. The wet/dry weight ratio (W/D) of the lung tissue and the lung coefficient were calculated, and these ratios were used to determine the lung water content, i.e., the degree of pulmonary edema.

Histological analysis of pulmonary tissue

After 6 h of modeling, the mice were euthanized for tissue collection. For mice not subjected to bronchoalveolar lavage, the fur was initially moistened with alcohol swabs and carefully removed to expose the thoracic cavity. Subsequently, a small portion of the left lung lobe was excised with meticulous attention to preserve structural integrity in order to avoid artifacts that could interfere with data interpretation. The harvested tissue was immediately fixed with 10% formalin for 24–48 h. Following fixation, the samples were subjected to dehydration using a graded series of ethanol solutions with increasing concentrations. The tissue was subsequently embedded in paraffin, and after solidification, serial sections of 5 μm thickness were prepared. Hematoxylin and eosin (H&E) staining was subsequently performed to facilitate microscopic examination of pathological alterations within the lung tissue. The pathological scores for lung injury were assessed according to previously established criteria [16].

Measurement of the total protein content, inflammatory cell count and cytokine levels in BALF

Following euthanasia, the thoracic cavity was surgically accessed, and the left bronchus was ligated. Subsequently, 0.6 mL of ice-cold PBS was delivered into the right lung lobe via a sterile blunt needle to collect BALF. Each mouse was injected with a total volume of 1.5 mL of ice-cold PBS. The total protein concentration in the collected BALF was quantified using a bicinchoninic acid (BCA) protein assay kit (SW201-02; Beijing Qihai Biotechnology Co., Ltd.) in accordance with the manufacturer's protocol, and this value served as an indicator of pulmonary permeability. Inflammatory cells were stained using a Wright-Giemsa staining kit for 20 min at room temperature (D010-1-2; Nanjing Jiancheng Bioengineering Institute) and visualized by light microscopy.

Enzyme-linked immunosorbent assay (ELISA)

Bronchoalveolar lavage fluid and lung tissue homogenates were centrifuged at 12,000 rpm for 10 min to separate the

supernatant. The concentrations of TNF-α, IL-4, IL-6, and IL-10 in both the BALF, serum, lung tissue samples were determined using ELISA kits (catalog numbers 88-7324, 88-7044, 88-7064, and 88-7105; Thermo Fisher Scientific, USA). All procedures were conducted in strict accordance with the manufacturers' protocols. Absorbance readings were obtained at 450 nm using a microplate reader, and cytokine concentrations were determined on the basis of the corresponding standard curves.

Measurement of NO release

The *in vivo* concentration of nitric oxide was determined utilizing a nitric oxide detection kit (S0021; Beyotime Biotechnology Co., Ltd., Shanghai, China). All procedures were conducted in strict accordance with the manufacturer's protocol. Absorbance measurements were obtained at 540 nm using a microplate reader, and nitric oxide concentrations were quantified on the basis of a standard calibration curve.

Assessment of oxidative stress in the ALI model

After 6 h of modeling, the mice were euthanized, and the right lung lobe was excised. The tissue was immediately immersed in ice-cold PBS, promptly homogenized, and centrifuged at 12,000 rpm for 10 min to obtain the supernatant for subsequent oxidative stress assays. The total antioxidant capacity (T-AOC; kit S0121), MDA concentration (kit S0131S), superoxide dismutase (SOD) activity (kit S0101S), and hydrogen peroxide concentration (H_2O_2; kit S0051) in both lung tissue homogenates and serum were quantified with kits purchased from Beyotime (Shanghai, China) following the manufacturer's protocols. Samples were aliquoted into 96-well plates, and absorbance readings were obtained using a microplate reader. The concentrations of each analyte were calculated in accordance with the instructions of the corresponding kit. All the procedures adhered strictly to the manufacturer's recommended protocols.

Real-time reverse transcription–PCR (qRT–PCR) analysis of mRNA expression

In this study, total RNA was first isolated from lung tissue samples utilizing AXYGEN buffer (Wujiang, China). cDNA synthesis was subsequently carried out using an All-in-One First-Strand cDNA Synthesis SuperMix kit (TrsanBiotechgen, China). qRT–PCR analysis was performed using a Tip Green qPCR SuperMix Kit (TrsanBiotechgen, China) with the primer sequences listed in Table 1. GAPDH served as the internal control for normalization purposes, and relative mRNA expression levels were calculated using the $2^{-\Delta\Delta CT}$ method.

Molecular dynamics simulations

GROMACS software was employed for molecular dynamics (MD) simulations. A simulation system was developed by combining the target protein with diallyl trisulfide (DATS), the principal small molecule component of garlic oil. The simulations were carried out under isothermal–isobaric (NPT) ensemble conditions with the application of periodic boundary conditions. The assembled complex was subjected to a 50000 ps molecular dynamics run, during which conformational snapshots were recorded at 10-picosecond intervals. Key parameters, including the root mean square deviation (RMSD), root mean square fluctuation (RMSF), and radius of gyration (Rg), were computed to assess the structural stability and flexibility of the complex. Furthermore, Gibbs free energy landscape analysis was employed to identify the lowest-energy conformational state, thereby confirming the presence and stability of the interaction between the Nrf2 protein and the natural compound DATS [17].

Statistical analysis

One-way ANOVA was used for statistical analysis. All the data are presented as the means ± SEMs, and GraphPad Prism version 10.0 (GraphPad Software, Inc., San Diego, CA, USA) was used for data analysis. After ANOVA, *post hoc* multiple comparisons were performed with Tukey's honestly significant difference test to determine the significance of the differences among the subgroups unless otherwise indicated. $p < 0.05$ was considered to indicate a significant difference, and n.s. was used to indicate a nonsignificant difference.

Results

Preparation and Characterization of GO-Loaded PEG-Stabilized liposomes

GO-loaded liposomes (GO-lips) were prepared using the thin-film dispersion method combined with ultrasonic hydration. GO was incorporated into the hydrophobic lipid bilayer. A schematic representation of the GO-lip nanostructure is shown in Figure 2A. The liposome exhibits a spherical configuration composed of DSPC and cholesterol, with a hydrophilic polyethylene glycol (PEG) edge chain formed by the DSPE-MPEG2000 incorporated into its structure, which stabilizes the hydrophobic periphery. The TEM images (Figure 2B) and particle size distribution analysis results (Figure 2C) confirmed the successful fabrication of GO-lips with a predominantly spherical morphology. The average particle diameter was measured to be 175 ± 3 nm, with a polydispersity index (PDI) of a PDI of 0.27 ± 0.02, a zeta potential of −0.292 ± 0.007 mV. The encapsulation efficiency

TABLE 1 Primer sequences used for quantitative real-time PCR.

Gene	Forward	Reverse
Nrf2	TCTCCTCGCTGGAAAAAGAA	AATGTGCTGGCTGTGCTTTA
HO-1	CAAGCCGAGAATGCTGAGTTCATG	GCAAGGGATGATTTCCTGCCAG
NQO1	TCAGCCAATCAGCGTTC	CTCCTTCATGGCGTAGTTG
GPX4	CAGGCAAGACCGAAGTAAACTAC	CCGAACTGGTTACACGGGAA
SOD	ATTGACGTGTGGGAGCA	AATGTGGCCGTGAGTGA
TNF-α	CAGGTTCTCTTCAAGGGACAAGGC	TGACGGCAGAGAGGAGGTTGAC
IL-1β	TGAAGTTGACGGACCCCAAAAGAT	GTTGATGTGCTGCTGCGAGATTTG
IL-6	AGACTTCCATCCAGTTGCCTTCTTG	TCTGTTGGGAGTGGTATCCTCTGTC
iNOS	AGACCCAGGAGTGTTCACAGACC	CATTGGCCAGCTGCTTTTGC
GAPDH	GGTTGTCTCCTGCGACTTCA	TGGTCCAGGGTTTCTTACTCC

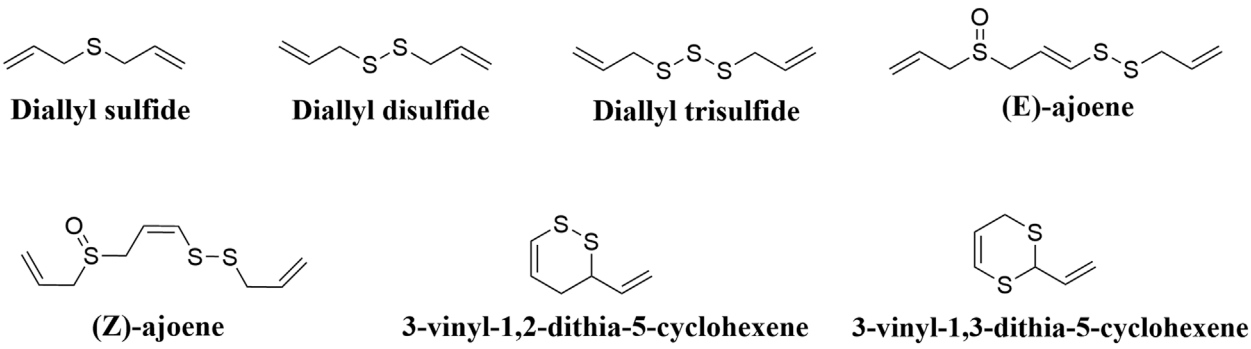

FIGURE 1
Sulfur-containing organic compounds present in GO.

of GO within the liposomes was approximately 70.74 ± 2.11%. Furthermore, owing to the increased density of GO compared with the buffer solution, the formulation exhibited increased stability, and the concentration of GO-lips was effectively increased through centrifugation.

GO-lips effectively ameliorated LPS-induced ALI

GO-lips significantly alleviated LPS-induced ALI in mice. Histopathological examination of lung tissue via H&E staining revealed that the mice in the control group exhibited a relatively intact alveolar architecture with minimal hemorrhage following intraperitoneal LPS administration, as shown in Figure 3. In contrast, the mice in the model group exhibited severe pulmonary damage characterized by extensive inflammatory cell infiltration within the alveolar spaces, marked congestion of lung tissue, and evident alveolar hemorrhage under microscopic observation. Administration of GO-lips, particularly in the liposomal formulation, attenuated these pathological changes, as evidenced by the reduced interstitial thickening, diminished neutrophil infiltration, and decreased number of hemorrhagic and congestive lesions. Notably, compared with the nonliposomal treatments, the GO liposomal formulation exerted a more pronounced anti-inflammatory effect against LPS-induced lung injury.

GO-lips mitigated pulmonary edema in murine models

In mice, LPS stimulation induces pulmonary edema, which can be quantitatively assessed by calculating the lung wet-to-dry weight ratio and the lung coefficient. As shown in Figures 4A,B, the lung W/D in the LPS-treated model group was markedly

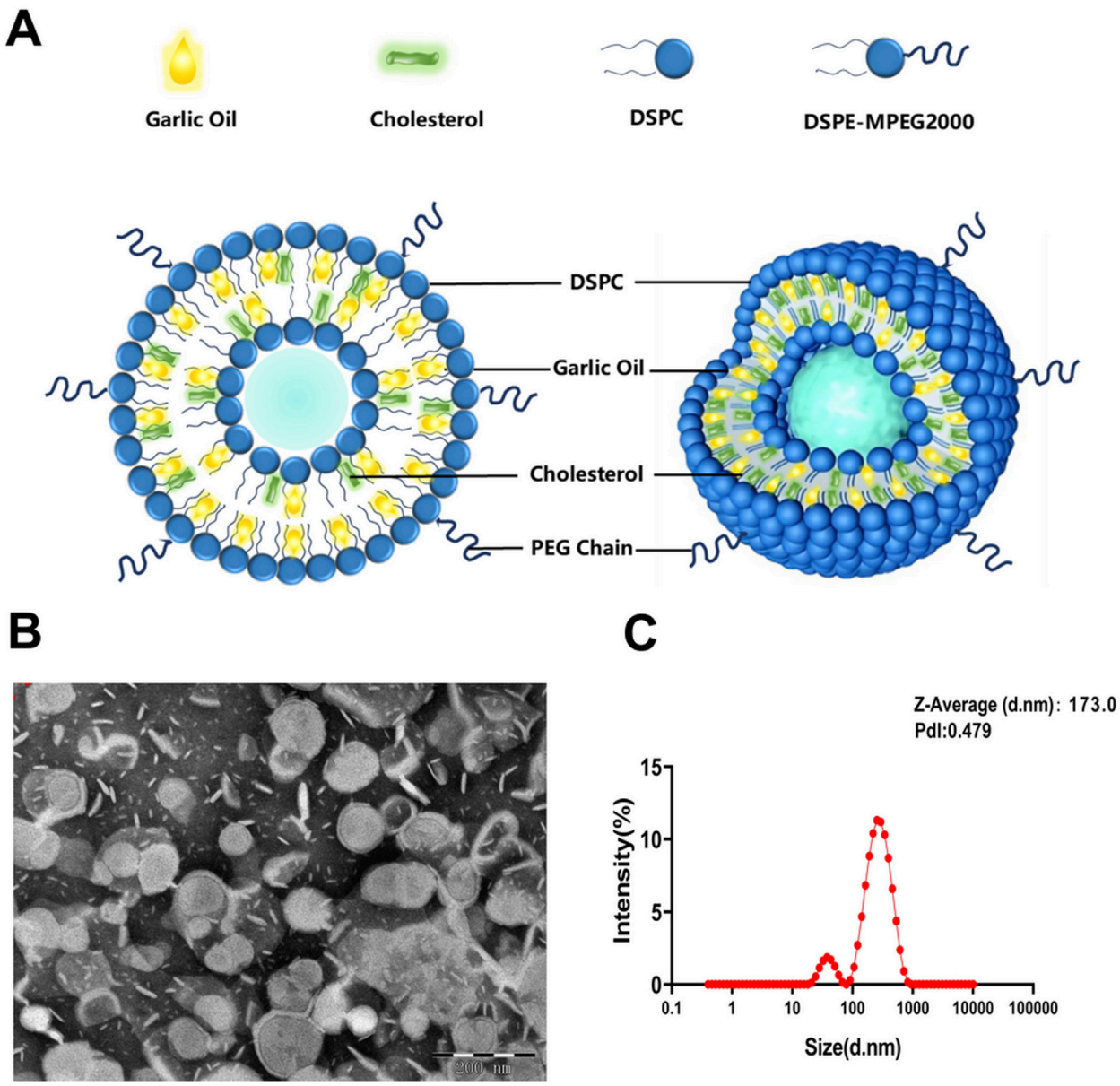

FIGURE 2
Preparation and Characterization of GO-Loaded PEG-Stabilized Liposomes. Spatial and planar structures of GO -loaded PEG-stabilized lipsomes (GO-lip). **(A)** Lipids with dark blue head groups symbolize phospholipids, those with blue-black head groups represent PEG-lipids, the yellow parts represent GO, and the green parts symbolize cholesterol. **(B)** TEM images of the GO loaded lipsomes. The scale bar on the TEM image is 200 nm. **(C)** Dynamic light scattering analysis of GO-lip. The results demonstrated that we successfully constructed GO-lip.

greater than that in the control group ($^{###}p < 0.001$). However, the administration of GO-lips resulted in significant decreases in both the lung wet-to-dry weight ratio and the lung coefficient ($^{**}p < 0.01$). Furthermore, LPS exposure increased capillary membrane permeability compared to that observed in the normal control group ($^{###}p < 0.001$), leading to the extravasation of macromolecular substances and a consequent significant increase in the protein concentration in BALF. Notably, the administration of GO-lips effectively decreased capillary membrane permeability, thereby substantially limiting the increase in the protein concentration in BALF (Figure 4C; $^{***}p < 0.001$), as well as neutrophil (Figure 4D; $^{***}p < 0.001$) and macrophage (Figure 4E; $^{***}p < 0.001$) numbers in mice BALF. Remarkably, GO encapsulated in liposomes exhibited an even greater capacity to reduce the protein content in alveolar lavage fluid.

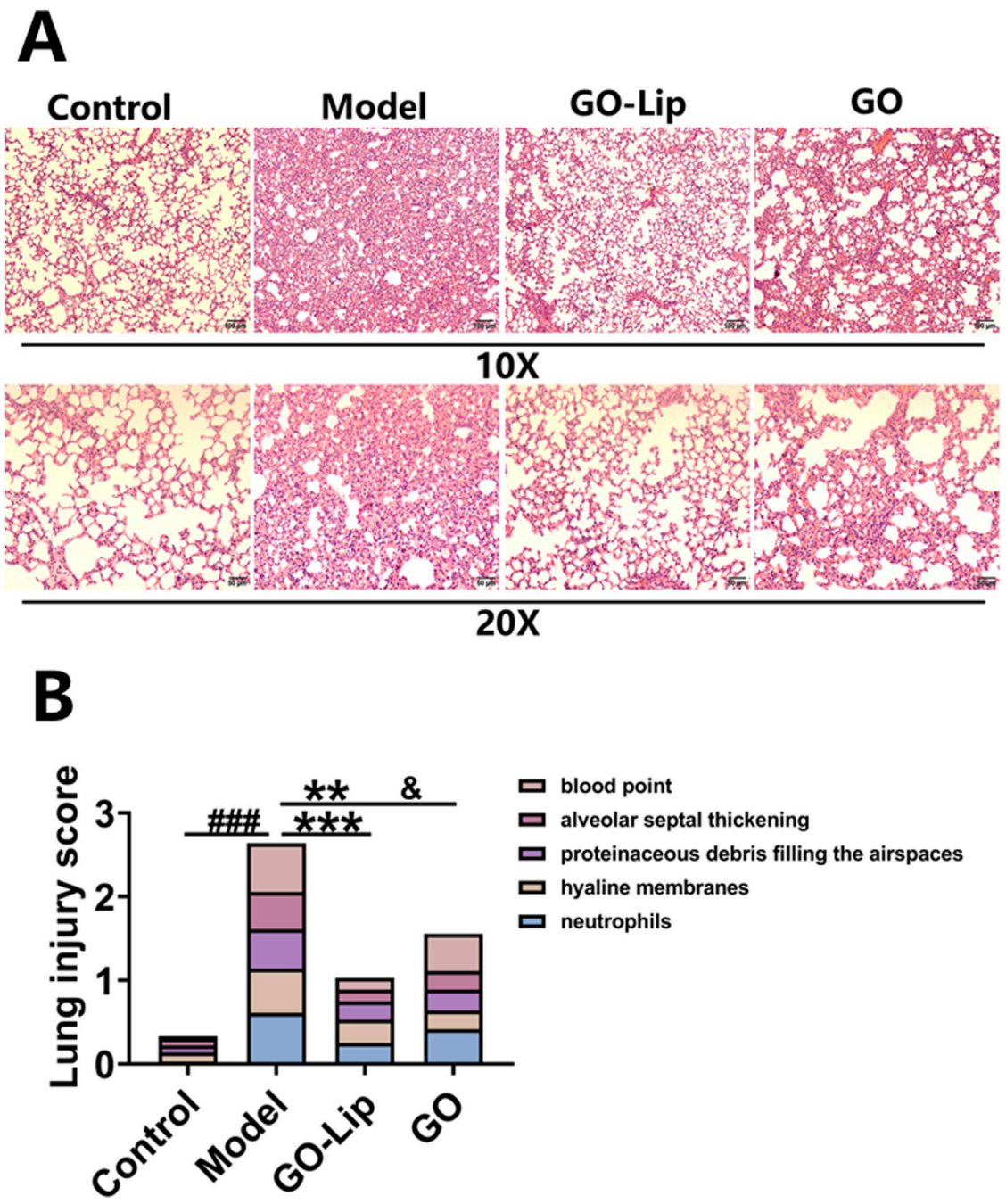

FIGURE 3
GO-lip effectively ameliorated LPS-induced ALI. **(A)** Representative H&E-stained lung tissue sections (magnification ×10, ×20 and scale bar 100 μm, 50 μm). **(B)** Pathology scores of lung tissues. The results confirmed that GO-lip can more effectively alleviate lung pathological lesions and reduce the lung injury score.

GO-lip mitigated the LPS-induced release of multiple cytokines in mice

ALI is characterized primarily by damage to lung tissue resulting from uncontrolled and progressively amplified inflammatory responses within the body. The activation and subsequent release of proinflammatory cytokines in lung tissue are crucial factors in the pathogenesis and progression of ALI and serve as key biomarkers for the systemic inflammatory status. In the present study, ELISAs

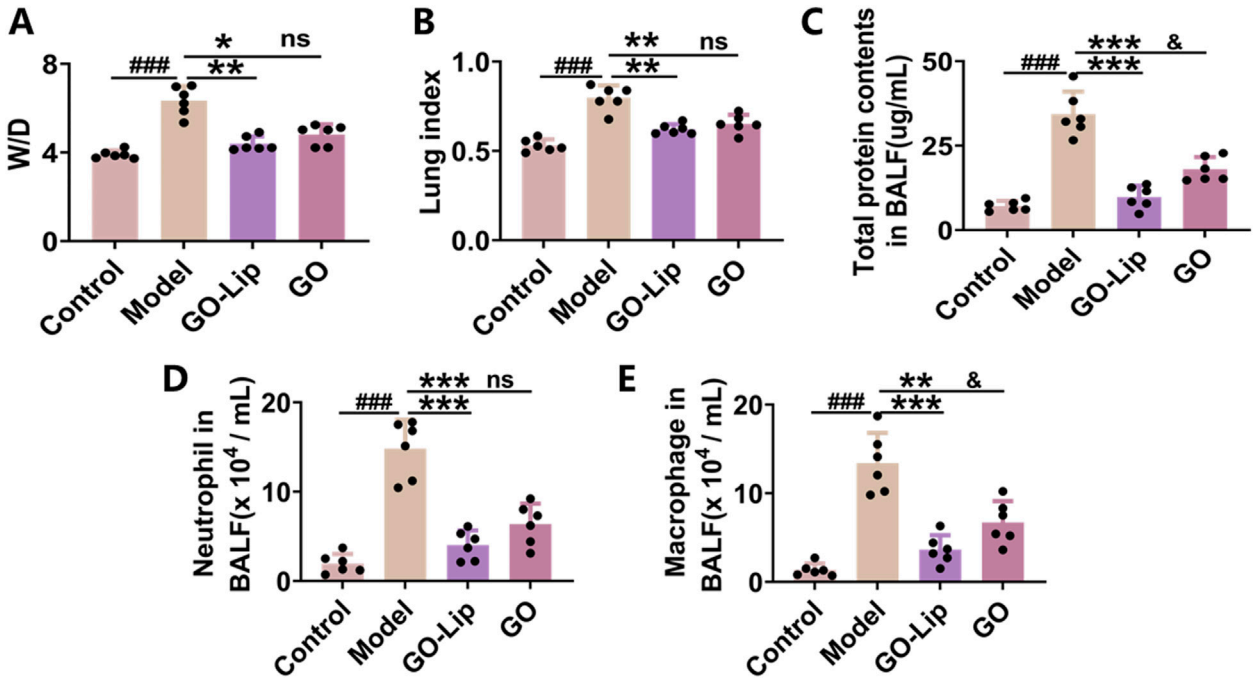

FIGURE 4
GO-lip mitigated pulmonary edema in murine models. The impact of GO-lip on lung tissue W/D **(A)**, lung index **(B)**, total protein concentration in BALF **(C)**, the number of neutrophil granulocytes **(D)** and macrophage **(E)** were in BALF was evaluated in LPS-induced ALI mice. Data are presented as means ± SDs. Statistical significance is indicated as follows: $^{###}p < 0.001$ versus the control group; $^{*}p < 0.05$, $^{**}p < 0.01$, and $^{***}p < 0.001$ versus the model group; $^{\$}p < 0.05$ compared to the GO-lip group, n.s.: no significant. The results indicated that GO-lip can more effectively attenuate pulmonary edema and diminish the infiltration of inflammatory cells.

were used to quantify the concentrations of proinflammatory cytokines, specifically TNF-α and IL-6, in both the BALF, lung tissue and serum of mice with LPS-induced ALI (Figures 5A–F). The findings demonstrated that LPS administration significantly increased TNF-α and IL-6 production compared to that in the blank control group ($^{###}p < 0.001$). Conversely, the administration of GO-lips markedly decreased the concentrations of these inflammatory mediators in mice stimulated with LPS ($^{***}p < 0.001$). Additionally, the concentrations of IL-4 and IL-10, recognized as pivotal anti-inflammatory cytokines that can modulate excessive inflammatory responses and are produced by various cell types, including B cells and macrophages, were evaluated. Quantitative analysis via ELISA revealed modest increases in IL-4 and IL-10 secretion in the ALI model group (Figures 5G–L, $^{#}p < 0.05$, $^{###}p < 0.001$). Notably, GO-lip treatment significantly increased the secretion of these anti-inflammatory cytokines compared to that in the model group ($^{***}p < 0.001$). Furthermore, at equivalent doses, GO encapsulated in liposomes had a more pronounced inhibitory effect on LPS-induced pulmonary inflammation and the production of inflammatory mediators than did unencapsulated GO.

GO-lips attenuate oxidative stress induced by LPS in murine models

A comprehensive review of the relevant literature indicated that oxidative stress interacts with inflammatory responses, leading to cellular damage. Accordingly, in the present study, the protective effects of GO-lips against LPS-induced oxidative stress were initially assessed by measuring the T-AOC and the activity of SOD and CAT in both lung tissue and serum from mice. Compared with the control and treatment groups, the LPS model group exhibited significant decreases in the T-AOC (Figures 6A,B, $^{###}p < 0.001$) and in the expression levels of the antioxidant enzymes CAT (Figure 6C, $^{###}p < 0.001$) and SOD (Figure 6D, $^{###}p < 0.001$). Notably, the administration of 50 mg/kg GO-lips markedly increased antioxidant enzyme activity and restored the total antioxidant capacity ($^{***}p < 0.001$). Building upon these results, we further investigated the effect of GO-lips on oxidative stress in mice with LPS-induced ALI. The concentrations of the oxidative stress markers MDA and NO in lung tissue and serum were quantified using MDA and NO assays. The LPS-induced ALI group presented significantly increased concentrations of NO (Figures 6E,F, $^{###}p < 0.001$) in the plasma and lung interstitium, as along

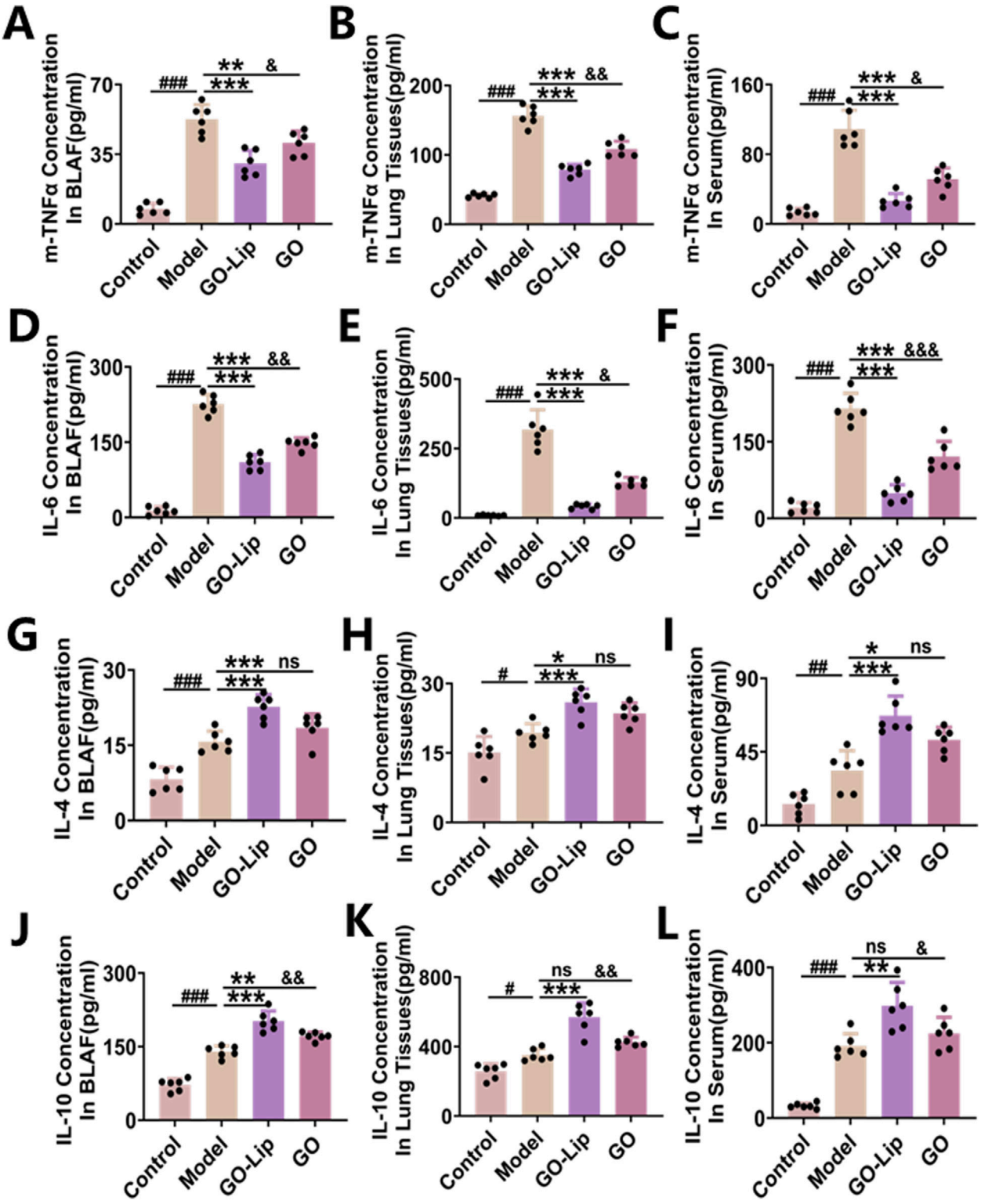

FIGURE 5
GO-lip mitigated the LPS-induced release of multiple cytokines in mice. In the context of LPS-induced acute lung injury, TNF-α **(A–C)**, IL-6 **(D–F)**, IL-4 **(G–I)**, and IL-10 **(J–L)** were measured. Data are presented as means ± SDs. Statistical significance is indicated as follows: $^{###}p < 0.001$ relative to the control group; $^{*}p < 0.05$, $^{**}p < 0.01$, and $^{***}p < 0.001$ relative to the model group; and $^{\&}p < 0.05$, $^{\&\&}p < 0.01$ relative to the GO-lip group, n.s.: no significant. The results confirmed that GO-lip can more effectively inhibit the secretion of pro-inflammatory cytokines and enhance that of anti-inflammatory cytokines.

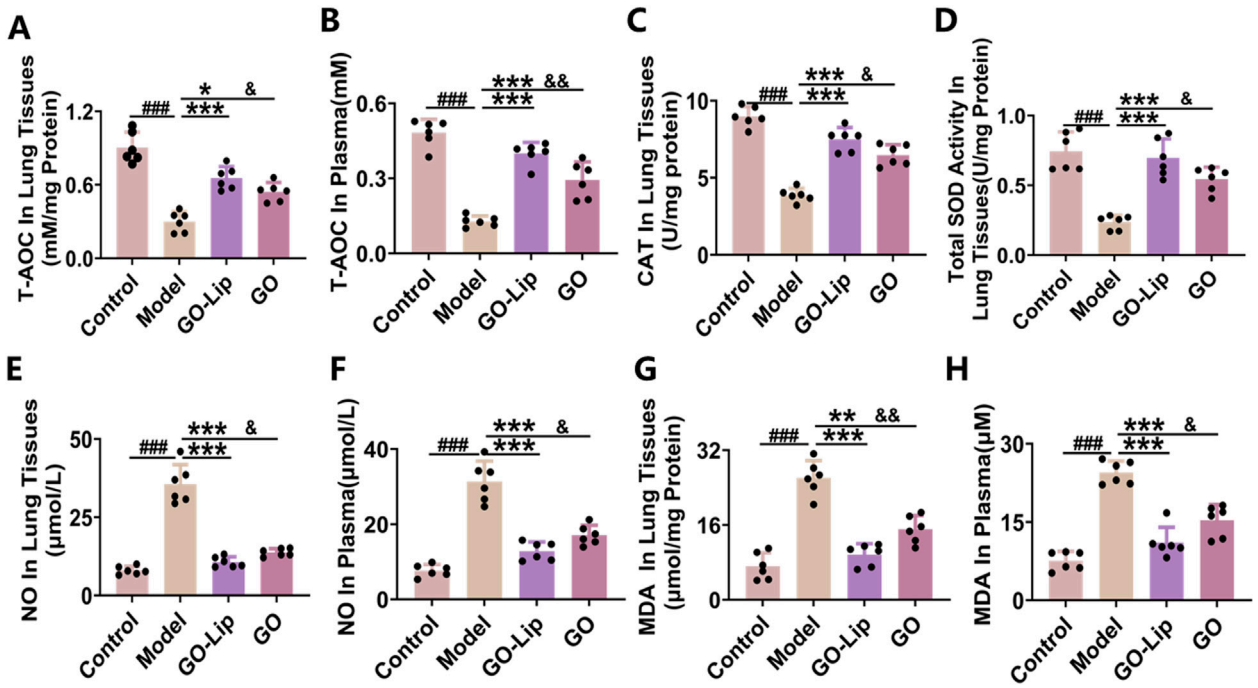

FIGURE 6
GO-lip attenuate oxidative stress induced by LPS in murine models. In the context of LPS-induced ALI, the levels of T-AOC **(A,B)**, CAT **(C)**, SOD **(D)**, NO **(E,F)**, MDA **(G,H)** were measured. Data are presented as means ± SDs. Statistical significance is indicated as follows: $^{\#\#\#}p < 0.001$ versus the control group; $^{*}p < 0.05$, $^{**}p < 0.01$, $^{***}p < 0.001$ versus the model group; $^{\&}p < 0.05$, $^{\&\&}p < 0.01$ versus the GO-lip group, n.s.: no significant. The results confirmed that GO-lip more effectively alleviate oxidative stress-induced damage and restore antioxidant capacity.

with increased concentrations of MDA (Figures 6G,H, $^{\#\#\#}p < 0.001$), a lipid peroxidation end product, indicating pronounced oxidative stress. Treatment with GO-lips effectively mitigated LPS-induced oxidative stress by significantly reducing the MDA and NO levels ($^{***}p < 0.001$). Importantly, at an equivalent dose, the therapeutic effect of GO encapsulated in liposomes was superior to that of unencapsulated GO.

GO-lips activate the Nrf2 signaling pathway in mice with ALI

The Keap1–Nrf2 signaling pathway is the main antioxidant defense mechanism against environmental stress-induced damage. To evaluate the anti-inflammatory and antioxidant mechanisms of GO-lips, RT–qPCR was used to quantify the mRNA expression levels of key components of relevant signaling pathways, including Nrf2, HO-1, NQO1, GPX4, and SOD. The RT–qPCR results revealed that following ALI induction, GO-lip treatment elicited more pronounced activation of the Nrf2 pathway than did free GO treatment, thereby increasing the antioxidant capacity *in vivo* (Figures 7A–E, $^{\&}p < 0.05$, $^{\&\&}p < 0.01$). The generation of ROS induces the nuclear translocation of p65, which subsequently upregulates the expression of proinflammatory mediators such as TNF-α, IL-1β, IL-6, and iNOS. Notably, treatment with GO-lips significantly decreased the levels of these proinflammatory cytokines in murine models, consistent with our prior ELISA results (Figures 7F–I, $^{\&}p < 0.05$, $^{\&\&}p < 0.01$, $^{\&\&\&}p < 0.001$). Collectively, these data suggest that the therapeutic effects of the GO-lip formulation on LPS-induced ALI may be attributed, at least partially, to its ability to activate the Nrf2 signaling pathway.

Molecular dynamics simulation of Nrf2 and compounds in GO

To comprehensively examine the anti-oxidative stress effects of GO, we elucidated the ligand-binding interaction between DATS, the principal small molecule component of GO, and the Nrf2 protein. Additionally, MD simulations were conducted to assess the stability and flexibility of the Nrf2–DATS complex. As shown in Figure 8A, the RMSD metric was employed to evaluate the structural stability of the complex throughout the MD simulations [18]. The all-atom MD simulations, performed over a duration of 50 ns, demonstrated that the Nrf2–DATS complex maintained its structural stability, with the backbone RMSD consistently remaining within an acceptable range and exhibiting minimal fluctuations during the simulation period. The RMSF was used to assess variations in the complex at the

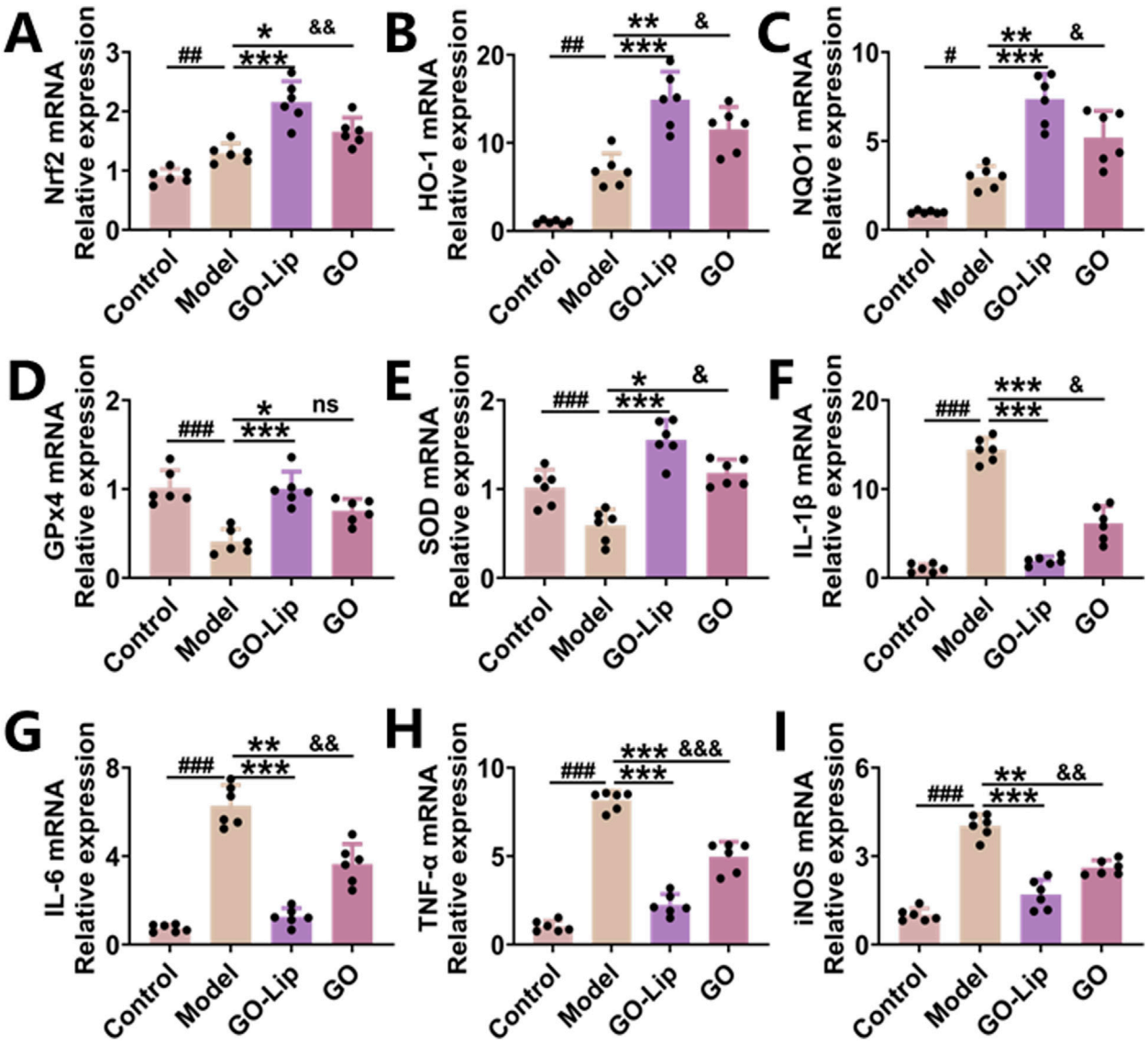

FIGURE 7
GO-lip inhibited oxidative stress and inflammatory responses via the Nrf2 signaling pathway. **(A–I)** Nrf2, HO-1, NQO1, GPx4, SOD, IL-1β, IL-6, TNF-α, iNOS, mRNA were detected using qRT-PCR. Data are presented as means ± SDs. Statistical significance is indicated as follows: $^{\#\#\#}p < 0.001$ versus the control group; $^{*}p < 0.05$, $^{**}p < 0.01$, $^{***}p < 0.001$ versus the model group; $^{\&}p < 0.05$, $^{\&\&}p < 0.01$, $^{\&\&\&}p < 0.001$ versus the GO-lip group, n.s.: no significant. The results confirmed that GO-lip more effectively activated Nrf2 signaling pathway to combat LPS-induced oxidative stress and inflammation responses.

residue level [19]. The RMSF values indicated differential flexibility across residues within the Nrf2 binding pocket, with the majority of the residues involved in the interaction with DATS exhibiting reduced flexibility (<0.6 Å), suggesting increased rigidity upon ligand binding (Figure 8B).

Rg, which is correlated with protein volume and tertiary structure, serves as a critical parameter for evaluating protein stability in biological systems [20]. Elevated Rg values are indicative of increased ligand flexibility and diminished system stability, whereas lower Rg values correspond to a more compact and well-organized protein conformation. As shown in Figure 8C, the Rg value of Nrf2 remained stable throughout the MD simulation, with an average value of between 2.5 and 3.0 nm.

The Gibbs free energy landscape (FEL) provides insight into the stability of a receptor–ligand complex, where lower Gibbs free energy values denote greater complex stability [21]. By utilizing the RMSD and Rg values, a 3D Gibbs free energy landscape was constructed to identify and analyze the steady-state conformational characteristics of the complex. The regions

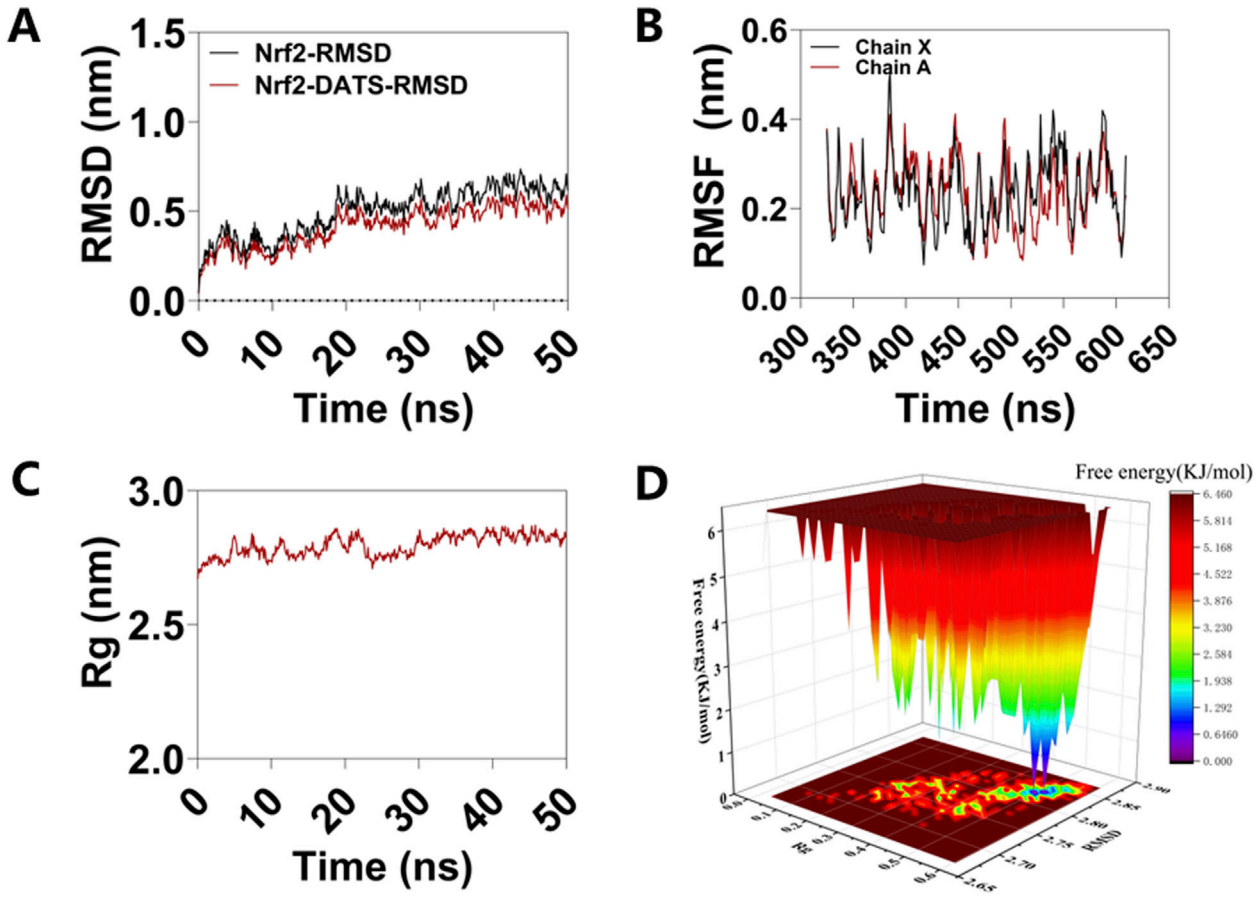

FIGURE 8
MD simulation of Nrf2-DATS in treatment of ALI. **(A)** RMSD curves of Nrf2-DATS complexes; **(B)** RMSF curve of Nrf2-DATS complexes; **(C)** Rg curves of Nrf2-DATS complexes; **(D)** 3D Gibbs free energy landscape of the Nrf2-DATS complex. MD simulations affirmed that DATS stably binds to Nrf2.

depicted in blue and purple within the landscape correspond to stable conformational states exhibiting the minimal free energy. The 3D Gibbs free energy landscapes of the Nrf2–DATS complex are presented in Figure 8D. These visualizations reveal that the complex predominantly occupies a low Gibbs free energy state when the Rg value is between 0.5 and 0.6 nm and the RMSD value is between 2.75 and 2.85 Å.

Discussion

ALI and ARDS represent sequential stages along the same pathological continuum. ALI constitutes the initial phase of the disease, which, upon further clinical deterioration, progresses to ARDS [22]. The recent COVID-19 pandemic has resulted in a significant increase in ALI incidence, underscoring the high mortality associated with this condition and the current lack of effective pharmacological interventions [23]. Currently, the most effective management approach for ALI is protective ventilation, and lung-protective ventilation combined with optimized supportive care is the preferred treatment modality. However, extended application of lung-protective ventilation may result in VILI, thereby worsening the patient's clinical status. Consequently, the identification and development of novel therapeutic agents are critical for reducing ALI-related mortality and improving patient quality of life. GO, a commercially available extract derived from natural garlic, has been demonstrated to modulate multiple signaling pathways and to exert broad biological effects across various disease models. LPS, a principal pathogenic component of Gram-negative bacteria, is an important etiological factor in ALI. LPS exposure induces the excessive production of cytokines, chemokines, and reactive oxygen species, thereby precipitating extensive pulmonary damage through inflammatory cascades [24–26]. The LPS-induced ALI model is widely utilized in experimental research because of its ability to rapidly reproduce acute injury to pulmonary epithelial and endothelial barriers as well as the acute inflammatory

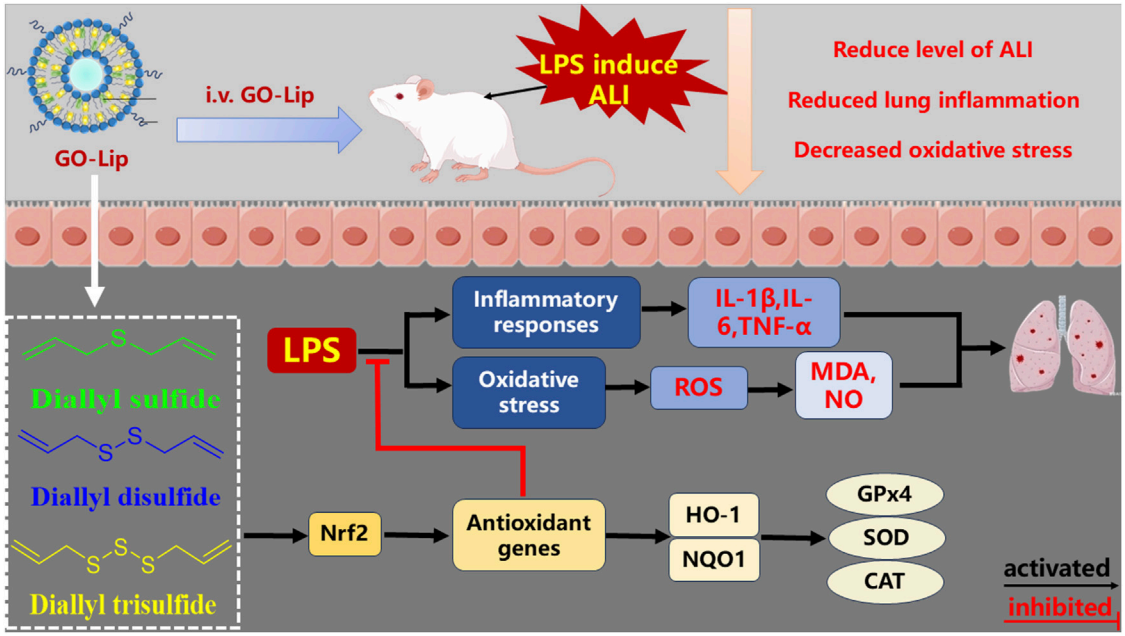

FIGURE 9
The schematic illustration of anti-ALI effects of GO-Lip. In ALI mice, LPS induced inflammation and oxidative stress, which damaged lung tissues. However, GO-Lip protects against LPS-induced ALI attenuates inflammation and oxidative stress by activated Nrf2 signaling pathway.

response within the airways [27]. Preclinical models play an essential role in elucidating pathogenic mechanisms and assessing therapeutic interventions; however, their translational value depends largely on the extent to which they accurately reproduce human disease conditions. Intraperitoneal (i.p.) administration of LPS can be used to model sepsis-associated acute lung injury (SA-ALI). Upon intraperitoneal delivery, LPS gains access to the systemic circulation, triggering a cascade of innate immune responses that culminate in systemic inflammatory response syndrome (SIRS). This inflammatory state frequently progresses to multiple organ dysfunction syndrome (MODS), which is characterized by impaired function of the pulmonary, hepatic, renal, and cardiovascular systems. This pathological progression constitutes the primary clinical manifestation of ALI commonly encountered in ICU settings [28, 29]. This particular model was employed in the current study to facilitate the translation of findings from preclinical investigations to clinical applications within the ICU setting.

Liposomes, which are spherical vesicular carriers composed primarily of phospholipid bilayers and cholesterol, have attracted considerable attention as drug delivery systems because of their structural similarity to cellular membranes. This similarity endows them with excellent biocompatibility, facilitates the targeted accumulation of therapeutic agents at sites of pathology, minimizes adverse effects associated with off-target drug distribution, maintains the pharmacological activity of the encapsulated drug during metabolism and circulation, and increases drug bioavailability [30, 31]. In addition, the unique structure of liposomes allows it to more easily cross the physiological barrier of the lungs to accomplish drug delivery [32]. By regulating their particle size between 100 and 200 nm, they can reduce the rapid clearance of the endothelial system to maintain the required blood drug concentration throughout the body [33]. Liposomal delivered drugs has played an importent therapeutic role in different lung diseases by passively and actively targeting the lesion site, such as viral pneumonia [34], COPD [35], lung cancer [36, 37] and so on. For GO with poor solubility and low bioavailability, the solubility and bioavailability of the drug can be greatly improved by being encapsulated in the hydrophobic core of the liposome, which in turn enhances the therapeutic efficacy of the GO. GO loaded liposomes can directly enter the bloodstream through intravenous injection. Average particle size of GO loaded liposomes is 175 ± 3 nm, they can reduce the rapid clearance of the endothelial system to maintain the required blood drug concentration by passively targeting the lesion site in ALI.

This study demonstrated that following intraperitoneal administration of LPS, mice predominantly exhibited reduced feeding and drinking behaviors, lethargy, an inability of the forelimbs to support the body, piloerection, limb tremors, hypothermia, and incontinence. Conversely, treatment with GO-lips resulted in increased activity levels and increased food consumption in the mice. Histopathological examination

of lung tissues via light microscopy revealed that the lung architecture in the control group mice remained normal and well defined, with no discernible pathological alterations. In contrast, the mice in the LPS-induced model group exhibited severe pulmonary injury and inflammation characterized by extensive infiltration of inflammatory cells within the lung interstitium, thickening of the alveolar septa, disruption of alveolar integrity, and evident intra-alveolar hemorrhage and congestion. Administration of GO-lips markedly attenuated LPS-induced pulmonary damage and inflammatory responses. During the early phase of ALI, substantial infiltration of inflammatory cells impairs alveolar epithelial cell function, resulting in the accumulation of proteins and fluids within the alveoli and lung interstitium instead of their clearance via lymphatic drainage, ultimately leading to pulmonary edema [38–40]. Accordingly, we assessed the extent of pulmonary edema and the integrity of the alveolar–capillary barrier by quantifying the lung W/D, lung coefficient, BALF protein concentration, and neutrophil and macrophage numbers in BALF. The findings indicated that LPS-induced ALI significantly increased the W/D, lung coefficient, BALF protein concentration, and neutrophil and macrophage numbers in BALF compared with those in the control group. Treatment with GO-lips significantly reduced these values, thereby decreasing intra-alveolar accumulation of fluid. These effects are critically important for preserving the pulmonary microenvironment and improving the clinical outcome of ALI.

Acute fulminant inflammation is a pathological hallmark of ALI. Research has indicated that during the initiation, amplification, and persistence phases of ALI-associated inflammation, alveolar macrophages undergo polarization toward the M1 phenotype within the proinflammatory microenvironment. These M1 macrophages subsequently secrete proinflammatory cytokines such as TNF-α, interleukin-1β (IL-1β), and interleukin-6 (IL-6), which facilitate the mobilization, recruitment, and activation of neutrophils, monocytes, and other effector immune cells [41]. TNF-α serves as a critical early mediator of inflammation and is rapidly released at the onset of the inflammatory process. Additionally, TNF-α stimulates the release of other inflammatory cytokines, including IL-1β and IL-6, thereby amplifying the inflammatory cascade [42, 43]. IL-6, which is secreted predominantly by macrophages, is a key proinflammatory cytokine involved in various pulmonary inflammatory disorders [44]. Clinical observations in patients with ALI or sepsis revealed significantly increased concentrations of TNF-α and IL-6 in BALF, which correlated with progressive respiratory dysfunction [45]. Consistent with this finding, resident alveolar macrophages in murine models become polarized toward the M2 phenotype, and this transition is accompanied by the production of diverse anti-inflammatory cytokines that facilitate inflammation resolution and promote local tissue repair [46]. M2 macrophages contribute to the accumulation of specific anti-inflammatory cytokines, notably interleukin-10 (IL-10), which is recognized as a principal anti-inflammatory mediator capable of suppressing the production of multiple proinflammatory factors. Elevated IL-10 levels indicate an enhanced anti-inflammatory response, mitigating tissue damage induced by proinflammatory cytokines [47]. Interleukin-4 (IL-4) also functions as an important anti-inflammatory cytokine, broadly inhibiting the expression of various proinflammatory mediators, including TNF-α and IL-6, and has been demonstrated to promote IL-10 secretion [48]. In the present study, administration of GO-lips via tail vein injection resulted in significant reductions in the TNF-α and IL-6 concentrations compared with those in the model group, along with markedly increased IL-4 and IL-10 secretion. These findings substantiate the ability of GO-lips to attenuate both systemic and local pulmonary inflammatory responses in murine models of endotoxin-induced ALI.

Oxidative stress commonly accompanies inflammation and can exacerbate inflammatory responses, whereas inflammatory mediators can, in turn, further promote oxidative stress. Under physiological conditions, ROS levels are maintained in a dynamic equilibrium through balanced production and elimination. However, external stimuli can induce excessive ROS generation, disrupting the clearance of oxygen free radicals and leading to oxidative imbalance, thus contributing to various pathological states [49]. In the context of ALI/ARDS, the phenomenon known as the respiratory burst results in excessive ROS production, which suppresses endogenous antioxidant defenses and causes oxidative damage [50]. Numerous studies have identified SOD and catalase (CAT) as key antioxidant enzymes capable of scavenging superoxide anions within cells or organisms. Their activity levels serve as indirect indicators of the cellular antioxidant capacity. Conversely, the level of MDA, a lipid peroxidation product, reflects the accumulation of free radicals and the extent of lipid peroxidation [51, 52]. The overall antioxidant capacity of a biological system is determined by the combined levels of antioxidant macromolecules, small molecules, and enzymes, collectively measured as T-AOC, which is a crucial parameter for assessing oxidative stress [53]. During oxidative stress, NO functions as an important biological signaling molecule that can react with free radicals to form nitrite (NO_2^-), a reactive nitrogen species (RNS) with potent oxidizing properties [54]. In the present study, treatment with GO-lips resulted in elevated expression of SOD and CAT, an increased T-AOC, and reduced concentrations of MDA and NO, suggesting a balanced oxidative–antioxidative state in treated mice. Conversely, the mice in the LPS-induced model group exhibited the opposite profile, indicating pronounced oxidative stress. These findings demonstrate that GO-lips possess significant antioxidant capacity and effectively suppress ROS production.

Inflammation and oxidative stress are interrelated processes. Importantly, apoptosis is critically involved in the pathogenesis of

ALI. During the initial phase of LPS-induced ALI, injured alveolar epithelial cells and activated macrophages release ATP via pannexin channels [55]. This extracellular ATP functions as a damage-associated molecular pattern (DAMP), thereby activating purinergic signaling pathways [56]. This activation not only stimulates the formation of the NLRP3 inflammasome, promoting the maturation and secretion of IL-1β, but also induces the production of ROS, exacerbating the reciprocal amplification between inflammatory responses and oxidative stress. Consequently, a cascade of inflammatory mediators activates apoptotic signaling pathways and disrupts mitochondrial homeostasis. Simultaneously, the reaction of ROS and NO generates peroxynitrite, leading to lipid peroxidation, protein and DNA damage, and further activation of apoptotic mechanisms [57].

The complex interplay among inflammation, oxidative stress, and apoptosis highlights the pivotal role of redox imbalance in the pathogenesis of ALI. This redox imbalance is precisely modulated via the Keap1–Nrf2 signaling pathway, which serves as the principal cellular defense mechanism against oxidative damage. The Keap1–Nrf2–ARE signaling pathway constitutes a fundamental mechanism in the regulation of cellular redox balance and the response to xenobiotic stress. Its principal role involves protecting cells against oxidative damage, environmental toxins, and deleterious chemical agents through the activation of transcriptional programs that upregulate cytoprotective genes. Under normal conditions, the transcription factor Nrf2 is retained in the cytoplasm through its interaction with Keap1 and is subjected to ubiquitin-mediated proteasomal degradation. Upon exposure to oxidative stress, Nrf2 escapes degradation and is translocated to the nucleus, where it binds to small Maf proteins and activates the transcription of genes containing antioxidant response elements (AREs) [58]. These processes results in the robust transcription of downstream antioxidant genes, including those encoding HO-1, NQO1, GPX4, and SOD. In summary, Nrf2 mitigates oxidative stress-induced damage by promoting the transcription of antioxidant genes, thereby performing a vital protective function in the pathogenesis of ALI. Additionally, the Nrf2/HO-1 signaling pathway mediates anti-inflammatory effects through the suppression of proinflammatory mediators such as NLRP3, TNF-α, IL-1β, and IL-6 [59, 60]. Consistent with the findings of previous studies, our findings revealed elevated mRNA expression levels of Nrf2, HO-1, and NQO1 after ALI induction. The administration of garlic oil-loaded liposomes markedly increased the expression of Nrf2, HO-1, NQO1, GPX4, and SOD while concurrently reducing the mRNA levels of IL-1β, TNF-α, IL-6, and iNOS.

Molecular simulation is a robust methodology for elucidating the stability and dynamic behavior of protein–ligand complexes. In this study, a 50 ns MD simulation was conducted to analyze the dynamic characteristics of the Nrf2–DATS complex. The MD simulation data, particularly the RMSD, RMSF, and Rg values, provided critical indicators for evaluating the stability of the Nrf2–DATS complex as well as the conformational integrity of the Nrf2 protein's tertiary structure following its interaction with small molecules, including assessments of amino acid residue hydrophobicity. The MD simulation results confirmed that DATS binds stably to Nrf2, thereby facilitating the activation of the Nrf2/HO-1/NQO-1 signaling pathway.

However, further investigations are needed to determine whether GO-lips can directly target pulmonary epithelial cells and pulmonary endothelial cells to exert protective effects and improve delivery efficacy.

Conclusion

In summary, this study focused initially on the development of GO-lips as a novel nanodrug delivery system. *In vivo* experiments were subsequently performed to assess the therapeutic efficacy of this formulation against LPS-induced ALI in Figure 9. The findings indicated that GO-lips markedly increased the therapeutic efficacy of GO. In particular, GO-lips exhibited antioxidant properties mediated through the activation of the Nrf2 signaling pathway, which in turn upregulated the expression of downstream effectors such as HO-1 and NQO1. This mechanism contributed to the attenuation of inflammatory responses induced by oxidative stress and resulted in downregulated expression of proinflammatory genes, including TNF-α and IL-6. Finally, these molecular and cellular effects culminated in the amelioration of pathological alterations in lung tissue architecture.

Author contributions

RH: Conceptualization, Methodology, Writing—original draft preparation, Writing—review and editing, Visualization. XZ: Methodology, Writing—original draft preparation. JZ: Writing—review and editing, Visualization. WZ: Project administration, Resources, Conceptualization, Supervision, Funding acquisition, Writing—original draft preparation, Writing—review and editing. All authors contributed to the article and approved the submitted version.

Data availability

The raw data supporting the conclusions of this article will be made available by the authors, without undue reservation.

Ethics statement

The animal study was approved by General Hospital of Ningxia Medical University Animal Care and Use Committee

(Certificate number no: KYLL-2025-0079). The study was conducted in accordance with the local legislation and institutional requirements.

Funding

The author(s) declared that financial support was received for this work and/or its publication. This work was supported by grants from the 2023 Young Top Talents from the Ningxia Province ([2024] 106).

Acknowledgements

We are grateful to all the participants involved in our research.

Conflict of interest

The author(s) declared no potential conflicts of interest with respect to the research, authorship, and/or publication of this article.

Generative AI statement

The author(s) declared that generative AI was not used in the creation of this manuscript.

Any alternative text (alt text) provided alongside figures in this article has been generated by Frontiers with the support of artificial intelligence and reasonable efforts have been made to ensure accuracy, including review by the authors wherever possible. If you identify any issues, please contact us.

References

1. Mowery NT, Terzian WTH, Nelson AC. Acute lung injury. *Curr Problems Surgery* (2020) **57**:100777. doi:10.1016/j.cpsurg.2020.100777

2. Bos LDJ, Ware LB. Acute respiratory distress syndrome: causes, pathophysiology, and phenotypes. *Lancet* (2022) **400**:1145–56. doi:10.1016/s0140-6736(22)01485-4

3. Wick KD, Ware LB, Matthay MA. Acute respiratory distress syndrome. *BMJ* (2024) **387**:e076612. doi:10.1136/bmj-2023-076612

4. Long ME, Mallampalli RK, Horowitz JC. Pathogenesis of pneumonia and acute lung injury. *Clin Sci (Lond)* (2022) **136**:747–69. doi:10.1042/cs20210879

5. Bezerra FS, Lanzetti M, Nesi RT, Nagato AC, Silva CPE, Kennedy-Feitosa E, et al. Oxidative stress and inflammation in acute and chronic lung injuries. *Antioxidants (Basel)* (2023) **12**:548. doi:10.3390/antiox12030548

6. Yamaguchi Y, Kumagai H. Characteristics, biosynthesis, decomposition, metabolism and functions of the garlic odour precursor, S-allyl-L-cysteine sulfoxide. *Exp Ther Med* (2020) **19**:1528–35. doi:10.3892/etm.2019.8385

7. Omar SH, Al-Wabel NA. Organosulfur compounds and possible mechanism of garlic in cancer. *Saudi Pharmaceutical Journal* (2010) **18**:51–8. doi:10.1016/j.jsps.2009.12.007

8. Lasheen NN, Elayat WM, Elrefai MFM, Zaki WS, Ahmed EH, El Sheikh RMN, et al. Possible role of garlic oil in ameliorating renal injury after liver ischemia/reperfusion in rats. *J Physiology Pharmacol* (2019) **70**. doi:10.26402/jpp.2019.5.12

9. Asdaq SMB, Challa O, Alamri AS, Alsanie WF, Alhomrani M, Asad M. The potential benefits of using garlic oil and its active constituent, dially disulphide, in combination with carvedilol in ameliorating isoprenaline-induced cardiac damage in rats. *Front Pharmacol* (2021) **12**:739758. doi:10.3389/fphar.2021.739758

10. Ko JW, Jeong SH, Kwon HJ, Shin NR, Seo YS, Kim JC, et al. Preventive effect of garlic oil and its organosulfur component diallyl-disulfide on cigarette smoke-induced airway inflammation in mice. *Nutrients* (2018) **10**:1659. doi:10.3390/nu10111659

11. Bian S, Cai H, Cui Y, Liu W, Xiao C. Nanomedicine-Based therapeutics to combat acute lung injury. *Int J Nanomedicine* (2021) **16**:2247–69. doi:10.2147/ijn.S300594

12. Viitala L, Pajari S, Gentile L, Maatta J, Gubitosi M, Deska J, et al. Shape and phase transitions in a PEGylated phospholipid system. *Langmuir* (2019) **35**:3999–4010. doi:10.1021/acs.langmuir.8b03829

13. Barenholz Y. Doxil®--the first FDA-approved nano-drug: lessons learned. *J Control Release* (2012) **160**:117–34. doi:10.1016/j.jconrel.2012.03.020

14. Filipczak N, Pan J, Yalamarty SSK, Torchilin VP. Recent advancements in liposome technology. *Adv Drug Delivery Reviews* (2020) **156**:4–22. doi:10.1016/j.addr.2020.06.022

15. Liao R, Sun ZC, Wang L, Xian C, Lin R, Zhuo G, et al. Inhalable and bioactive lipid-nanomedicine based on bergapten for targeted acute lung injury therapy via orchestrating macrophage polarization. *Bioact Mater* (2025) **43**:406–22. doi:10.1016/j.bioactmat.2024.09.020

16. Su L, Tu Y, Kong DP, Chen DG, Zhang CX, Zhang WN, et al. Drug repurposing of anti-infective clinical drugs: discovery of two potential anti-cytokine storm agents. *Biomed Pharmacother* (2020) **131**:110643. doi:10.1016/j.biopha.2020.110643

17. Xu Y, Liang X, Hyun CG. Isolation, characterization, genome annotation, and evaluation of tyrosinase inhibitory activity in secondary metabolites of paenibacillus sp. JNUCC32: a comprehensive analysis through molecular docking and molecular dynamics simulation. *Int J Mol Sci* (2024) **25**:2213. doi:10.3390/ijms25042213

18. Wargasetia TL, Ratnawati H, Widodo N, Widyananda MH. Antioxidant and anti-inflammatory activity of sea cucumber (Holothuria scabra) active compounds against KEAP1 and iNOS protein. *Bioinformatics Biology Insights* (2023) **17**:11779322221149613. doi:10.1177/11779322221149613

19. Baskin LS. Electric conductance and pH measurements of isoionic salt-free bovine mercaptalbumin solutions. An evaluation of root-mean-square proton fluctuations. *The J Physical Chemistry* (1968) **72**:2958–62. doi:10.1021/j100854a047

20. Chai TT, Wong CC, Sabri MZ, Wong FC. Seafood paramyosins as sources of anti-angiotensin-converting-enzyme and anti-dipeptidyl-peptidase peptides after gastrointestinal digestion: a cheminformatic investigation. *Molecules* (2022) **27**:3864. doi:10.3390/molecules27123864

21. Bharatiy SK, Hazra M, Paul M, Mohapatra S, Samantaray D, Dubey RC, et al. *In silico* designing of an industrially sustainable carbonic anhydrase using molecular dynamics simulation. *ACS Omega* (2016) **1**:1081–103. doi:10.1021/acsomega.6b00041

22. Hsieh PC, Wu YK, Yang MC, Su WL, Kuo CY, Lan CC. Deciphering the role of damage-associated molecular patterns and inflammatory responses in acute lung injury. *Life Sci* (2022) **305**:120782. doi:10.1016/j.lfs.2022.120782

23. Rubin EJ, Baden LR, Morrissey S. Audio interview: acute lung injury in Covid-19. *N Engl J Med* (2020) **383**:e32. doi:10.1056/NEJMe2024719

24. Babu S, Manoharan S, Ottappilakkil H, Perumal E. Role of oxidative stress-mediated cell death and signaling pathways in experimental fluorosis. *Chem Biol Interact* (2022) **365**:110106. doi:10.1016/j.cbi.2022.110106

25. Rojas M, Woods CR, Mora AL, Xu J, Brigham KL. Endotoxin-induced lung injury in mice: structural, functional, and biochemical responses. *Am J Physiol Lung Cell Mol Physiol* (2005) **288**:L333–41. doi:10.1152/ajplung.00334.2004

26. Matthay MA, Zemans RL. The acute respiratory distress syndrome: pathogenesis and treatment. *Annu Review Pathology* (2011) **6**:147–63. doi:10.1146/annurev-pathol-011110-130158

27. Zhang S, Tu Y, Sun YM, Li Y, Wang RM, Cao Y, et al. Swiprosin-1 deficiency impairs macrophage immune response of septic mice. *JCI Insight* (2018) **3**:e95396. doi:10.1172/jci.insight.95396

28. Kumar V. Pulmonary innate immune response determines the outcome of inflammation during pneumonia and sepsis-associated acute lung injury. *Front Immunol* (2020) **11**:1722. doi:10.3389/fimmu.2020.01722

29. Wu D, Spencer CB, Ortoga L, Zhang H, Miao C. Histone lactylation-regulated METTL3 promotes ferroptosis via m6A-modification on ACSL4 in sepsis-associated lung injury. *Redox Biol* (2024) **74**:103194. doi:10.1016/j.redox.2024.103194

30. Yu J, Wang Y, Zhou S, Li J, Wang J, Chi D, et al. Remote loading paclitaxel-doxorubicin prodrug into liposomes for cancer combination therapy. *Acta Pharmaceutica Sinica B* (2020) **10**:1730–40. doi:10.1016/j.apsb.2020.04.011

31. Guimarães D, Cavaco-Paulo A, Nogueira E. Design of liposomes as drug delivery system for therapeutic applications. *Int J Pharm* (2021) **601**:120571. doi:10.1016/j.ijpharm.2021.120571

32. Zhang X, Tu S, Tian J, Liang Y, An Y, Zhang T, et al. Liposome-based nanoparticle delivery systems for lung diseases: opportunities and challenges. *Int J Nanomedicine* (2025) **20**:12485–509. doi:10.2147/ijn.S538382

33. Bhattacharjee S. DLS and zeta potential - what they are and what they are not? *J Control Release* (2016) **235**:337–51. doi:10.1016/j.jconrel.2016.06.017

34. Zhao G, Xue L, Geisler HC, Xu J, Li X, Mitchell MJ, et al. Precision treatment of viral pneumonia through macrophage-targeted lipid nanoparticle delivery. *Proc Natl Acad Sci U S A* (2024) **121**:e2314747121. doi:10.1073/pnas.2314747121

35. Yin C, Tian Y, Yan A, Wang H, Lu F, Li X, et al. Mitigating inflammation and fibrosis: the therapeutic potential of quercetin liposomes in COPD. *Front Pharmacol* (2024) **15**:1503283. doi:10.3389/fphar.2024.1503283

36. Moles E, Chang DW, Mansfeld FM, Duly A, Kimpton K, Logan A, et al. EGFR targeting of liposomal doxorubicin improves recognition and suppression of non-small cell lung cancer. *Int J Nanomedicine* (2024) **19**:3623–39. doi:10.2147/ijn.S450534

37. Spigel DR, Dowlati A, Chen Y, Navarro A, Yang JC, Stojanovic G, et al. RESILIENT part 2: a randomized, open-label phase III study of liposomal irinotecan *versus* topotecan in adults with relapsed small cell lung cancer. *J Clinical Oncology : Official Journal Am Soc Clin Oncol* (2024) **42**:2317–26. doi:10.1200/jco.23.02110

38. Herrero R, Sanchez G, Lorente JA. New insights into the mechanisms of pulmonary edema in acute lung injury. *Ann Translational Medicine* (2018) **6**:32. doi:10.21037/atm.2017.12.18

39. Qiao Q, Liu X, Yang T, Cui K, Kong L, Yang C, et al. Nanomedicine for acute respiratory distress syndrome: the latest application, targeting strategy, and rational design. *Acta Pharmaceutica Sinica B* (2021) **11**:3060–91. doi:10.1016/j.apsb.2021.04.023

40. Duan Y, Learoyd J, Meliton AY, Leff AR, Zhu X. Inhibition of Pyk2 blocks lung inflammation and injury in a mouse model of acute lung injury. *Respir Res* (2012) **13**:4. doi:10.1186/1465-9921-13-4

41. Hassibi S, Donnelly LE. Macrophage dysfunction in respiratory disease. *Results Problems Cell Differentiation* (2024) **74**:239–56. doi:10.1007/978-3-031-65944-7_9

42. Wang J, Xue X, Zhao X, Luo L, Liu J, Dai S, et al. Forsythiaside A alleviates acute lung injury by inhibiting inflammation and epithelial barrier damages in lung and colon through PPAR-γ/RXR-α complex. *J Adv Res* (2024) **60**:183–200. doi:10.1016/j.jare.2023.08.006

43. Groß CJ, Mishra R, Schneider KS, Médard G, Wettmarshausen J, Dittlein DC, et al. K(+) efflux-independent NLRP3 inflammasome activation by small molecules targeting mitochondria. *Immunity* (2016) **45**:761–73. doi:10.1016/j.immuni.2016.08.010

44. Peng W, Chang M, Wu Y, Zhu W, Tong L, Zhang G, et al. Lyophilized powder of mesenchymal stem cell supernatant attenuates acute lung injury through the IL-6-p-STAT3-p63-JAG2 pathway. *Stem Cell Res Ther* (2021) **12**:216. doi:10.1186/s13287-021-02276-y

45. Hommes DW, Peppelenbosch MP, van Deventer SJ. Mitogen activated protein (MAP) kinase signal transduction pathways and novel anti-inflammatory targets. *Gut* (2003) **52**:144–51. doi:10.1136/gut.52.1.144

46. Herold S, Mayer K, Lohmeyer J. Acute lung injury: how macrophages orchestrate resolution of inflammation and tissue repair. *Front Immunol* (2011) **2**:65. doi:10.3389/fimmu.2011.00065

47. Mazer M, Unsinger J, Drewry A, Walton A, Osborne D, Blood T, et al. IL-10 has differential effects on the innate and adaptive immune systems of septic patients. *J Immunology (Baltimore, Md : 1950)* (2019) **203**:2088–99. doi:10.4049/jimmunol.1900637

48. Harris AJ, Mirchandani AS, Lynch RW, Murphy F, Delaney L, Small D, et al. IL4Rα signaling abrogates hypoxic neutrophil survival and limits acute lung injury responses *in vivo*. *Am J Respir Crit Care Med* (2019) **200**:235–46. doi:10.1164/rccm.201808-1599OC

49. Herb M, Schramm M. Functions of ROS in macrophages and antimicrobial immunity. *Antioxidants (Basel)* (2021) **10**:313. doi:10.3390/antiox10020313

50. Jin Z, Chun SK, Ma D. Perioperative "remote" acute lung injury: recent update. *J Biomedical Research* (2017) **31**:197–212. doi:10.7555/jbr.31.20160053

51. Ho E, Karimi GK, Liu CC, Bhindi R, Figtree GA. Biological markers of oxidative stress: applications to cardiovascular research and practice. *Redox Biol* (2013) **1**:483–91. doi:10.1016/j.redox.2013.07.006

52. Kozower BD, Christofidou-Solomidou M, Sweitzer TD, Muro S, Buerk DG, Solomides CC, et al. Immunotargeting of catalase to the pulmonary endothelium alleviates oxidative stress and reduces acute lung transplantation injury. *Nat Biotechnology* (2003) **21**:392–8. doi:10.1038/nbt806

53. Liu H, Li Y, Sun S, Xin Q, Liu S, Mu X, et al. Catalytically potent and selective clusterzymes for modulation of neuroinflammation through single-atom substitutions. *Nat Communications* (2021) **12**:114. doi:10.1038/s41467-020-20275-0

54. Rochette L, Lorin J, Zeller M, Guilland JC, Lorgis L, Cottin Y, et al. Nitric oxide synthase inhibition and oxidative stress in cardiovascular diseases: possible therapeutic targets? *Pharmacol Ther* (2013) **140**:239–57. doi:10.1016/j.pharmthera.2013.07.004

55. Ozkanlar S, Ozkanlar Y, Kara A, Dalkilinc E. Astaxanthin alleviates lung injury by regulating oxidative stress, inflammatory response, P2X7 receptor, NF-kappaB, Bcl-2, and Caspase-3 in LPS-induced endotoxemia. *Environ Toxicol* (2025) **40**:924–34. doi:10.1002/tox.24481

56. Ulas N, Ozkanlar S, Yildirim S, Aydin O, Ozkanlar Y. French maritime pine bark extract alleviates lung injury by regulating inflammatory-oxidative-apoptotic pathway and P2X7 receptor expression in LPS-induced sepsis. *Curr Issues Mol Biol* (2025) **47**:770. doi:10.3390/cimb47090770

57. Ulas N, Ustundag H, Ozkanlar S, Erbas E, Kara A, Ozkanlar Y. D-carvone attenuates LPS-induced acute lung injury via TLR4/NF-kappaB and Nrf2/HO-1 signaling pathways in rats. *Naunyn Schmiedebergs Arch Pharmacol* (2025) **398**:12215–25. doi:10.1007/s00210-025-04024-y

58. Suzuki T, Takahashi J, Yamamoto M. Molecular basis of the KEAP1-NRF2 signaling pathway. *Mol Cells* (2023) **46**:133–41. doi:10.14348/molcells.2023.0028

59. Chen Z, Zhong H, Wei J, Lin S, Zong Z, Gong F, et al. Inhibition of Nrf2/HO-1 signaling leads to increased activation of the NLRP3 inflammasome in osteoarthritis. *Arthritis Research & Therapy* (2019) **21**:300. doi:10.1186/s13075-019-2085-6

60. Kang JY, Xu MM, Sun Y, Ding ZX, Wei YY, Zhang DW, et al. Melatonin attenuates LPS-induced pyroptosis in acute lung injury by inhibiting NLRP3-GSDMD pathway via activating Nrf2/HO-1 signaling axis. *Int Immunopharmacol* (2022) **109**:108782. doi:10.1016/j.intimp.2022.108782

EBM Experimental Biology and Medicine

EBM is the official journal of the Society for Experimental Biology and Medicine

Experimental Biology and Medicine (EBM) is a global, peer-reviewed journal dedicated to the publication of multidisciplinary and interdisciplinary research in the biomedical sciences.

Discover more of our Special Issues

See more →

Contact

development@ebm-journal.org

See more

ebm-journal.org

publishingpartnerships.frontiersin.org/our-partners